Structural characterisation of MDM2 RING domain: E2-ubiquitin binding and activation by phosphorylation

Helge Magnus Magnussen
MSc

Submitted in fulfilment of the requirement for the degree of Doctor of Philosophy (PhD)

Cancer Research UK - Beatson Institute

Institute of Cancer Sciences
College of Medicine, Veterinary and Life Sciences
University of Glasgow

September 2019

Abstract

The RING E3 ligase MDM2 is a primary negative regulator of the tumour suppressor protein p53. It blocks transcriptional activity and ubiquitinates p53, resulting in proteasomal degradation. MDM2's ligase activity depends on the dimerisation of its C-terminal RING domain with either itself or its homologue MDMX. The crystal structure of the MDM2-MDMX heterodimer RING domain in complex with E2-ubiquitin has recently been crystallised. In this complex, only the MDM2 RING domain binds an E2-ubiquitin complex whereas the MDMX RING domain does not. However, MDMX's C-terminal tail supports ubiquitin binding. This complex assembly results in one MDM2-MDMX RING heterodimer bound to one E2-ubiquitin complex. Due to extensive aggregation of the MDM2 homodimer, no structural information of the homodimeric MDM2-E2-ubiquitin complex has been obtained to date.

During the course of my studies, I developed a purification protocol to generate non-aggregated homodimeric MDM2 RING domain. Sufficient amounts of homogeneous protein could be isolated for crystallisation purposes and crystal structures of the MDM2 homodimer alone and in complex with E2-ubiquitin were obtained. The crystal structures show that the homodimer can simultaneously bind two molecules of E2-ubiquitin. The E2-ubiquitin binding surface resembles the heterodimer but shows significant differences in the arrangement of helices adjacent to the RING domain.

Upon DNA damage, p53 needs to be stabilised in order to trigger cell cycle arrest or apoptosis. This requires p53 to be uncoupled from MDM2-mediated downregulation and is achieved by a number of phosphorylation events on both proteins, which reduce the binding affinity between p53 and MDM2. However, mouse models suggest that additional mechanisms exist as p53 is stabilised even when the corresponding phosphorylation sites are mutated. In addition, p53 is reportedly stabilised by phosphorylation of MDM2 near the RING domain, a region that is sequentially far away from the p53-binding domain. So far, the molecular basis of this mechanism has been elusive. Here, I show that phosphorylation near the RING domain enhances MDM2's catalytic activity. With my MDM2 purification protocol, homodimeric phospho-MDM2 was generated and the crystal structure in complex with E2-ubiquitin was obtained. The molecular basis and homodimer-specificity of this novel phosphoregulation will be discussed.

The results presented here help to understand the molecular function of MDM2, particularly under DNA damage conditions, and might be beneficial in diagnostics. The purification protocol of homogeneous MDM2 RING domain will be helpful for further structure-based studies such as the design of an MDM2 RING domain inhibitor.

Table of Contents

Abstract i

Table of Contents ii

List of Tables vi

List of Figures viii

Acknowledgements xxi

Author's Declaration xxii

Abbreviations xxiii

Chapter 1 Introduction 1

1.1 The ubiquitin system 1

1.1.1 Ubiquitin 3

1.1.2 Other UBLs 5

1.1.3 E1s 6

1.1.4 E2s 7

1.1.5 E3s 11

1.1.6 Downstream pathway of ubiquitinated substrates 19

1.2 The E3 RING ligase MDM2 20

1.2.1 C-terminal RING domain 21

1.2.2 N-terminal p53 binding domain 24

1.2.3 Domains between p53 binding domain and RING domain 25

1.2.4 MDM2 regulation 26

1.2.5 MDM2 evolution 28

1.3 MDM2's role in p53 regulation 28

1.3.1 p53 28

1.3.2 MDM2-p53 interaction under unstressed conditions 29

1.3.3 MDM2-p53 interaction under DNA damage 30

1.3.4 MDM2 as a drug target for p53 activation 33

1.4 Objectives 35

Chapter 2 Methods 36

2.1 Cloning 36

2.1.1 Traditional cloning 37
2.1.2 Overlap extension PCR 37
2.1.3 Site-directed mutagenesis 38
2.1.4 Transformation and plasmid amplification 38
2.2 Protein expression 38
2.2.1 *Escherichia coli* BL21(DE3) GOLD 39
2.2.2 *Escherichia coli* EcAr7 40
2.2.3 Glycerol stocks 40
2.3 Protein purification 41
2.3.1 Lysis 41
2.3.2 Chromatography 41
2.3.3 Concentrating and storage 44
2.4 Biochemical techniques 45
2.4.1 SDS-PAGE 45
2.4.2 Western blot 45
2.4.3 Protein quantification 46
2.5 Crystallisation 46
2.5.1 Initial screening 46
2.5.2 Crystal optimisation and seeding 47
2.5.3 Cryo protection and data collection 48
2.5.5 Data processing and model building 51
2.6 Surface Plasmon Resonance 53
2.7 Autoubiquitination assays 53
2.7.1 Rate determination 54
Chapter 3 Purification and Structural characterisation of the MDM2 homodimer in complex with E2-Ub 55
3.1 Strategies for purification of human MDM2 RING domain 55
3.1.1 Aggregation of the RING domain 55
3.1.2 Extended N-terminal linker increases dimeric fraction 56
3.1.3 MBP fusion constructs stabilise the RING domain 59
3.2 Structural characterisation of zebrafish (*Danio rerio*) MDM2 RING domain 62
3.2.1 Purification and E2-Ub binding 64
3.2.2 Crystallisation and structure determination 66
3.2.3 Crystal structure 67
3.3 Structural characterisation of western clawed frog MDM2 RING domain 71
3.3.1 Purification and E2-Ub binding 72

3.3.2 Crystallisation 73
3.3.4 Crystal structure of MDM2^{f} 76
3.3.5 Crystal structure of MDM2^{f} in complex with UbcH5B-Ub 78
3.3.6 Extending the N-terminal linker in MDM2^{f} 82
3.4 Structural characterisation of human MDM2 RING domain (G443T) 84
3.4.1 Construct design 84
3.4.2 Purification and E2-Ub binding 87
3.4.3 Crystallisation 89
3.4.4 Crystal structure of the MDM2^{G443T}-UbcH5B-Ub complex 90
3.5 Structural characterisation of human MDM2 RING domain (wild-type) 93
3.5.1 Purification 94
3.5.2 Crystallisation 94
3.5.3 Crystal structure of the MDM2WT-UbcH5B-Ub complex 96
3.6 Structure validation 97
3.7 Summary and Discussion 99
Chapter 4 Phosphoregulation of MDM2 homodimer 104
4.1 Phosphorylation effect on catalytic activity of MDM2 104
4.1.1 SPR binding analyses of phosphomimetic MDM2 variants 104
4.1.2 Catalytic activity of phosphomimetic MDM2 107
4.2 Structural characterisation of phosphomimetic MDM2 108
4.2.1 Crystallisation of MDM2 S429D 108
4.2.2 Design of MDM2 S429E constructs with different N-terminal linkers 109
4.2.4 Crystallisation of MDM2 S429E 111
4.2.5 Crystal structure of MDM2 S429E 114
4.3 Structural characterisation of phospho-MDM2 119
4.3.1 Purification strategy 119
4.3.2 Initial crystallisation attempts 122
4.3.3 Crystal structure of phospho-MDM2^{c}-UbcH5B-Ub 126
4.4 Structural difference between homodimer and heterodimer 128
4.4.1 Positioning of S429 128
4.4.2 Crystal structure of MDM2^{c} in the absence of UbcH5B-Ub 132
4.5 S429-phosphorylation in cells 135
4.6 Crystal structure of MDM2 '5D1E' with UbcH5B-Ub 138
4.7 Summary and Discussion 142
Chapter 5 Conclusion 144

Bibliography 148

List of Tables

Table 2-1: Expression vectors used in this study. The sequence of the TEV cleavage site, which connects the N-terminal fusion tag with the protein, is ENLYFQGS in all vectors. 36

Table 2-2: Separation techniques used for the first purification step. Nickel and GSH affinity chromatography buffers contained 400 mM NaCl for MDM2 constructs shorter than 390-C and 200 mM NaCl for all other proteins. 42

Table 2-3: Commercial crystal screens used for initial screening attempts. The screens used for each protein construct are indicated with (X). The following screens were used: Cl (JBScreen Classic HTSI), In (Index), Mo (Morpheus®), PA (PACT *premier*™), PE (PEGs Suite), Pr (ProPlex™), JC (JCSG-*plus*™), BC (The BCS Screen), MI (MIDASplus™). 47

Table 2-4: Crystallisation and cryoprotection buffer for each diffracting crystal of this study. Wherever a crystallisation buffer of a commercial screen was used, the corresponding screen is indicated in parenthesis. No cryoprotection buffer was added to crystallisation buffers that already contained cryoprotectants. 49

Table 2-5: Software packages used for data processing of each dataset. 51

Table 2-6: NCS and TLS restraints and B-factor calculation used for each dataset. 52

Table 3-1: Yields of MDM2 350-C '6D' after AIEC and SEC obtained per L of *E. coli* cells. 59

Table 3-2: Yields of MBP-MDM2 418-C after AIEC and SEC obtained per L of *E. coli* cells. 61

Table 3-3: Sequence comparison of MDM2 423-C (human nomenclature) for all known sequences (UniProtKB). Residues that are conserved among all listed species are highlighted in green in the human sequence. Residues that differ from the human sequence are coloured in red. Zn^{2+}-coordinating residues are highlighted in yellow, residues critical for E2-Ub recruitment are highlighted in purple. The number of amino acids that differ from the human sequence is indicated. Where more than one species was found with an identical sequence, only one species is listed and the number of identical sequences indicated in parenthesis. 63

Table 3-4: Yields of MDM2^{z} 423-C after AIEC and SEC obtained per L of *E. coli* cells. 65
Table 3-5: Data collection and refinement statistics for MDM2^{z} 423-C. Numbers in parenthesis indicate the statistics for the outer shell..... 67
Table 3-6: Data collection and refinement statistics for all MDM2^{f} datasets. Numbers in parenthesis indicate the statistics for the outer shell. 74
Table 3-7: Data collection and refinement statistics for MDM2^{f}-UbcH5B-Ub. Numbers in parenthesis indicate the statistics for the outer shell. 75
Table 3-8: Comparison of all MDM dimers. RMSD values (given in Å) of the MDM2^{f} dimers for MDM2^{z} (Chapter 3.2), MDM2-MDMX (PDB: 2VJF, chain A and B) and MDM2 (NMR, PDB: 2HDP, model 19). Where a dataset contained more than one dimer in the unit cell, the individual dimers are indicated with #..... 78
Table 3-9: Yields of MDM2^{f} 361-C and 389-C after SEC obtained per L of *E. coli* cells. 83
Table 3-10: Data collection and refinement statistics for MDM2^{f} 389-C in complex with UbcH5B-Ub. Numbers in parenthesis indicate the statistics for the outer shell. 83
Table 3-11: Data collection and refinement statistics for MDM2^{G443T} in complex with UbcH5B-Ub. Numbers in parenthesis indicate the statistics for the outer shell. 90
Table 3-12: Data collection and refinement statistics for MDM2^{WT} in complex with UbcH5B-Ub. Numbers in parenthesis indicate the statistics for the outer shell. 96
Table 3-13: Summary of the purified MDM2 constructs. Overview of the yields of dimeric protein after the final purification step (SEC) and the crystallisation success. 100
Table 4-1: Sequence of MDM2 423-435 from selected species. Species were selected where the sequence of residues 423-425 significantly differed from other sequences and where S429 was conserved..... 110
Table 4-2: RING domain residues (436-C) of selected species that are not conserved in either human, frog or zebrafish MDM2..... 110
Table 4-3: Data collection and refinement statistics for MDM2^{c} S429E and MDM2^{g} S429E in complex with UbcH5B-Ub. Numbers in parenthesis indicate the statistics for the outer shell. 112

Table 4-4: Data collection and refinement statistics for MDM2^{o} S429E in complex with UbcH5B-Ub. Numbers in parenthesis indicate the statistics for the outer shell. 113
Table 4-5: Data collection and refinement statistics for MDM2^{t} S429E in complex with UbcH5B-Ub. Numbers in parenthesis indicate the statistics for the outer shell. 114
Table 4-6: Data collection and refinement statistics for MDM2 pS429 (phospho-crystal A) in complex with UbcH5B-Ub. Numbers in parenthesis indicate the statistics for the outer shell. 122
Table 4-7: Data collection and refinement statistics for MDM2^{c} pS429 (phospho-crystal B) in complex with UbcH5B-Ub. Numbers in parenthesis indicate the statistics for the outer shell. 124
Table 4-8: Data collection and refinement statistics for MDM2^{c} pS429 (phospho-crystal C) in complex with UbcH5B-Ub. Numbers in parenthesis indicate the statistics for the outer shell. 126
Table 4-9: Data collection and refinement statistics for MDM2^{c} S429E. Numbers in parenthesis indicate the statistics for the outer shell..... 133
Table 4-10: Data collection and refinement statistics for MDM2 380-C '5D1E' in complex with UbcH5B-Ub. Numbers in parenthesis indicate the statistics for the outer shell. 139

List of Figures

Figure 1-1: Ubiquitination cascade. (1) Ub is activated by E1 in a $Mg2^{+}$-ATP dependent manner. (2) Ub is transferred from E1 to E2. (3) E3 recruits E2 and the substrate. (4) E3 catalyses the Ub transfer from E2 to a substrate. (5) Substrate ubiquitination can be reversed by a DUB. 1
Figure 1-2: Crystal structure of Ub. The C-terminal tail covering L72-G76 is highlighted in red. M1 is highlighted in orange. Sticks are shown for residues through which chain elongation can occur (PDB: 1UBQ) (Vijay-Kumar et al., 1987). 3
Figure 1-3: Crystal structures of di-Ub. The proximal Ub (the Ub that serves as substrate for chain elongation) is shown in yellow, the distal Ub in orange. Linkage type/PDB: M1/3AXC (Rohaim et al., 2012), K6/2XK5 (Virdee et al.,

2010), K11/3NOB) (Matsumoto et al., 2010), K27/5GOD (Gao et al., 2016), K29/4S22 (Kristariyanto et al., 2015a), K33/ 4XYZ (Kristariyanto et al., 2015b), K48/1AAR (Cook et al., 1992), K63/2JF5 (Komander et al. (2009)...4
Figure 1-4: Crystal structure of UbcH5B. The catalytic cysteine (C85), highlighted as stick, is the conjugation site for Ub. The fold of UbcH5 involving four α-helices and four ß-strands, is called UBC domain and highly conserved among other E2s (PDB: 2ESK) (Ozkan et al., 2005). 8
Figure 1-5: Crystal structures of the UbcH5B-Ub conjugate. The E2-Ub conjugate is shown in the unbound state (left, PDB: 3A33) (Sakata et al., 2010), where it adopts an 'open conformation' and in complex with a RING E3 ligase (here: RNF38, shown in grey), without (middle, PDB: 4V3K) and with (right, PDB: 4V3L) (Buetow et al., 2015) backside binding of a non-covalent Ub. Independently of the backside Ub, E2-Ub adopts a 'closed conformation' in the presence of a RING E3. UbcH5B is shown in cyan, Ub in yellow. A single point mutation (S22R) prevents backside binding. The corresponding residue is highlighted in red and shown as stick. 9
Figure 1-6: Examples for E2s. The NMR model of UBE2W (left, PDB: 2MT6) shows the disordered C-terminus of this E2 (Vittal et al., 2015). UBE2S (middle, PDB: 1ZDN) adopts a more rigid structure, comparable to UbcH5B (Sheng et al., 2012), whereas UBE2K (right, PDB: 6IF1) (Lee et al., 2018) has an additional C-terminal UBA domain (coloured in grey). The catalytic cysteine residues are shown as sticks. 10
Figure 1-7: Mechanism of RING E3 ligase mediated ubiquitination. RING E3s act as scaffolds by simultaneously recruiting E2~Ub (to the RING domain) and the substrate (to the substrate binding domain). This allows direct Ub transfer from the E2 to the substrate. 11
Figure 1-8: Crystal structures of monomeric RING E3s in complex with E2-Ub. In the RNF38-UbcH5B-Ub complex (left, PDB: 4V3K) (Buetow et al., 2015), RNF38 is coloured in grey, UbcH5B in cyan and Ub in yellow. In the CBL-B-UbcH5B-Ub complex (right, PDB: 3ZNI) (Dou et al., 2013), only residues 351-427 of CBL-B (orange) are shown. Close-up views (bottom) show the stabilisation mechanisms of the RING E3s for E2-Ub. Dashes indicate hydrogen bonds, grey spheres Zn^{2+} ions. 13
Figure 1-9: Crystal structures of homodimeric RING E3 ligases in complex with E2-Ub. In each crystal structure, the dimer binds two E2-Ub simultaneously.

For simplification, only one E2-Ub is shown. (A) BIRC7-UbcH5B-Ub (PDB 4AUQ) (Dou et al., 2012b). (B) RNF4-UbcH5A-Ub (PDB 4AP4) (Plechanovova et al., 2012). (C) TRIM25-UbcH5A-Ub (PDB 5FER) (Koliopoulos et al., 2016). (D) TRAF6-UBE2N-Ub (PDB 5VO0) (Middleton et al., 2017). 14
Figure 1-10: Mechanism of HECT E3 ligase mediated ubiquitination. HECT E3s recruit E2~Ub, from where the Ub is first transferred onto a cysteine residue within the HECT domain, forming a covalent E3~Ub intermediate. In a second step, Ub is further transferred onto a substrate. 16
Figure 1-11: Mechanism of RBR E3 ligase mediated ubiquitination. RBR E3s contain two RING domains. They recruit E2~Ub to the first RING domain (RING1), from where it is then transferred onto the catalytic cysteine of the second RING domain (RING2), forming an E3~Ub intermediate. From RING2, Ub is further transferred onto a substrate. 17
Figure 1-12: Mechanism of RCR E3 ligase mediated ubiquitination. RCR E3s contain two catalytic cysteines. They recruit E2~Ub to the RING domain and form an E3~Ub through a cysteine on a flexible loop. This loop then undergoes a conformational change and transfers Ub onto a second catalytic cysteine, from which it is further transferred onto a a threonine or serine residue on the substrate. 18
Figure 1-13: Domain architecture of MDM2 and MDMX. Regions coloured in cream are predicted to be mainly disordered..... 21
Figure 1-14: Crystal structures of the MDM2-MDMX heterodimer. MDM2-MDMX (upper left, PDB: 2VJF) (Linke et al., 2008). MDM2-MDMX in complex with UbcH5B-Ub (upper right, PDB: 5MNJ) (Nomura et al., 2017). MDM2 is coloured in orange, MDMX in green, UbcH5B in cyan and Ub in yellow. A close-up view of MDM2-MDMX-UbcH5B-Ub (bottom) shows important residues for E2-Ub stabilisation. 22
Figure 1-15: NMR model of the MDM2 RING homodimer. 20 solution structures with the lowest energy are superimposed (PDB: 2HDP) (Kostic et al., 2006), where each dimer is shown in a different colour. 23
Figure 1-16: Model for the MDM2 homodimer RING in complex with UbcH5B-Ub. The protomers are coloured in orange and purple. The model was created by superimposing monomeric MDM2-UbcH5B-Ub from the MDM2-MDMX-UbcH5B-Ub structure onto MDMX within the MDM2-MDMX-UbcH5B-Ub complex. 23

Figure 1-17: Crystal structure of MDM2-p53. MDM2 (residues 25-109) is shown in green, p53 (residues 17-28) in blue (PDB: 1YCR) (Kussie et al., 1996). 25
Figure 1-18: Crystal structure of MDM2-RPL11. MDM2's zinc finger domain (293-334) is shown in green, RPL11 (PDB: 4XXB) in orange (Zheng et al., 2015). The Zn^{2+} ion is shown as a grey sphere. 26
Figure 1-19: Domain architecture of p53. Regions coloured in cream are predicted to be mainly disordered. 29
Figure 2-1: Purification of UbcH5B-Ub. Reaction before the addition of Ub (RXN-Ub), reaction after 18 h (RXN 18 h), Nickel affinity chromatography elution (Nickel elution), TEV cleavage, Pass-back onto Nickel beads, CIEC, SEC. .. 43
Figure 3-1: Initial purification attempt of MDM2 428-C. (A) Chromatogram of an AIEC run showing the elution profile of MBP-tagged MDM2 (blue) using a NaCl gradient (red). (B) SDS-PAGE of the peak fraction of the AIEC run. (C) Chromatogram of a SEC run of cleaved (green) and uncleaved (blue) MDM2. Elution profiles are normalised. (D) SDS-PAGE for the SEC elution profile of cleaved MDM2. 56
Figure 3-2: SPR binding analyses of MDM2 350-C WT and '6D' for UbcH5B-Ub. Representative sensorgrams (left) and binding curves with the estimated K_d (right). 57
Figure 3-3: Purification of MDM2 350-C '6D'. (A) Chromatogram of an AIEC run showing the elution profile of cleaved MDM2 350-C '6D' (blue) using a NaCl gradient (red). (B) SDS-PAGE of different fractions of the AIEC run. (C) Chromatogram of a SEC run of the first (blue) and second (green) peak in the AIEC run. (D) SDS-PAGE for the SEC elution of the first AIEC peak. 58
Figure 3-4: Design of the MBP-MDM2 fusion constructs. (A) Crystal structure of MDM2 (yellow)-MDMX (grey) bound to E2-Ub (black). MDM2's S429 is highlighted in red. (B) Design of MBP-MDM2 fusion constructs with different linker lengths. (C) SPR binding affinity experiments for E2-Ub. Representative sensorgrams (left) and binding curves with the estimated K_d (right). 60
Figure 3-5: Purification of MBP-MDM2 418-C. (A) Chromatogram of an AIEC run showing the elution profile (blue) using a NaCl gradient (red). (B) Chromatogram of a SEC run of MBP-MDM2 418-C (green) in comparison to MBP-TEV MDM2 428-C (blue). Elution profiles are normalised. 61

Figure 3-6: Purification of MDM2^{Z} 423-C. (A) Chromatogram of an AIEC run showing the elution profile (blue) using a NaCl gradient (red). (B) SDS-PAGE showing the AIEC elution (el) peak and the separation of MDM2 from His-MBP after TEV cleavage via pass-back. (C) Chromatogram of a SEC run of the cleaved protein. (D) SDS-PAGE of single fractions of C. 64
Figure 3-7: SPR binding analysis of MDM2^{Z} 423-C. (A) Crystal structure of human MDM2-MDMX (yellow-grey) bound to E2-Ub (black). Residues that are not conserved between MDM2^{Z} and human MDM2 are highlighted in red. (B) E2-Ub binding analysis for MDM2^{Z}. Representative sensorgrams (left) and binding curves with the estimated K_d (right). 65
Figure 3-8: Representative MDM2^{Z} crystals. Needle-shaped crystals were obtained in many conditions, the crystals shown in the right image diffracted to 2.87 Å. The length of the white bar corresponds to 300 µm. 66
Figure 3-9: Crystal structure of MDM2^{Z}. MDM2^{Z} (green; top panel) in comparison to the NMR model (PDB: 2HDP) for the human homodimer (pink/purple; bottom left panel) and the crystal structure (PDB: 2VJF) of the human MDM2-MDMX heterodimer (purple/orange; bottom right panel). RMSD values are given for residues for the C_α atoms of 436-C. Zn^{2+} ligands are shown as grey spheres. 68
Figure 3-10: Close-up of the C-terminal tail of MDM2^{Z}. (A) Human MDM2-MDMX (PDB: 2VJF). MDMX is coloured in orange, MDM2 in purple. (B) MDM2^{Z}. The two protomers are coloured in bright and dark green. (C) Superimposition of MDM2^{Z} and MDM2-MDMX. In MDM2^{Z}, M490 blocks the formation of N-terminal helices such as in the heterodimer structure. In the heterodimer, the corresponding residue (I489) lies within a hydrophobic environment consisting of L433, L457, V487 (MDMX) and A434 (MDM2). M490 would clash with a helix like in the heterodimer, thus requiring a different structural arrangement. As a consequence, A434 (MDM2) and C434^{Z} are positioned differently. 69
Figure 3-11: The N-terminal helices of the heterodimer form crystal contacts. Symmetry related molecules are coloured in grey. (A) Crystal packing of MDM2^{Z} (left) and the heterodimer (right). (B) Crystal contacts of MDM2^{Z} (left) and both dimers in the asymmetric unit of the heterodimer structure (middle and right). 70

Figure 3-12: MDM2^{z} might be stabilised by two additional hydrogen bonds. Crystal structure of MDM2^{z} (green; left) in comparison to the NMR model (pink/purple; right). Potential hydrogen bonds L458^{z}-S491^{z} (3.5 Å) and R454^{z}-Y462^{z} (4.5 Å) are indicated with dashes. 71

Figure 3-13: Purification and binding analysis of MDM2^{f} 423-C. (A) Chromatogram of a SEC run of the cleaved protein. (B) SDS-PAGE of single SEC fractions. (C) SPR binding analysis for UbcH5B-Ub. Representative sensorgrams (left) and binding curves with the estimated K_d (r ight)..... 72

Figure 3-14: Thick needle-shaped crystals were obtained for MDM2^{f}. The crystals shown here were obtained from identical buffer conditions, at pH 8 (left) and pH 7 (r ight) (Table 2-4). The length of the white bar corresponds to 300 µm. 73

Figure 3-15: Crystals of the MDM2^{f}-UbcH5B-Ub complex. Initial crystals (left), after optimisation (m iddle) and seeding (right). The length of the white bar corresponds to 300 µm..... 75

Figure 3-16: Crystal structure of MDM2^{f}. (A) Overall structure. The two protomers are coloured in bright and dark blue. (B) Close-up of the C-terminal tail. (C) Superimposition with human MDM2-MDMX heterodimer (purple/orange) shows that F490 adopts, in contrast to M490 in MDM2^{z} (Figure 3-10), a similar conformation as MDMX's I489..... 76

Figure 3-17: Comparison of the seven crystallographic independent dimers for MDM2^{f}. Hydrogen bonds and salt bridges are indicated in red, other crystal contacts in yellow. Residues that are not involved in crystal contacts in any of the dimers are coloured in green. Residues that are not involved in crystal contacts in a particular chain are coloured in bright and dark blue as in Figure 3-16A. For dimer #D, crystal 3, a representative measurement of the diameter is shown. 77

Figure 3-18: Crystal structure of MDM2^{f} bound to E2-Ub. MDM2^{f} (blue) binds two UbcH5B-Ub conjugates (cyan/yellow) simultaneously. UbcH5B-Ub adopts the closed conformation like in other reported RING E3-E2-Ub complexes..... 78

Figure 3-19: MDM2^{f} is more compressed when bound to E2-Ub. (A) MDM2^{f} bound to E2-Ub (dark red) superimposed on free MDM2^{f} (green, crystal 3, dimer #A). (B) Close-up view of residues affected by the re-orientation of the α-helix upon E2-Ub binding. (C) In the absence of E2-Ub, the hydrogen bond

network between K469, Q483 and G453 is missing and I485 orientates towards the α-helix. 79
Figure 3-20: Interactions between MDM2^{f} and UbcH5B-Ub. (A) A hydrophobic batch around I440 stabilises UbcH5B. (B) The linchpin arginine R479 stabilises UbcH5B-Ub in its closed conformation. (C) The C-terminal tail of the second MDM2 molecule interacts with Ub. 80
Figure 3-21: Secondary structure prediction for MDM2^{f} using different tools provided by the server Jpred 4. Comparison between MDM2^{f} 359-C and the crystal structure obtained in this study. Helices are indicated in green, ß-barrels in orange. Residues that were not present in the construct used for crystallisation are indicated with a dash. Residues with no observable electron density are indicated in blue. 82
Figure 3-22: Solubility of human MDM2 constructs with point mutations of MDM2^{f} and MDM2^{z}. Human WT (h), I435V (IxV), G443T (GxT), K454R (KR), Q480E (QE), chimera MDM2^{z}/human MDM2 (z/h), chimera frog MDM2^{f}/human MDM2 (f/h), MDM2^{f} (f). (A-D) Purification attempt 1 (1 L LB). (A) Cell lysate after sonication. (B) Supernatant after sonication. (C) GSH Sepharose elution. (D) Yield after GSH Sepharose affinity chromatography relative to human MDM2. (E-G) Purification attempt 2 (3 L LB). (E) SEC run of cleaved human MDM2. (F) SEC run of cleaved MDM2^{f}. (G) Yield after GSH Sepharose affinity chromatography relative to human MDM2 (h)..... 86
Figure 3-23: Purification of human MDM2^{G443T}. (A) Chromatogram of a SEC run of the cleaved protein. (B) SDS-PAGE of single SEC fractions. 87
Figure 3-24: Contribution of MDM2's GT443 to UbcH5B-Ub binding. (A) In the crystal structure of MDM2^{f} in complex with UbcH5B-Ub, T443 forms different interactions with UbcH5B's K4 in the four MDM2^{f} molecules of the asymmetric unit. (B) SPR binding analysis for UbcH5B-Ub of human MDM2 in the presence of G443T. Representative sensorgrams (left) and binding curves with the estimated K_d (r ight). 88
Figure 3-25: Crystals of the human MDM2^{G443T}-UbcH5B-Ub complex. Crystals were obtained in the BCS Screen F3 (left) and E9 (r ight). The length of the white bar corresponds to 300 µm..... 89
Figure 3-26: Crystal structure of MDM2^{G443T} bound to UbcH5B-Ub. (A) Overall structure. (B) Close-up of the N-terminal helices in the homodimer. (C) The N-terminal helices in the MDM2 homodimer adopt a 3_{10}-helix. (D) Close-up of

L430 in the homodimer showing that it is stabilised by a hydrophobic clamp consisting of two proline residues. (E) Close-up of N433 in the homodimer showing that it stabilises the C-terminus of the second MDM2 molecule through hydrogen bonds, thereby creating a hydrogen bond network with Ub's K11. (F) Close-up of the N-terminal helices in the heterodimer (PDB: 5MNJ). (G) The N-terminal residues of MDM2 in the heterodimer form an α-helix, leading to a shift of residues beyond L432 as compared to the homodimer in D. (H) Close-up of L430 in the heterodimer showing that it is stabilised by different residues. (I) Close-up of N433 in the heterodimer showing that it cannot stabilise MDMX's C-terminal tail due to steric restriction of MDMX's I489. The stabilisation of Ub's K11 is therefore weaker than in the homodimer. 92

Figure 3-27: Interaction between MDM2's G443T and UbcH5B's K4 in both crystals structures. In each dimer, one G443T forms a weak hydrogen bond and the other one a hydrophobic interaction with K4. 93

Figure 3-28: Purification of $MDM2^{WT}$. (A) Chromatogram of a SEC run of the cleaved protein. (B) SDS-PAGE of single SEC fractions. 94

Figure 3-29: Crystals of the $MDM2^{WT}$-UbcH5B-Ub complex. Crystals were obtained in condition B6 of the BCS Screen (left) and optimised (r ight). The length of the white bar corresponds to 300 µm. 95

Figure 3-30: Position of G443 in the $MDM2^{WT}$-UbcH5B-Ub complex. G443 forms a hydrophobic interaction with UbcH5B's K4 in both molecules. The distance between the C_α atom of G443 and the C_δ atom of K4 is 4.2-4.3 Å. 97

Figure 3-31: Importance of the residues adjacent to the RING domain. (A) Autoubiquitination assay of MDM2. (B) Quantification of the autoubiquitination products in (A) relative to WT. (C) Autoubiquitination assay of human MDM2 and $MDM2^{f}$. (*) indicates the formation of E1-Ub. ... 99

Figure 3-32: Sequence similarity between human MDM2 and $MDM2^{f/z}$. The sequence of human MDM2 is shown. Residues that are either identical in $MDM2^{f}$, $MDM2^{z}$ or in both proteins are highlighted in green. Similar residues are highlighted in yellow and residues that are not conserved in $MDM2^{f/z}$ are highlighted in red. 102

Figure 4-1: SPR binding analysis of MDM2 homodimer variants for UbcH5B-Ub. Only MDM2 '6D' and S429D show an enhanced binding affinity for UbcH5B-

Ub. Dr Danny Huang expressed and purified the proteins and Dr Gary Sibbet undertook the SPR experiments..... 105
Figure 4-2: Position of S429 in the crystal structures of MDM2 bound to UbcH5B-Ub. (A) Homodimer (Chapter 3.5). There is no electron density for S429 in any of the crystal structures obtained for the homodimer, so that the position of S429 has to be estimated based on L430. (B) MDM2-MDMX heterodimer (PDB: 5MNJ). S429 faces towards the donor-Ub and is in close proximity to T12 (3.4-4.6 Å) and K11 (4.6-5.5 Å). 105
Figure 4-3: SPR binding analysis of '6D' MDM2-MDMX heterodimer for UbcH5B-Ub. The '6D' construct does not cause the same binding enhancement as in the homodimer. Dr Danny Huang expressed and purified the proteins and Dr Gary Sibbet undertook the SPR experiments..... 106
Figure 4-4: SPR binding analysis of $MDM2^{G443T}$ 419-C variants for UbcH5B-Ub. $MDM2^{G443T}$ 419-C S429D and S429E show a similar binding enhancement for UbcH5B-Ub as in MDM2 350-C. In contrast, a much weaker binding enhancement could be observed in the heterodimer..... 107
Figure 4-5: Autoubiquitination assay of $MDM2^{G443T}$ S429E using fluorescently labelled Ub. (A) Reduced SDS-PAGE showing the autoubiquitination products of MDM2 variants after 90 s. (B) A bar graph showing the relative ubiquitination of MDM2 S429E in comparison to WT in (A). (C) Reduced SDS-PAGE showing the autoubiquitination products of MDM2-MDMX variants after 90 s. (D) A bar graph showing the relative ubiquitination of MDM2-S429E-MDMX in comparison to WT in (C). (E) Reduced SDS-PAGE showing the autoubiquitination reaction at a fixed UbcH5B concentration over time. (F) A plot showing the rate of ubiquitination as measured in (E). (*) indicates E1-Ub. 108
Figure 4-6: Autoubiquitination assay of $MDM2^{f}$ S429E using fluorescently labelled Ub. Reduced SDS-PAGE showing the autoubiquitination products of MDM2 variants after 90 s. The $MDM2^{f}$ S429E variant does not boost the activity like in human MDM2. (*) indicates E1-Ub. 109
Figure 4-7: Crystals of MDM2 S429E from different species in complex with UbcH5B-Ub. The crystals diffracted to 1.6-2.2 Å. (A) $MDM2^{c}$. (B) $MDM2^{g}$. (C) $MDM2^{o}$ (Crystal A). (E) $MDM2^{t}$ (Crystal A). 111
Figure 4-8: Crystal structure of $MDM2^{c}$ S429E-UbcH5B-Ub. The crystal structure is very similar to human MDM2-UbcH5B-Ub. (A) Overall structure. (B) Close-up

of MDM2's N-terminal residues. E429 interacts with Ub's K33 and T14 via a water molecule, thereby stabilising E2-Ub in the closed conformation. (C) Extensive crystal contacts with a symmetry related UbcH5B molecule stabilise residues E424-E427. 116
Figure 4-9: Crystal structure of MDM2^{g} S429E-UbcH5B-Ub. The crystal structure is isomorphous to MDM2^{c}-UbcH5B-Ub. (A) Overall structure. (B) Close-up of the MDM2 molecule (orange) that formed the E429-K33 hydrogen bond in MDM2^{c}. The sidechain of E429 is invisible so this residue was built with an alanine stub instead. E427 forms a hydrogen bond with K144 of a symmetry related UbcH5B molecule. (C) In another MDM2 molecule, E429 is able to interact with Ub's K33 and T14 like in MDM2^{c} although the N-terminal residues of this MDM2 molecule are not involved in crystal contacts. 117
Figure 4-10: S429E has the same effect in MDM2^{c} and MDM2^{g} as in human MDM2. (A) SPR binding analysis of MDM2^{c} for UbcH5B-Ub. (B) Reduced SDS-PAGE showing the autoubiquitination products of MDM2 variants after 90 s using fluorescently labelled Ub. (*) indicates E1-Ub. 118
Figure 4-11: Effect of S429-phosphorylation on UbcH5B-Ub binding. (A) Western-blot of GST-phospho-MDM2 and phospho-MDM2^{c} using a pS429 specific antibody. (B) Coomassie-stained SDS-PAGE of the protein samples shown in (A). (C) SPR binding analysis of phospho-MDM2 for UbcH5B-Ub. 121
Figure 4-12: Position of (p)S429 in the crystal structure of phospho-MDM2^{c} in complex with UbcH5B-Ub (phospho-crystal A). The electron density map around residue 429, or if not visible, 430, is shown (radius: 10 Å). Hydrogen bonds formed by the ε-NH_2 of Ub's K33 are indicated with dashes. 123
Figure 4-13: Position of (p)S429 in the crystal structure of phospho-MDM2^{c} in complex with UbcH5B-Ub (phospho-crystal B). The electron density map around residue 429 is shown (radius: 10 Å). Hydrogen bonds formed by the ε-NH_2 of Ub's K33 are indicated with dashes. 125
Figure 4-14: Crystal structure of phospho-MDM2^{c}-UbcH5B-Ub (phospho-crystal C). (A) Close-up view of pS429 and the local electron density map (radius: 10 Å). Hydrogen bonds are indicated with dashes. (B) Overall structure. pS429 and Ub's K33 are presented as sticks. 127
Figure 4-15: Autoubiquitination assay with perturbed E429-K33 interaction using fluorescently labelled Ub. (A) Reduced SDS-PAGE showing the autoubiquitination products of MDM2 variants with Ub K33M. (B) A bar graph

showing the relative ubiquitination of MDM2 S429E in comparison to WT in (A). (C) Reduced SDS-PAGE showing the autoubiquitination products of MDM2 variants with Ub's K33E. (D) A bar graph showing the relative ubiquitination of MDM2 S429R in comparison to WT in (C). (*) indicates E1-Ub. 128
Figure 4-16: Superimposition of phospho-MDM2 and MDM2-MDMX in complex with UbcH5B-Ub. In the heterodimer, S429 is shifted by 10 Å, so that it cannot interact with Ub's K33, even if phosphorylated. 129
Figure 4-17: MDM2 autoubiquitination assay with disrupted 3_{10}-helices using fluorescently labelled Ub. (A) Reduced SDS-PAGE showing the autoubiquitination products of MDM2 variants. (*) indicates E1-Ub. (B) A bar graph showing the relative ubiquitination of the MDM2 variants in comparison to WT in (A). 129
Figure 4-18: Homodimer and heterodimer autoubiquitination assay with modified C-terminal tail using fluorescently labelled Ub. (A) Reduced SDS-PAGE showing the autoubiquitination products of MDM2 homodimer variants. (B) A bar graph showing the relative ubiquitination of the MDM2 variants in comparison to WT in (A). (C) Reduced SDS-PAGE showing the autoubiquitination products of MDM2-MDMX variants. (D) A bar graph showing the relative ubiquitination of the MDM2-MDMX variants in comparison to WT in (C). (*) indicates E1-Ub. 130
Figure 4-19: Homodimer and heterodimer autoubiquitination assay with misplaced S429 using fluorescently labelled Ub. (A) Reduced SDS-PAGE showing the autoubiquitination products of MDM2 variants. (*) indicates E1-Ub. (B) A bar graph showing the relative ubiquitination of the MDM2 variants in comparison to WT in (A). 131
Figure 4-20: Crystal structure of the MDM2-MDMX heterodimer 428-C. (A) In complex with UbcH5B-Ub (PDB: 5MNJ). (B) In the absence of UbcH5B-Ub (PDB: 2VJF). (C) Superimposition of (A) and (B). Upon E2-Ub binding, the N-terminal 3_{10}-helix transforms into an α -helix, thereby bringing S429 closer to the donor-Ub. 132
Figure 4-21: Crystal structure of $MDM2^{C}$ S429E. (A) Crystal structure as in three out the four crystallographic independent dimers. (B) In the fourth dimer, one of the N-terminal extensions faces perpendicular to the helices. (C). Superimposition of (A) and (B) with phospho-MDM2-UbcH5B-Ub (phospho-crystal C, phospho-MDM2 is shown in green). The homodimer adopts an

identical conformation in the presence of UbcH5B-Ub, as indicated by the position of F430. In the dimer shown in (B), F430 sits in a different environment, where it is no longer stabilised by hydrophobic residues of the second protomer. The sidechain for E429 was not visible in the absence of UbcH5B-Ub, so that alanine stubs were built instead. (D) Reduced SDS-PAGE showing the autoubiquitination products of MDM2 variants after 90 s. (*) indicates E1-Ub. 134

Figure 4-22: Stability and catalytic activity of phosphomimetic MDM2 variants in modified USOS cells. (A) Immunoblot showing the stability of GFP-MDM2 S429D and S429E after cycloheximide treatment for the indicated time, 24 h after transfection. (B) Immunoblot showing the ubiquitination of phosphomimetic MDM2 in cells that were additionally transfected with His-Ub and treated with MG132. The phosphomimetic variants show an enhanced ubiquitination, which is abolished in the presence of I440K, a mutation that disrupts E2-Ub binding. Hence, the Ub_n-MDM2 species are a product of MDM2 autoubiquitination. All experiments were performed by Dr Syed Feroj Ahmed. 135

Figure 4-23: p53 is stabilised in the presence of phosphomimetic MDM2. Immunoblot showing p53 and p21 levels in the presence of phosphomimetic MDM2 in unmodified U2OS cells transfected with GFP-MDM2 and Myc-p53. The experiment was performed by Dr Syed Feroj Ahmed. 136

Figure 4-24: Effect of DNA damage on MDM2's stability and activity. (A) Immunoblot showing the stability of MDM2 under unstressed conditions, and etoposide treatment after cycloheximide treatment for the indicated time. (B) Immunoblot showing S429 phosphorylation in the absence and presence of etoposide treatment. (C) Immunoblot showing the ubiquitination of MDM2 in cells that were additionally transfected with His-Ub after etoposide treatment in the presence of MG132. All experiments were performed by Dr Syed Feroj Ahmed. 138

Figure 4-25: Crystal structure of MDM2 380-C S386D, S395D, S407D, T419D, S425D, S429E in complex with UbcH5B-Ub. (A) Overall structure. There is no electron density beyond E427 in MDM2. E429 interacts with Ub's K33 and T14 via a water molecule like in the crystal structures of $MDM2^c$ and $MDM2^g$. The symmetry related MDM2 molecule is highlighted in purple. (B) Crystal

packing. MDM2 dimers face towards each other, with a distance of 37 Å between E427 of two adjacent dimers..... 141
Figure 5-1: Superimposition of two MDM2-E2-Ub complexes with different E2 conformations. MDM2c S429E-UbcH5B-Ub is shown in purple/orange-cyan-yellow, MDM2c (p)S429-UbcH5B-Ub is shown in pale colours. Sidechains are shown for UbcH5B's R15..... 146

Acknowledgements

I would like to thank my supervisor Professor Danny T. Huang for giving me the opportunity to carry out this challenging project in his lab. I learned a lot about structural biology thanks to excellent supervision throughout the four years.

I am thankful for all R04 members (Dr Gary Sibbet, Dr Lori Buetow, Dr Mads Gabrielsen, Dr Mark Nakasone, Dr Syed Feroj Ahmed, Dr Karolina Majorek, Dr Amrita Patel, Dr Dominika Kowalczyk, Chatrin) for their great support in the lab.

A special thanks also to my interns Patricia Bryce and Fiona Kerr, who did a great job helping me with my project.

I enjoyed working in the CRUK Beatson Institute and I couldn't have done most of my work without the fantastic research services, particularly Central Service and Molecular Technology Services.

I am grateful to the European Research Council (Grant agreement ID 647849) that provided the funding to make this work possible.

Schließlich möchte ich mich bei meiner Familie bedanken für die Unterstützung zu jedem Zeitpunkt während meiner Studienzeit. Ohne Euch wäre all dies nicht möglich gewesen. Danke!!

Author's Declaration

This project was carried out in the Cancer Research UK Beatson Institute between October 2015 and September 2019 under the supervision of Professor Danny T. Huang.

I declare that this dissertation is a result of my own work unless otherwise indicated. This work has not been submitted for any other degree at the University of Glasgow or any other institution.

Helge Magnus Magnussen 30/09/2019

Abbreviations

APC/C	Anaphase promoting complex/cyclosome
AIEC	Anion exchange chromatography
ARF	Alternative open reading frame
ATG	Autophagy-related protein
ATM	Ataxia telangectasia mutated
ATP	Adenosine triphosphate
ß-Me	ß-Mercaptoethanol
ß-TRCP	ß-Transducin repeat containing
BARD1	BRCA1-associated RING domain protein 1
BIRC6,7	Baculoviral IAP repeat-containing protein 6,7
BRCA1	Breast cancer type 1 susceptibility protein
CBL	Casitas B-lineage lymphoma
CD	Circular dichroism
CIEC	Cation exchange chromatography
CIP	Alkaline phosphatase, calf intestinal
CK1	Casein kinase 1
CP	20S Core particle
COPS5	Constitutive photomorphogenic-9 signalosome subunit 5
CUL1	Cullin 1
DMSO	Dimethyl sulphoxide
DNA	Deoxyribonucleic acid
DNA-PK	DNA dependent protein kinase
DTT	Dithiothreitol
DUB	Deubiquitinating enzyme
DYRK1A	Dual specificity tyrosine-phosphorylation-regulated kinase 1A
E1	Ubiquitin activating enzyme
E2	Ubiquitin conjugating enzyme
E3	Ubiquitin ligase
E. coli	*Escherichia coli*
EDTA	Ethylenediaminetetraacetic acid
EM	Electron microscopy
ESCRT	Endosomal sorting complexes required for transport
FAT10	Human leukocyte antigen-F adjacent transcript 10

GSK3	Glycogen synthase kinase-3
GST	Glutathione *S*-transferase
HECT	Homologous to E6AP C-terminus
HEPES	4-(2-hydroxyethl)-1-piperazineethanesulphonic acid
IEC	Ion exchange chromatography
IPTG	Isopropyl ß-*D*-1-thiogalactopyranoside
ISG15	Interferon-stimulated gene 15
ITC	Isothermal titration calorimetry
JNK1	Mitogen-activated protein kinase 8
LB	Luria Bertani medium
MARCH7	Membrane-associated RING-CH-type finger 7
MBP	Maltose-binding protein
MDM2[c,f,g,t,o,z]	Mouse double minute 2 (cat, frog, galago, opossum, turkey, zebrafish)
MDMX	Mouse double minute 4
MPD	2-methyl-2,4-pentanediol
MYCBP2	Myc-binding protein 2
NAE	NEDD8 activating enzyme
NAT10	N-acetyltransferase 10
NEDD	Neural precursor cell expressed developmentally downregulated protein
NES	Nuclear export signal
NF-κB	Nuclear factor kappa light chain enhancer of activated B cells
NFATc2	Nuclear factor of activated T-cells, cytoplasmic 2
NLS	Nuclear localisation signal
NMR	Nuclear magnetic resonance
NUB1L	NEDD8 ultimate buster 1 long
OD	Optical density
OTUB1	Ubiquitin aldehyde binding 1
OTULIN	OTU Deubiquitinase with linear linkage specificity
p53	Tumour suppressor protein p53
PARKIN	Parkinson's associated E3 ligase
PBS	Phosphate buffered saline
PCAF	p300/CBP associated factor
PCR	Polymerase chain reaction
PCTP	Propionate, sodium cacodylate, Bis-Tris propane buffer
PDB	Protein data bank

PEG	Polyethylene glycol
PMSF	Phenylmethanesulphonylfluoride
PTM	Posttranslational modification
RBR	RING-between-RING
RBX1	RING-box protein 1
RCR	RING-Cys-relay
RF-1	Release factor 1
RING	Really interesting new gene
RMSD	Root mean square deviation
RNA	Ribonucleic acid
RNF	RING finger protein
RP	19S Regulatory particle
RPN	Regulatory particle non-ATPase
SAE	SUMO activating enzyme
SCF	SKP1, CUL1, F-box containing complex
SD75/200	Superdex 75/200 HiLoad 26/60
SDS-PAGE	Sodium dodecyl sulphate-polyacrylamide gel electrophoresis
SEC	Size-exclusion chromatography
SENP	SUMO specific protease
shRNA	Small hairpin RNA
SINA2	Seven in absentia 2
SKP1	S-phase kinase-associated protein 1
SPG	Succinic acid, sodium dihydrogen phosphate, glycine buffer
SPR	Surface plasmon resonance
SUMO	Small ubiquitin-like modifier
T. adhaerens	*Trichoplax adhaerens*
TB	Terrific Broth medium
TBS(-T)	Tris-buffered saline (with Tween® 20)
TCEP	Tris(2-carboxyethyl)phosphine
TEV	Cleavage site for tobacco etch virus protease
TRAF	TNF receptor associated factor
TRIM	Tripartite motif containing protein
Tris	Tris(hydroxymethyl)aminomethane
Ub	Ubiquitin
UBA	Ubiquitin activating enzyme

UBC	Ubiquitin conjugating enzyme
UBD	Ubiquitin binding domain
UBE2	Ubiquitin conjugating enzyme
UBL	Ubiquitin like protein
UFM1	Ubiquitin fold modifier 1
U2OS^{mod}	U2OS MDM2 knock-out cells with doxycycline-inducible p53 shRNA
UPS	Ubiquitin proteasome pathway
URM1	Ubiquitin-related modifier 1
USP	Ubiquitin specific protease
USPL1	Ubiquitin specific protease like 1

Chapter 1 Introduction

1.1 The ubiquitin system

Ubiquitination is one of the most important posttranslational modifications, mostly due to its crucial role in the ubiquitin proteasome pathway (UPS), where degradation of a target protein depends on its ubiquitination status. However, the role of ubiquitination is not limited to the UPS, it is also important for protein trafficking (Hicke and Dunn, 2003), DNA repair (Hoege et al., 2002) and protein-protein interactions (Schnell and Hicke, 2003). Ubiquitination of a target protein occurs in a cascade reaction initiated by the activation of Ubiquitin (Ub) by a Ub activating enzyme (E1), transfer to a Ub conjugating enzyme (E2) and Ub ligation to a substrate, which is catalysed by a Ub ligase (E3). Finally, substrate ubiquitination can also be reversed by a deubiquitinating enzyme (DUB) (Figure 1-1).

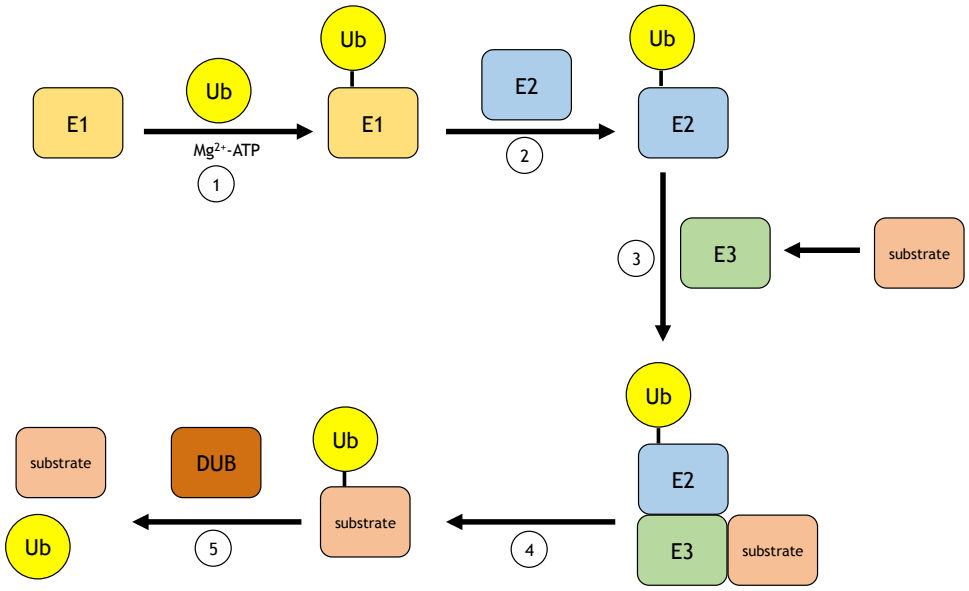

Figure 1-1: Ubiquitination cascade. (1) Ub is activated by E1 in a $Mg2^{+}$-ATP dependent manner. (2) Ub is transferred from E1 to E2. (3) E3 recruits E2 and the substrate. (4) E3 catalyses the Ub transfer from E2 to a substrate. (5) Substrate ubiquitination can be reversed by a DUB.

In the first step of the ubiquitination reaction, E1 recruits Ub in a Mg^{2+}-ATP dependant manner by catalysing the formation of C-terminal adenylated Ub, which forms a tight complex with E1 (Haas et al., 1982) (Haas and Rose, 1982).

Ub is then transferred to a conserved cysteine on the surface of E1 (catalytic cysteine), which forms a thioester linkage with Ub's C-terminal glycine residue (from here on denoted as E1~Ub, where '~' indicates a thioester linkage). E1~Ub adenylates and binds a second Ub molecule, thereby creating a more reactive species from which the thioester linked Ub is transferred to the catalytic cysteine of E2, thereby forming a reactive E2~Ub conjugate. Ub can then be transferred from E2 onto a residue of the substrate to form a covalent isopeptide bond (from here on denoted with '-') between the C-terminal carboxyl group and, in most cases, the ε-NH_2 group of a lysine residue on the substrate. Although this reaction can be observed for a few E2s such as UBE2K (Haldeman et al., 1997) and UBE2S (Wickliffe et al., 2011), the reaction is often too slow to accompany with cellular processes (Stewart et al., 2016). A sufficient ubiquitination rate and specificity towards the target substrate is achieved by E3. It catalyses Ub transfer from E2 to a residue, mostly lysine, on the target. Some E3s form an E3~Ub intermediate whereas other E3s do not bind Ub during catalysis (Chapter 1.1.5). The ubiquitination target can also be a Ub molecule that is already conjugated to a substrate, leading to the formation of Ub chains (Chapter 1.1.1).

There are two distinct E1s in human cells, more than 30 different E2s and more than 600 E3 ligases, leading to a large number of possible E2-E3 pairs, which can catalyse distinct ubiquitination reactions. Another layer of complexity is added by more than 100 different DUBs that can remove ubiquitin from substrates, a process that is involved in a large number of cellular events. In the following sections, an overview will be given about the diversity of the above-mentioned enzymes and their cellular functions.

1.1.1 Ubiquitin

Ubiquitin is a globular, monomeric, protein consisting of 76 amino acid residues (Figure 1-2) (Vijay-Kumar et al., 1987). It has a flexible C-terminal tail, which allows efficient conjugation of the C-terminal carboxyl group onto E1, E2, E3 and ubiquitination substrates. Ub contains seven lysine residues (K6, K11, K27, K29, K33, K48, K63), which are all located on its surface and have together with the N-terminal M1 been shown to be a ubiquitination target themselves, leading to a variety of different chain elongation patterns. Chain elongation can occur both on ubiquitinated substrate and free Ub molecules, depending on the involved E2s (Chapter 1.1.4) and E3s (Chapter 1.1.5).

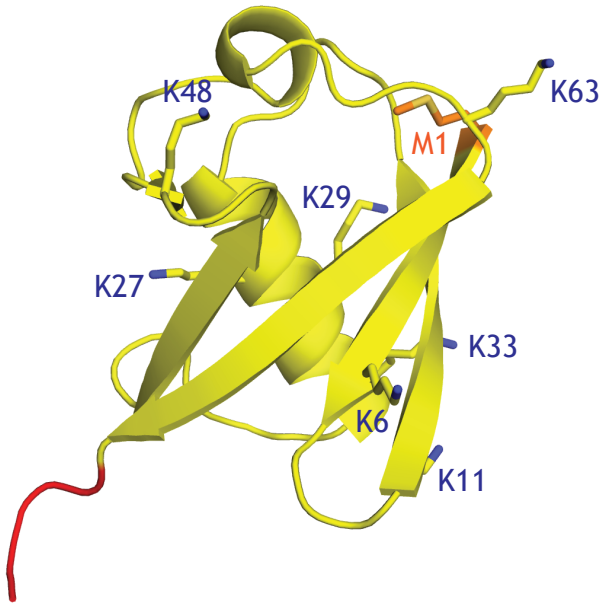

Figure 1-2: Crystal structure of Ub. The C-terminal tail covering L72-G76 is highlighted in red. M1 is highlighted in orange. Sticks are shown for residues through which chain elongation can occur (PDB: 1UBQ) (Vijay-Kumar et al., 1987).

Depending on the lysine to which an additional Ub is linked (linkage type), Ub chains adopt different geometries that are recognised by distinct binding partners such as the proteasomal machinery. Crystal structures for Ub_2 formed through all linkage types have been determined, demonstrating the structural differences (Figure 1-3).

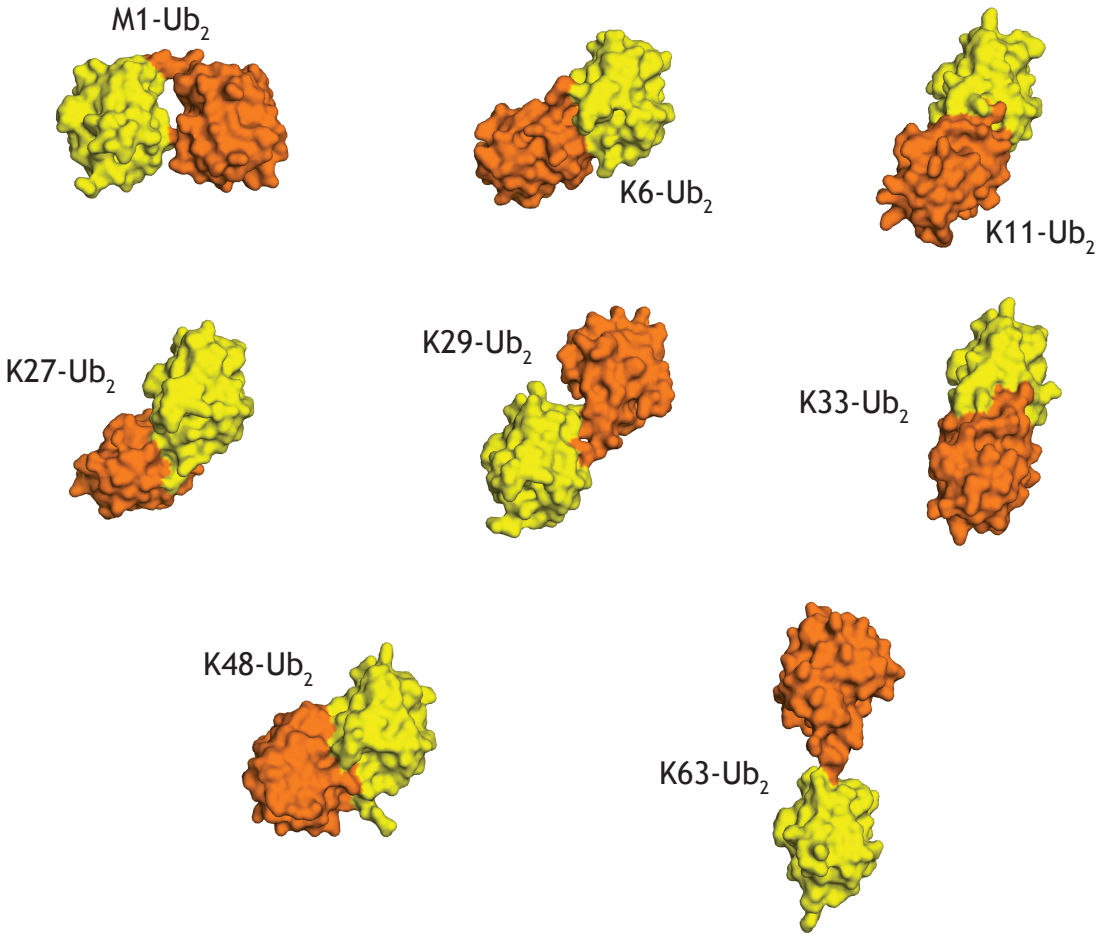

Figure 1-3: Crystal structures of di-Ub. The proximal Ub (the Ub that serves as substrate for chain elongation) is shown in yellow, the distal Ub in orange. Linkage type/PDB: M1/3AXC (Rohaim et al., 2012), K6/2XK5 (Virdee et al., 2010), K11/3NOB) (Matsumoto et al., 2010), K27/5GOD (Gao et al., 2016), K29/4S22 (Kristariyanto et al., 2015a), K33/ 4XYZ (Kristariyanto et al., 2015b), K48/1AAR (Cook et al., 1992), K63/2JF5 (Komander et al. (2009).

Ub chains can be formed by two or more molecules, where chain elongation can either occur on the same lysine residue, leading to a linear chains, or on different lysine residues, resulting in branched chains. Thus, a large number of different ubiquitination patterns can be achieved, which can have distinct physiological functions (Komander and Rape, 2012).

The most common Ub chain type is formed by K48-linkages and primarily involved in substrate degradation where chains consisting of four Ub molecules have been shown to be recognised by the proteasome (Thrower et al., 2000). This is achieved by the rigid tetra-Ub structure initiated by the K48-linkage (Eddins et al., 2007), which stabilises the substrate-Ub conjugate by protecting it from DUBs (Sun et al., 2019). However, tetra-Ub and K48-linkaged ubiquitin chains are not exclusively required for degradation (Lu et al., 2015). Depending on the substrate, linkages of different types facilitate efficient proteasomal

degradation and even monoubiquitination was shown to be sufficient for smaller substrates (Shabek et al., 2012). K11-linked chains were shown to be involved in proteasomal degradation, although this chain linkage is less common because unlike K48-linked chains, it requires a particular E2, UBE2S (Williamson et al., 2009). In contrast, K63-linkages lead to much more elongated Ub chains because this linkage type does not promote interactions between the linked Ub molecules like in K11- or K48-linked Ub (Figure 1-3). This allows them to be recognised by proteins of the endosomal sorting complexes required for transport (ESCRT), and as a consequence, substrates with K63-linked Ub chains are protected from proteasomal degradation (Nathan et al., 2013). Instead, this linkage type has other roles such as NF-κB signalling (Xu et al., 2009), protein trafficking (Hicke and Dunn, 2003) and DNA repair (Ulrich, 2002). Linkages involving any of the other four lysine residues or the N-terminal methionine occur less frequently. Although their cellular function and relevance are poorly understood, they have all been observed in cells (Ikeda and Dikic, 2008) and might have distinct functions due to the different geometries of poly-Ub chains induced by each linkage type. M1-linked Ub chains are similarly extended as K63-linked chains. Although their function partly overlaps with K63-chains, they are selectively recognised by proteins involved in NF-κB signalling (Herhaus et al., 2019).

On top of the chain linkage type, branched chains or ubiquitination events on multiple residues of a substrate allow the formation of more complex ubiquitination patterns with potentially distinct physiological roles. For recognition by the UPS system, ubiquitination of a single lysine residue is sufficient, whereas for other purposes such as histone regulation (Spencer and Davie, 1999) and endocytosis (Rotin et al., 2000), monoubiquitination on multiple lysine residues is required.

1.1.2 Other UBLs

Although ubiquitination is the most important protein-based posttranslational modification, there are a number of other proteins belonging to the family of Ub like proteins (UBL), which fulfil different cellular roles. They adopt a similar globular fold as Ub and typically contain a flexible C-terminal tail terminating with two glycine residues from where they can likewise be conjugated on

substrate lysine residues in an E1, E2 and E3 dependant manner. To date, there are nine known UBLs besides Ub. Small ubiquitin-like modifier (SUMO) is the most multifunctional UBL after Ub. Like Ub, it can form polymeric chains (Tatham et al., 2001) and is involved in a number of non-degradative cellular processes such as protein shuttling and stress response (reviewed in (Hay, 2005)). In contrast to Ub, it possesses a C-terminal extension that needs to be removed by SUMO specific proteases (SENP) so that its C-terminus consists of two glycine residues like Ub (Mukhopadhyay and Dasso, 2007), a pre-requirement for the conjugation of all known UBLs. Other UBLs have more distinct functions. Neuronal-precurser-cell-expressed-developmentally-down-regulated protein 8 (NEDD8) is the UBL with the highest sequence identity with Ub (>50 %). It is an activator for Cullin RING E3 mediated ubiquitination, where it introduces a conformational change within the catalytic Skp, Cullin, F-box containing (SCF) complex that is required for ubiquitination reactions to occur (Liu et al., 2002). ISG15 is a UBL with an antiviral role in the innate immune system (Lenschow et al., 2007). Human leukocyte antigen F-associated (FAT10), which plays a role in the immune response, is the only other UBL apart from Ub that is involved in proteasomal degradation (Hipp et al., 2005). In contrast to other UBLs, it consists of two distinct, consecutive Ub like domains that can recruit an activator enzyme (NUB1L) to the proteasome to promote degradation (Rani et al., 2012). Other UBLs include ATG8 and ATG12, which are involved in lysosomal degradation and URM1, which is involved in the thiolation of transfer RNA (tRNA), thereby regulating translation (Leidel et al., 2009).

1.1.3 E1s

There are eight known, mostly UBL-specific E1s in human cells. They contain three catalytic important domains: First, an adenylation domain that recognises the C-terminal di-glycine motif of the corresponding UBL and activates it via adenylation of the UBL's C-terminal carboxyl group. Second, a domain harbouring the catalytic cysteine, to which the adenylated UBL is transferred to, leading to the formation of E1~UBL. Third, an E2-binding domain that recruits the E2 onto which the UBL is transferred. Ub has two specific E1s, UBA1 and the more specialised E1 UBA6, which specifically recruits the E2 UBE2Z for Ub transfer (Jin et al., 2007). UBA1 cannot charge UBE2Z but all other Ub related

E2s, making it the predominant E1. Surprisingly, UBA6 also binds the UBL FAT10 (Chiu et al., 2007), which it can then transfer to UBE2Z like Ub (Aichem et al., 2010). Other UBLs are recognised by UBL-specific E1s such as UBA7 for ISG15, ATG7 for ATG12, UBA4 for URM1 and UBA5 for UFM1. NEDD8 and SUMO are activated by the heterodimeric E1s NAE1-UBA3 and SAE1-UBA2, respectively.

1.1.4 E2s

There are more than 30 different E2s that have been reported to conjugate Ub or a UBL. They all have a UBC domain harbouring the catalytic cysteine through which they form a thioester linkage with Ub. The architecture of all UBC domains is highly conserved in all E2s for which the crystal structures are available. However, the adjacent regions adopt a variety of folds. Some E2s such as UBE2K contain additional domains, whereas other E2s such as UBE2O and BIRC6 are multi-domain proteins. In the first step of Ub conjugation, an E2 binds Ub-E1~Ub via an E1 recognition site at an N-terminal α-helix of the UBC domain. The thioester linked Ub is then transferred from the E1 to the catalytic cysteine of the E2, thereby forming a thioester bond. From the E2~Ub conjugate, Ub is transferred onto the ε-amino group of a lysine residue on the surface of a substrate, a reaction that is often, but not exclusively catalysed by an E3. Because of the large number of E2s and E3s it is not a surprise that there are a lot of discrepancies from this general transfer. First, some E3s form an E3~Ub intermediate before Ub is transferred to the substrate (Chapter 1.1.5). Second, ubiquitin transfer is not limited to lysine residues but has also been reported for serine, threonine (Wang et al., 2009b), cysteine (Williams et al., 2007) and the N-terminal amino group of the substrate (Tatham et al., 2013). Even for lysine ubiquitination, E2s catalyse, different ubiquitination reactions and have different levels of specificity. In the following chapters, the most promiscuous E2 family, UbcH5 (Chapter 1.1.4.1) will be introduced, followed by a summary of the diversity achieved by other E2s (Chapter 1.1.4.2).

1.1.4.1 UbcH5 family

The UbcH5 family consists of four E2s, UbcH5A, UbcH5B, UbcH5C and UbcH5D, also known as UBE2D1, UBE2D2, UBE2D3 and UBE2D4, respectively. They all share a very high sequence identity and adopt an identical fold where the position of the catalytic cysteine is strictly conserved (Figure 1-4).

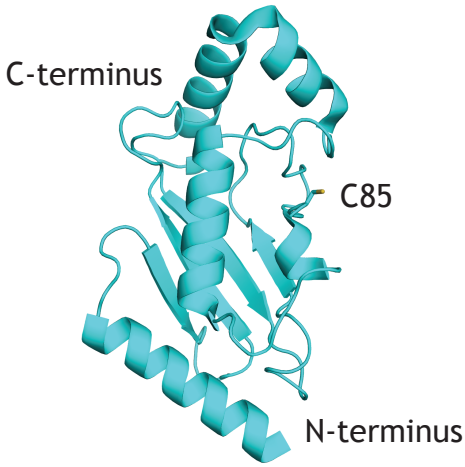

Figure 1-4: Crystal structure of UbcH5B. The catalytic cysteine (C85), highlighted as stick, is the conjugation site for Ub. The fold of UbcH5 involving four α-helices and four ß-strands, is called UBC domain and highly conserved among other E2s (PDB: 2ESK) (Ozkan et al., 2005).

UbcH5 E2s belong to the most versatile group of E2s as they work with a large number of E3s and catalyse different types of ubiquitination, including monoubiquitination and chain elongation through K11 and K48 (David et al., 2010). Mutation of the catalytic cysteine to serine or lysine is a common trick used to produce stable oxyester or isopeptide linked conjugates, respectively, which could successfully be used for crystallisation purposes (Sakata et al., 2010) (Plechanovova et al., 2012) (Dou et al., 2012b). The UbcH5-Ub conjugate adopts a flexible structure where UbcH5 and Ub barely contact each other. However, NMR studies have shown that they occasionally adopt a more rigid conformation, called the 'closed conformation' (Pruneda et al., 2011). When bound to a RING E3 (Chapter 1.1.5.1), this closed conformation is strongly stabilised because both UbcH5 and Ub contact the catalytic domain of the E3 (Figure 1-5). It has been shown that the closed conformation is in this case the catalytic active conformation.

The reactivity of UbcH5 can be further stimulated by a second Ub molecule binding UbcH5 on the other side than the E3 (Brzovic et al., 2006). This backside Ub stabilises E2-Ub in the closed conformation, thereby making Ub transfer more efficient (Buetow et al., 2015). A single point mutation (S22R) is sufficient to completely abolish this backside binding effect. This mutation is often included in biophysical and biochemical experiments as it simplifies experiments by taking out a second binding site without affecting the E2-E3 binding surface (Brzovic et al., 2006).

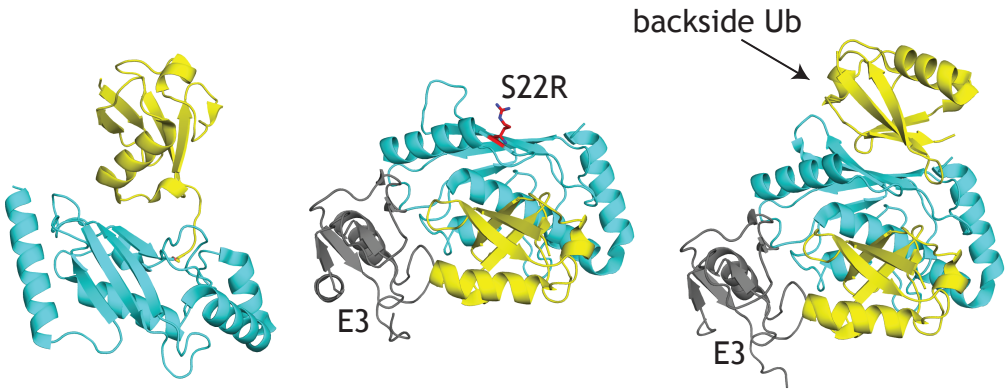

Figure 1-5: Crystal structures of the UbcH5B-Ub conjugate. The E2-Ub conjugate is shown in the unbound state (left, PDB: 3A33) (Sakata et al., 2010), where it adopts an 'open conformation' and in complex with a RING E3 ligase (here: RNF38, shown in grey), without (middle, PDB: 4V3K) and with (right, PDB: 4V3L) (Buetow et al., 2015) backside binding of a non-covalent Ub. Independently of the backside Ub, E2-Ub adopts a 'closed conformation' in the presence of a RING E3. UbcH5B is shown in cyan, Ub in yellow. A single point mutation (S22R) prevents backside binding. The corresponding residue is highlighted in red and shown as stick.

1.1.4.2 Other E2s

Over the last decade, crystal structures of many E2-Ub conjugates, unbound and in complex with an E3, have been determined, which help to understand the catalytic mechanism of E2s. Most E2s contain a UBC domain like UbcH5 but can have additional features such as extensions or additional domains (Figure 1-6).

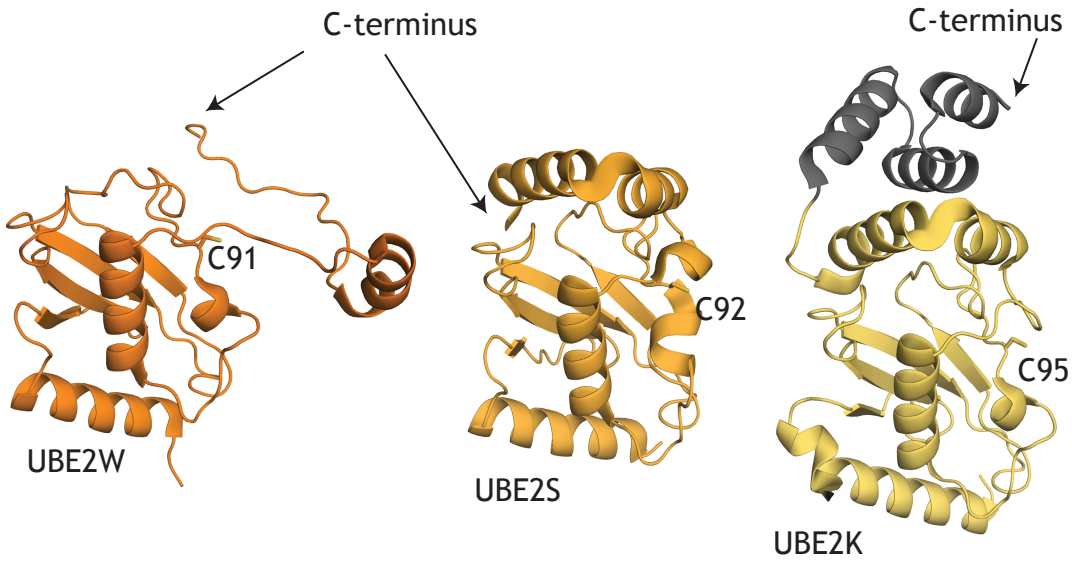

Figure 1-6: Examples for E2s. The NMR model of UBE2W (left, PDB: 2MT6) shows the disordered C-terminus of this E2 (Vittal et al., 2015). UBE2S (middle, PDB: 1ZDN) adopts a more rigid structure, comparable to UbcH5B (Sheng et al., 2012), whereas UBE2K (right, PDB: 6IF1) (Lee et al., 2018) has an additional C-terminal UBA domain (coloured in grey). The catalytic cysteine residues are shown as sticks.

Like UbcH5 family members, UbcH6, UBE2K, UBE2S, UBE2W and other E2s have been shown to adopt similar closed conformations upon E3 binding. Strikingly, UBE2K can efficiently form free K48-linked di-Ub without the presence of an E3 or a substrate. The same holds true for UBE2S, which forms, despite the remarkable structural similarity with UbcH5, even longer chains of K11-linked Ub (Wickliffe et al., 2011). In contrast, UbcH7 exclusively transfers Ub to cysteine residues (Wenzel et al., 2011), and the reaction only occurs when UbcH7-Ub adopts an open conformation (Dove et al., 2017).

Despite the structural similarity of E2s, they can catalyse distinct ubiquitination reactions. For instance, UBE2W catalyses the ubiquitination of the N-terminal amino group (Tatham et al., 2013). E2s of the UBE2E family exclusively catalyse monoubiquitination (Nguyen et al., 2014). UBE2K catalyses K48-linked chain elongations but is unable to catalyse the attachment of the first Ub onto the

substrate (Haldeman et al., 1997). This demonstrates that E2s, at least to some extent, need to work in concert, where a first E2, the 'priming E2', initiates monoubiquitination followed by a second E2 that elongates Ub chains.
Like E1s, E2s are specific for a particular UBL. Most UBLs other than Ub are thus not transferred by the above-mentioned E2s but have their own E2s instead. NEDD8 is conjugated by either UBE2F or UBE2M (Huang et al., 2009), whereas SUMO is conjugated by UBE2I (Lee et al., 1998). Exceptions are UBE2L6 and UBE2Z, which are involved in ISG15ylation (Zhao et al., 2004) and FAT10ylation (Aichem et al., 2010), respectively but also catalyse ubiquitination reactions.

1.1.5 E3s

There are more than 700 different E3s. They are classified based on the mechanism they use to catalyse substrate ubiquitination.

1.1.5.1 RING type E3 ligases

Really interesting new gene (RING) E3 ligases represent the largest group among E3s. In contrast to other E3s, they do not covalently bind Ub but work as a scaffold to promote direct Ub transfer from E2~Ub to the substrate. The RING domain binds E2 and the conjugated Ub simultaneously, thereby stabilising E2~Ub in the closed conformation (Chapter 1.1.4.1) (Figure 1-7).

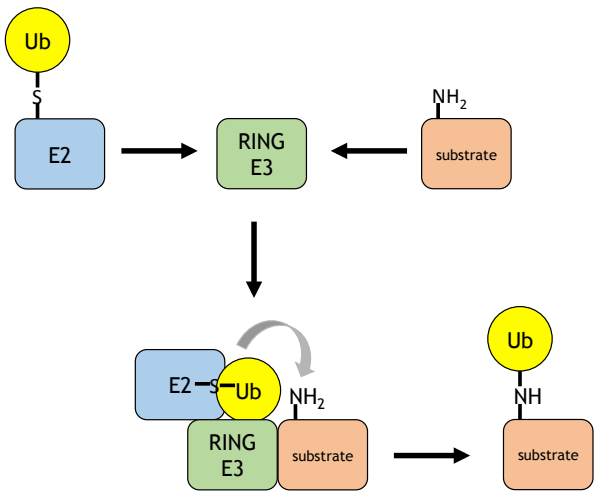

Figure 1-7: Mechanism of RING E3 ligase mediated ubiquitination. RING E3s act as scaffolds by simultaneously recruiting E2~Ub (to the RING domain) and the substrate (to the substrate binding domain). This allows direct Ub transfer from the E2 to the substrate.

Over the last seven years, crystal structures of many $E3_{RING\ domain}$-E2-Ub complexes have been determined, which helped to uncover characteristics that are shared among RING E3s as well as unique features. It was shown that some RING E3s function as monomers (Figure 1-8), whereas others require dimerisation with either themselves or a partner protein in order to function as a Ub ligase (Figure 1-9) (Metzger et al., 2014). The RING domain is a globular protein consisting of one or more α-helices and ß-strands, which are connected by loops involved in E2~Ub binding. It is also a zinc finger domain, which coordinates two Zn^{2+} ions, using different combinations of cysteine (C) and histidine (H) residues, most commonly C3H for the first and C4 for the second Zn^{2+} (Deshaies and Joazeiro, 2009). The importance of Zn^{2+} for the correct fold of the RING domain is best demonstrated by point mutations of any of the coordinating residues, which abolishes the E3 ligase activity likewise the removal of Zn^{2+} by chelating agents such as EDTA (Moududee et al., 2018).

In order to stabilise E2-Ub in the closed conformation, RING E3s share three common features: (i) A hydrophobic patch that interacts with complementary residues on E2 (Budhidarmo et al., 2012), (ii) arginine residue that anchors E2 and Ub in the closed conformation, called the 'linchpin arginine' (Pruneda et al., 2012) and (iii) additional residues adjacent to the RING domain that further stabilise Ub. These interactions position Ub optimally for substrate recognition by exposing the C-terminal tail such that it can easily be transferred to the substrate. The most basic RING E3 features can be seen best in the monomeric E3-E2-Ub complexes of RNF38-UbcH5B-Ub (Buetow et al., 2015) (Figure 1-5) and CBL-B-UbcH5B-Ub (Dou et al., 2013) (Figure 1-8).

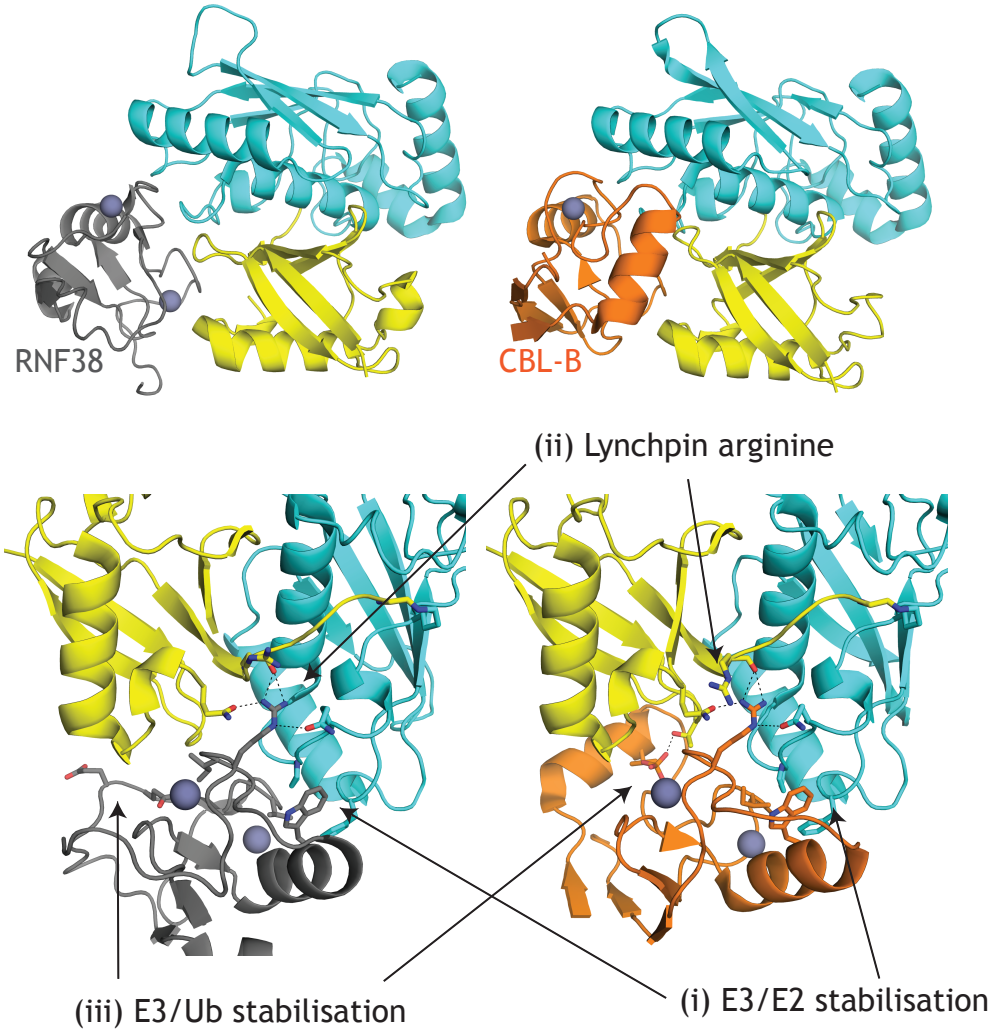

Figure 1-8: Crystal structures of monomeric RING E3s in complex with E2-Ub. In the RNF38-UbcH5B-Ub complex (left, PDB: 4V3K) (Buetow et al., 2015), RNF38 is coloured in grey, UbcH5B in cyan and Ub in yellow. In the CBL-B-UbcH5B-Ub complex (right, PDB: 3ZNI) (Dou et al., 2013), only residues 351-427 of CBL-B (orange) are shown. Close-up views (bottom) show the stabilisation mechanisms of the RING E3s for E2-Ub. Dashes indicate hydrogen bonds, grey spheres Zn^{2+} ions.

Other RING E3s such as RNF4 (Plechanovova et al., 2012), TRAF6, TRIM25 and BIRC7 homodimerise or form heterodimers consisting of an active RING domain and a catalytic inactive homologue like in BRCA1-BARD1 (Brzovic et al., 2001) and MDM2-MDMX (Chapter 1.2). Although the interactions between monomeric E3s and E2-Ub are conserved in dimeric RING E3s, the second protomer further stabilises the E2-Ub interaction of the first protomer by contacting Ub similar to the non-RING elements in RNF38 and CBL-B (Figure 1-8, (iii)). The essentiality of these additional contacts is underscored by dimer-disrupting mutations, which completely abolish the E3 ligase activity in most RING E3s (Plechanovova et al., 2012) (Nomura et al., 2017). Dimeric RING E3s with existing crystal structures show a great variety of N-terminal or C-terminal helical extensions, depending

on the relative position of the RING domain within the protein. These extensions either stabilise the dimer by providing additional interactions or contact E2-Ub (Figure 1-9).

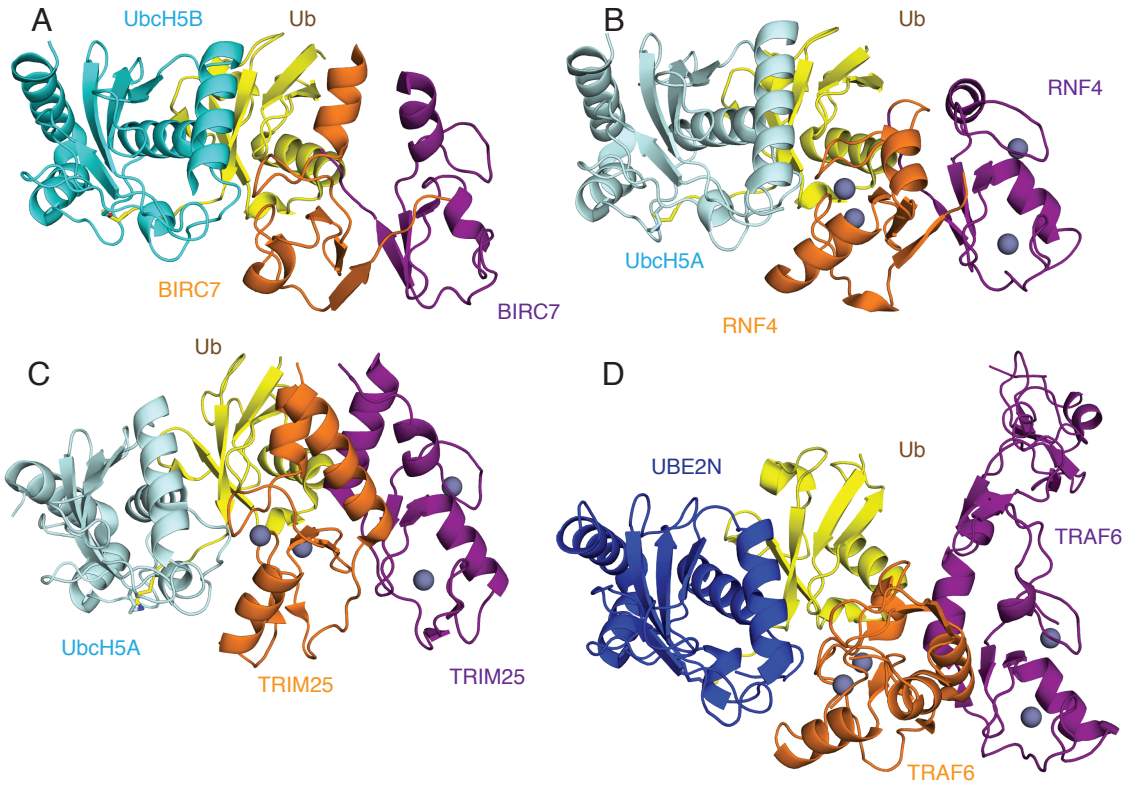

Figure 1-9: Crystal structures of homodimeric RING E3 ligases in complex with E2-Ub. In each crystal structure, the dimer binds two E2-Ub simultaneously. For simplification, only one E2-Ub is shown. (A) BIRC7-UbcH5B-Ub (PDB 4AUQ) (Dou et al., 2012b). (B) RNF4-UbcH5A-Ub (PDB 4AP4) (Plechanovova et al., 2012). (C) TRIM25-UbcH5A-Ub (PDB 5FER) (Koliopoulos et al., 2016). (D) TRAF6-UBE2N-Ub (PDB 5VO0) (Middleton et al., 2017).

In BIRC7, parallel α-helices adjacent to the RING domain form extensive hydrophobic interactions, thereby potentially stabilising the dimer formation. They are in close proximity to UbcH5B although the hydrogen bond between $E248^{BIRC7}$ and $R15^{UbcH5B}$ is the only direct interaction visible in the crystal structure (Dou et al., 2012b). The N-terminal α-helices in RNF4 are perpendicular to the helices in BIRC7. They are antiparallel and face towards different directions. Although they do not interact with each other, they stabilise the C-terminal tail of the other protomer via hydrophobic interactions (Plechanovova et al., 2012). The RING domain in E3s of the TRIM family is in contrast not located at either of the termini. This allows helical extensions to not only form N-terminal but also C-terminal to the RING domain, resulting in a four-helix bundle present in a dimer, which is stabilised by extensive inter- and

intramolecular hydrophobic interactions (Koliopoulos et al., 2016). These helices pack against E2-Ub and stabilise the complex, potentially compensating for a missing C-terminal tail like in BIRC7 and RNF4. Yet another helix arrangement exists in the TRAF6 dimer, which is also flanked by two α-helices. However, unlike in TRIM25, they do not form a bundle but face away from each other while being stabilised by intramolecular hydrophobic contacts between both helices of the same protomer. The C-terminal helix adopts the function of the C-terminal tail in RNF4 and BIRC7 by stabilising Ub of the E2-Ub bound to the other protomer. The crystallised construct of TRAF6 includes additional zinc finger domains, which also contacted Ub. In RNF25, an α-helix adjacent to the RING domain clamps UbcH5B by forming extensive contacts with its backside (Li et al., 2015), demonstrating the variety of different stabilisation mechanisms for E2-Ub in RING E3s beyond the RING domain. This is supported by the large variety of extensions ranging from short helical turns like in MDM2-MDMX (Linke et al., 2008) to α-helices longer than 70 Å such as in RNF8 (Mattiroli et al., 2012). Given the fact that structural information of most of the 600 RING E3s is still missing, it is likely that many more stabilisation mechanisms exist.

Some RING E3s are parts of multi protein complexes. In SCF, the RING-box protein 1 (RBX1), which itself does not have a substrate binding domain, binds to the scaffold protein Cullin 1 (CUL1). CUL1 recruits the substrate by forming a complex with an F-box protein, which is the substrate recognition subunit of the complex, via the adaptor protein S-phase kinase-associated protein 1 (SKP1) (Petroski and Deshaies, 2005) (Lydeard et al., 2013). The same holds true for the E3 APC11, which is part of the Anaphase promoting complex/cyclosome (APC/C). In this complex, the Cullin-like scaffold protein APC2 simultaneously binds APC11 and more than ten other subunits including additional scaffold proteins and substrate receptors (Chang and Barford, 2014). In both complexes, Ub transfer is like in other RING E3s achieved by bringing E2-Ub and the substrate close together, enabling a direct Ub transfer from the E2 to the substrate. The only difference is that the substrate specificity is not achieved by the RING E3 but instead by the substrate binding protein of the complex. In the case of SCF, there are approximately 70 different F-box proteins, allowing it to ubiquitinate a vast number of substrates.

A number of E3 ligases has been identified that function in a similar way as RING E3s although they do not coordinate Zn^{2+}. These ‘RING type’ E3s, called U-Box

E3s, contain charged residues at positions corresponding to the Zn^{2+} coordinating residues in RING E3s, which form hydrogen bonds and salt bridges with each other in such a way that the overall fold is conserved (Aravind and Koonin, 2000) (Ohi et al., 2003) (Vander Kooi et al., 2006).

Besides the catalytic RING domain, RING E3s are composed of a variety of additional domains, most importantly a substrate binding domain. Although the RING domain itself possesses robust ligase activity, other domains are important for the function of the E3 by bringing the substrate closer to E2~Ub to enable an efficient Ub transfer. Due to the inherent flexibility of the domains to each other, crystallisation approaches of full-length RING E3s, and substrate-E3-E2~Ub complexes remain one of the main challenges in the field.

1.1.5.2 HECT E3 ligases

E3s of the Homologous to E6AP C-Terminus (HECT) E3 family catalyse Ub transfer in a two-step reaction by first forming an E3~Ub intermediate with a catalytic cysteine that is conserved among all 28 known HECT E3s (Scheffner and Kumar, 2014). Unlike RING E3s, they do not stabilise E2~Ub in the closed conformation. Instead, E2 is recruited to an N-terminal lobe (Huang et al., 1999) whereas Ub is stabilised by a C-terminal domain (Kamadurai et al., 2009) from which Ub is transferred to the HECT E3's catalytic cysteine, (Maspero et al., 2013). This is followed by Ub transfer to the substrate, which occurs unlike in RING E3s independently of an E2 (Figure 1-10).

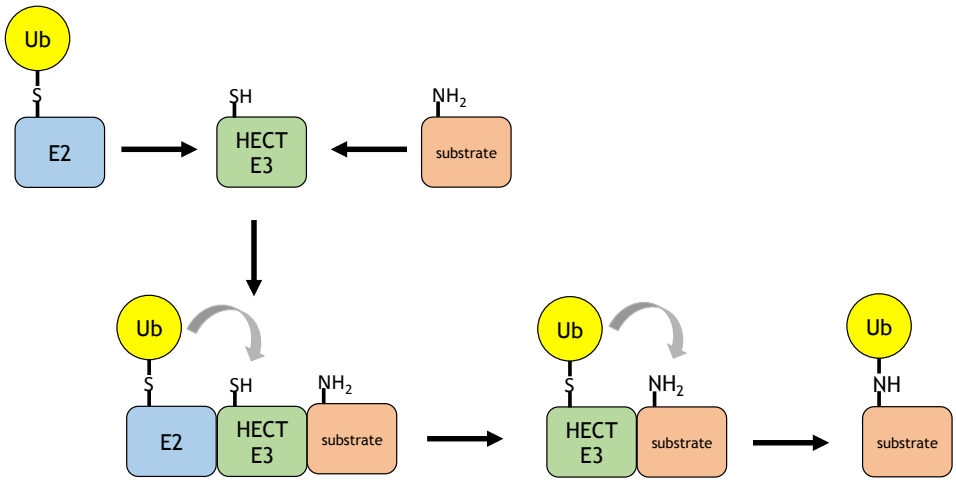

Figure 1-10: Mechanism of HECT E3 ligase mediated ubiquitination. HECT E3s recruit E2~Ub, from where the Ub is first transferred onto a cysteine residue within the HECT domain, forming a covalent E3~Ub intermediate. In a second step, Ub is further transferred onto a substrate.

1.1.5.3 RBR E3 ligases

RING-between-RING (RBR) E3s are RING-HECT hybrid E3s that consist of two catalytic domains involved in Ub transfer from an E2~Ub conjugate to a substrate. The first domain, RING1, recruits E2~Ub like in RING E3s. However, E2~Ub is not stabilised in the closed conformation due to missing features such as the linchpin arginine or additional stabilisation mechanisms beyond the RING domain, not allowing direct Ub transfer to a substrate. Instead, Ub is first transferred onto a catalytic cysteine of another domain, RING2, like in HECT E3s and subsequently transferred onto the substrate (Figure 1-11).

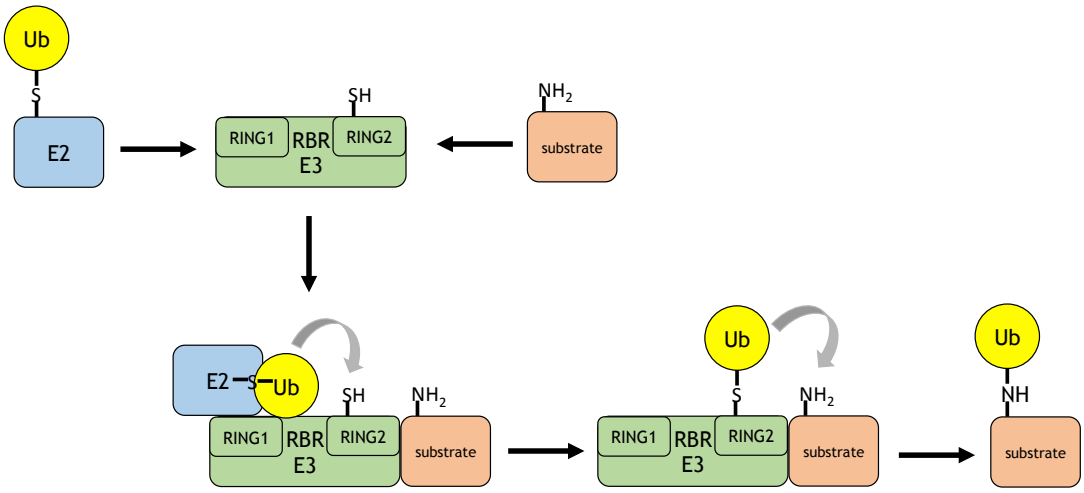

Figure 1-11: Mechanism of RBR E3 ligase mediated ubiquitination. RBR E3s contain two RING domains. They recruit E2~Ub to the first RING domain (RING1), from where it is then transferred onto the catalytic cysteine of the second RING domain (RING2), forming an E3~Ub intermediate. From RING2, Ub is further transferred onto a substrate.

1.1.5.4 RCR E3 ligase(s)

The E3 ligase Myc-binding protein 2 (MYCBP2) does not fit into any of the three above-mentioned E3 classes but uses a mechanism that was denoted as RING-Cys-relay (RCR) E3 (Pao et al., 2018). It recruits E2~Ub to its RING domain and forms a MYCBP2~Ub intermediate through a cysteine on the flexible mediator loop. This loop can then undergo a conformational change and transfer Ub to a second cysteine residue, from which it is conjugated on either serine or threonine on a target substrate (Figure 1-12).

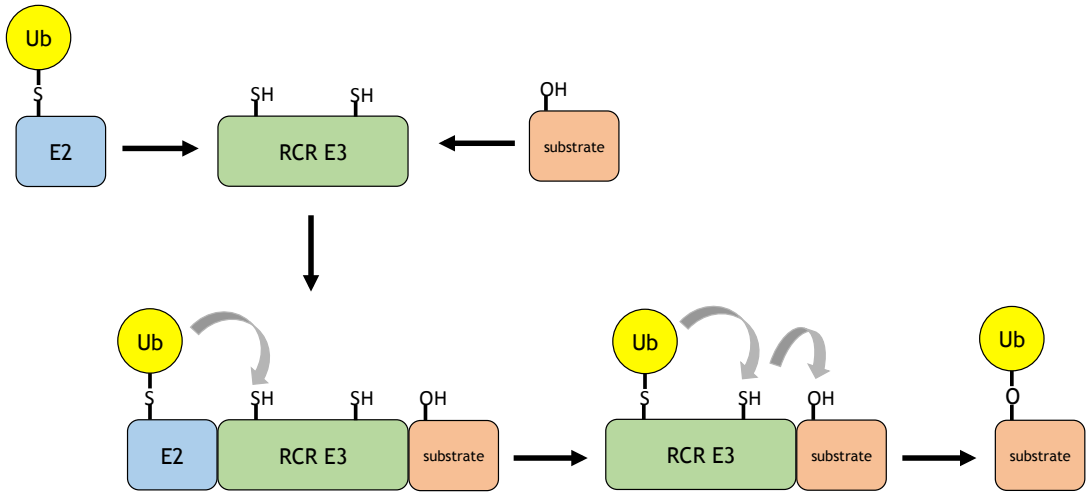

Figure 1-12: Mechanism of RCR E3 ligase mediated ubiquitination. RCR E3s contain two catalytic cysteines. They recruit E2~Ub to the RING domain and form an E3~Ub through a cysteine on a flexible loop. This loop then undergoes a conformational change and transfers Ub onto a second catalytic cysteine, from which it is further transferred onto a a threonine or serine residue on the substrate.

It is unclear, whether there are more E3s following the same mechanism or whether MYCBP2 is the only RCR E3. Nonetheless, this example shows that there might be more E3s to be identified that do not follow any of the established mechanisms.

1.1.5.5 E3 regulation via posttranslational modifications

Posttranslational modifications (PTMs) play a crucial role in all E3 classes. The RBR Parkinson's associated E3 ligase (PARKIN) adopts an autoinhibited conformation and not only requires PINK1-mediated phosphorylation on its UBL domain but also on Ub's S65 for full activity (Gladkova et al., 2018). In contrast, phosphorylation at S131 by Dual specificity tyrosine-phosphorylation-regulated kinase 1A (DYRK1A) lowers its binding affinity for E2-Ub, thereby reducing PARKIN's ligase activity (Im and Chung, 2015). Likewise, the HECT E3 ligase Itch adopts an autoinhibited state when dephosphorylated but becomes active upon a conformational change initiated by Mitogen-activated protein kinase 8 (JNK1) mediated phosphorylation (Gallagher et al., 2006). The RING E3 CBL-B requires phosphorylation near the RING domain (Y363) in order to undergo a conformational change from an autoinhibited to a catalytic active state, where pY363 also stabilises E2-Ub in the closed conformation (Dou et al., 2013)

(Figure 1-8, bottom). Other examples of E3-activation via phosphorylation include the RING E3 ligases TRIM21 (Stacey et al., 2012) and SINA2 (Chen et al., 2018) although the underlying mechanisms are not yet fully understood due to the lack of structural studies. Acetylation has also been reported to alter the ligase activity of the RING E3 MDM2 (Nihira et al., 2017), and other PTMs are likely to be involved in E3 regulation and could either introduce conformational changes or affect substrate and E2-Ub recruitment. PTMs involving entire proteins such as UBLs also play a major role in E3 regulation. For instance, neddylation activates Cullin RING E3s by introducing conformational changes (Duda et al., 2008). Many E3s possess an intrinsic autoubiquitination activity, which controls their activity via proteasomal degradation.

1.1.6 Downstream pathway of ubiquitinated substrates

Ubiquitinated substrates are targets for downstream events. The faith of this event depends on the substrate and to a large extent on the ubiquitination pattern. The most prominent interaction partner is the 26S proteasome, which recognises K48-polyubiquitinated substrates and initiates their degradation (Chapter 1.1.6.1). Other ubiquitination patterns such as monoubiquitination or uncommon polyubiquitination chains are not recognised by the proteasome. They interact with a variety of proteins through their Ub binding domain (UBD). Ubiquitination can also be reversed by DUBs (Chapter 1.1.6.2).

1.1.6.1 Proteasome

The 26S proteasome (26S indicates the Svedberg sedimentation coefficient (Arrigo et al., 1988)) is the most common degradation machinery for ubiquitinated substrates (Tanaka, 2009). The 2.5 MDa complex is composed of a barrel-shaped 20S core particle (CP), in which proteolysis occurs, and flanked by two 19S regulatory particles (RPs), which recognise ubiquitinated substrate and position it for CP-mediated degradation.

Initially, ubiquitin receptors such as RPN10 and RPN13 recognise ubiquitinated substrates, and transfer them to a hexameric ATPase motor, in which Ub is first removed by a DUB (Chapter 1.1.6.2) so that the substrate can be unfolded in an ATP dependant manner (Smith et al., 2011). The RP then opens the central pore of the CP where the unfolded protein is cleaved into smaller peptides by a number of different β-type subunits with trypsin-like, chymotrypsin-like and

caspase-like proteolytic activities (Tanaka, 2009) (Dong et al., 2019). These peptides are then released from the proteasome and further chopped into single amino acids (Kloetzel and Ossendorp, 2004).

1.1.6.2 DUBs

DUBs recycle Ub by breaking the isopeptide bond formed between Ub and the protein it is conjugated to, thereby recovering Ub such that it is identical to a freshly synthesised Ub. This allows cells to reuse Ub and lowers the demands of translating new Ub molecules. Human cells contain more than 100 different DUBs, which have been classified into seven different families based on their domain architecture. They differ in their functional properties such as substrate and chain linkage specificity. The DUBs RPN11, UCH37 and USP14, which are part of the RP particle of the 26S proteasome, cleave Ub chains from the substrate upon recognition by the proteasome (de Poot et al., 2017). Cleaved Ub chains are then independently of the proteasome chopped into single Ub molecules by other DUBs such as USP5 (Bonnet et al., 2008). DUBs can also prevent substrates from being degraded by deubiquitinating them before they are recognised by the proteasome (Brooks and Gu, 2006).
Some DUBs are specific for a certain chain-linkage such as OTUB1, which cleaves K48-linked Ub chains (Wang et al., 2009a), whereas OTUD7B and OTULIN cleave K11- and M1-linked chains, respectively (Bremm et al., 2010) (Keusekotten et al., 2013). Other DUBs are less specific, underlying the complexity of these enzymes (Faesen et al., 2011). They also exist for other UBLs than Ub with USPL1 and COPS5 being examples for desumoylation and deneddylation enzymes, respectively (Schulz et al., 2012) (Cavadini et al., 2016).

1.2 The E3 RING ligase MDM2

The E3 RING ligase Murine Double Minute 2 (MDM2) is the main E3 for p53. Its ligase activity is dependent on dimerisation with either itself (homodimer) or its catalytic inactive homologue MDMX (heterodimer) through the C-terminal RING domain, whereas the substrate p53 is recruited through the N-terminal p53 binding domain. Furthermore, both MDM proteins contain a central acidic domain and a second zinc finger domain between the acidic domain and the RING finger domain (Figure 1-13). In addition, MDM2, but not MDMX contains a

nuclear export signal (NES), which enables the protein to shuttle between the nucleus and the cytosol and a nuclear localisation domain (NLS). Thus, the cytosolic MDMX requires heterodimerisation with MDM2 in order to be imported to the nucleus. Nevertheless, both MDM proteins have a sequence similarity of 37 %, where the highest number of conserved residues can be found in the p53 binding domain and the RING domain.

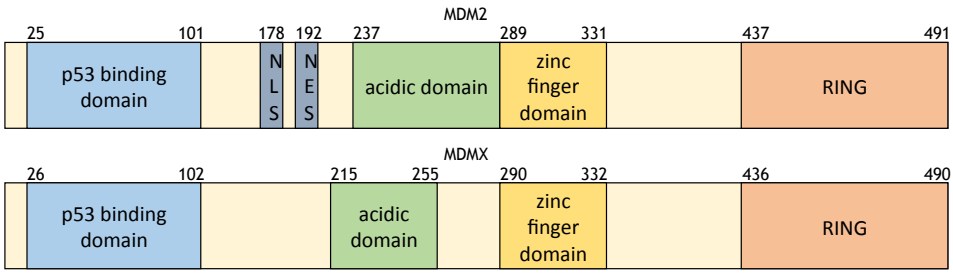

Figure 1-13: Domain architecture of MDM2 and MDMX. Regions coloured in cream are predicted to be mainly disordered.

1.2.1 C-terminal RING domain

The RING domain of MDM is essential for its ligase activity, which itself requires dimerisation. Thus, MDMX's inability to form homodimers restricts it from acting as a ligase. The RING domain is composed of the C-terminal 55 residues (437-C in MDM2 and 436-C in MDMX). For the heterodimer but not the homodimer, crystal structures are available for RING domain constructs by itself (PDB: 2VJE and 2VJF) (Linke et al., 2008) and in complex with UbcH5B-Ub (PDB: 5MNJ) (Nomura et al., 2017). Both crystal structures also contain residues adjacent to the RING domain (428-436), which adopt helices that stabilise each other. The fold of the RING domain is fully conserved in both structures. It recruits E2-Ub in a similar way as other dimeric RING E3s (Chapter 1.1.5.1), although only MDM2 but not MDMX binds E2-Ub. The binding surface is comparable to other RING E3s and involves a hydrophobic patch (V439, I440, L458) that stabilises the E2 and the linchpin arginine (R479), which stabilises E2-Ub in the closed conformation. Ub is further stabilised by the N-terminal helix (N433) and the C-terminal tail of MDMX (F488, I489, A490) (Figure 1-14).

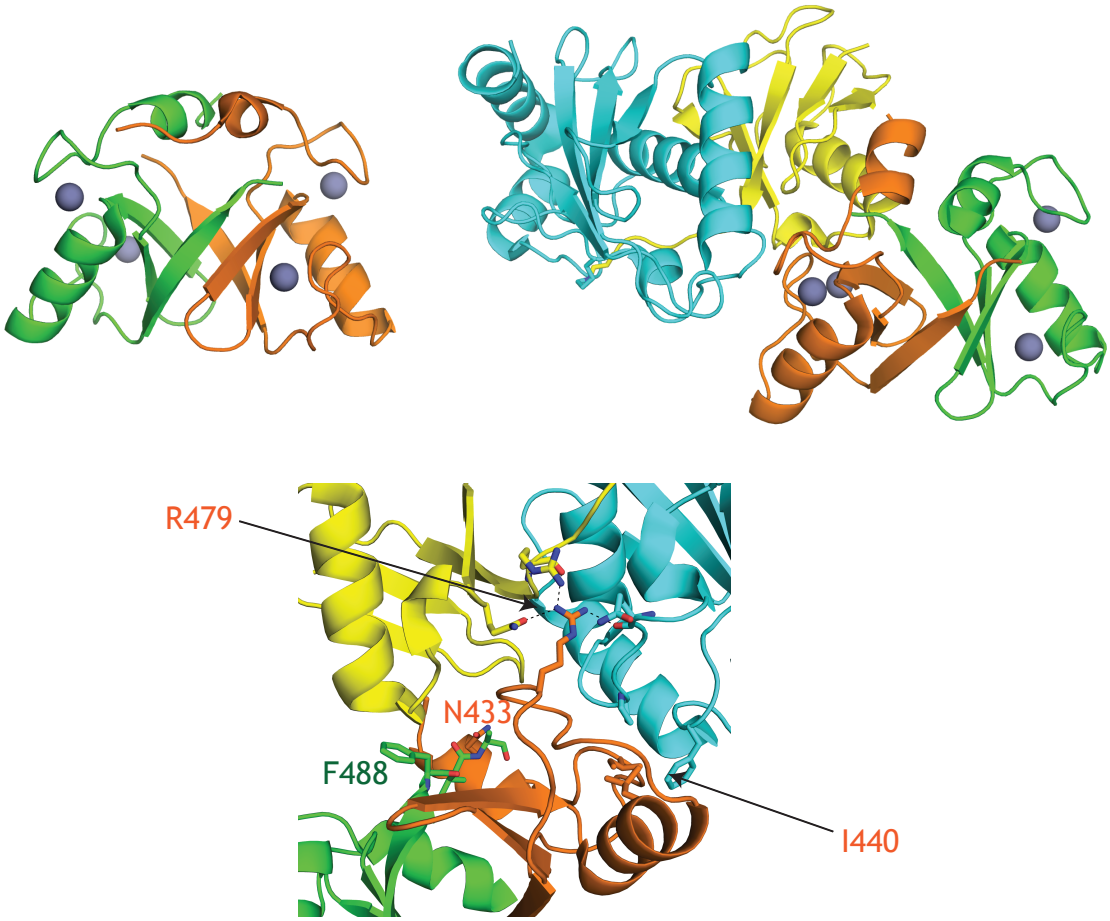

Figure 1-14: Crystal structures of the MDM2-MDMX heterodimer. MDM2-MDMX (upper left, PDB: 2VJF) (Linke et al., 2008). MDM2-MDMX in complex with UbcH5B-Ub (upper right, PDB: 5MNJ) (Nomura et al., 2017). MDM2 is coloured in orange, MDMX in green, UbcH5B in cyan and Ub in yellow. A close-up view of MDM2-MDMX-UbcH5B-Ub (bottom) shows important residues for E2-Ub stabilisation.

The C-terminal residues of MDMX are deeply buried in the E2-Ub binding surface. Consequently, the addition of a C-terminal 6XHis-tag completely abolishes the ligase activity of the heterodimer (Nomura et al., 2017). So far, no crystal structure has been obtained for the homodimer due to the pronounced aggregation tendency of homodimeric MDM2 RING constructs (Kostic et al., 2006) (Poyurovsky et al., 2007) (Linke et al., 2008). Nonetheless, an NMR based structure was obtained (PDB: 2HDP) (Kostic et al., 2006), showing that both dimers adopt a similar conformation with a RMSD between the C_α atoms of <2 Å. Both dimers coordinate four Zn^{2+} ions through the same conserved cysteine and histidine residues. Based on the NMR model, residues N-terminal of E436 do not adopt helical structures as in the heterodimer but are instead disordered, although this might be a consequence of the restraints used for the structure calculation (Figure 1-15).

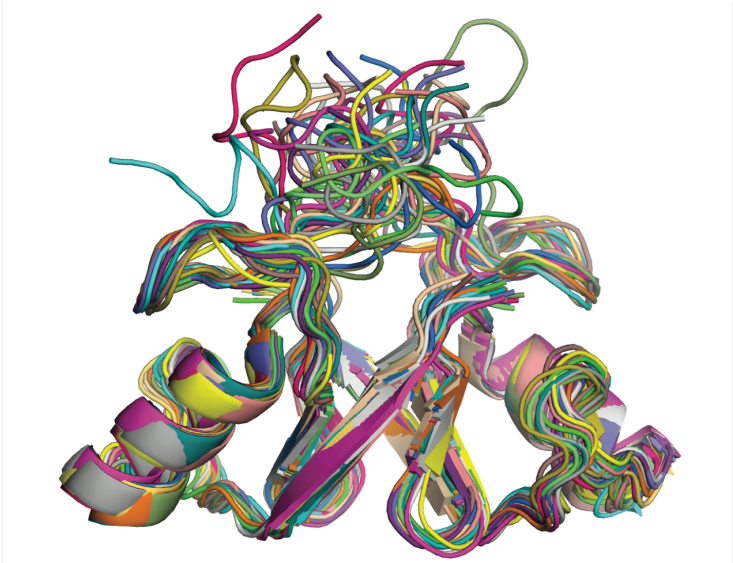

Figure 1-15: NMR model of the MDM2 RING homodimer. 20 solution structures with the lowest energy are superimposed (PDB: 2HDP) (Kostic et al., 2006), where each dimer is shown in a different colour.

Based on the crystal structure of the heterodimer in complex with E2-Ub (Figure 1-14), a model for the homodimer in complex with E2-Ub was created (Nomura et al., 2017), which suggested that it would use similar residues to stabilise E2-Ub although it was hypothesised that it could bind two E2-Ub conjugates simultaneously (Figure 1-16).

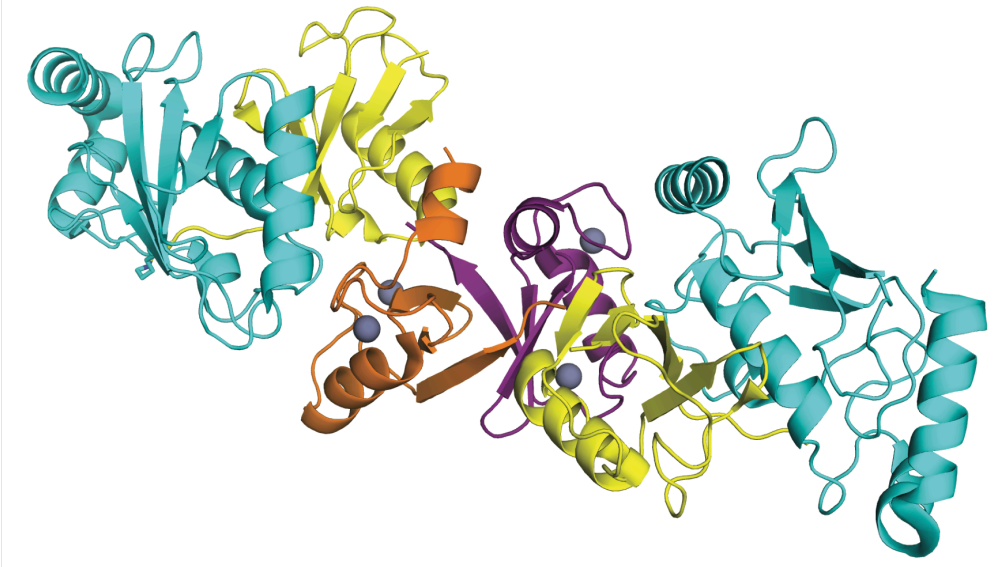

Figure 1-16: Model for the MDM2 homodimer RING in complex with UbcH5B-Ub. The protomers are coloured in orange and purple. The model was created by superimposing monomeric MDM2-UbcH5B-Ub from the MDM2-MDMX-UbcH5B-Ub structure onto MDMX within the MDM2-MDMX-UbcH5B-Ub complex.

The model was validated by *in vitro* assays, where residues that are critical for the ligase activity of the heterodimer were also found to be critical for the homodimer (Nomura et al., 2017). A C-terminal 6XHis-tag abolished the activity of the homodimer whereas in the heterodimer, a C-terminal extension of MDM2 did not affect the catalytic activity, suggesting that it might have the same role as MDMX's tail in the heterodimer. However, in other studies, mutational analyses of the RING domains showed contradictory enzymatic activities between the dimers, suggesting that they might be structurally different (Uldrijan et al., 2007) (Kosztyu et al., 2019). Besides E2-Ub recruitment, the RING domain has also been reported to recruit ATP via a P-loop motif (residues 448-455) (Poyurovsky et al., 2003) and bind RNA (involving G448) (Elenbaas et al., 1996).

1.2.2 N-terminal p53 binding domain

MDM contains a conserved, hydrophobic N-terminal domain, through which it recruits its ubiquitination substrate p53. The crystal structure in complex with the transactivation domain of p53 (Kussie et al., 1996) shows that an α-helix (residues 51-63) stabilises p53 through complementary hydrophobic interactions (Figure 1-17). An N-terminal batch (16-24) was also suggested to function as a lid (McCoy et al., 2003) that needs to open upon p53 binding whereas it is closed in the absence of p53, thereby stabilising MDM2 in the unbound state (Showalter et al., 2008). Surprisingly, this lid is also able to bind the C-terminus of p53 (Poyurovsky et al., 2010).

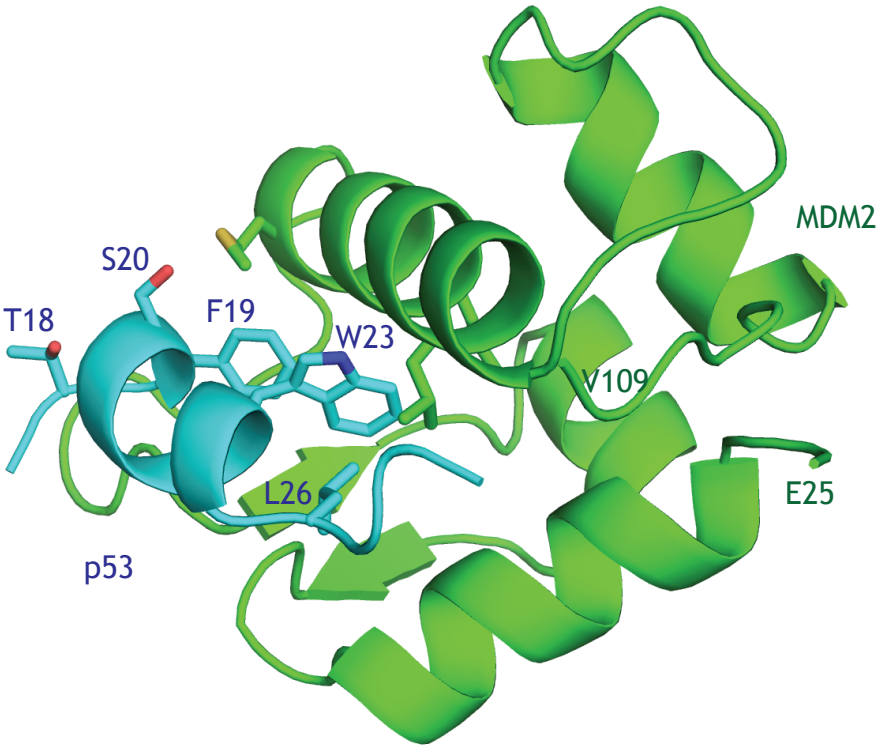

Figure 1-17: Crystal structure of MDM2-p53. MDM2 (residues 25-109) is shown in green, p53 (residues 17-28) in blue (PDB: 1YCR) (Kussie et al., 1996).

1.2.3 Domains between p53 binding domain and RING domain

To date, the structure of full-length MDM2 is unknown. The residues between the substrate and the E2-Ub binding site (110-427) need to adopt a conformation that allows efficient Ub transfer onto p53. However, no information is available about the overall shape of MDM2, the distance between p53 binding domain and RING domain or the relative flexibility of these domains towards each other. The disordered central acidic domain (243-299) plays a versatile role. It contains a second p53 binding site, which involves p53's DNA binding domain and has been shown to be critical for p53 ubiquitination (Ma et al., 2006). It also assists MDM2 to oligomerise (Leslie et al., 2015) and has been shown to interact with the RING domain in an intra- and intermolecular manner (Cheng et al., 2014) (Dang et al., 2002). The tumour suppressor protein p14ARF binds to the acidic domain and inhibits p53 ubiquitination by restricting the catalytic activity of MDM2 and blocking its ability to translocalise into the cytoplasm (Sherr, 2001).

The acidic domain is flanked by a C-terminal C4 zinc finger domain, which binds the ribosomal protein RPL11, and the crystal structure of this complex has been determined (Figure 1-18). Due to sequence mismatches between the MDM

proteins in this region, only MDM2 interacts with RPL11, which plays an important role in the proteasomal degradation of MDMX (Li and Gu, 2011).

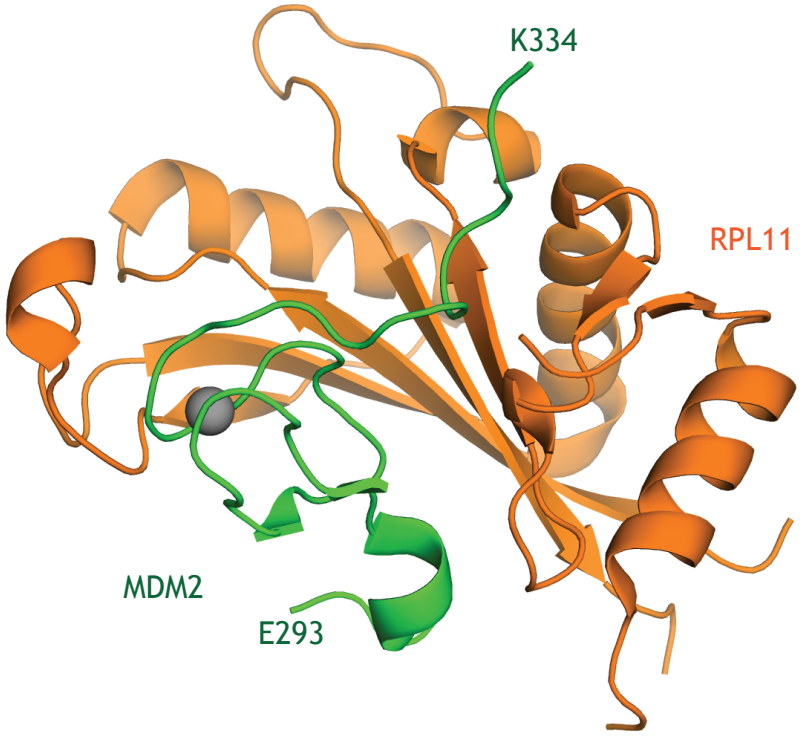

Figure 1-18: Crystal structure of MDM2-RPL11. MDM2's zinc finger domain (293-334) is shown in green, RPL11 (PDB: 4XXB) in orange (Zheng et al., 2015). The Zn^{2+} ion is shown as a grey sphere.

In addition, MDM contains presumably disordered regions that connect either the p53 binding domain with the acidic domain (89-243) or the zinc finger domain with the RING domain (328-427). The former contains the NES and NLS in MDM2 whereas the latter contains a number of phosphorylation sites (Chapter 1.3.3).

1.2.4 MDM2 regulation

Homodimeric MDM2 and heterodimeric MDM2-MDMX are mainly regulated by autoubiquitination, leading to the formation of K48-linked polyubiquitination chains that trigger MDM's proteasomal degradation (Fang et al., 2000) (Pan and Chen, 2003). However, this process can be altered by ubiquitination and deubiquitination events mediated by other proteins and depends on the exact cellular circumstances.

A number of E3s has been associated with MDM2 degradation. The p300/CBP associated factor (PCAF) is an E3 ligase that further promotes MDM2's proteasomal degradation through ubiquitination (Linares et al., 2007). Interestingly, PCAF itself can also be ubiquitinated by MDM2 so that the net result of the PCAF-MDM2 interaction might be context dependent (Jin et al., 2004). N-acetyltransferase 10 (NAT10) similarly ubiquitinates and degrades MDM2 *in vitro* and in cells although little is known about the mechanism of this E3 (Liu et al., 2016). The $SCF^{\beta\text{-}TRCP}$ and APC/C complexes were also shown to ubiquitinate MDM2, although the former requires CK1δ dependent phosphorylation of MDM2 (Chapter 1.3.3). In the APC/C complex, MDM2 directly binds to the scaffold protein APC2 (Chapter 1.1.5.1) (He et al., 2014). The HECT E3 ligase NEDD4-1 and the RING E3 ligase membrane-associated RING-CH-type finger 7 (MARCH7) polyubiquitinate MDM2 via non-degradative K63-chains (Chapter 1.1.1), which reduces MDM2's autoubiquitination activity by competing with the formation of K48-linked chains, ultimately leading to increased MDM2 stability (Zhao et al., 2018). This observation was validated in U2OS NEDD4-1 knock-out cells, where the half-life of MDM2 was reduced (Xu et al., 2015). On the other hand, MARCH7 knock-out mice were viable (Metcalfe et al., 2005), in contrast to MDM2 knock-out cells (Chapter 1.3.2), suggesting that the importance of K63-polyubiquitination might be context dependent.

MDM2 can also be stabilised by deubiquitination events catalysed by a number of DUBs. USP7, interestingly also a DUB for p53, was shown to be essential for MDM2's ligase activity towards p53 in H1299 und U2OS cells (Li et al., 2004). USP2a also deubiquitinates MDM2 although it binds MDM2 at the p53 binding domain and a region C-terminal to the acidic domain (Stevenson et al., 2007) whereas the binding sites for USP7 are located between the p53 binding domain and the acidic domain (Sheng et al., 2006) (Hu et al., 2006). Furthermore, USP15 was shown to deubiquitinate MDM2 in T-cells, which are in turn deactivated due to the MDM2-mediated degradation of the transcription factor NFATc2 (Zou et al., 2014).

1.2.5 MDM2 evolution

MDM2 and p53 genes have been found for the most basic multicellular animals like *Trichoplax adhaerens* (*T. adhaerens*), suggesting that both proteins have co-evolved (Lane et al., 2010). The above-mentioned domains are conserved in all known MDM2 sequences with the highest sequence identity observed for the catalytic RING domain. For instance, the sequence identity between human and *T. adhaerens* MDM2 is 22 % and 57 % for the overall sequence and the RING domain, respectively. Zn^{2+} coordinating residues within the RING domain, which are essential for the fold of the RING domain, and key residues for E2-Ub binding like the linchpin arginine, are fully conserved among all known MDM2 sequences. Indeed, *T. adhaerens* has been shown to be catalytically active and bind both, *T. adhaerens* and human p53, underlying the likely conservation of MDM2's function throughout evolution (Siau et al., 2016). In contrast, MDMX has only been found in vertebrates, suggesting that a single MDM protein could fulfil the roles of both human MDM proteins. Moreover, ancestral MDMX from zebrafish (*Danio rerio*) was less important for p53 regulation than in mammals (Chua et al., 2015).

1.3 MDM2's role in p53 regulation

1.3.1 p53

p53 is one of the main tumour suppressor proteins, and in nearly half of all human tumours, p53 is found to be mutated at a position that affects its function. It recognises and binds damaged DNA, thereby activating the transcription of cell cycle arrest and apoptosis inducing genes. The tetrameric 393 amino acid long protein consists of an N-terminal transactivation domain, a proline-rich region, a central DNA binding domain, followed by its tetramerisation domain and a disordered C-terminus, which contains a lot of lysine residues and is the predominant site for ubiquitination (Rodriguez et al., 2000) (Figure 1-19).

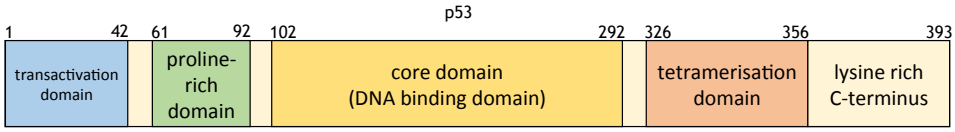

Figure 1-19: Domain architecture of p53. Regions coloured in cream are predicted to be mainly disordered.

Upon translation, p53 dimerises, and two dimers then form a tetramer, which can therefore be denoted as a dimer of dimers. Although a single dimer is able to recognise DNA (Zhao et al., 2001), tetramerisation is required for p53's anti-tumour function. This is illustrated best by the available low-resolution cryo EM structure of the full-length protein in complex with DNA, where two dimers work in concert for optimal DNA binding, and a disruptive mutation in only one dimer strongly reduces the activity of the p53 tetramer (Aramayo et al., 2011). In agreement with this model, it is not a surprise that most missense mutations in tumour cells either reduce the binding affinity for DNA or interfere with the tetramerisation. The DNA binding domain is also the target of a complex formed by the high-risk human papillomavirus (HPV) induced oncoprotein E6 and the HECT E3 ligase E6AP (Martinez-Zapien et al., 2016). This enables E6AP to catalyse the polyubiquitination of p53, which leads to its proteasomal degradation, and potentially stimulates the formation of HPV dependant head-to-neck cancers and cervical carcinomas (Tumban, 2019).

1.3.2 MDM2-p53 interaction under unstressed conditions

MDM2 regulates p53 through two distinct mechanisms. First, it can act as an inhibitor that blocks p53's from transcriptional function (Chen et al., 1996). Second, it can mono- and polyubiquitinate p53. The former ubiquitination pattern promotes p53's export from the nucleus into the cytoplasm whereas the latter involves the formation of K48-chains that signal p53 for degradation (Li et al., 2003).

Each mechanism involves complex formation via the N-terminal domains of both proteins (Figure 1-17). For MDM2's inhibitory function, this interaction is crucial as hydrophobic residues such as $W23^{p53}$ are also involved in binding E1B-55K, a protein within the transcriptional machinery (Lin et al., 1994). Accordingly,

deletion of p53's MDM2 binding domain abolishes MDM2's ability to block p53's transcriptional activity (Marston et al., 1994). However, this does not block MDM2 mediated ubiquitination of p53 due to additional MDM2-p53 interactions involving $MDM2^{N\text{-terminus}}$-$p53^{C\text{-terminus}}$ and $MDM2^{\text{acidic domain}}$-$p53^{\text{DNA binding domain}}$.

Importantly, p53 itself induces the expression of MDM2, resulting in a negative feedback loop that keeps the concentration of both proteins at a controlled, low level under normal conditions. The essentiality of this mechanism is underscored by p53 knock-out mice, which have a very high chance of developing cancer due to missing DNA damage protection and die at an early stage (Donehower, 2014). On the other hand, MDM2 knock-out mice are embryonic lethal due to hyperactive p53 activity, leading to uncontrolled apoptosis (Montes de Oca Luna et al., 1995) (Jones et al., 1995). The same result is obtained with MDM2 mutants where the RING domain is disrupted by disturbing the Zn^{2+} coordination (C464A) (Itahana et al., 2007). This highlights that efficient p53 regulation cannot be acquired by MDM's inhibitory effect but requires its ligase activity. Interestingly, knock-out of MDMX is also lethal, which indicates that homodimeric MDM2 is not able to robustly regulate p53 (Pant et al., 2011). In contrast, mice are viable when MDM2 carries a C-terminal mutation (Y489A) that exclusively abolishes the ligase activity of the homodimer, demonstrating that the ligase activity of the heterodimer is critical at an embryonic state (Tollini et al., 2014). Consequently, a dimerisation disrupting mutation in MDMX (C463A) has a similar effect (Huang et al., 2011). In all mice studies, the lethality could be rescued when p53 was knocked-out simultaneously.
The importance of the heterodimer, which is the predominant dimer *in vivo*, has been demonstrated by a number of studies in cells. The heterodimer is more stable than homodimeric MDM2 and was shown to be a more potent E3 ligase for polyubiquitination p53 (Kawai et al., 2007), whereas the homodimer mainly monoubiquitinates of p53.

1.3.3 MDM2-p53 interaction under DNA damage

The feedback loop (Chapter 1.3.2) ensures that the cellular p53 levels are kept at a constant, low level so that it can respond quickly to occasional DNA replication errors (Wu et al., 1993).

Upon cellular stress such as DNA damage, p53 needs to be quickly upregulated to stop cell proliferation. Therefore, it needs to be uncoupled from MDM2-mediated downregulation. In this context, a number of DNA damage dependant phosphorylation events occur on both proteins that mainly affect their binding affinity for each other. Phosphorylation at $S15^{p53}$ $T18^{p53}$, $S20^{p53}$ and $T37^{p53}$, which are located within the MDM2 binding domain (Figure 1-17), was shown to stabilise p53 in cells and associated with perturbed MDM2 binding (Shieh et al., 1997) (Chehab et al., 1999) (Craig et al., 1999). Despite a reduction in binding affinity for MDM2, p53 could still be stabilised upon DNA damage in cells with corresponding alanine mutations (Ashcroft et al., 1999). Mice carrying $p53^{S20A}$ were more susceptible to develop tumours in the absence of DNA damage, and this effect could be amplified by mutating S15 in parallel. Nevertheless, these mutations did not abolish p53's increased stability following DNA damage (Chao et al., 2006).

Phosphorylation events have not only been reported for p53 but also for MDM2. Upon DNA damage, DNA-PK phosphorylates $S17^{MDM2}$, which is located in the N-terminal lid (Chapter 1.2.2) and in proximity to the p53 binding site (Figure 1-13). However, the role of this phosphorylation site is unclear since *in vitro* assays showed contradictory effects of $pS17^{MDM2}$ on p53 binding (Mayo et al., 1997) (Worrall et al., 2009).

The acidic domain is heavily phosphorylated by CK1δ in the absence of DNA damage. Upon DNA damage, these residues are partly dephosphorylated, which stabilises p53 although it does not affect MDM2's ability to bind or to ubiquitinate p53. The fact that p53 degradation but not ubiquitination is reduced, suggests that this phosphoregulatory mechanism might affect the binding between the acidic domain and another protein, which ultimately stabilises p53 (Blattner et al., 2002). A potential candidate is the $SCF^{β\text{-}TRCP}$ complex that ubiquitinates MDM2 upon DNA damage, leading to MDM2's degradation (Inuzuka et al., 2010). Paradoxically, $SCF^{β\text{-}TRCP}$ requires MDM2 to be phosphorylated by CK1δ. This indicates that phosphoregulation involving MDM2's acidic domain is not yet fully understood and might depend on the precise experimental setup. Reversely, GSK3-ß-mediated phosphorylation of MDM2 at S242 and S256 caused p53 to be destabilised in U2OS cells. However, GSK3-ß itself is also phosphorylated under DNA damage, which inactivates it so that its

negative regulatory effect is masked (Kulikov et al., 2005). Nevertheless, this might be context dependant and could add another layer of complexity to DNA damage induced p53 stabilisation.

ATM phosphorylates MDM2 at residues between the zinc finger domain and the RING domain (S386, S395, S407, T419, S425, S429), thus far away from domains associated with p53 binding (Cheng et al., 2009). When these residues are simultaneously mutated to alanine ('6A'), p53 could not be efficiently stabilised in H1299 cells upon DNA damage. In contrast, aspartic acid substitutions ('6D') stabilised p53 even in the absence of DNA damage. Although the mechanism for this observation is unknown, the molecular weight of MDM2 was reduced upon DNA damage based on size-exclusion chromatography (SEC), suggesting that a change of the oligomeric state might be responsible for this effect. The same observation was made for MDM2 constructs (362-C) with the corresponding aspartic acid mutations purified from *Escherichia coli* (*E. coli*). This indicates that the effect was independent of not only other DNA damage responses but also conformational changes involving any of the domains within the first 361 amino acids. So far, detailed studies of the individual phosphorylation in this region are incomplete, so their relevance or the number of underlying mechanisms is unknown. Phosphorylation of S395 alone was sufficient to stabilise p53 in H1299 cells (Maya et al., 2001) and mice. However, in the latter study, p53 was still upregulated in mice, where S395 was mutated to alanine, following DNA damage (Gannon et al., 2012). Individual phosphomimetic mutations at two additional residues, S386E and S429D, was sufficient to stabilise p53 in H1299 cells in the absence of DNA damage (Cheng et al., 2011), which was also seen for S395D in mice (Gannon et al., 2012). S395-phosphorylation was also reported to enhance MDM2's autoubiquitination activity (Stommel and Wahl, 2004), which could explain why p53 is stabilised, although this observation was not observed in subsequent studies and could have been a result of inaccurate MDM2 detection due to epitope masking of the used antibody (Cheng and Chen, 2011).

Collectively, these results show that several phosphorylation events on both, p53 and MDM2, contribute to p53's stability following DNA damage. Nevertheless, none of the phosphorylation sites per se could be identified as the main phosphorylation site, suggesting that several phosphorylation sites might work in concert to achieve a robust DNA damage response. Especially for phosphorylation events outside of the N-terminal binding domains, no molecular

mechanism has been established so far. This includes the question whether additional interaction partners are involved in the DNA damage response. For instance, MDM2 ubiquitinates MDMX directly following DNA damage, even before p53 levels start to rise. This leads to immediate proteasomal degradation of the heterodimer (Pan and Chen, 2003).

1.3.4 MDM2 as a drug target for p53 activation

Around half the human cancers develop in the presence of wild-type p53, and in most of these cases, p53 is inactivated by another protein. As one of the main negative regulators, MDM2 plays an important role in this context. In particular, overexpression of MDM2 has been associated with cancer due to uncontrolled p53 inhibition and degradation (Wade et al., 2013), which makes a cell vulnerable to DNA replication errors. In this case, MDM2 is a promising drug target with the idea to uncouple it from p53, thereby allowing p53 to regain its anti-tumour function. Reactivation of p53 has indeed been shown to stop cell growth of tumour cells by inducing cell cycle arrest or apoptosis (Ventura et al., 2007).

In order to inactivate MDM2 as a p53 regulator, two different strategies have been explored for the development of small molecule inhibitors: (i) Molecules that bind MDM2's N-terminal p53 binding pocket (Figure 1-17) and (ii) RING domain inhibitors that abolish MDM2's ligase activity.

The first potent MDM2 inhibitor that was used in clinical trials was Nutlin, which is a *cis*-imidazoline analogue that binds MDM2 with a high affinity at the same position as p53's N-terminal helix, thereby blocking the interaction between MDM2 and p53. This could stabilise p53 in cells and prevented tumour growth in mouse models (Vassilev et al., 2004). In order to increase the potency and the specificity, a large number of other small molecules including Nutlin derivatives with higher binding affinity have been designed since. For example, Idasanutlin has a 200-fold improved potency with an IC_{50} in the low nM range (Ding et al., 2013) and has been used for a number of clinical trials (Nguyen et al., 2017) including a phase 3 trial (NCT02545283) with 440 patients, which is scheduled to be completed by 2022. The spiro-oxindole compound SAR405838 gains an additional binding improvement by also interacting with the N-terminal lid of MDM2 (Wang et al., 2014), which might be a starting point for the development

of even more potent inhibitors. One approach that makes use of this additional interaction involves stapled peptides based on the p53 peptide in the MDM2-p53 crystal structure (Chang et al., 2013) (Figure 1-17).

Although targeting the p53 binding pocket has been successful, this strategy is prone to on-target toxicities related to effects caused by uncontrolled p53 activity.

As MDM2 has been reported to be crucial in this context (Ringshausen et al., 2006), the development of drugs that allow MDM2 to still bind p53 might be promising. This could be achieved by targeting the RING domain instead, with the idea to disrupt MDM2's ligase activity while maintaining its ability to bind p53, thereby inhibiting its transcriptional activity. As a proof of concept, 5-deazaflavin derivatives like HLI98 could inhibit MDM2's ligase activity *in vitro* (Dickens et al., 2013) and in cells. Nevertheless, they showed a relatively low potency and had undesirable off-target effects by also affecting other E3 ligases (Yang et al., 2005) and despite further optimisation approaches, those issues could not yet been overcome (Roxburgh et al., 2012). In order to unveil the precise inhibitory mechanism of these inhibitors, co-crystal structures with the MDM2 RING domain would be highly desirable, which would then allow a structure-guided compound design like in the case of Nutlin, potentially yielding RING domain inhibitors with improved potency and specificity.

1.4 Objectives

To date, structural studies of the RING domain homodimer of MDM2 have been limited by the pronounced aggregation tendencies of this protein as reported by others (Kostic et al., 2006) (Poyurovsky et al., 2007) (Linke et al., 2008) and as observed in our laboratory. How the homodimer recruits E2-Ub is unknown and current knowledge relies on a model (Figure 1-16) based on the crystal structure of the MDM2-MDMX heterodimer in complex with E2-Ub (Nomura et al., 2017). However, mutational analyses suggested that that the RING domain of the homodimer is structurally distinct from the heterodimer (Dolezelova et al., 2012) (Kosztyu et al., 2019). As both dimers play a role in p53 ubiquitination, the RING domains are attractive targets for drug development, with the aim being to restore p53's anti-tumour function (Chapter 1.3.4). In this context, a precise structure-function relationship is required to effectively design RING domain inhibitors. The aim of this thesis was to develop a purification protocol that would yield protein of sufficiently high quality to investigate structural aspects of MDM2 homodimer function.

Several constructs were designed and tested; optimisation of purification protocols yielded significant quantities of homogeneous, dimeric MDM2. The protein was subsequently used for crystallisation purposes. Crystal structures of several MDM2 RING domain constructs were obtained, including the complex of the homodimer with E2-Ub (Chapter 3).

Structural differences between the homodimer and the heterodimer account for homodimer-specific phosphoregulation upon DNA damage. The mechanism behind this observation was unveiled by determining the crystal structure of phospho-MDM2 in complex with E2-Ub. The molecular basis of this novel mechanism and the homodimer specificity is discussed in Chapter 4.

Chapter 2 Methods

All chemicals used in this study were purchased from Sigma-Aldrich, if not stated otherwise.

2.1 Cloning

All gene fragments used in this study were codon-optimised and either available in the lab at the beginning of this project or purchased from IDT. Expression vectors used in this study including the proteins they were used for, protease cleavage sites and if applicable N-terminal fusion-tags are listed in Figure 2-1. pET21d UBA1 was purchased from AddGene (#34965) (Berndsen and Wolberger, 2011). The following constructs were designed by other lab members: pAblo GGS-Ub, pGEX-GGSC-Ub, RSF_Duet-6-His-GGS-Ub, RSF_Duet-UbcH5B S22R±C85K, pAblo-MDM2 350-C, RSF_Duet-6-His-MBP-MDM2 428-C. PCRs were performed using the ProFlex PCR System (Thermo Fisher).

Table 2-1: Expression vectors used in this study. The sequence of the TEV cleavage site, which connects the N-terminal fusion tag with the protein, is ENLYFQGS in all vectors.

Vector	**N-terminal fusion-tag**	**TEV cleavage site**	**Proteins**
pGEX4T1	GST	yes	GGSC-Ub
pAblo	GST	yes	MDM2, GGS-Ub
pET21d	6-His	yes	UBA1
pRSFDuet-1	-	no	UbcH5B
	6-His	yes	GGS-Ub
	12-His	yes	MDMX, MBP-MDM2
	6-His-MBP	yes	MDM2 428-C

Target proteins were cloned into the desired vector (Table 2-1) by using standard cloning techniques consisting of PCR amplification of the gene of interest followed restriction enzyme digest and ligation (Chapter 2.1.1 and Chapter 2.1.2) or PCR amplification of the whole plasmid (Chapter 2.1.3).

2.1.1 Traditional cloning

The gene fragment of interest was obtained from PCR amplification using *PfuUltra* II Fusion HS DNA Polymerase (Agilent, #600674) following the manufacturer's instruction manual. Complementary primers with a length of at least 20 nucleotides were designed with 5'-BamHI and 3'-EcoR1 restriction sites followed by addition of two nucleotides, guanine (G) and cytosine (C), to enhance the recognition efficiency by the polymerase. They were optimised to achieve a G+C content of more than 50 %, a melting temperature above 60 °C and if necessary elongated, so that the first and last nucleotide was either G or C. Amplified DNA products were purified using the QIAquick PCR Purification Kit (Qiagen, #28104) and double digested with restriction enzymes HF-BamHI (New England BioLabs, #R3136L) and HF-EcoRI (New England BioLabs, #R3101L). The same digestion reaction was performed for the target vectors where 1 µL CIP (New England BioLabs, #M0290L) was added to 50 µL reaction mixture to prevent self-ligation. Digested DNA fragments were isolated by gel electrophoresis using agarose gel (1.2-4 %) containing 1xGelRed (Biotium, #41003). DNA was visualised under UV light (SafeImager, Invitrogen), bands of the correct size were cut out from the gel and the DNA was extracted using the QIAquick Gel Extraction Kit (Qiagen, #28115). The DNA fragment was then ligated into the desired vector using Quick Ligase (New England BioLabs, #M2200) following the manufacturer's instructions.

2.1.2 Overlap extension PCR

Overlap extension PCR was used for constructs consisting of two templates (non-cleavable MBP-MDM2, MDM2^{c}, MDM2^{g}, MDM2^{o}, MDM2^{t}) and for MDM2 S429^{STOP}. For this approach, DNA fragments of each of the constructs containing an overhang of ten nucleotides complementary to the second construct were amplified. Internal primers were designed that contained at least 20 nucleotides of the template and at least ten nucleotides of the fusion gene. The PCR was carried out as in Chapter 2.1.1, and the PCR products were separated by gel electrophoresis using agarose gel as described above. They were then used as templates for a second PCR reaction to obtain the fusion construct, using

primers with BamHI and EcoRI restriction sites as described in Chapter 2.1.1 and the Q5 Hot Start HF Master Mix (New England BioLabs, #M0494S), followed by PCR clean-up, restriction digest, gel extraction and ligation as described in Chapter 2.1.1.

2.1.3 Site-directed mutagenesis

Site-directed mutagenesis was used to introduce point mutations other than MDM2 S429^{STOP} or nucleotide insertions into gene fragments that were already ligated into a vector. Complementary primers were designed with the desired mutation(s), an overlap of at least 15 nucleotides, followed by an overhang of at least nine nucleotides. They were optimised to achieve a G+C content of more than 50 %, a melting temperature above 70 °C and if necessary elongated, so that the first and last nucleotide was either G or C. PCR products were treated with DpnI for 1 h at 37 °C to destroy template vector.

2.1.4 Transformation and plasmid amplification

Ligation products (Chapter 2.1.1 and 2.1.2) or DpnI-treated PCR products (Chapter 2.1.3) were transformed into competent DH5α cells by adding 1-5 µL to a ten times higher volume of cells. The cells were kept on ice for 20-30 min, incubated at 42 °C for 45 s (heat shock), kept on ice for 2 min, and shaken at 37 °C for 1 h after the addition of 1 mL Luria Bertani medium (LB). Cells were spread on LB-agar containing the appropriate antibiotics and incubated at 37 °C for 16-24 h. Single colonies were picked and grown in 6 mL LB for 16-24 h. After centrifugation, cell pellets were sent to the internal Sequencing facility, where the DNA was extracted and sequenced, using primers covering the full sequence of the insert including the restriction sites.

2.2 Protein expression

Reagents for protein expression were purchased from Formedium, if not stated otherwise. 1 mg/mL Ampicillin was added to cells transformed with pAblo, pGEX or pET21d and 0.5 mg/mL kanamycin were added to cells transformed with pRSFDuet-1. OD_{600} values were measured with a spectrophotometer (DU720,

Beckman-Coulter). All proteins in this study were expressed in *Escherichia coli* BL21(DE3) GOLD (Chapter 2.2.1) except phospho-MDM2, which was expressed in *Escherichia coli* EcAr7 (Chapter 2.2.2). In EcAr7, the gene encoding release factor 1 (RF-1) is knocked out, which initiates the termination of the translation at the amber codon (UAG). As this alone would be lethal due to uncontrolled translation, the amber codon of seven essential genes was replaced by the ochre codon (TAA), leading to the correct translation of these proteins (Heinemann et al., 2012). When supplemented with a vector encoding a modified tRNA, phosphoserine can be inserted at the amber codon. Co-expression with a protein of interest that is encoded by a gene containing the amber codon allows specific incorporation of phosphoserine at a desired position.

2.2.1 *Escherichia coli* BL21(DE3) GOLD

1 µL (10-300 ng) of the desired expression vector (Table 2-1) was transformed into 10 µL *Escherichia coli* BL21(DE3) GOLD cells, kept on ice for 5-30 min, incubated at 42 °C for 45 s (heat shock), kept on ice for 2 min, and shaken at 37 °C for 10-60 min after the addition of 1 mL LB. Cells were spread on LB-agar containing the appropriate antibiotics and incubated at 37 °C for 16-24 h. A single colony was picked and shaken in LB with the appropriate antibiotics at 37 °C overnight (starter culture). For protein expression, 10 mL starter culture were added to 1 L autoclaved LB containing the appropriate antibiotics and shaken in an incubator (innova44, New Brunswick) at 200 rpm and 37 °C to an OD_{600} of 0.3-0.5. Then, the temperature was reduced to 20 °C, and the cells were further grown to an OD_{600} of 0.6-1.0. Protein expression was induced by the addition of 0.2 mM IPTG. After induction, cells were shaken for additional 16-24 h. Cells were centrifuged for 15 min at 4,000 rpm (J6-MI, Beckman-Coulter), and the pellet was resuspended in 8-15 mL lysis buffer per 1 L LB. The composition of the lysis buffer was identical to the wash buffer of the first purification step (Chapter 2.3), supplemented with 2.5 mM PMSF. When not lysed at the same day, resuspended cells were flash frozen with liquid nitrogen and stored at -40 °C.

2.2.2 *Escherichia coli* EcAr7

5 µL (0.05-1.5 µg) of the expression vector (pAblo) were co-transformed with a similar amount of pKD-SepRS-EFSep-5x tRNASep (AddGene, Plasmid #52054) into 100 µL *Escherichia coli* EcAr7 cells (AddGene, #52055) (Heinemann et al., 2012), kept on ice for 30 min, incubated at 42 °C for 45 s (heat shock), kept on ice for 2 min, and shaken at 37 °C for 2 h after the addition of 1 mL LB. Cells were spread on LB-agar containing ampicillin and kanamycin and incubated at 30 °C for 2 days. Five colonies were picked and shaken in Terrific Broth medium (TB) containing 0.08 % *w/v* glucose, 1 mg/mL ampicillin and 0.25 mg/mL kanamycin at 30 °C overnight (starter culture). For protein expression, 50 mL of starter culture were added to 1.6 L autoclaved TB supplemented with glucose and antibiotics as described above, 2 mM L-*O*-phosphoserine, pH 6.8 (TCI America, #P0773) and 0.3 mL/L Antifoam 204. Cells were grown under moderate bubbling at 30 °C to an OD_{600} of approximately 2 using the LEX Bubbling System. Then, the temperature was reduced to 25 °C, and protein expression was induced by the addition of 0.5 mM IPTG. After induction, cells were shaken for additional 16-24 h. Cells were centrifuged for 15 min at 4,000 rpm, and the pellet was resuspended in 10-15 mL lysis buffer (50 mM Tris pH 7.6, 400 mM NaCl, 50 mM NaF, 1 mM Na_3VO_4, 1 mM DTT and 2.5 mM PMSF per 1 L TB. When not lysed at the same day, resuspended cells were frozen with liquid nitrogen and stored at -40 °C.

2.2.3 Glycerol stocks

For all constructs except pET21d-UBA1, cells from the starter culture were 1:1 mixed with glycerol and stored at -80 °C. Whenever a protein was expressed again, a starter culture was set up using cells from the glycerol stock to save time and reagents and to achieve a better reproducibility of protein expression results.

2.3 Protein purification

2.3.1 Lysis

Cell lysates were kept on ice throughout the whole lysis procedure, when possible. Proteins expressed from no more than 6 L LB or TB were lysed using sonication. Resuspended cell pellets were supplemented with 1 mg/mL lysozyme and gently rocked at 4 °C for 20-40 min. 30 mL aliquots of cells were lysed with 8x8 s pulses (Vibra-Cell, Sonics) with 8 s breaks between each pulse. This procedure was repeated 1-2 times, with at least 10 min time between each cycle to avoid overheating of the lysate. When proteins were expressed from more than 6 L, lysis was accomplished using a microfluidizer (M-110P, Microfluidics). Cells, supplemented with 1 µg/mL Deoxyribonuclease I, were disrupted at 15,000 psi and two times reloaded to achieve a total number of three lysis passes. Cell lysate was centrifuged at 20,000 rpm and 4 °C for 30 min (JXN-26, Avanti with rotor JA-25.50, Beckman-Coulter) and the supernatant was directly used for protein purification.

2.3.2 Chromatography

If not mentioned otherwise, cell lysate was loaded on a gravity column packed with Nickel beads (ABT, #6BCL-QHNi), glutathione agarose (ABT, #4B-GLU) or SP Sepharose Fast Flow beads (GE Healthcare, #17-0729), depending on the fusion-tag of the protein. GST-tagged proteins were incubated with GSH Sepharose for 1 h prior to washing. Proteins were washed and eluted with buffers depending on the resin type (Table 2-2). For cleavage on the beads, the column was connected to a peristaltic pump overnight. Where required, eluted protein was purified further. For salt-gradient based anion and cation exchange chromatography (AIEC and CIEC, respectively), manually packed columns with Source 15Q (GE Healthcare, 17-0947) or Source 15S (GE Healthcare, 17-0944) resin were used, respectively. Size-exclusion chromatography (SEC) was performed using a Superdex 75 HiLoad 26/60 (GE Healthcare, #17-1070) or a Superdex 200 HiLoad 26/60 (GE Healthcare, #17-1071-01) column (from here on SD75 and SD200, respectively).

For analytical SEC, an SD75 10/300 increase column (GE Healthcare, #17-5174) was used. IEX and SEC were performed on ÄKTA purifier (GE Healthcare) and the NGC Chromatography System (BIO-RAD).

Table 2-2: Separation techniques used for the first purification step. Nickel and GSH affinity chromatography buffers contained 400 mM NaCl for MDM2 constructs shorter than 390-C and 200 mM NaCl for all other proteins.

Separation technique	**Fusion-tag**	**Buffer**	**Buffer composition**
Nickel affinity chromatography	6XHis	Wash buffer	50 mM Tris, 200mM NaCl, 20 mM imidazole, 5 mM ß-Me (pH 7.6)
	12XHis	Wash buffer	50 mM Tris, 200mM NaCl, 30 mM imidazole, 5 mM ß-Me (pH 7.6)
	6XHis, 12XHis	Elution buffer	50 mM Tris, 200-400 mM NaCl, 300 mM imidazole, 5 mM ß-Me (pH 7.6)
GSH affinity chromatography	GST	Wash buffer	50 mM Tris, 200-400 mM NaCl, 1 mM DTT (pH 7.6)
		Cleavage on the beads buffer	50 mM Tris, 200-400 mM NaCl, 1 mM DTT, 0.1 mg/mL TEV protease (pH 7.6)
		Elution buffer	50 mM Tris, 200-400 mM NaCl, 10 mM glutathione, 1 mM DTT (pH 7.6)
CIEC	no fusion tag	Wash buffer	50 mM MES, 50 mM NaCl (pH 6.5)
		Elution buffer	50 mM MES, 200 mM NaCl (pH 6.5)

2.3.2.1 Purification of GGS-Ub

For purification of His-GGS-Ub, protein was dialysed against 50 mM Tris, 200 mM NaCl, 5 mM ß-Me (pH 7.6). For GGS-Ub, the 6X-His-TEV fusion tag was removed by the addition 1:50 TEV protease. Cleavage was done at 23 °C overnight while dialysing against the same dialysis buffer as described above. Cleaved protein was passed-back onto Nickel beads, the flow-through was concentrated and the protein was purified from SD75 in PBS.

2.3.2.2 Purification of UBA1

Lysate of UBA1 was 6:1 mixed with lysate of GST-TEV-GGS-Ub and stirred for 2 h in the presence of 3 mM ATP and 3 mM $MgCl_2$. The lysate was loaded on GSH Sepharose, stirred for 1 h and eluted with 50 mM Tris, 200 mM NaCl, 25 mM DTT (pH 7.6). Eluted protein was 1:2 diluted with 50 mM Tris (pH 7.6) and further purified from AIEC using a NaCl gradient (0-1 M).

2.3.2.3 Purification of UbcH5B

All UbcH5B constructs used in this study contained the mutation S22R, which blocks backside binding of Ub (Buetow et al., 2015). Cell lysate was 1:2 diluted with 50 mM MES (pH 6.0), applied on SP Sepharose, washed and eluted. The protein was 1:4 diluted with 50 mM MES (pH 6.0) and purified from CIEC using a NaCl (0-1 M) and pH (6.0-6.5) gradient. Eluted protein was applied on SD200 in 50 mM HEPES, 200 mM NaCl, 1 mM DTT (pH 7.5).

2.3.2.4 Purification of UbcH5B-Ub

UBA1 (2-6 µM), UbcH5B (120 µM), His-GGS-Ub (0.2 mM), 10 mM ATP and 10 mM $MgCl_2$ were mixed and the pH was adjusted to 7.8 by titrating with 1 M HEPES (pH 8.0). The mixture was incubated at 30 °C for 18 h. Formation of UbcH5B-6His-GGS-Ub was verified by SDS-PAGE. The reaction mixture was loaded on Nickel beads, washed, eluted and dialysed against 50 mM Tris, 200 mM NaCl, 5 mM ß-Me (pH 7.6) at 23 °C overnight after addition of 1:50 TEV protease. Cleaved UbcH5B-Ub was passed back onto Nickel beads, 1:3 diluted with 50 mM MES (pH 6.0) and purified from CIEC using a NaCl (0-1 M) and pH (6.0-6.5) gradient. Eluted protein was applied on SD200 in 50 mM HEPES, 200 mM NaCl, 1 mM DTT (pH 7.5). A purification attempt is shown in Figure 2-1.

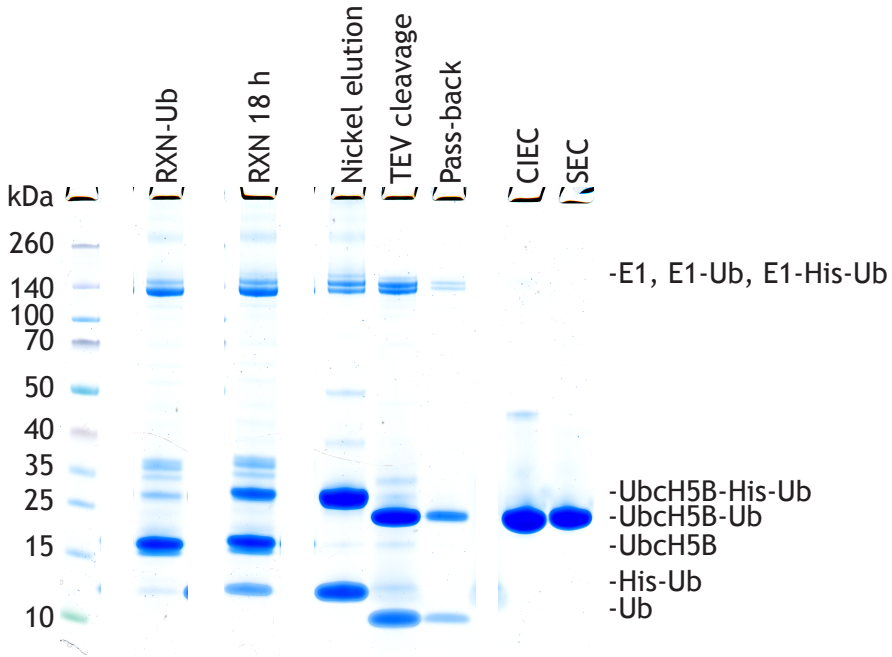

Figure 2-1: Purification of UbcH5B-Ub. Reaction before the addition of Ub (RXN-Ub), reaction after 18 h (RXN 18 h), Nickel affinity chromatography elution (Nickel elution), TEV cleavage, Pass-back onto Nickel beads, CIEC, SEC.

2.3.2.5 Purification of fluorescently labelled GGSC-Ub

GGSC-Ub was eluted by cleavage on the beads (Table 2-2) at 23 °C overnight. Eluted protein was applied on SD75 in PBS buffer, concentrated and incubated with IRDye 800CW Maleimide (LI-COR, #929-80020) for 3 h at 23 °C, using a molar protein to dye ratio of 5:1. The protein was buffer exchanged twice into 50 mM HEPES, 200 mM NaCl (pH 7.0) using Zeba Spin Desalting Columns (Thermo Scientific, #89890).

2.3.2.6 Purification of MDM2

For MDM2 constructs shorter than 390-C, 400 mM NaCl was used in all purification buffers whereas for MDM2 constructs longer than 390-C, 200 mM were used instead. For phospho-MDM2 (batch 2), 50 mM NaF were added to all buffers. GST-TEV MDM2 was eluted using GSH elution buffer and not further purified. MDM2 cleaved from GST-TEV was eluted using GSH cleavage on the beads buffer. MDM2 constructs longer than 390-C and MBP-MDM2 418-C were 1:3 diluted with 50 mM Tris (pH 7.6) and purified from AIEC using a NaCl gradient (0-1 M), followed by SEC (SD200). MDM2 constructs shorter than 390-C were directly applied on SEC (SD75) after cleavage. SEC buffers were composed of 50 mM Tris pH 7.6 or HEPES pH 7.5, 200-400 mM NaCl and 1 mM DTT. GST-TEV-MDM2/His-TEV-MDMX heterodimer constructs were obtained from co-expression. Cell lysate was applied on Nickel beads, washed, eluted and applied on GSH Sepharose. After stirring for 1 h, protein was washed and eluted with GSH elution buffer.

2.3.3 Concentrating and storage

All proteins except MDM2 were, if required, concentrated using Amicon Ultra Centrifugal Filters (Merck). MDM2 was concentrated in Amicon Stirred Cells under nitrogen gas flow using Ultracel Ultrafiltration Discs (Merck). After the final purification step, aliquots of protein (20-100 µL) were flash frozen in liquid nitrogen and stored at -80 °C upon further usage.

2.4 Biochemical techniques

2.4.1 SDS-PAGE

Protein was mixed with denaturing 1X NuPAGE LDS Sample Buffer (invitrogen, #NP0007), loaded in wells of pre-cast 4-12 % Novex NuPAGE Bis-Tris Protein Gels (invitrogen) in 1X NuPAGE MES SDS Running Buffer (invitrogen, #NP0002) and separated by electrophoresis (35 min, 200 V). PageRuler Prestained Protein Ladder (Thermo Scientific, #26616) was used as size standards. For autoubiquitination assays using fluorescently labelled Ub, SDS-PAGE was performed under reduced conditions by adding 100 mM DTT to the denatured protein. For reduced SDS-PAGE, 1X NuPAGE MOPS SDS Running Buffer (invitrogen, #NP0001) was used with an extended running time (50 min).

2.4.2 Western blot

First, proteins were separated by SDS-PAGE (Chapter 2.4.1). Transfer (25 V, 7 min) from the polyacrylamide gel to a polyvinylidene fluoride membrane (BIO-RAD, #1704270) was conducted using the Trans-Blot Turbo Transfer System (BIO-RAD). Membranes were blocked by incubation with TBS-T (50 mM Tris pH 7.6, 150 mM NaCl, 0.1 % *v*/*v* TWEEN® 20) containing 0.1 mg/mL BSA for at least 30 min. Incubation with primary antibody rabbit polyclonal anti-MDM2-pS429 (Eurogentec) was carried out in TBS-T containing 0.05 mg/mL BSA at 4 °C overnight. The membranes were washed three times with TBS-T for 5 min each followed by a wash step in TBS (50 mM Tris pH 7.6, 150 mM NaCl) for 5 min. Incubation with secondary antibody goat-anti rabbit IRDye 800CW (LI-COR, #32211) was carried out in TBS-T containing 0.05 mg/mL BSA for 1 h at 23 °C. Following three wash steps in TBS-T and one wash step in TBS, the blots were visualised with the Odyssey CLx imaging system (LI-COR).

2.4.3 Protein quantification

Protein concentration was determined using the Bradford assay (Bradford, 1976). 2-100 µL protein were added to 1 mL 1:5 Protein Assay Dye Reagent Concentrate (Bio-Rad, #5000006), the absorbance at 595 nm was measured spectrophotometrically and the protein concentration was calculated using a standard curve obtained for BSA. Ub poorly stains using the above-mentioned dye, so that the concentration was determined spectrophotometrically by measuring the absorbance at 280 nm (DS-11, DeNovix), from which the protein concentration could be calculated after Lambert-Beer, using the protein specific extinction coefficient ε=1490 $M^{-1}cm^{-1}$ obtained from the ProtParam tool (Wilkins et al., 1999).

2.5 Crystallisation

2.5.1 Initial screening

All crystallisation attempts were undertaken at 19 °C. Wherever co-crystallisation attempts were undertaken (MDM2 + UbcH5B-Ub) both proteins were mixed at a molar ratio of 1:1. Stock concentrations were 14-15 mg/mL for UbcH5B-Ub and 3-15 mg/mL for MDM2, depending on the construct. For all initial screening attempts, crystallisation was conducted using the sitting drop vapour diffusion technique, where 0.2 µL protein were mixed with 0.2 µL crystallisation buffer using the Mosquito crystallisation robot (TTP Labtech). Commercially available screens were used as listed in Table 2-3. The following screens were used: PACT *premier*™ (Molecular Dimensions, #MD1-36), ProPlex™ (Molecular Dimensions, #MD1-38), Morpheus® (Molecular Dimensions, #MD1-46), JCSG-*plus*™ (Molecular Dimensions, #MD1-37), MIDASplus™ (Molecular Dimensions, #MD1-106), The BCS Screen (Molecular Dimensions, #MD1-104), Index (Hampton Research, #HR2-144), JBScreen Classic HTSI (Jena Bioscience, #CS-201L), PEGs Suite (Qiagen, #130704), Additive Screen (Hampton Research, #HR2-428). PEG Smear Broad and PEG Smear Medium were obtained from Molecular Dimensions (#MD2-261, #MD2-259). Crystal growth was followed for at least 21 days, if not flash frozen before, by regular imaging using the ROCK IMAGER 1000 (FORMULATRIX).

Table 2-3: Commercial crystal screens used for initial screening attempts. The screens used for each protein construct are indicated with (X). The following screens were used: Cl (JBScreen Classic HTSI), In (Index), Mo (Morpheus®), PA (PACT *premier*™), PE (PEGs Suite), Pr (ProPlex™), JC (JCSG-*plus*™), BC (The BCS Screen), MI (MIDASplus™).

Construct	Cl	In	Mo	PA	PE	Pr	JC	BC	MI
$MDM2^{z}$	X	X	X	X	X	X	X		
$MDM2^{z}$ + UbcH5B-Ub	X	X	X	X	X	X	X		
$MDM2^{f}$	X	X	X	X	X	X	X	X	X
$MDM2^{f}$ 421-C + UbcH5B-Ub	X	X	X	X	X	X	X	X	X
$MDM2^{f}$ 389-C + UbcH5B-Ub	X	X	X	X	X	X	X	X	X
$MDM2^{f}$ 361-C + UbcH5B-Ub	X	X	X	X	X	X	X	X	X
MDM2 350-C '6D' + UbcH5B-Ub	X	X	X	X	X	X	X		
MBP-MDM2 418-C	X	X	X	X	X	X	X		
MBP-MDM2 418-C + UbcH5B-Ub	X	X	X	X	X	X	X		
$MDM2^{G443T}$ + UbcH5B-Ub	X	X	X	X	X	X	X	X	X
$MDM2^{WT}$ + UbcH5B-Ub								X	
MDM2 S429D + UbcH5B-Ub	X	X	X	X	X	X	X	X	X
$MDM2^{c}$ S429E								X	
$MDM2^{c}$ S429E + UbcH5B-Ub								X	
$MDM2^{g}$ S429E + UbcH5B-Ub								X	
$MDM2^{o}$ S429E + UbcH5B-Ub								X	
$MDM2^{t}$ S429E + UbcH5B-Ub								X	
$MDM2^{c}$ pS429 (batch 1) + UbcH5B-Ub								X	
$MDM2^{c}$ pS429 (batch 2) + UbcH5B-Ub						X		X	
MDM2 380-C '5D1E' + UbcH5B-Ub		X		X		X	X	X	
MDM2 363-C '5D1E' + UbcH5B-Ub		X		X		X	X	X	

2.5.2 Crystal optimisation and seeding

Where initial crystallisation attempts did not yield crystals of sufficient quality for data collection, they were individually optimised by varying precipitant concentration, buffer composition, pH, salt concentration or protein concentration. Where no single crystals of sufficient size could be obtained, crystals were used as microseeds for seeding approaches using the hanging drop method. Crystals were manually crushed and added to an equilibrated protein drop using a hairpin. For all crystallisation attempts using the hanging drop vapour diffusion technique, 1 µL protein was manually mixed with 1 µL crystallisation buffer and where applicable, at least equilibrated for 1 h before seeding.

2.5.2.1 Crystals for $MDM2^{z}$

Optimisation was performed using the sitting drop methodology at 6 °C and 19 °C. The precipitant concentration was varied between 15-25 % w/v PEG 3350 in 0.1 M HEPES, pH 8.0, 0.2 M NaCl. The salt concentration was varied between

0.1-0.7 M NaCl in 0.1 M HEPES, pH 8.0, 21 % *w/v* PEG 3350. Additionally, 3.5 µL additives were added to 31.5 µL 0.1 M HEPES pH 8, 0.2 M NaCl, 15 % *w/v* PEG 3350 and screened at 19 °C.

2.5.2.2 Crystals for MDM2^{f} 414-C in complex with UbcH5B-Ub

Initial optimisation was performed using the sitting drop methodology at 19 °C. The following precipitants were screened at different concentrations (% *w/v*) in two different buffers (0.1 M HEPES, pH 7.0 and MES, pH 6.5): PEG 1500 (10-35), PEG 4000 (10-35), PEG 8000 (10-25), PEG 20000 (10-20). Crystals grown for 10 days in 0.1 M HEPES, pH 7.0, 12 % *w/v* PEG 20000 were used as microseeds for subsequent optimisation using the hanging drop methodology using 5.5-13 % *w/v* PEG 20000, 0.1 M HEPES, pH 7.0.

2.5.2.3 Crystals for MDM2^{WT} in complex with UbcH5B-Ub

All optimisation attempts were performed by seeding with crystals obtained in the BCS Screen, position 1-24 using the hanging drop methodology. Two separat optimisation approaches were followed with varying the buffer components as follows: (i) Buffer: 0.1 M SPG, pH 7.0-8.0; 0.1 M Tris, pH 7.0-8.0, 0.1 M HEPES, pH 7.0-8.0, precipitant: 9-15 % *v/v* PEG Smear Broad, additives: 0-0.2 M NH_4NO_3,. (ii) Buffer: 0.1 M SPG, pH 6.3-8.0; 0.1 M Tris, pH 7.5-8.5, 0.1 M HEPES, pH 7.0-8.0, precipitant: 7-16 % *v/v* PEG Smear Medium, additives: 0-0.3 M NaCl, 0-0.1 M NaOAc.

2.5.3 Cryo protection and data collection

Crystals were flash-frozen in cryoprotection buffer and sent to beamline I03, I04 or I04-1 at Diamond Light Source for data collection. Crystallisation buffers of crystals for which datasets were obtained and the corresponding cryoprotection buffers are listed in Table 2-4.

Table 2-4: Crystallisation and cryoprotection buffer for each diffracting crystal of this study. Wherever a crystallisation buffer of a commercial screen was used, the corresponding screen is indicated in parenthesis. No cryoprotection buffer was added to crystallisation buffers that already contained cryoprotectants.

Crystal	Method	Crystallisation buffer	Cryoprotection buffer
MDM2[z]	sitting drop	0.1 M Buffer system 1 (pH 6.5), 37.5 % *v/v* Precipitant Mix 4, 0.12 M monosaccharides (Morpheus® F4)	n/a
MDM2[f] (Crystal A+B)	sitting drop	0.1 M PCTP (pH 8.0), 25 % *w/v* PEG 1500 (PACT *premier*™ C5)	66% PACT C5, 33% *v/v* MPD
MDM2[f] (Crystal C)	sitting drop	0.1 M PCTP (pH 7.0), 25 % *w/v* PEG 1500 (PACT *premier*™ C4)	66% *v/v* PACT *premier*™ C4, 33% *v/v* MPD
MDM2[f] + UbcH5B-Ub	hanging drop	0.1 M HEPES (pH 7.0), 10 % *w/v* PEG 20000	0.1 M HEPES (pH 7.0), 10 % *w/v* PEG 20000, 30 % *v/v* glycerol
MDM2[f] 389-C + UbcH5B-Ub	hanging drop	0.1 M SPG (pH 9.0), 25 % *w/v* PEG 1500 (PACT *premier*™ A6)	
MDM2^{G443T} + UbcH5B-Ub (Crystal A)	sitting drop	0.1 M Tris (pH 8.0), 15 % *w/v* PEG Smear Medium, 0.15 M NaCl, 0.08 M NaOAc (The BCS Screen 2-15)	0.1 M HEPES (pH 7.5), 22 % *w/v* PEG 3350, 0.2 M NaCl, 25 % *v/v* ethylene glycol
MDM2^{G443T} + UbcH5B-Ub (Crystal B)	sitting drop	0.1 M HEPES (pH 7.5), 20 % *w/v* PEG Smear Broad, 0.2 M NH_4NO_3 (The BCS Screen 2-9)	0.1 M HEPES (pH 7.5), 15 % *w/v* PEG 8000, 0.2 M NaCl, 25 % *v/v* ethylene glycol
MDM2^{WT} + UbcH5B-Ub	hanging drop	0.1 M SPG (pH 7.0), 10 % *w/v* PEG Smear Broad, 0.15 M NH_4NO_3	0.1 M SPG (pH 7.0), 13 % *w/v* PEG Smear Broad, 0.12 M NH_4NO_3, 25 % *v/v* glycerol
MDM2[c] S429E + UbcH5B-Ub	sitting drop	0.1 M Tris (pH 8.5), 20 % *w/v* PEG Smear High (The BCS Screen 1-20)	0.1 M Tris (pH 8.5), 20 % *w/v* PEG 8000, 0.2 M NH_4NO_3, 25 % *v/v* ethylene glycol
MDM2[g] S429E + UbcH5B-Ub	sitting drop	0.1 M HEPES (pH 7.5), 20 % *w/v* PEG Smear Broad, 0.2 M NH_4NO_3 (The BCS Screen 2-9)	
MDM2[o] S429E + UbcH5B-Ub (Crystal A)	sitting drop	0.1 M Bis-Tris propane (pH 8.0), 22.5 % *w/v* PEG Smear Medium, 0.01 M $CoCl_2$, 0.2 M $MgCl_2$, 2 % *v/v* glycerol (The BCS Screen 1-48)	
MDM2[o] S429E + UbcH5B-Ub (Crystal B)	sitting drop	0.1 M BICINE (pH 9.0), 20 % *w/v* PEG Smear Medium, 0.2 M $(NH4)_2SO_4$, 0.05 M Mg_2SO_4 (The BCS Screen 2-17)	0.1 M Tris (pH 8.5), 20 % *w/v* PEG 8000, 0.2 M NH_4NO_3, 25 % *v/v* ethylene glycol
MDM2[t] S429E + UbcH5B-Ub (Crystal A)	sitting drop	0.1 M Bis-Tris (pH 6.8), 25 % *w/v* PEG Smear Low, 0.15 M Li_2SO_4, 0.05 M $MgCl_2$ (The BCS Screen 2-26)	

$MDM2^t$ S429E + UbcH5B-Ub (Crystal B)	sitting drop	0.1 M HEPES (pH 7.5), 20 % *w/v* PEG Smear Broad, 0.2 M NH_4NO_3 (The BCS Screen 2-9)	
$MDM2^c$ pS429 + UbcH5B-Ub (Crystal A)	sitting drop	0.1 M PCTP (pH 9.0), 25 % *w/v* PEG 1500 (PACT *premier*™ C6)	
$MDM2^c$ pS429 + UbcH5B-Ub (Crystal B)	hanging drop	0.1 M HEPES (pH 7.5), 10 % *w/v* PEG Smear Medium, 0.15 M naCl, 0.075 M NaOAc	
$MDM2^c$ pS429 + UbcH5B-Ub (Crystal C)	sitting drop	0.1 M Tris (pH 8.0), 15 % *w/v* PEG 2000 MME, 0.1 M KCl (ProPlex™ 1-10)	0.1 M HEPES (pH 8.0), 27 % *w/v* PEG 3350, 0.2 M NaCl, 25 % *v/v* ethylene glycol
$MDM2^c$ S429E (Crystal A)	sitting drop	0.1 M MMT (pH 9.0), 25 % *w/v* PEG 1500 (PACT *premier*™ A6)	0.1 M Tris (pH 8.5), 20 % *w/v* PEG 8000, 0.2 M NH_4NO_3, 25 % *v/v* ethylene glycol
$MDM2^c$ S429E (Crystal B)	sitting drop	0.1 M HEPES (pH 7.5), 25 % *w/v* PEG Smear Medium, (The BCS Screen 1-16)	0.1 M Tris (pH 7.6), 25 % *w/v* PEG Smear Medium, 50 mM NaCl, 5 mM $MgCl_2$, 5 mM ATP, 30 % *v/v* ethylene glycol

2.5.5 Data processing and model building

Datasets were processed by automated XDS pipeline (Kabsch, 2010) and reduced with software packages as listed in Table 2-5 (Winn et al., 2011) (Vonrhein et al., 2011) (Evans, 2006) (Evans and Murshudov, 2013) (Winter et al., 2018).

Table 2-5: Software packages used for data processing of each dataset.

Crystal	Software package
MDM2^{z}	autoPROC
MDM2^{f} (Crystal A)	xia2 DIALS
MDM2^{f} (Crystal B)	xia2 DIALS
MDM2^{f} (Crystal C)	xia2 3dii
MDM2^{f} + UbcH5B-Ub	xia2 3dii
MDM2^{f} 380-C + UbcH5B-Ub	xia2 DIALS
MDM2^{G443T} + UbcH5B-Ub (Crystal A)	2x Multixia2 DIALS
MDM2^{G443T} + UbcH5B-Ub (Crystal B)	autoPROC
MDM2^{WT} + UbcH5B-Ub	xia2 DIALS
MDM2^{c} S429E + UbcH5B-Ub	xia2 3dii
MDM2^{g} S429E + UbcH5B-Ub	xia2 3d
MDM2^{o} S429E + UbcH5B-Ub (Crystal A)	xia2 3dii
MDM2^{o} S429E + UbcH5B-Ub (Crystal B)	xia2 3dii
MDM2^{t} S429E + UbcH5B-Ub (Crystal A)	xia2 3d
MDM2^{t} S429E + UbcH5B-Ub (Crystal B)	xia2 DIALS
MDM2^{c} pS429 + UbcH5B-Ub (Crystal A)	xia2 3dii
MDM2^{c} pS429 + UbcH5B-Ub (Crystal B)	xia2 3dii
MDM2^{c} pS429 + UbcH5B-Ub (Crystal C)	fastDP
MDM2^{c} S429E (Crystal A)	xia2 3d
MDM2^{c} S429E (Crystal B)	autoPROC STARANISO
MDM2 380-C '5D1E' + UbcH5B-Ub	xia2 DIALS

Matthews coefficient (Matthews, 1968) (Kantardjieff and Rupp, 2003) was used to estimate the content of the asymmetric unit. Initial phasing was accomplished by molecular replacement with PHASER (Storoni et al., 2004) using previously published crystal structures of the MDM2-MDMX heterodimer (PDB: 2VJF) and UbcH5B-Ub from the crystal structure of MDM2-MDMX-UbcH5B-Ub (PDB: 5MNJ) as search models. For crystal structures containing human MDM2, MDM2^{c}, MDM2^{g}, MDM2^{o} or MDM2^{t}, the crystal structure of MDM2^{f} 436-C (Crystal A, this study) was used as a search model instead. If required, a free R set was created using the CCP4i2 software package. The structures were refined using REFMAC5 (Murshudov et al., 2011) with geometry restraints for the isopeptide bond between UbcH5B's C85 and Ub's G76. Multiple refinement runs were executed to optimise the geometry weight. Non-crystallographic symmetry restraints (NCS) and TLS restraints were used as listed in Table 2-6. Where the resolution was high enough, anisotropic B-factors were used (Table 2-6). The model was built

using COOT (Emsley and Cowtan, 2004). Only residues for which sufficient electron density at 1 Ω contour level was observed in the $2F_o$-F_c map were built. Where electron density was only visible for the main chain, alanine stubs were built for the sidechains. Graphical representations were created with PyMol (Schrödinger). Where sticks are shown, oxygen and nitrogen atoms are coloured in red and blue, respectively. Zn^{2+} ions are represented as grey spheres and dashes indicate hydrogen bonds. Electron density is shown for $2F_o$-F_c maps at 1 Ω contour level. All RMSD values presented are based on C_α atoms. Model validation was performed with Molprobity (Chen et al., 2010) and crystal contacts were analysed using PISA (Krissinel and Henrick, 2007).

Table 2-6: NCS and TLS restraints and B-factor calculation used for each dataset.

Crystal	**NCS**	**TLS**	**B-factor**
$MDM2^z$	local	none	isotropic
$MDM2^f$ (Crystal A)	global	none	isotropic
$MDM2^f$ (Crystal B)	local	none	isotropic
$MDM2^f$ (Crystal C)	local	none	isotropic
$MDM2^f$ + UbcH5B-Ub	no	yes	isotropic
$MDM2^f$ 380-C + UbcH5B-Ub	no	none	isotropic
$MDM2^{G443T}$ + UbcH5B-Ub (Crystal A)	local	yes	anisotropic
$MDM2^{G443T}$ + UbcH5B-Ub (Crystal B)	local	yes	isotropic
$MDM2^{WT}$ + UbcH5B-Ub	no	yes	anisotropic
$MDM2^c$ S429E + UbcH5B-Ub	no	none	isotropic
$MDM2^g$ S429E + UbcH5B-Ub	local	yes	isotropic
$MDM2^o$ S429E + UbcH5B-Ub (Crystal A)	local	none	anisotropic
$MDM2^o$ S429E + UbcH5B-Ub (Crystal B)	no	yes	anisotropic
$MDM2^t$ S429E + UbcH5B-Ub (Crystal A)	local	yes	isotropic
$MDM2^t$ S429E + UbcH5B-Ub (Crystal B)	local	yes	isotropic
$MDM2^c$ pS429 + UbcH5B-Ub (Crystal A)	local	yes	isotropic
$MDM2^c$ pS429 + UbcH5B-Ub (Crystal B)	local	yes	anisotropic
$MDM2^c$ pS429 + UbcH5B-Ub (Crystal C)	local	yes	isotropic
$MDM2^c$ S429E (Crystal A)	local	yes	anisotropic
$MDM2^c$ S429E (Crystal B)	local	yes	anisotropic
MDM2 380-C '5D1E' + UbcH5B-Ub	no	none	isotropic

2.6 Surface Plasmon Resonance

Surface Plasmon Resonance (Williams et al.) experiments were performed with a Biacore T200 (GE Healthcare) using a CM-5 Series S chip (GE Healthcare) with coupled anti-GST antibody. GST-TEV was captured on flow cell 1 (reference cell) and ligand protein (GST-tagged MDM2) on flow cells 2,3 and 4. Running buffer consisted of 25 mM Tris, 150 mM NaCl, 0.1 mg/ml BSA, 0.5 mM DTT and 0.005 % *v/v* TWEEN® 20 (Sigma-Aldrich, #P9416) (pH 7.6). Analyte protein (UbcH5B-Ub) was 1:2.5 mixed with SPR running buffer and serially (1:3) diluted to obtain 7 different concentrations. All experiments were performed at 25 °C. Two technical replicates were performed with ascending and descending analyte concentrations and a blank measurement in between each replicate. Data were analysed using Biacore T200 BIAevaluation (GE Healthcare) and Scrubber2 (BioLogic Software) after background subtraction (GST alone).

2.7 Autoubiquitination assays

MDM2 and MDM2/MDMX were diluted with PBS containing 1 mg/mL BSA in all assays. UbcH5B was pre-charged with Ub for 20-30 min at 23 °C by mixing 60-80 µM GGS-Ub, 5-10 µM maleimide-GGSC-Ub, 5 µM UbcH5B and 0.2 µM UBA1 in 1X reaction buffer (50 mM Tris, 50 mM NaCl, 5 mM ATP, 5 mM $MgCl_2$, pH 7.6). The reaction mixture was split into 6 µL aliquots and the reaction was started by adding 2 µL E3 (400 nM MDM2 homodimer or 1 µM MDM2-MDMX heterodimer) and stopped after 90 s by adding NuPAGE LDS Sample Buffer and DTT to achieve a final concentration of 100 mM. For the control reaction, LDS Sample buffer and DTT were directly added to reaction mixture without MDM2. Proteins were separated by SDS-PAGE (Chapter 2.3.3) and visualised with the Odyssey CLx imaging system at a wavelength of 800 nm. For quantification of Ub_n-MDM2 products, intensities of each lane were measured for proteins >40 kDa using the Image Studio Lite software (LI-COR). Background subtraction was performed with the signal for the control reaction. Where three independent reactions were performed, error bars are shown indicating the standard deviation. For visualisation purposes, the relative ubiquitination compared to the wild-type protein is shown.

2.7.1 Rate determination

MDM2 (400 nM) was added to a three times larger volume of pre-charged reaction mixture (composition as described above; incubated for 30 min at 37 °C) without splitting. After every 20 s, 8 µL were mixed with LDS Sample buffer and DTT as described above. In total, seven time points were taken. For the control reaction, 6 µL reaction mixture without MDM2 were added to LDS Sample buffer and DTT. Formation of MDM2-Ub_n products was quantified with a standard curve for fluorescently labelled Ub. Signals for Ub and MDM2-Ub_n on different gels were normalised by loading identical amounts of the same control reaction on each gel.

Chapter 3 Purification and Structural characterisation of the MDM2 homodimer in complex with E2-Ub

3.1 Strategies for purification of human MDM2 RING domain

MDM2 has been reported to form oligomers of various sizes both *in vitro* and in cells (Poyurovsky et al., 2007) (Cheng et al., 2009). In particular, MDM2 constructs containing the RING domain have been associated with heavy aggregation, making it challenging to purify sufficient amounts of protein for crystallisation attempts (Linke et al., 2008) (Poyurovsky et al., 2007) (Nomura et al., 2017). In this chapter, purification strategies for various constructs of the human MDM2 homodimer RING domain will be discussed, with the aim to obtain sufficient quantities of homogeneous, dimeric protein that are required for crystallisation.

3.1.1 Aggregation of the RING domain

RING domain constructs of MDM2 have previously been purified with a GST-tag and showed robust enzymatic activity in lysine discharge and autoubiquitination assays (Linke et al., 2008) (Nomura et al., 2017). However, upon GST cleavage the protein aggregates heavily, making it a poor candidate for crystallisation (Linke et al., 2008) (Kostic et al., 2006) (Cheng et al., 2009) (Poyurovsky et al., 2007). Since the behaviour of the protein in solution was found to be highly buffer sensitive (Kostic et al., 2006), an initial purification attempt was undertaken using a buffer that gave sufficient yields of dimeric MDM2-MDMX heterodimer for crystallisation purposes in our lab (Nomura et al., 2017). When fused to an N-terminal MBP-tag, MDM2 RING domain (428-C) eluted as a single peak during AIEC chromatography (Figure 3-1A) and ran as a single band on SDS-PAGE (Figure 3-1B), indicating that the protein was pure. It eluted as a single, albeit broad peak during SEC, suggesting that the protein was homogenous and did not form oligomers of different sizes as reported previously (Poyurovsky et al., 2007) (Figure 3-1C,D). However, upon cleavage the protein partly precipitated and the remaining soluble fraction eluted in the void volume. The

cleaved protein has a molecular weight of 7.2 kDa. The fact that it eluted even before the uncleaved protein (103 kDa for a dimer) indicates that it was heavily aggregated and thus not suitable for crystallisation attempts.

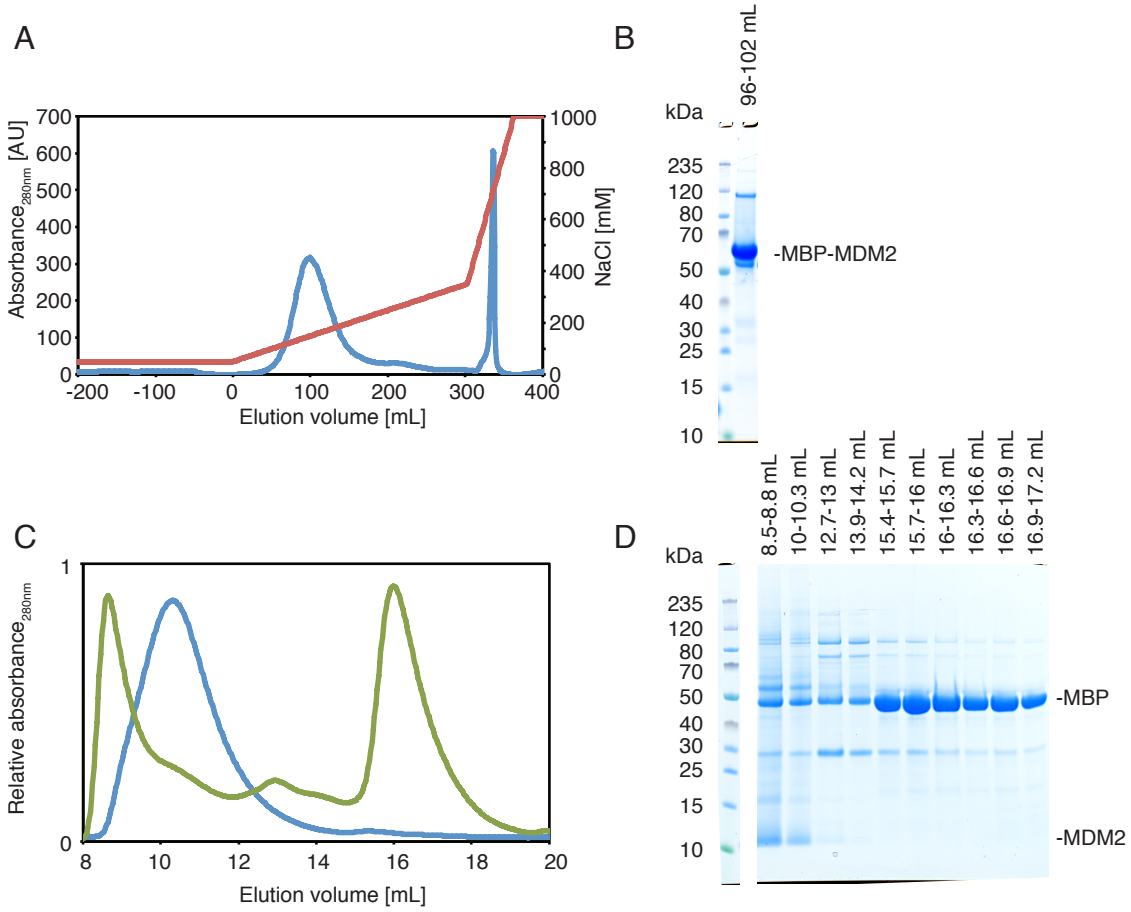

Figure 3-1: Initial purification attempt of MDM2 428-C. (A) Chromatogram of an AIEC run showing the elution profile of MBP-tagged MDM2 (blue) using a NaCl gradient (red). (B) SDS-PAGE of the peak fraction of the AIEC run. (C) Chromatogram of a SEC run of cleaved (green) and uncleaved (blue) MDM2. Elution profiles are normalised. (D) SDS-PAGE for the SEC elution profile of cleaved MDM2.

3.1.2 Extended N-terminal linker increases dimeric fraction

In order to overcome the aggregation problem upon cleavage, a longer MDM2 construct, 350-C, was used, hypothesising that the additional residues might contribute to the stability of the construct similarly to a fusion tag such as GST or MBP. In a previous publication, simultaneous substitution of six residues in this region (S386, S395, S407, T419, S425, S429) to aspartic acid was found to reduce the oligomeric state of MDM2 362-C purified from *E. coli* (Cheng et al., 2009). In order to reduce the amount of aggregated protein during purification, the aspartic acid substitutions (denoted as '6D') were included in the construct

design. The '6D' construct had been reported to stabilise p53 in cells, while still being competent for autoubiquitination (Cheng et al., 2009). To ensure that this construct would be able to form a tight complex with E2-Ub, a pre-requirement for processive ligase activity, the binding affinity for E2-Ub had to be tested (Figure 3-2). MDM2 350-C WT and '6D' both have a low μM binding affinity for UbcH5B-Ub. Surprisingly, the '6D' mutant showed a two-fold enhanced binding affinity for E2-Ub, potentially making it an even better E3 ligase. The explanation for this observation will be discussed in Chapter 4. The strong binding affinity made the '6D' construct a promising candidate for crystallisation with E2-Ub.

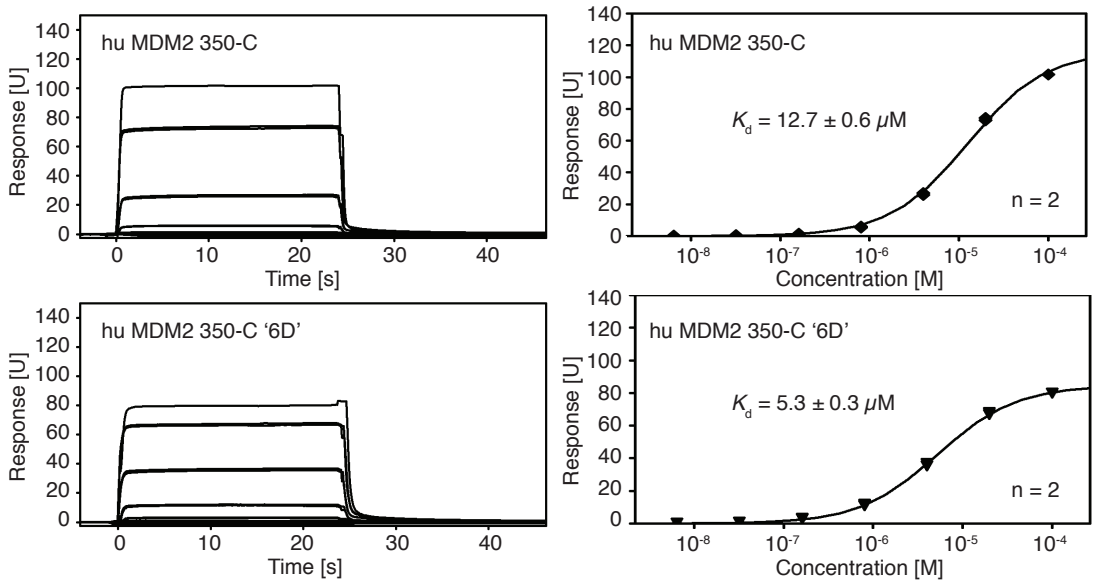

Figure 3-2: SPR binding analyses of MDM2 350-C WT and '6D' for UbcH5B-Ub. Representative sensorgrams (left) and binding curves with the estimated K_d (right).

Cleaved MDM2 350-C '6D' eluted with two distinct peaks during AIEC (Figure 3-3A) and fractions of both peaks showed a similar level of purity (Figure 3-3B). Strikingly, they showed very different elution profiles during SEC. The first peak of the AIEC run eluted as a homogeneous peak corresponding to a dimer whereas the second AIEC peak eluted as an inhomogeneous peak, drastically shifted towards higher molecular weight species (Figure 3-3C). The fact that the two AIEC peaks showed a completely different SEC profile indicated that this construct was not homogeneous after cleavage but that the different complexes were stable throughout the purification procedure so that they could be separated. The homogeneity of the dimeric fractions was sufficient for crystallisation attempts (Figure 3-3D). The suitability was, however, limited by

the yield after the final purification step (Table 3-1). Nevertheless, sufficient amounts of protein were obtained for an initial crystallisation attempt with UbcH5B-Ub under 672 different crystallisation conditions (Table 2-3). However, crystals could not be observed, indicating that the construct was not optimal for crystallisation. This could be due to unfavourable flexibility of the N-terminal extension, as residues 350-434 are predicted to be unstructured based on the secondary structure prediction server JPred 4 (Drozdetskiy et al., 2015). It is also unclear whether the protein will remain purely dimeric under crystallisation conditions and over a period of time that is required for initial nucleation to occur, due to its general tendency to aggregate. Therefore, a different approach had to be made in order to stabilise MDM2 more robustly, hence prevent aggregation and increase the yield.

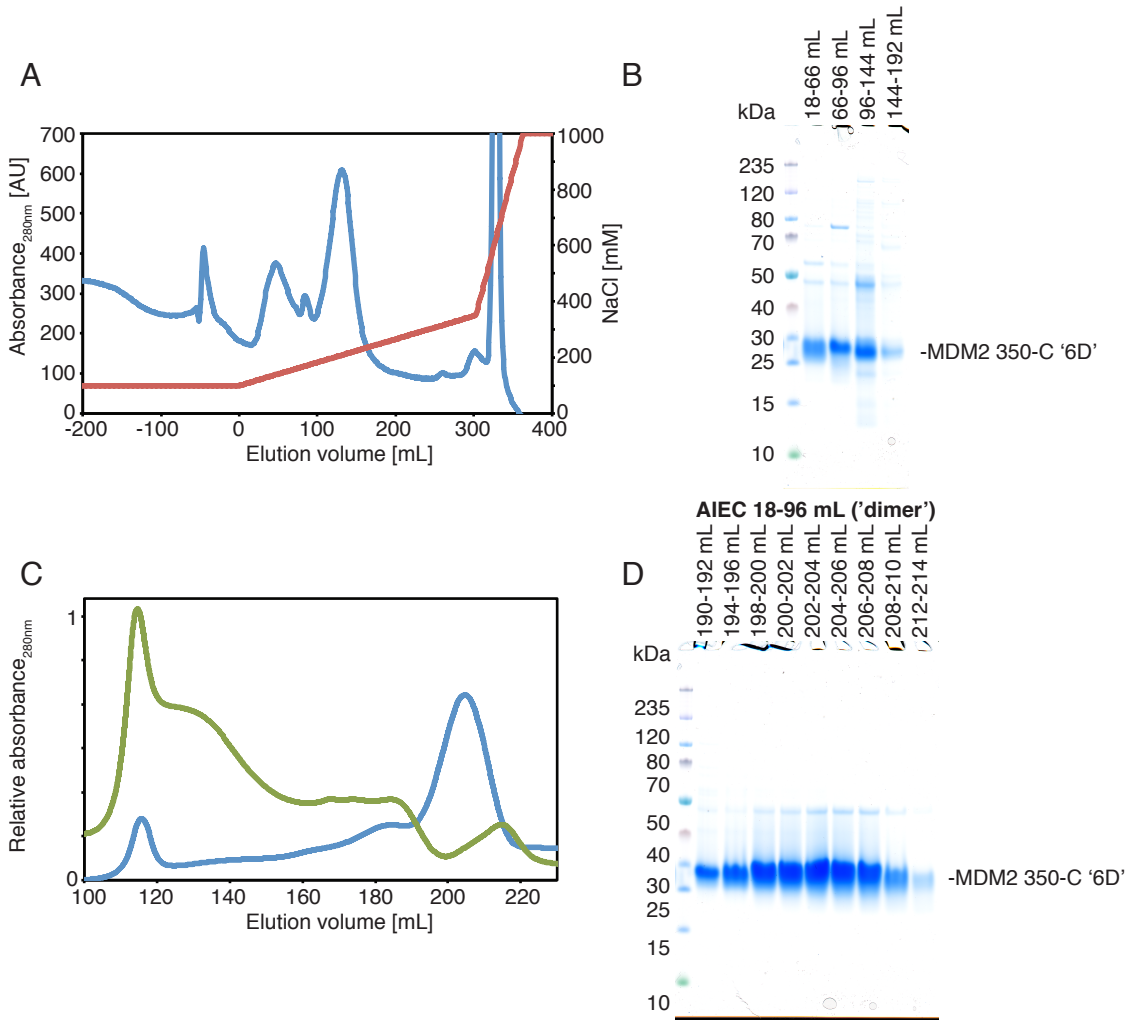

Figure 3-3: Purification of MDM2 350-C '6D'. (A) Chromatogram of an AIEC run showing the elution profile of cleaved MDM2 350-C '6D' (blue) using a NaCl gradient (red). (B) SDS-PAGE of different fractions of the AIEC run. (C) Chromatogram of a SEC run of the first (blue) and second (green) peak in the AIEC run. (D) SDS-PAGE for the SEC elution of the first AIEC peak.

Table 3-1: Yields of MDM2 350-C '6D' after AIEC and SEC obtained per L of *E. coli* cells.

Purification step	Fraction	Yield [mg/L LB]
AIEC	dimer	0.1-0.2
AIEC	larger oligomer	0.4
SEC	dimer	0.02-0.06

3.1.3 MBP fusion constructs stabilise the RING domain

In the initial purification attempt of MDM2 428-C, the MBP tagged protein eluted as a single peak (Figure 3-1A), indicating that it was well folded and homogenous, hence suitable for crystallisation. MBP has become a popular crystallisation chaperone for proteins with low solubility (Waugh, 2016). The construct introduced in Chapter 3.1.1 contained an extensive linker including a TEV cleavage site, allowing the two fusion partners to adopt a vast number of conformations relative to each other. In order to use this MBP-fusion construct for crystallisation purposes, this linker had to be removed in order to enhance the rigidity of the construct. Although residues adjacent to the MDM2 RING domain were predicted to be unstructured it was not clear whether those residues would be involved in E2-Ub binding for the homodimer. In the heterodimer structure, S429 was in close proximity to E2-Ub (Figure 3-4A). Therefore, additional spacer residues would likely be required to rule out that an N-terminal MBP-tag could interfere with the E2-Ub binding site on MDM2, hence block the complex formation. To achieve the highest degree of rigidity without affecting E2-Ub binding, fusion constructs of different lengths were designed (Figure 3-4B) and their E2-Ub binding affinity was measured (Figure 3-4C). All three constructs showed a comparable binding affinity, demonstrating that a spacer of eleven residues between MBP and MDM2 S429 was sufficient to allow optimal E2-Ub binding. The binding affinities also indicate that residues 398-418 do not significantly contribute to E2-Ub binding. As MBP-MDM2 418-C was not defect for E2-Ub binding and supposed to be the most rigid of the three constructs, it was used for purification.

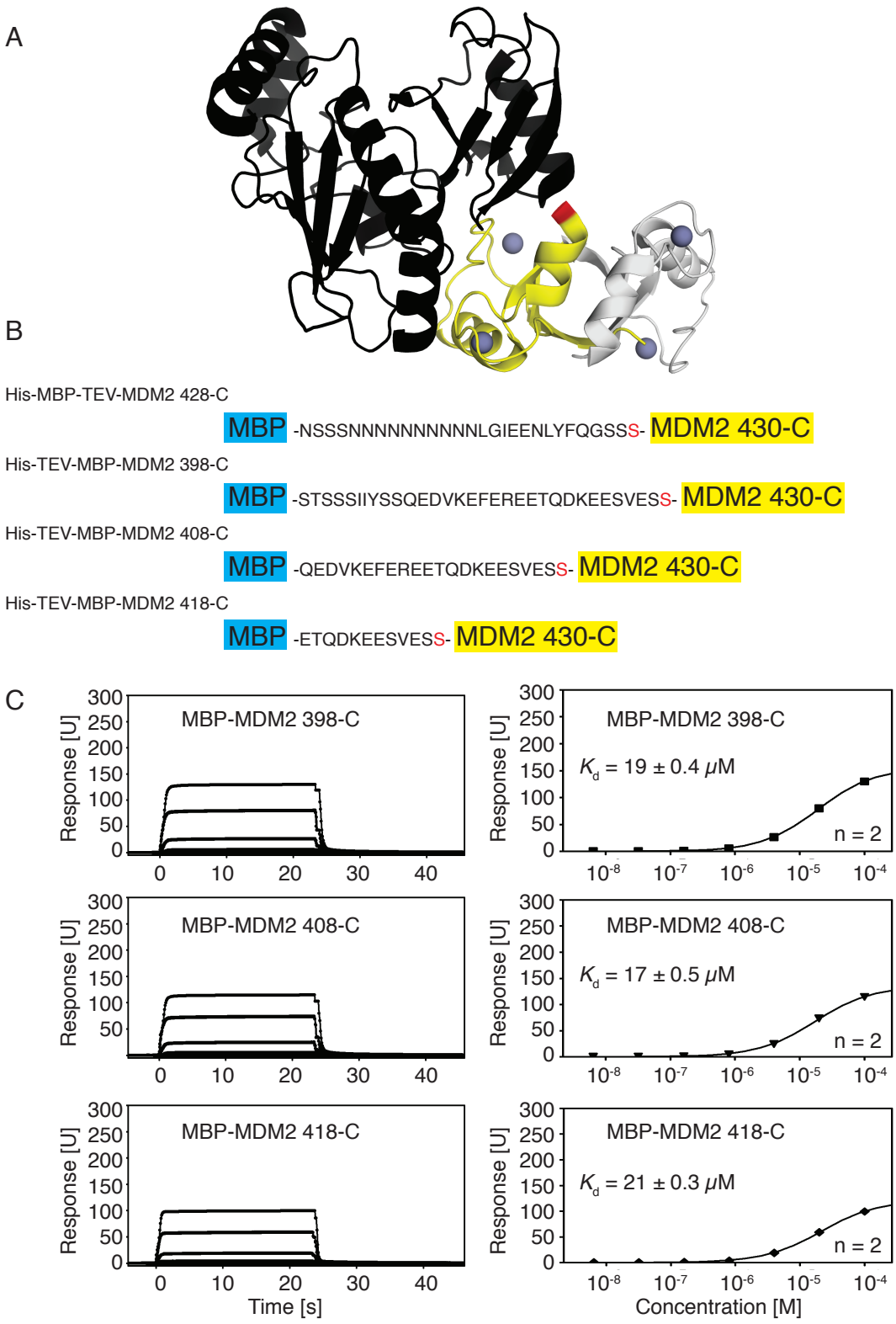

Figure 3-4: Design of the MBP-MDM2 fusion constructs. (A) Crystal structure of MDM2 (yellow)-MDMX (grey) bound to E2-Ub (black). MDM2's S429 is highlighted in red. (B) Design of MBP-MDM2 fusion constructs with different linker lengths. (C) SPR binding affinity experiments for E2-Ub. Representative sensorgrams (left) and binding curves with the estimated K_d (right).

The purification was conducted in the same manner as MBP-TEV MDM2 428-C in Chapter 3.1.1. After cleavage of the N-terminal His-tag, MBP-MDM2 418-C eluted as a single peak from AIEC (Figure 3-5A) and SEC (Figure 3-5B).

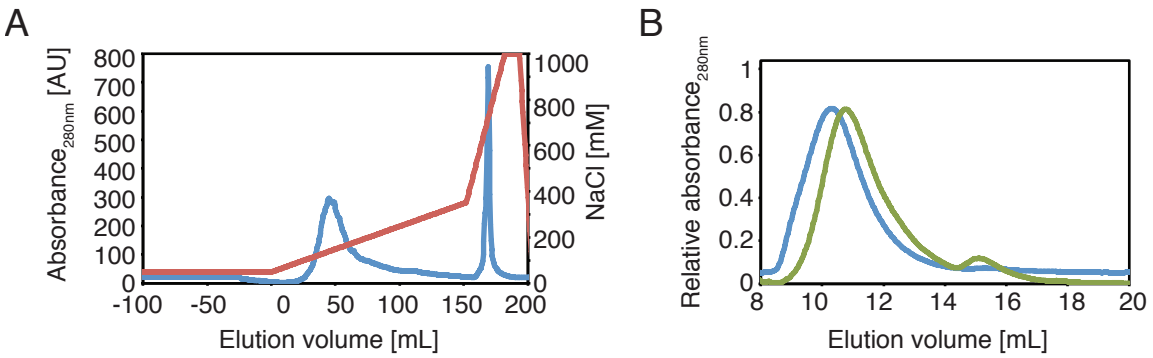

Figure 3-5: Purification of MBP-MDM2 418-C. (A) Chromatogram of an AIEC run showing the elution profile (blue) using a NaCl gradient (red). (B) Chromatogram of a SEC run of MBP-MDM2 418-C (green) in comparison to MBP-TEV MDM2 428-C (blue). Elution profiles are normalised.

The yield was significantly better than for MDM2 350-C '6D' (Table 3-2), because this construct did not aggregate, which accounted for a loss of at least two third of the '6D' construct after AIEC (Table 3-1).

Table 3-2: Yields of MBP-MDM2 418-C after AIEC and SEC obtained per L of *E. coli* cells.

Purification step	**Yield [mg/L LB]**
AIEX	0.67
SEC	0.34

Crystallisation attempts were undertaken for MBP-MDM2 418-C alone and in complex with E2-Ub. Unfortunately, no crystals were obtained from 672 crystallisation conditions (Table 2-3). Although a drastic increase in crystal structures with an MBP-fusion tag has been reported over the last few years, no information is available about the success rate of this methodology as negative crystallisation attempts are rarely mentioned. Nevertheless, this construct might be promising for co-crystallisation with other binding partners than UbcH5B-Ub that would facilitate different forms of crystal packing. In order to crystallise MDM2 homodimer with UbcH5B-Ub, a different approach was required.

3.2 Structural characterisation of zebrafish (*Danio rerio*) MDM2 RING domain

Thanks to advances in genome sequencing, the *mdm2* gene of more than 60 different (sub)species has been identified. MDM2 is conserved among Euteleostomes and the RING domain in particular shows a high sequence identity among all animals (Table 3-3). 39 out of the 69 C-terminal residues are fully conserved, including Zn^{2+}-coordinating cysteines and histidines, and residues that were shown to be critical for E2-Ub binding (I440, R479) (Nomura et al., 2017) or dimerisation (C448) (Kosztyu et al., 2019). This indicates that the overall structure and the mechanism for E2-Ub recruitment are similar if not identical. Among mammalians, MDM2 is even more conserved where the RING domain (437-C) differs only in a few cases by more than two residues from the human sequence. In other animal classes such as fish (*Actinopterygii*) and amphibia, the sequences were more distinct from the human one, with the most pronounced discrepancy located N-terminal to the RING domain (residues 423-435). I designed an MDM2 construct of a different species for purification purposes, hypothesizing that the aggregation issues of human MDM2 might be sequence dependant. The sequence of zebrafish (*Danio rerio*) MDM2 showed one of the most pronounced sequence differences to human MDM2 with only 50 out 69 C-terminal residues being conserved.

Table 3-3: Sequence comparison of MDM2 423-C (human nomenclature) for all known sequences (UniProtKB). Residues that are conserved among all listed species are highlighted in green in the human sequence. Residues that differ from the human sequence are coloured in red. Zn^{2+}-coordinating residues are highlighted in yellow, residues critical for E2-Ub recruitment are highlighted in purple. The number of amino acids that differ from the human sequence is indicated. Where more than one species was found with an identical sequence, only one species is listed and the number of identical sequences indicated in parenthesis.

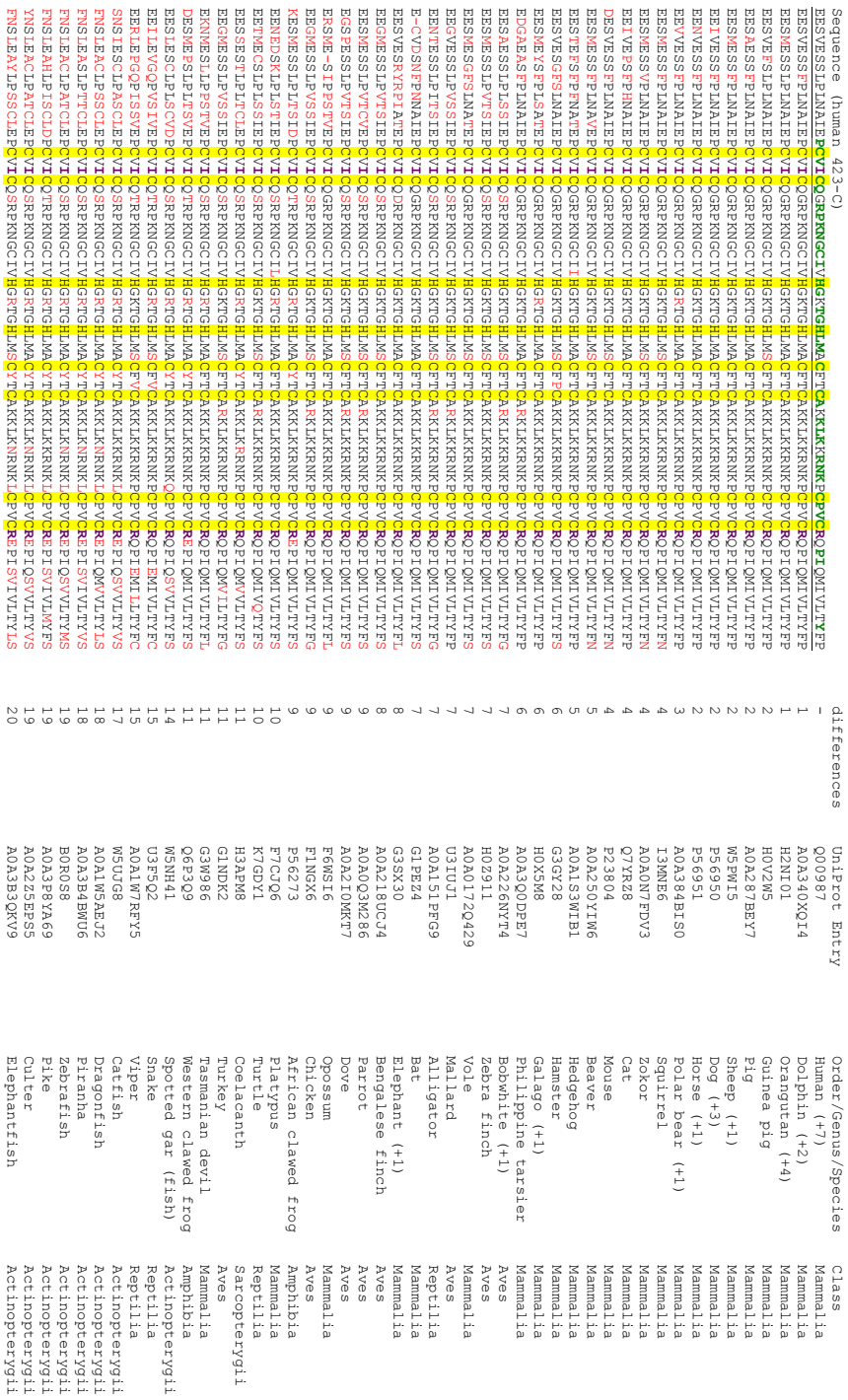

Sequence (human 423-C)	differences	UniProt Entry	Order/Genus/Species	Class
EESVESSLPLNAIEPCVICQGRPKNGCIVHGKTGHLMACFTCAKKLKKRNKPCPVCRQPIQMIVLTYFP	-	Q00987	Human (+7)	Mammalia
EESVESSFPLNAIEPCVICQGRPKNGCIVHGKTGHLMACFTCAKKLKKRNKPCPVCRQPIQMIVLTYFP	1	A0A340XQI4	Dolphin (+2)	Mammalia
EESVESSLPLNAIEPCVICQGRPKNGCIVHGKTGHLMACFTCAKKLKKRNKPCPVCRQPIQMIVLTYFP	1	H2NI01	Orangutan (+4)	Mammalia
EESVEFSLPLNAIEPCVICQGRPKNGCIVHGKTGHLMSCFTCAKKLKKRNKPCPVCRQPIQMIVLTYFP	2	H0V2W5	Guinea pig	Mammalia
EESAESSFPLNAIEPCVICQGRPKNGCIVHGKTGHLMACFTCAKKLKKRNKPCPVCRQPIQMIVLTYFP	2	A0A287BEY7	Pig	Mammalia
EESMESSFPLNAIEPCVICQGRPKNGCIVHGKTGHLMACFTCAKKLKKRNKPCPVCRQPIQMIVLTYFP	2	W5FWI5	Sheep (+1)	Mammalia
EEIVESSFPLNAIEPCVICQGRPKNGCIVHGKTGHLMACFTCAKKLKKRNKPCPVCRQPIQMIVLTYFP	2	P56950	Dog (+3)	Mammalia
EENVESSFPLNAIEPCVICQGRPKNGCIVHGKTGHLMACFTCAKKLKKRNKPCPVCRQPIQMIVLTYFP	2	P56951	Horse (+1)	Mammalia
EEVVESSFPLNAIEPCVICQGRPKNGCIVHGRTGHLMACFTCAKKLKKRNKPCPVCRQPIQMIVLTYFP	3	A0A384BIS0	Polar bear (+1)	Mammalia
EESMESSFPLNAIEPCVICQGRPKNGCIVHGKTGHLMSCFTCAKKLKKRNKPCPVCRQPIQMIVLTYFN	4	I3MNE6	Squirrel	Mammalia
EESMESSVPLNAIEPCVICQGRPKNGCIVHGKTGHLMACFTCAKKLKKRNKPCPVCRQPIQMIVLTYFN	4	A0A0N7FDV3	zokor	Mammalia
EETVEFSFPHNAIEPCVICQGRPKNGCIVHGKTGHLMACFTCAKKLKKRNKPCPVCRQPIQMIVLTYFP	4	Q7YR28	Cat	Mammalia
DESVESSFPLNAIEPCVICQGRPKNGCIVHGKTGHLMSCFTCAKKLKKRNKPCPVCRQPIQMIVLTYFN	4	P23804	Mouse	Mammalia
EESMESSFPLNAVEPCVICQGRPKNGCIVHGKTGHLMSCFTCAKKLKKRNKPCPVCRQPIQMIVLTYFN	5	A0A250YIW6	Beaver	Mammalia
EESTEFSFPNAIEPCVICQGRPKNGCIIHGKTGHLMACFTCAKKLKKRNKPCPVCRQPIQMIVLTYFP	5	A0A1S3WIB1	Hedgehog	Mammalia
EESVESGFSLNAIEPCVICQGRPKNGCIVHGKTGHLMSCFTCAKKLKKRNKPCPVCRQPIQMIVLTYFS	6	G3GY28	Hamster	Mammalia
EESMEYSFPLSATEPCVICQGRPKNGCIVHGRTGHLMACFTCAKKLKKRNKPCPVCRQPIQMIVLTYFP	6	H0X5M8	Galago (+1)	Mammalia
EDGAEASFPLNAIEPCVICQGRPKNGCIVHGKTGHLMACFTCARKLKKRNKPCPVCRQPIQMIVLTYFP	6	A0A3Q0DPE7	Philippine tarsier	Mammalia
EESAESSLPLSSIEPCVICQSRPKNGCIVHGKTGHLMSCFTCAKKLKKRNKPCPVCRQPIQMIVLTYFG	7	A0A226NYT4	Bobwhite (+1)	Aves
EESMESSLPVTSIEPCVICQSRPKNGCIVHGKTGHLMSCFTCAKKLKKRNKPCPVCRQPIQMIVLTYFS	7	H0Z911	Zebra finch	Aves
EESMESGFSLNATEPCVICQGRPKNGCIVHGKTGHLMSCFTCAKKLKKRNKPCPVCRQPIQMIVLTYFS	7	A0A0172Q429	Vole	Mammalia
EEGVESSLPVSSIEPCVICQSRPKNGCIVHGKTGHLMSCFTCARKLKKRNKPCPVCRQPIQMIVLTYFP	7	U3IUJ1	Mallard	Aves
EEGTESSLPTSSIEPCVICQSRPKNGCIVHGKTGHLMSCFTCARKLKKRNKPCPVCRQPIQMIVLTYFP	7	A0A151FFG9	Alligator	Reptilia
E-CVDSNFPNNAIEPCVICQGRPKNGCIVHGKTGHLMACFTCAKKLKKRNKPCPVCRQPIQMIVLTYFS	7	G1PE24	Bat	Mammalia
EESVESRYRPIATEPCVICQDRPKNGCIVHGKTGHLMACFTCAKKLKKRNKPCPVCRQPIQMIVLTYFL	8	G3SX30	Elephant (+1)	Mammalia
EEGMESSLPVTSIEPCVICQSRPKNGCIVHGKTGHLMSCFTCARKLKKRNKPCPVCRQPIQMIVLTYFS	8	A0A218UCJ4	Bengalese finch	Aves
EESMESSLPVTCVEPCVICQSRPKNGCIVHGKTGHLMSCFTCARKLKKRNKPCPVCRQPIQMIVLTYFS	9	A0A0Q3M286	Parrot	Aves
EGSPESSLPVTSIEPCVICQSRPKNGCIVHGKTGHLMSCFTCARKLKKRNKPCPVCRQPIQMIVLTYFS	9	A0A2I0MKT7	Dove	Aves
ERSME-SIPSTVEPCVICQGRPKNGCIVHGKTGHLMACFTCAKKLKKRNKPCPVCRQPIQMIVLTYFL	9	F6WSI6	Opossum	Mammalia
EEGMESSLPVSSIEPCVICQSRPKNGCIVHGKTGHLMSCFTCARKLKKRNKPCPVCRQPIQMIVLTYFG	9	F1NGX6	Chicken	Aves
KESMESSLPTSIDPCVICQTRPKNGCIVHGRTGHLMACYTCAKKLKKRNKPCPVCREPIQMIVLTYFS	9	P56273	African clawed frog	Amphibia
EENEDSKLPSLSTIEPCVICQSRPKNGCILHGRTGHLMACFTCAKKLKKRNKPCPVCRQPIQMIVLTYFS	10	F7CJQ6	Platypus	Mammalia
EETMECSLPLSSIEPCVICQSRPKNGCIVHGKTGHLMSCFTCARKLKKRNKPCPVCRQPIQMIVQTYFS	10	K7GDY1	Turtle	Reptilia
EESSESTLPTCLEPCVICQSRPKNGCIVHGRTGHLMACYTCAKKLKRNKPCPVCRQPIQMVVLTYFS	11	H3APM8	Coelacanth	Sarcopterygii
EEGMESSLPVSSIEPCVICQSRPKNGCIVHGKTGHLMSCFTCARKLKKRNKPCPVCRQPIQMVILTYFG	11	G1NDK2	Turkey	Aves
EKNMESLLPSTVEPCVICQSRPKNGCIVHGETGHLMACYTCAKKLKKRNKPCPVCREPIQMIVLTYFL	11	G3W986	Tasmanian devil	Mammalia
DESMEPSLPLTSVEPCVICQTRPKNGCIVHGRTGHLMACYTCAKKLKKRNKPCPVCREPIQMIVLTYFS	11	Q6P3Q9	Western clawed frog	Amphibia
EESLESCLPLSCVDPCVICQSRPKNGCIVHGRTGHLMACYTCAKKLKKRNKQCPVCREPIQSVVLTYFS	14	W5NH41	Spotted gar (fish)	Actinopterygii
EEILEVSGPVSIVEPCVICQTRPKNGCIVHGRTGHLMSCFVCAKKLKKRNKPCPVCRQPIEMIVLTYFC	15	U3F5Q2	Snake	Reptilia
EERLEPSGPISSVEPCVICQTRPKNGCIVHGKTGHLMSCFVCAKKLKKRNKPCPVCRQPIEMLILTYFC	15	A0A1W7REY5	Viper	Reptilia
SNSLESCLPASCLEPCVICQSRPKNGCIVHGRTGHLMACYTCAKKLKKRNKLCPVCREPIQSVVLTYVS	17	W5UJG8	Catfish	Actinopterygii
FNSLEACLPSSCLEPCVICQSRPKNGCIVHGRTGHLMACYTCAKKLKNRNKLCPVCREPIQMVVLTYLS	18	A0A1W5AEJ2	Dragonfish	Actinopterygii
FNSLEASLPTTCLEPCVICQSRPKNGCIVHGRTGHLMACYTCAKKLKNRNKLCPVCREPISVIVLTYVS	18	A0A3B4BWU6	Piranha	Actinopterygii
FNSLEACLPATCLEPCVICQSRPKNGCIVHGRTGHLMACYTCAKKLKNRNKLCPVCREPIQSVVLTYMS	19	B0R0S8	Zebrafish	Actinopterygii
FNSLEAHLPISCLDPCVICQTRPKNGCIVHGRTGHLMACYTCAKKLKKRNKLCPVCREPISVTLMYFS	19	A0A3P8YA69	Pike	Actinopterygii
YNSLEACLPATCLEPCVICQSRPKNGCIVHGRTGHLMACYTCAKKLKNRNKLCPVCREPIQSVVLTYVS	19	A0A225EPS5	Culter	Actinopterygii
FNSLEAVLPSSCLEPCVICQSRPKNGCIVHGRTGHLMSCYTCAKKLKNRNKLCPVCREPISVILTYLS	20	A0A3B3QKV9	Elephantfish	Actinopterygii

3.2.1 Purification and E2-Ub binding

Zebrafish MDM2 407-C, corresponding to human MDM2 423-C (for simplification purposes, the human nomenclature will be used throughout this thesis with a superscript ^{z}, e.g. MDM2^{z} indicating zebrafish MDM2), was expressed with a cleavable His-MBP tag. It eluted similar to human MBP-tagged MDM2 as a single peak during AIEC chromatography (Figure 3-6A) and showed a comparable purity level (Figure 3-6B) as the human RING domain construct. Strikingly, the cleaved protein did not aggregate but eluted as a single peak at 195-215 mL (fractions A78-A93) during SEC (Figure 3-6C,D), which corresponds to a molecular weight of 16 kDa based on the elution profile of a gel filtration size kit. This indicates, that the 7.8 kDa protein was purely dimeric after cleavage. The final yield of dimeric protein was 14 times higher than for human MDM2 350-C (Table 3-4). Upon concentrating, the protein started to precipitate, limiting the final concentration to 3 mg/mL (0.4 mM).

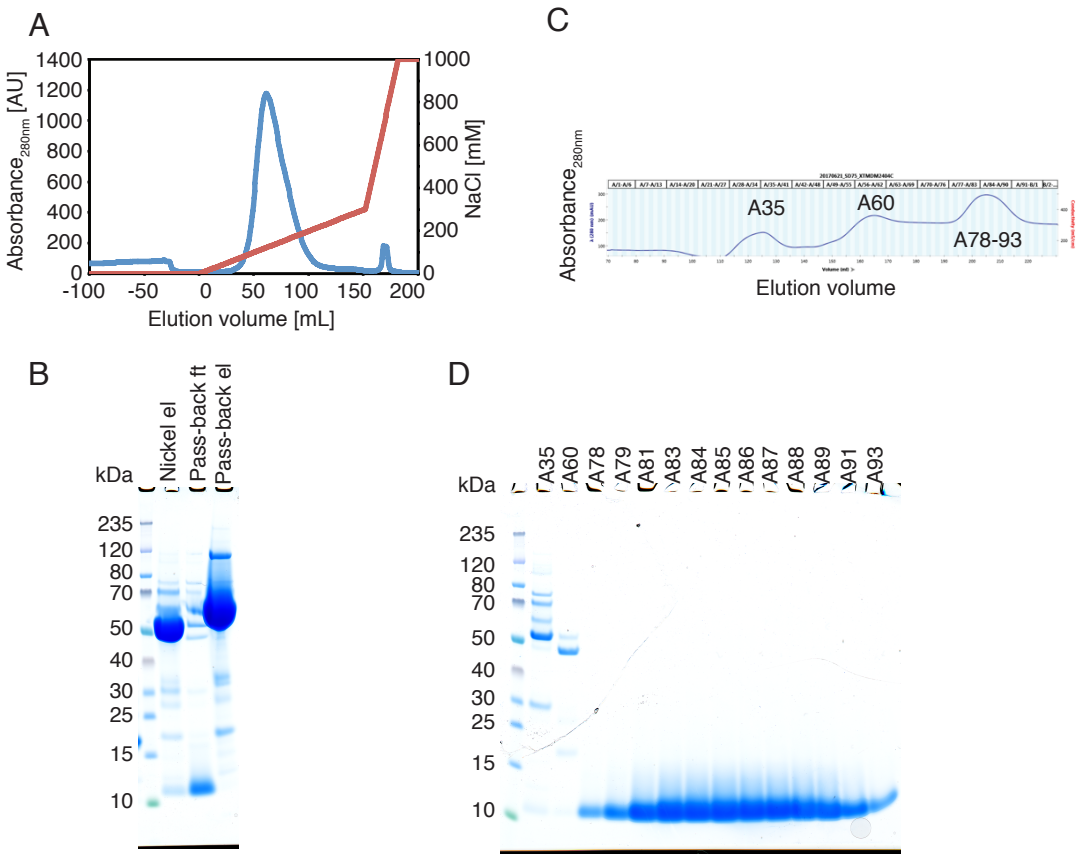

Figure 3-6: Purification of MDM2^{z} 423-C. (A) Chromatogram of an AIEC run showing the elution profile (blue) using a NaCl gradient (red). (B) SDS-PAGE showing the AIEC elution (el) peak and the separation of MDM2 from His-MBP after TEV cleavage via pass-back. (C) Chromatogram of a SEC run of the cleaved protein. (D) SDS-PAGE of single fractions of C.

Table 3-4: Yields of MDM2^{z} 423-C after AIEC and SEC obtained per L of *E. coli* cells.

Purification step	Protein status	Yield [mg/L LB]
Nickel elution	MBP-tagged	7.0
AIEC	MBP-tagged	6.1
Pass-back	cleaved	1.3
SEC	cleaved	0.24-0.28

Some of the residues that are different from human MDM2 are either in vicinity to the E2-Ub binding site of the human MDM2-MDMX heterodimer (S429→C429^{z}, N433→T433^{z} where → indicates the corresponding residue in MDM2^{z}) or at the MDM2-MDMX interface (L432→A432^{z}, A434→C434^{z}, I435→L435^{z}, F490→M490^{z}, P491→S491^{z}) (Figure 3-7A) so that the ability of MDM2^{z} to recruit E2-Ub had to verified. The sequence discrepancy caused a two-fold binding decrease for UbcH5B-Ub (Figure 3-7B), indicating that MDM2^{z} is catalytically less active in the context of UbcH5B and might use additional residues beyond residue 423 or a different E2 to achieve robust ubiquitination.

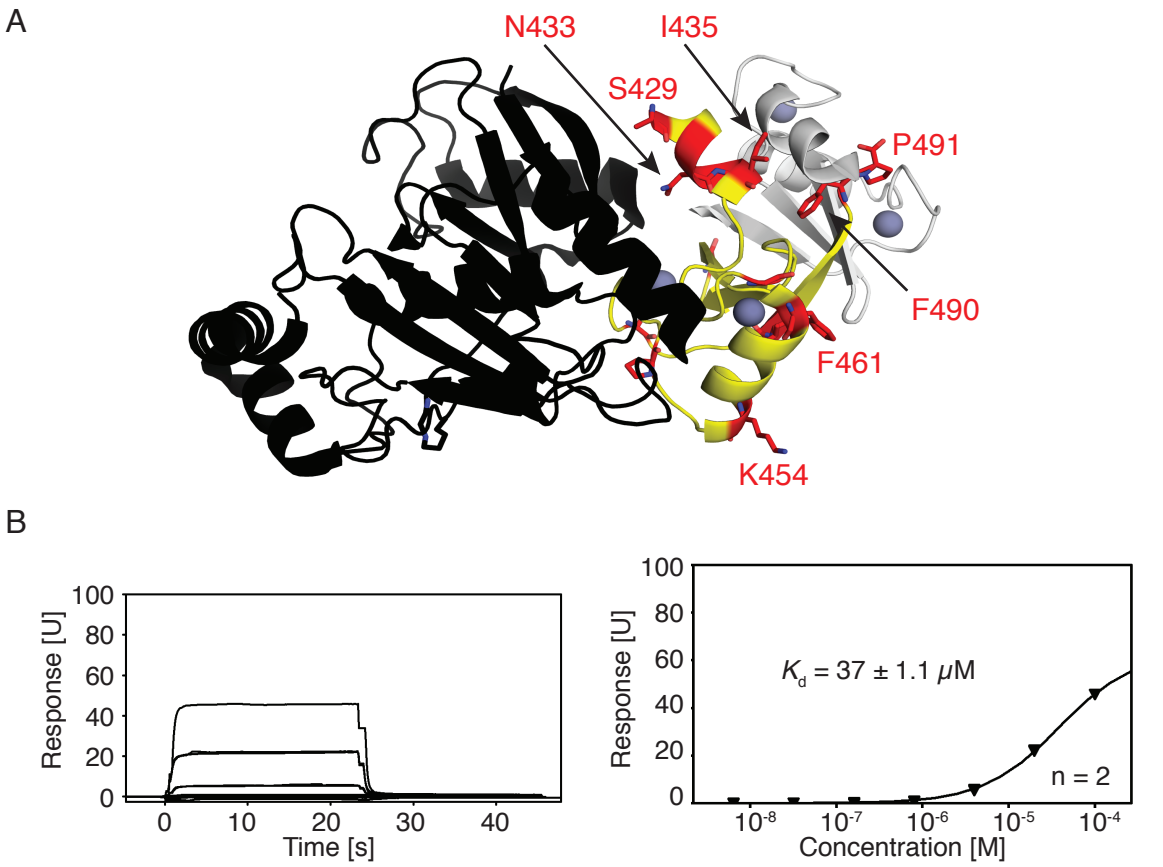

Figure 3-7: SPR binding analysis of MDM2^{z} 423-C. (A) Crystal structure of human MDM2-MDMX (yellow-grey) bound to E2-Ub (black). Residues that are not conserved between MDM2^{z} and human MDM2 are highlighted in red. (B) E2-Ub binding analysis for MDM2^{z}. Representative sensorgrams (left) and binding curves with the estimated K_d (right).

3.2.2 Crystallisation and structure determination

The protein was screened for crystallisation by itself and in complex with UbcH5B-Ub because the final MDM2 concentration in the drop (0.14 mM) was nevertheless well above the K_d for UbcH5B-Ub. In conditions with MDM2 alone, thin needle shaped crystals (Figure 3-8) appeared after 12-36 h in 109 out of 672 crystallisation conditions (Table 2-3). Crystals grew in the presence of PEG as a precipitant and under a variety of different buffers with pH values from 4 to 9. The small diameter and the huge number of crystals in each drop indicated that the crystallisation conditions were not optimal or that the protein or precipitant concentration was too high. In order to reduce the number of nucleation events, with the aim to obtain fewer but larger crystals, different optimisation approaches were followed (Chapter 2.5.2.1). However, none of the approaches improved the morphology of the crystals so that crystals from the initial screen were sent for data collection at the synchrotron. They diffracted to 2.87 Å and the crystal structure was solved by molecular replacement (PHASER) using the crystal structure of the human MDM2-MDMX heterodimer (PDB 2VJF) as a search model (Table 3-5).

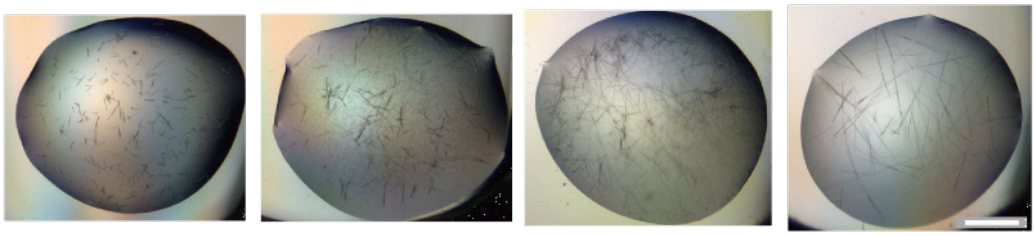

Figure 3-8: Representative MDM2^Z crystals. Needle-shaped crystals were obtained in many conditions, the crystals shown in the right image diffracted to 2.87 Å. The length of the white bar corresponds to 300 µm.

Table 3-5: Data collection and refinement statistics for $MDM2^{Z}$ 423-C. Numbers in parenthesis indicate the statistics for the outer shell.

Data collection	
Space group	P 1 2_1 1
Unit cell dimensions (a, b, c [Å] / a, β, γ [°])	46, 24, 54 / 90, 102, 90
Resolution [Å]	45.2-2.87 (2.92-2.87)
Unique reflections	2817
R_{merge}	0.237 (0.636)
Mean I/ σ	6.3 (2.4)
$CC_{1/2}$	0.949 (0.667)
Completeness	100.0 (100.0)
Multiplicity	3.2 (3.3)
Refinement	
Resolution [Å]	53.2-2.87
Unique reflections	2641
R_{work} / R_{free}	0.226 / 0.275
Content of the asymmetric unit	1 dimer
Atoms (Protein)	1612
Atoms (non protein)	4 (Zn^{2+})
B-factor (Protein)	23.6
B-factor (Zn^{2+})	17.8
Bond length RMSD [Å]	0.004
Bond angle RMSD [°]	1.332
Ramachandran outliers [%]	0
Rotamer outliers [%]	6.45
Clashscore	4.87
Molprobity score	2.11

3.2.3 Crystal structure

Overall, the structure of $MDM2^{Z}$ RING is very similar to the published crystal structure of the heterodimer (PDB: 2VJF, RMSD of 0.5 Å for C_α atoms of residues 436-C/435-C in the heterodimer) and the NMR model of the human homodimer (RMSD of 1.8 Å) (Figure 3-9).

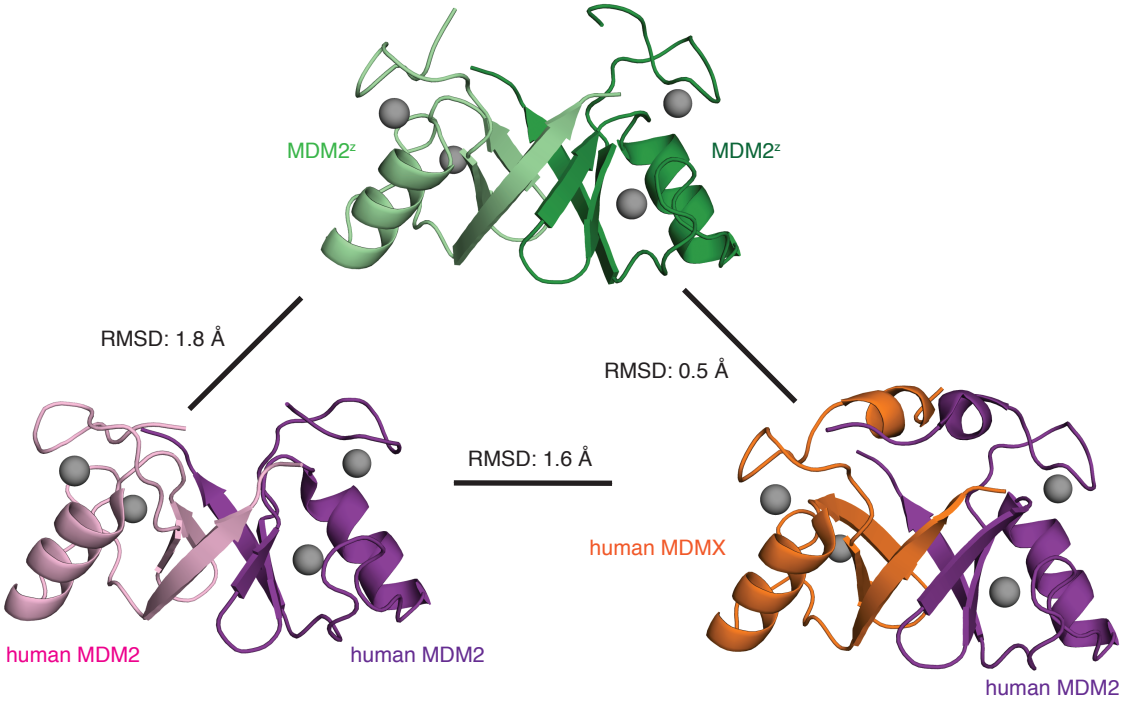

Figure 3-9: Crystal structure of $MDM2^z$. $MDM2^z$ (green; top panel) in comparison to the NMR model (PDB: 2HDP) for the human homodimer (pink/purple; bottom left panel) and the crystal structure (PDB: 2VJF) of the human MDM2-MDMX heterodimer (purple/orange; bottom right panel). RMSD values are given for residues for the C_α atoms of 436-C. Zn^{2+} ligands are shown as grey spheres.

Similar to the human dimeric structures, the $MDM2^z$ dimer forms a six-stranded ß-barrel, which is flanked by an α-helix between the second and the third ß-strand of each MDM2 molecule. Zn^{2+} is coordinated in an identical manner, as the positions of the involved cysteine and histidine residues are fully conserved. In contrast to the crystal structure of MDM2-MDMX, no electron density was observed for residues beyond $C434^z$. It is unclear whether this is due to differences between homo- and heterodimer or a consequence of the sequence discrepancy between $MDM2^z$ and human MDM2. The former explanation is supported by an NMR model where residues up to I435 were disordered (Kostic et al., 2006). In the heterodimer, the N-terminal helices are stabilised by the C-terminal residues of the second MDM molecule. In particular, the second last residues, $MDM2^{F490}$ and $MDMX^{I489}$, form intermolecular hydrophobic interactions with $L433^{MDMX}$ and $A434^{MDM2}$, respectively (Figure 3-10A). In $MDM2^z$, the equivalent residue is methionine (Figure 3-10B), which would clash with the helix when superimposed with the heterodimer structure (Figure 3-10C). In fact, it is located in a hydrophobic region (L458, T488) and would clash with other residues no matter which orientation the sidechain adopts. Considering the fact that both helices stabilise each other in the heterodimer, it is likely that both of

them are affected when one of them is disturbed. For instance, A434 (homodimer) and L433 (heterodimer) stabilise the helices via hydrophobic interactions. The corresponding residue in MDM2^{z}, C434^{z}, points in the opposite direction as A434 in the heterodimer, thus away from the second MDM2 molecule, which further indicates that this region may lack stabilising interactions as in the heterodimer.

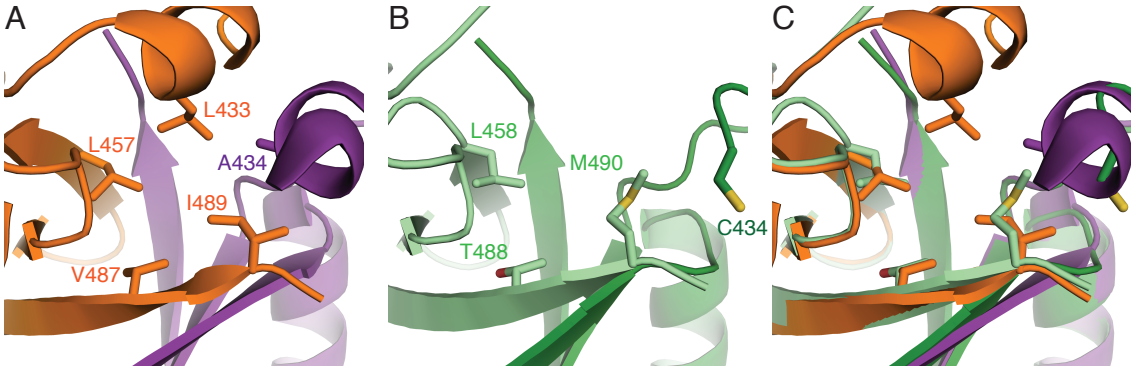

Figure 3-10: Close-up of the C-terminal tail of MDM2^{z}. (A) Human MDM2-MDMX (PDB: 2VJF). MDMX is coloured in orange, MDM2 in purple. (B) MDM2^{z}. The two protomers are coloured in bright and dark green. (C) Superimposition of MDM2^{z} and MDM2-MDMX. In MDM2^{z}, M490 blocks the formation of N-terminal helices such as in the heterodimer structure. In the heterodimer, the corresponding residue (I489) lies within a hydrophobic environment consisting of L433, L457, V487 (MDMX) and A434 (MDM2). M490 would clash with a helix like in the heterodimer, thus requiring a different structural arrangement. As a consequence, A434 (MDM2) and C434^{z} are positioned differently.

The N-terminal helices in the heterodimer are energetically unstable 3_{10}-helices, which might require additional stabilisation. In the MDM2^{z} crystal structure, the N-terminal residues are not involved in crystal packing whereas they play a crucial role in the crystal structure of the heterodimer (Figure 3-11A). In fact the most N-terminal residues involved in packing of MDM2^{z} are V439^{z} and I440^{z} whereas residues N433, E436 (MDM2) and L434 (MDMX) form hydrogen bonds with symmetry related molecules in the crystal structure of the heterodimer (Figure 3-11B). However, whether the crystal contacts ultimately stabilise the helices or whether the helices are responsible for crystal packing like in the heterodimer structure, remains unclear.

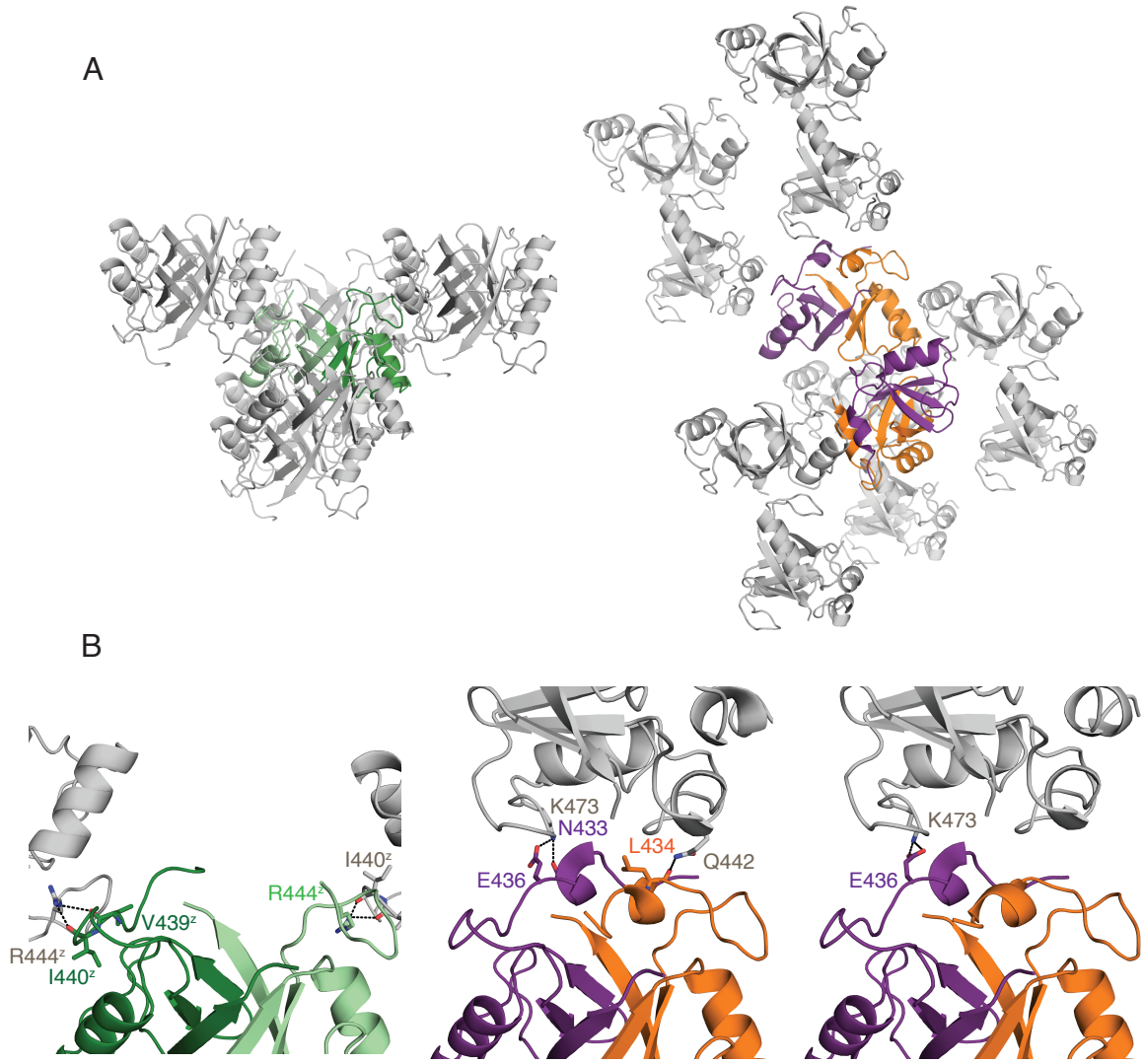

Figure 3-11: The N-terminal helices of the heterodimer form crystal contacts. Symmetry related molecules are coloured in grey. (A) Crystal packing of MDM2^{z} (left) and the heterodimer (right). (B) Crystal contacts of MDM2^{z} (left) and both dimers in the asymmetric unit of the heterodimer structure (middle and right).

Most of the remaining residues that are different between MDM2^{z} and human MDM2 are located at the surface and not involved in dimer-dimer interactions. An exception is R454^{z}, which potentially forms an intermolecular hydrogen bond with the sidechain of Y462^{z}, with a distance of 4.5 Å between hydrogen bond donor and acceptor (Figure 3-12). Although there is no electron density for R454^{z} in the second MDM2 molecule and the resolution of the crystal structure is not sufficient to make a clear statement, it is worthwhile to note that R454^{z} is a lysine in human MDM2 and Y462^{z} a phenylalanine. Whenever an MDM2 sequence contains a tyrosine at position 462, the corresponding arginine is conserved (Table 3-3). The arginine-tyrosine pair can only be found in fish and frog MDM2, suggesting that the stabilisation effect of this hydrogen bond was either redundant or that the corresponding lysine-phenylalanine pair in mammalians

expresses a similar effect through hydrophobic interactions. Another difference between the species lies within their C-terminal residue. A C-terminal serine allows for an additional hydrogen bond between the amine group and the backbone carbonyl of L458^{z}, which might further stabilise the dimer.

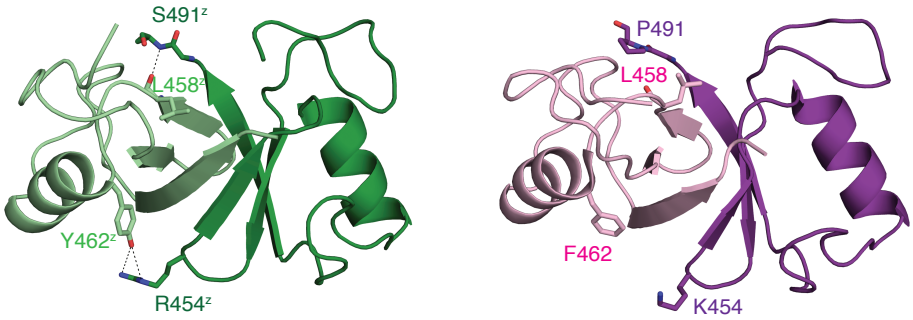

Figure 3-12: MDM2^{z} might be stabilised by two additional hydrogen bonds. Crystal structure of MDM2^{z} (green; left) in comparison to the NMR model (pink/purple; right). Potential hydrogen bonds L458^{z}-S491^{z} (3.5 Å) and R454^{z}-Y462^{z} (4.5 Å) are indicated with dashes.

No crystals were obtained in complex with UbcH5B-Ub. Although the overall structure of the dimers was similar, the flexibility of the N-terminus could have destabilised the complex formation and might explain the two-fold weaker binding affinity in comparison to human MDM2. The final MDM2 concentration in the drop was just 3.5 times above the K_d, which requires a substantial fraction of both proteins, MDM2 and UbcH5B-Ub, to be able to form a complex. In order to overcome this limitation, an MDM2 construct with a lower tendency to aggregate upon concentrating would be desirable.

3.3 Structural characterisation of western clawed frog MDM2 RING domain

Encouraged by the fact that MDM2^{z} was, despite the structural similarity, much less prone to aggregation than human MDM2, different species were screened with the aim to crystallise the homodimer in complex with E2-Ub. Western clawed frog (*Xenopus tropicalis*, from here on denoted as frog) MDM2 was selected for purification because the sequence differed from human MDM2 by eleven residues, hence to a smaller extent than MDM2^{z} where 19 residues were different. Importantly, residues N-terminal to human E436 differed from both species (Table 3-3), whereas the second last residue was phenylalanine like in

human MDM2, which might allow a helix formation like in the heterodimer unlike the corresponding methionine in MDM2^{z}.

3.3.1 Purification and E2-Ub binding

The stability of frog MDM2 414-C (from here on MDM2^{f}), corresponding to human MDM2 423-C, was similar to MDM2^{z} throughout the purification. The cleaved protein eluted at 180-210 mL, indicating that the soluble fraction of this construct was exclusively dimeric (Figure 3-13A,B). The final yield of 0.33-0.40 mg of protein per litre of LB was even better than for MDM2^{z}, likely because the protein was more stable upon concentrating, so that a final concentration of 9.3 mg/mL (1.2 mM) could be obtained without significant precipitation. The binding affinity for UbcH5B-Ub was similar to MDM2^{z}, indicating that MDM2^{f} was folded properly (Figure 3-13C).

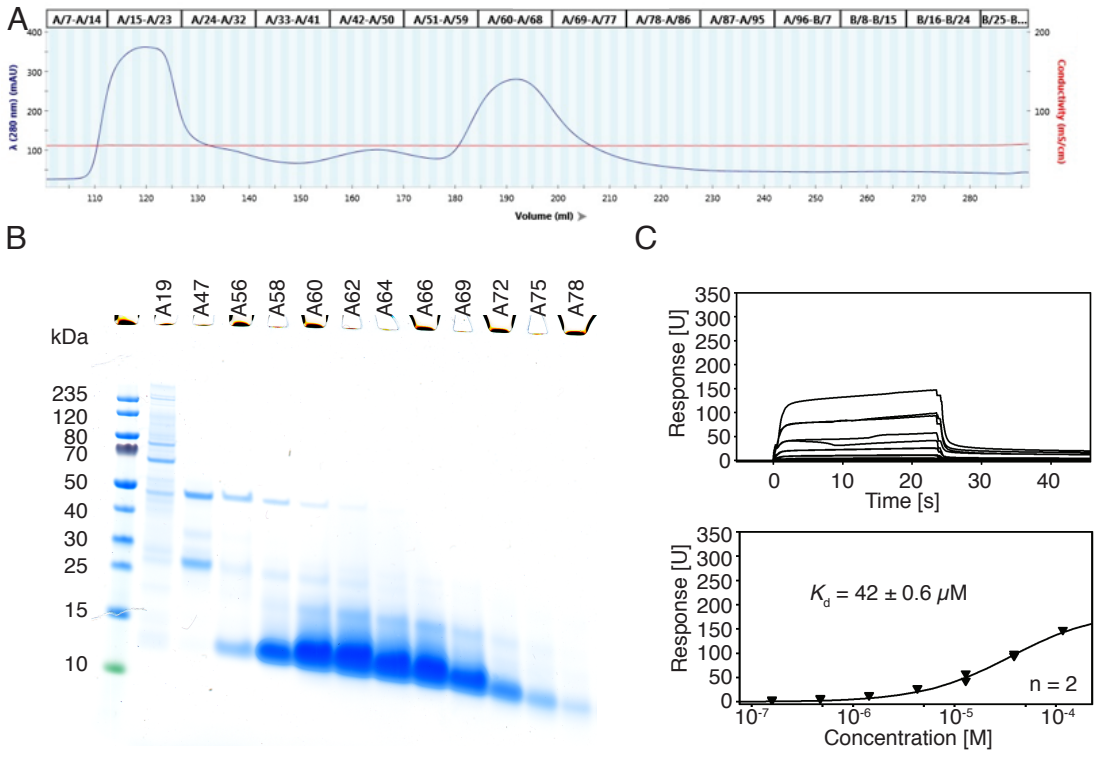

Figure 3-13: Purification and binding analysis of MDM2^{f} 423-C. (A) Chromatogram of a SEC run of the cleaved protein. (B) SDS-PAGE of single SEC fractions. (C) SPR binding analysis for UbcH5B-Ub. Representative sensorgrams (left) and binding curves with the estimated K_d (right).

3.3.2 Crystallisation

Crystallisation attempts were undertaken for $MDM2^{f}$ by itself and in complex with UbcH5B-Ub. After 12-36 h, needle like crystals appeared in 32 out of 864 crystallisation conditions (Figure 3-14) for $MDM2^{f}$ alone. Although the shape was similar, the crystals appeared to be thicker than the crystals obtained for $MDM2^{z}$ (Figure 3-8). Three datasets of diffracting crystals were collected and the structure was determined to 2.5-2.9 Å (Table 3-6).

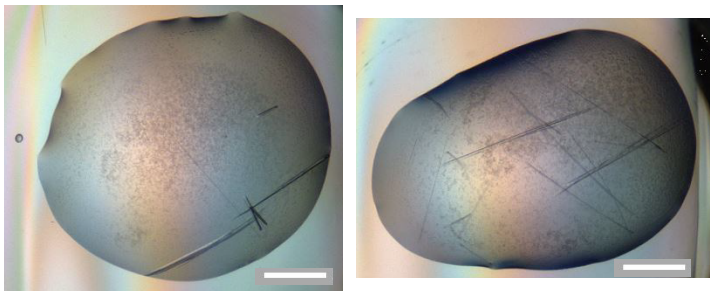

Figure 3-14: Thick needle-shaped crystals were obtained for $MDM2^{f}$. The crystals shown here were obtained from identical buffer conditions, at pH 8 (left) and pH 7 (right) (Table 2-4). The length of the white bar corresponds to 300 µm.

Table 3-6: Data collection and refinement statistics for all MDM2^{f} datasets. Numbers in parenthesis indicate the statistics for the outer shell.

Name in this study	1	2	3
Data collection			
Space group	P 1 2_1 1	P 1 2_1 1	P 1
Unit cell dimensions (*a*, *b*, *c* [Å] / *a*, *B*, *γ* [°])	43, 24, 56 / 90, 101, 90	63, 24, 77 / 90, 105, 90	24, 63, 76 / 75, 88, 90
Resolution [Å]	41.8-2.53 (2.60-2.53)	74.1-2.27 (2.33-2.27)	60.9-2.50 (2.56-2.50)
Unique reflections	3836	10462	14100
R_{merge}	0.137 (0.693)	0.131 (0.852)	0.143 (0.288)
Mean I/ σ	3.7 (0.8)	5.3 (1.4)	3.0 (1.3)
$CC_{1/2}$	0.983 (0.529)	0.990 (0.532)	0.960 (0.576)
Completeness [%]	99.8 (100)	98.5 (99.0)	06.0 (95.1)
Multiplicity	3.1 (3.1)	3.1 (3.0)	1.7 (1.7)
Refinement			
Resolution [Å]	41.7-2.53	74.1-2.65	60.9-2.92
Unique reflections	3632	6301	8391
R_{work} / R_{free}	0.224 / 0.282	0.262 / 0.284	0.257 / 0.308
Content of the asymmetric unit	1 dimer	2 dimers	4 dimers
Atoms (Protein)	813	1623	3208
Atoms (non protein)	4 (Zn^{2+})	8 (Zn^{2+})	16 (Zn^{2+})
B-factor (Protein)	48.47	46.15	44.45
B-factor (Zn^{2+})	38.08	38.45	36.22
Bond length RMSD [Å]	0.0054	0.0044	0.0048
Bond angle RMSD [°]	1.468	1.331	1.318
Ramachandran outliers [%]	0	0	0
Rotamer outliers [%]	4.55	2.89	2.35
Clashscore	0.63	10.37	7.49
Molprobity score	1.89	2.48	2.30

For the co-crystallisation attempts with UbcH5B-Ub, crystals appeared in nine out of 864 crystallisation conditions (Figure 3-15 left). Crystals were optimised (Chapter 2.5.2.2), which promoted the growth of larger clusters of crystals (Figure 3-15 middle). After a final seeding step, single crystals could be obtained that diffracted to 1.82 Å. The structure was solved by using molecular replacement using the crystal structures of MDM2^{f} and UbcH5B-Ub from the crystal structure in complex with MDM2-MDMX (PDB: 5MNJ) (Table 3-7).

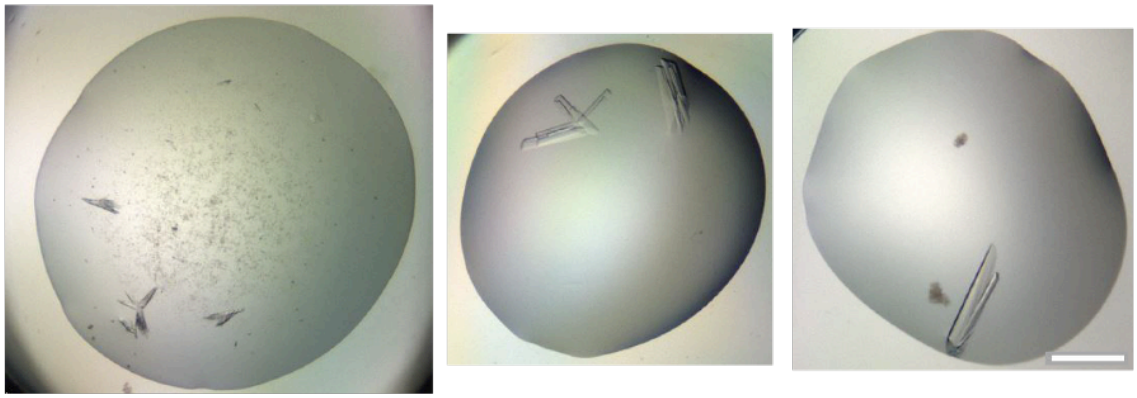

Figure 3-15: Crystals of the MDM2^{f}-UbcH5B-Ub complex. Initial crystals (left), after optimisation (middle) and seeding (right). The length of the white bar corresponds to 300 µm.

Table 3-7: Data collection and refinement statistics for MDM2^{f}-UbcH5B-Ub. Numbers in parenthesis indicate the statistics for the outer shell.

Data collection	
Space group	P 1 2_1 1
Unit cell dimensions (a, b, c [Å] / α, β, γ [°])	55, 153, 82 / 90, 107, 90
Resolution [Å]	52.6-1.82 (1.85-1.82)
Unique reflections	113701
R_{merge}	0.047 (0.989)
Mean I/ σ	13.8 (1.2)
$CC_{1/2}$	0.998 (0.652)
Completeness	98.1 (97.2)
Multiplicity	3.4 (3.4)
Refinement	
Resolution [Å]	52.6-1.82
Unique reflections	108144
R_{work} / R_{free}	0.204 / 0.249
Content of the asymmetric unit	2 dimers bound to 2 E2-Ub each
Atoms (Protein)	8712
Atoms (non protein)	8 (Zn^{2+}), 119 (Water)
B-factor (Protein)	52.85
B-factor (Zn^{2+})	39.1
B-factor (Water)	46.85
Bond length RMSD [Å]	0.009
Bond angle RMSD [°]	1.605
Ramachandran outliers [%]	0.09
Rotamer outliers [%]	1.78
Clashscore	5.04
Molprobity score	1.62

3.3.4 Crystal structure of MDM2^{f}

The datasets were obtained for crystals that either grew in the same drop (crystals 1 and 2, Table 3-6) or under very similar conditions (crystal 3, Table 3-6). Despite an indistinguishable morphology, their unit cells were different. Crystal 1 was isomorphous to the crystal structure of MDM2^{z}, indicating that the overall structure and residues involved in crystal contacts were conserved. The structures were indeed identical with an overall RMSD of 0.3 Å for C_{α} atoms (Figure 3-16A). Although F490 (Figure 3-16B), the corresponding residue to M490 in MDM2^{z}, did not face towards the N-terminal helix of the heterodimer when superimposed (Figure 3-16C), there was no additional electron density, indicating that this residue was not responsible for the differences between the crystal structures of MDM2^{z} and the heterodimer. The hydrogen bond between L458^{f} and S491^{f} was conserved whereas no electron density was observed for R454^{f}, indicating that the hydrogen bond with Y462 (Figure 3-12) was not critical.

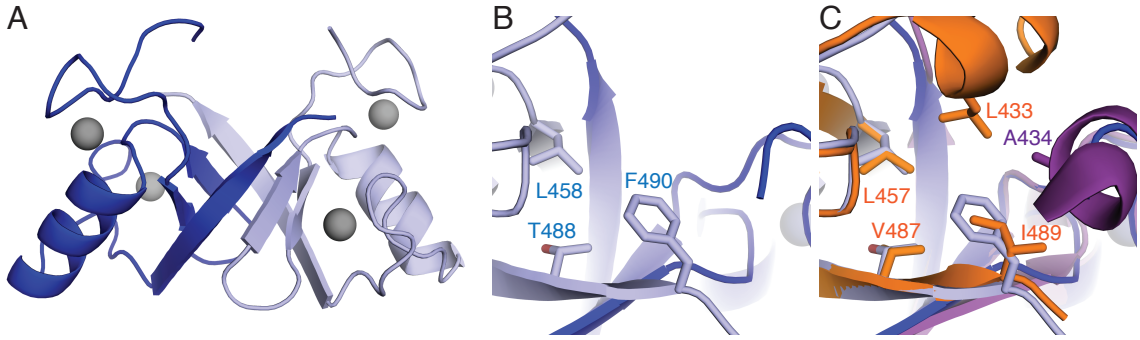

Figure 3-16: Crystal structure of MDM2^{f}. (A) Overall structure. The two protomers are coloured in bright and dark blue. (B) Close-up of the C-terminal tail. (C) Superimposition with human MDM2-MDMX heterodimer (purple/orange) shows that F490 adopts, in contrast to M490 in MDM2^{z} (Figure 3-10), a similar conformation as MDMX's I489.

The unit cells of crystals 2 and 3 contained two and four dimers, respectively, resulting in seven crystallographic unique dimers for this construct. Differences in crystal packing accounted for a variety of crystal contact combinations (Figure 3-17). The number of formed crystal contacts varied especially for crystal 3, where dimers #C and #D were heavily involved in crystal contacts whereas dimers #A and #B were much more exposed to solvent. Where the α-helices were heavily involved in crystal packing, they were slightly more compressed, comparable to the differences between the heterodimer crystal structure and

the NMR model of the homodimer (Figure 3-9). This indicates that the angle between the ß-barrel and the α-helices is not fixed and suggests that the NMR model might represent this aspect of the RING domain structure in solution better than the crystal structure of the heterodimer. Nevertheless, the overall difference between the dimers is very subtle, with diameters of the dimers (distance between the C_α atoms of R471, Figure 3-17) differing by less than 2 Å. The overall structure of any of the seven MDM2^f dimers is closer to the heterodimer than the NMR model (Table 3-8). Only twelve residues are not involved in crystal contacts in any of the seven dimers. Those residues are either buried or sterically restricted from intermolecular interactions. There is no electron density for residues beyond T433 in any of the dimers, which suggests that these residues are disordered and are not involved in crystal packing as observed in the crystal structure of MDM2^z.

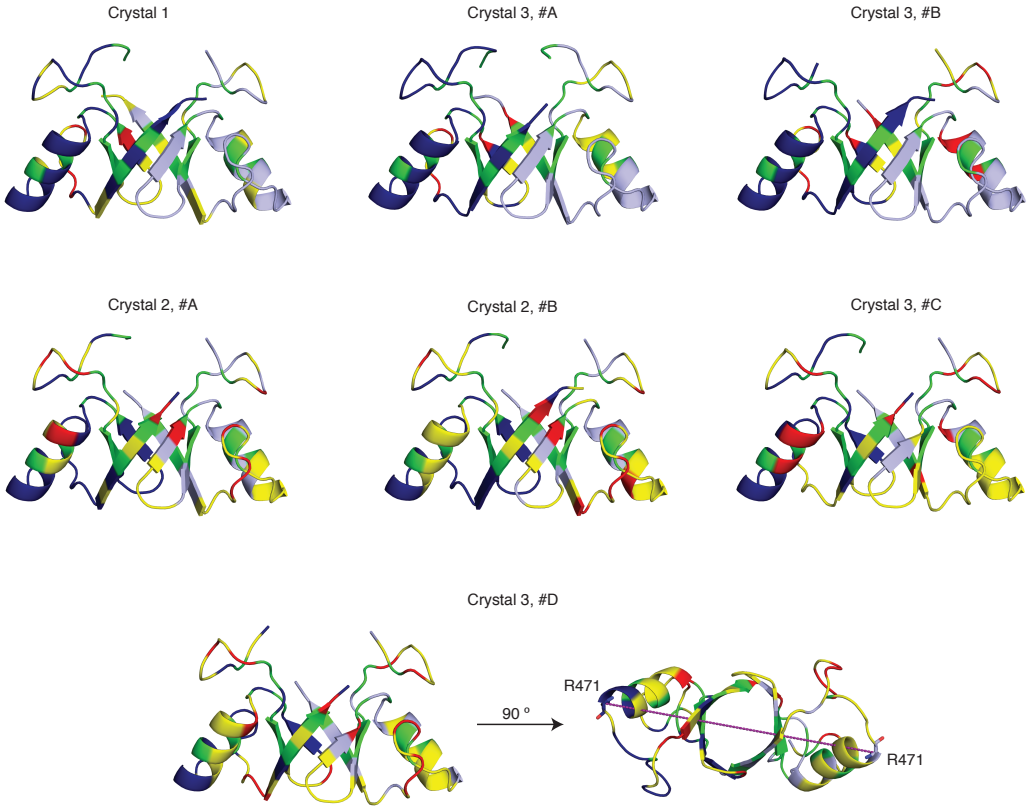

Figure 3-17: Comparison of the seven crystallographic independent dimers for MDM2^f. Hydrogen bonds and salt bridges are indicated in red, other crystal contacts in yellow. Residues that are not involved in crystal contacts in any of the dimers are coloured in green. Residues that are not involved in crystal contacts in a particular chain are coloured in bright and dark blue as in Figure 3-16A. For dimer #D, crystal 3, a representative measurement of the diameter is shown.

Table 3-8: Comparison of all MDM dimers. RMSD values (given in Å) of the MDM2^{f} dimers for MDM2^{z} (Chapter 3.2), MDM2-MDMX (PDB: 2VJF, chain A and B) and MDM2 (NMR, PDB: 2HDP, model 19). Where a dataset contained more than one dimer in the unit cell, the individual dimers are indicated with #.

Dimer	MDM2^{z}	MDM2-MDMX	MDM2 (NMR)
Crystal 1	0.33	0.57	1.71
Crystal 2, #A	0.40	0.43	1.70
Crystal 2, #B	0.40	0.50	1.59
Crystal 3, #A	0.65	0.55	1.78
Crystal 3, #B	0.48	0.67	1.76
Crystal 3, #C	0.48	0.58	1.78
Crystal 3, #D	0.67	0.59	1.80

3.3.5 Crystal structure of MDM2^{f} in complex with UbcH5B-Ub

The crystals obtained for MDM2^{f} in complex with UbcH5B-Ub contained two MDM2 dimers in the unit cell, each of them bound to two UbcH5B-Ub molecules (Figure 3-18). The RMSD between the two complexes is 1.3 Å due to small differences between the dimers (RMSD of 0.5 Å), which causes the two E2-Ub conjugates to be slightly offset when both complexes are superimposed. However, the interactions between MDM2^{f} and E2-Ub are fully conserved for all for MDM2^{f} molecules, resulting in a RMSD of 0.3-0.4 Å for each of the four MDM2 monomers bound to E2-Ub.

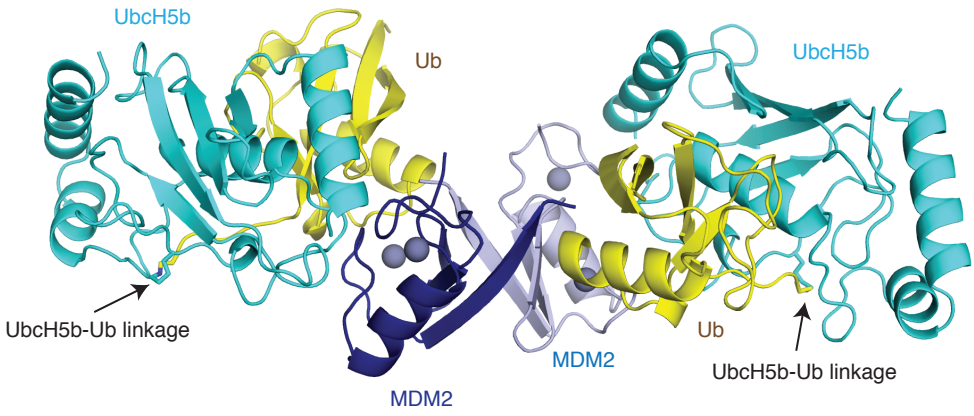

Figure 3-18: Crystal structure of MDM2^{f} bound to E2-Ub. MDM2^{f} (blue) binds two UbcH5B-Ub conjugates (cyan/yellow) simultaneously. UbcH5B-Ub adopts the closed conformation like in other reported RING E3-E2-Ub complexes.

MDM2^{f} adopts the similar conformation as in the unbound state with an RMSD of 0.6-0.9 Å. Upon E2-Ub binding, the dimer gets more compressed, resulting in a diameter of 37.3-37.4 Å, which is significantly smaller than in any of the seven crystallographic unique MDM2^{f} dimers presented in Chapter 3.3.3 (Figure 3-19A).

This does, however, not alter the overall conformation of the dimer and only brings the α-helix and the β3-sheet in closer proximity to each. The interface of the two secondary structure elements mainly consists of hydrophobic interactions. In the E2-Ub bound state, I485 adopts a 'closed' conformation (Figure 3-19B), which is a requirement for the α-helix to move towards the β-barrel. The rigid conformation is additionally stabilised by a hydrogen bond between K469 and the backbone carbonyl of Q483 and might at least partly compensate for the compressed, energetically less favourable interface between the α-helix and the β-barrel upon E2-Ub binding. Notably, K469 is conserved among all species (Table 3-3), indicating that this hydrogen bond might help to stabilise MDM2 in the E2-Ub bound state.

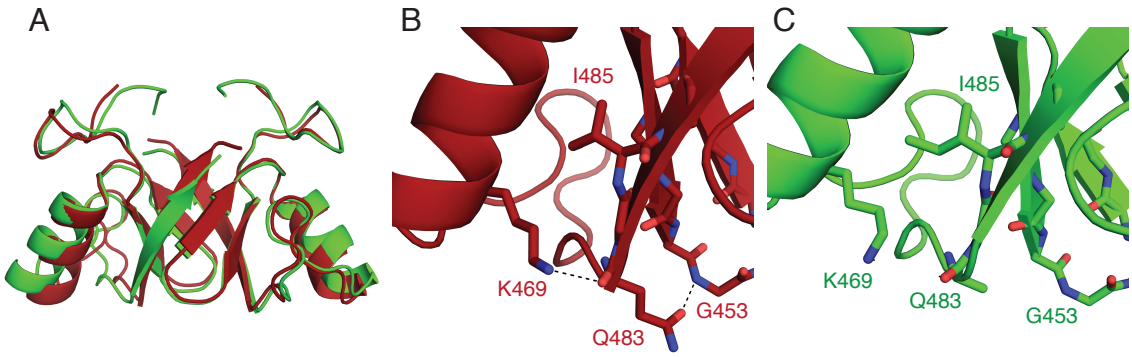

Figure 3-19: $MDM2^{f}$ is more compressed when bound to E2-Ub. (A) $MDM2^{f}$ bound to E2-Ub (dark red) superimposed on free $MDM2^{f}$ (green, crystal 3, dimer #A). (B) Close-up view of residues affected by the re-orientation of the α-helix upon E2-Ub binding. (C) In the absence of E2-Ub, the hydrogen bond network between K469, Q483 and G453 is missing and I485 orientates towards the α-helix.

In the complex, E2-Ub adopts the closed conformation, consistent with other reported RING E3-E2-Ub complexes (Figure 1-5) (Dou et al., 2012b) (Plechanovova et al., 2012). MDM2 stabilises E2-Ub through a number of interactions. A hydrophobic patch consisting of V439, I440 and L468 stabilises UbcH5B's F62 (Figure 3-20A). The importance of I440 has previously been demonstrated in our lab where an alanine substitution completely abolished E2-Ub binding (Nomura et al., 2017). V439, I440 and L468 are conserved in all species, highlighting their role in E2-Ub recruitment. Another conserved residue is the linchpin arginine R479, which is located at the interface between UbcH5B and Ub and forms hydrogen bonds with residues of both proteins (Figure 3-20B). This does not only stabilise the complex but also the E2-Ub conjugate in its closed conformation. Partly disrupting the hydrogen bond network (R479K) lowered the E2-Ub binding 20-fold (Nomura et al., 2017). The complex is further

stabilised by the C-terminus of the second MDM2 protomer, which forms a hydrogen bond with Ub's K11 (Figure 3-20C). This is in agreement with the previously proposed model for how the homodimer recruits UbcH5B-Ub where an E2-Ub bound MDM2 monomer was superimposed on MDMX in the crystal structure of the heterodimer bound to UbcH5B-Ub (Figure 1-16) and explains why mutations affecting the C-terminus such as the insertion of a C-terminal His-tag on MDM2 eliminated its catalytic activity (Uldrijan et al., 2007) (Nomura et al., 2017).

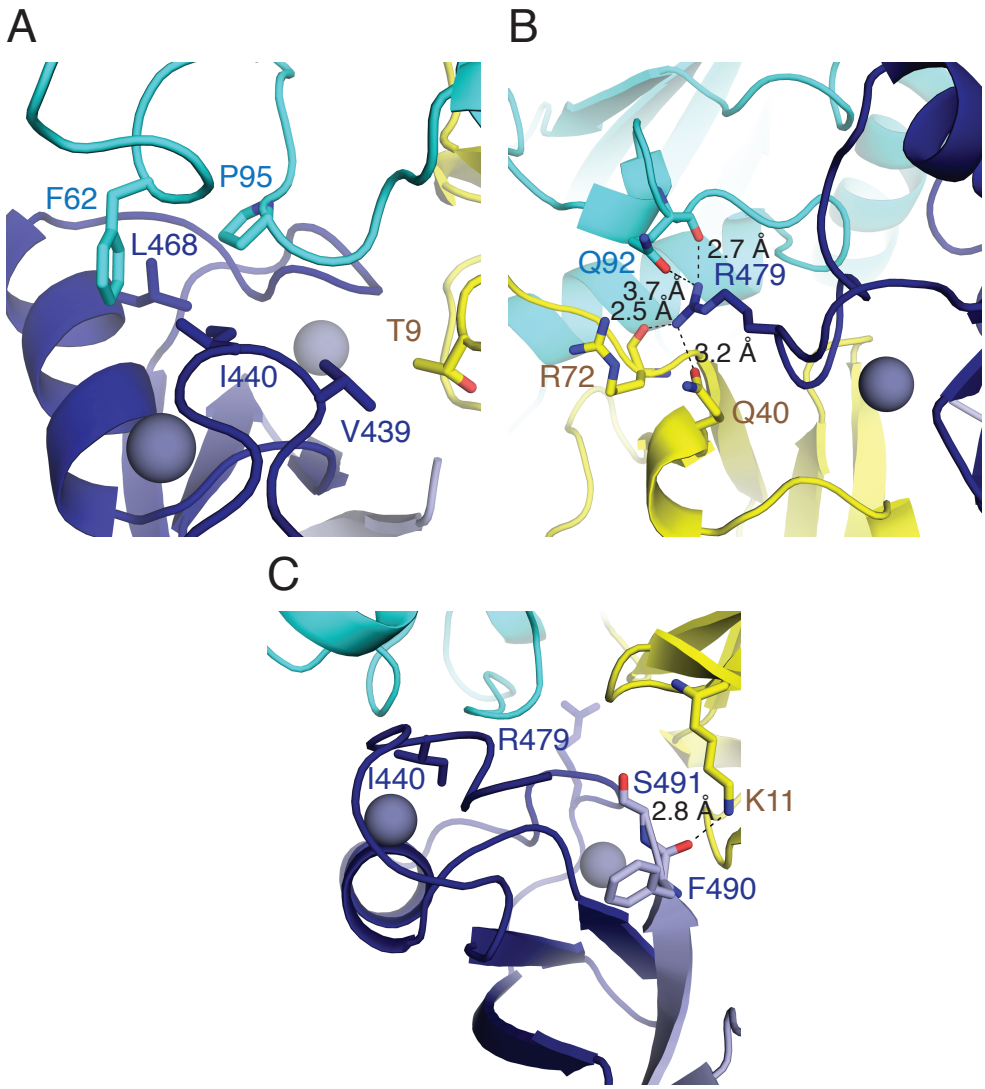

Figure 3-20: Interactions between MDM2^{f} and UbcH5B-Ub. (A) A hydrophobic batch around I440 stabilises UbcH5B. (B) The linchpin arginine R479 stabilises UbcH5B-Ub in its closed conformation. (C) The C-terminal tail of the second MDM2 molecule interacts with Ub.

The RMSD between the MDM2^{f} homodimer and the heterodimer in the E2-Ub bound state is 0.6 Å, with an indistinguishable MDM2-E2-Ub interface in both dimers. For example, the presence and the position of the linchpin arginine and the hydrophobic batch including I440 are fully conserved. This indicates that the frog homodimer recruits E2-Ub in the same way as the human heterodimer, with the only exception that it can bind two E2-Ub conjugates simultaneously. MDMX RING domain lacks key E2-Ub interacting residues and therefore can only bind E2-Ub via the MDM2 RING domain in the heterodimer (Nomura et al., 2017). Like in the crystal structures of MDM2^{f} alone, no electron density was observed for residues beyond S434^{f}. This rules out the idea that those residues might be stabilised upon E2-Ub binding which is the case in the heterodimer, where MDM2's 3_{10}-helix adopts an energetically more stable α-helix (Figure 1-14).

3.3.6 Extending the N-terminal linker in MDM2^{f}

In total, the structures of nine crystallographic distinct MDM2^{f} dimers have been determined, of which two were bound to E2-Ub, whereas the remaining seven were obtained in the absence of E2-Ub, but stabilised through a variety of different crystal contacts. However, there was no electron density of the N-terminal eleven residues (423-433) for any of the dimers, indicating that the region was disordered. This is in agreement with the secondary structure prediction server JPred 4 (Figure 3-21), which suggests that those residues lack a distinct secondary structure. JPred correctly predicted the presence of an α-helix around residue 460 and the three ß-sheets that are involved in the ß-barrel formation of the dimer. In contrast, the reliability of the tool is poor for regions that are involved in intermolecular interactions. For instance, the prediction was inaccurate for regions containing Zn^{2+}-coordinating cysteine residues. The tool also failed to predict the existence of helices around residues 430-436 in human MDM2 and MDMX. In the heterodimer, these helices stabilise each other and might require each other as discussed in Chapter 3.2. In the homodimer structure in complex with E2-Ub, the last visible residue (S434^{f}) is located near E2-Ub, potentially allowing N-terminal residues to interact with either UbcH5B, Ub or both proteins, thereby further stabilising the complex. In order to test this hypothesis, two constructs with additional 34 (389-C) and 62 (361-C) residues, which had been predicted as unstructured, were designed.

```
jnetpred    359 EDEGFDVPDC KKSKLTSSQD TNIDKKEAES IQISESQETE DCSQPSTSGS IASCSQEATK EDTRDESMEP
JNETHMM     359 EDEGFDVPDC KKSKLTSSQD TNIDKKEAES IQISESQETE DCSQPSTSGS IASCSQEATK EDTRDESMEP
JNETPSSM    359 EDEGFDVPDC KKSKLTSSQD TNIDKKEAES IQISESQETE DCSQPSTSGS IASCSQEATK EDTRDESMEP
Structure   359 ---------- ---------- ---------- ---------- ---------- ---------- ----DESMEP

jnetpred    429 SLPLTSVEPC VICQTRPKNG CIVHGRTGHL MACYTCAKKL KKRNKPCPVC REPIQMIVLT YFS
JNETHMM     429 SLPLTSVEPC VICQTRPKNG CIVHGRTGHL MACYTCAKKL KKRNKPCPVC REPIQMIVLT YFS
JNETPSSM    429 SLPLTSVEPC VICQTRPKNG CIVHGRTGHL MACYTCAKKL KKRNKPCPVC REPIQMIVLT YFS
Structure   429 SLPLTSVEPC VICQTRPKNG CIVHGRTGHL MACYTCAKKL KKRNKPCPVC REPIQMIVLT YFS
```

Figure 3-21: Secondary structure prediction for MDM2^{f} using different tools provided by the server Jpred 4. Comparison between MDM2^{f} 359-C and the crystal structure obtained in this study. Helices are indicated in green, ß-barrels in orange. Residues that were not present in the construct used for crystallisation are indicated with a dash. Residues with no observable electron density are indicated in blue.

Both proteins expressed and eluted likewise the shorter construct as dimers during SEC. The increased lengths of the constructs resulted in even better yields than the shorter MDM2 423-C. This result is in accordance with an earlier observation in human MDM2 (Chapter 3.1.2.), where the introduction of 78

additional residues allowed the isolation of at least a small dimeric fraction. Nevertheless, the stability difference between human and frog MDM2 is conserved for longer constructs, resulting in a 20-times higher yield (Table 3-9).

Table 3-9: Yields of MDM2^{f} 361-C and 389-C after SEC obtained per L of *E. coli* cells.

Construct	Yield after SEC [mg/L LB]	Concentration [mg/mL]
361-C	0.88	13.8
389-C	0.75	10.5

Both constructs were screened for crystallisation with UbcH5B-Ub under 864 different crystallisation conditions. For MDM2 389-C, small crystals appeared in nine different conditions, whereas no crystals were observed with MDM2 361-C. The crystals were optimised and diffracted to 3.42 Å (Table 3-10). The structure was solved by taking one MDM2 molecule in complex with E2-Ub from the structure in Chapter 3.3.4 as a search model. The unit cell contained only one MDM2 molecule bound to E2-Ub and formed a dimer with a symmetry related molecule. Due to the low resolution and the high R_{meas} value, it was not possible to successfully refine the structure. There was no electron density for MDM2 389-435, suggesting that this region is, in accordance with the secondary structure prediction (Figure 3-21), unstructured. However, due to the low quality of the dataset and the poor refinement, no final conclusion can be made. The crystal packing of this construct will be discussed in more detail in Chapter 4.6.

Table 3-10: Data collection and refinement statistics for MDM2^{f} 389-C in complex with UbcH5B-Ub. Numbers in parenthesis indicate the statistics for the outer shell.

Data collection	
Space group	C 1 2 1
Unit cell dimensions (*a*, *b*, *c* [Å] / *α*, *β*, *γ* [°])	125, 31, 78 / 90, 101, 90
Resolution [Å]	30.7-3.42 (3.48-3.42)
Unique reflections	4225
R_{meas}	0.401 (0.884)
Mean I/ σ	2.7 (1.5)
$CC_{1/2}$	0.9 (0.5)
Completeness [%]	99.7 (99.5)
Multiplicity	3.2 (3.4)
Refinement	
Content of the asymmetric unit	half an MDM2 dimer bound to 1 E2-Ub

3.4 Structural characterisation of human MDM2 RING domain (G443T)

The homogeneity of $MDM2^z$ and $MDM2^f$ RING domain raises the question, why the human protein mostly aggregated, despite the high sequence similarity. The strong structural similarity between the homodimer structures and the human MDM2-MDMX structure indicates that the human homodimer would most likely adopt a similar fold. By converting $MDM2^z$/$MDM2^f$ into human MDM2 through point mutations, the design of a less aggregating human MDM2 construct will be discussed with the aim to obtain the crystal structure of human MDM2 homodimer.

3.4.1 Construct design

In the initial purification attempt, human MDM2 428-C was shown to fully aggregate upon cleavage (Chapter 3.1.1.) whereas an N-terminal extension of 78 residues yielded at least a small amount of dimeric protein. The constructs of $MDM2^z$ and $MDM2^f$ corresponded to human MDM2 423-C, which could favour the formation of a dimeric species in comparison to the 428-C construct. Nonetheless, this does not explain why the yield for all $MDM2^f$ constructs, 361-C, 389-C and 423-C was significantly higher than for human MDM2 350-C. Therefore, single point mutations (I435V, G443T, K454R, Q480E) were introduced into human MDM2 at residues that were different from both, $MDM2^f$ and $MDM2^z$. Although there was only partial electron density for residues 432-435, these residues were located in near proximity to the C-terminus of the second MDM2 molecule. An $MDM2^z$/human MDM2 chimera (L432A, N433T, A434C, F490M, P491S) was designed to figure out whether intermolecular interactions between these residues were contributing to the stability of $MDM2^z$. To avoid aggregation issues related to the construct length, a slightly longer construct, 419-C, was used for all human MDM2 variants. As some of the residues in the N-terminal extension were not conserved, an $MDM2^f$/human MDM2 chimera (E423D, V426M, S428P) was included in the screen. In order to identify differences in the final yield of dimeric protein, a suitable read-out was required. Biophysical methods measuring protein stability such as ITC or CD spectroscopy were not suitable as the majority of human MDM2 was insoluble after cleavage (Chapter 3.1.1),

making a direct comparison more difficult. In a test expression from 1 L LB, the expression levels (Figure 3-22A) and the solubility (Figure 3-22B) were compared. No significant differences of protein levels were detected. The proteins were purified from GSH Sepharose affinity chromatography (Figure 3-22C). MDM2^{f} yielded two times more protein than human MDM2 (Figure 3-22D). The difference might have been more pronounced as contaminants in the samples contributed to the total amount of protein. Of the six mutants, only human MDM2 G443T (two-fold) and the MDM2^{z}/human MDM2 chimera (1.5-fold) yielded more protein than human MDM2. In order to test whether those variants were more dimeric than human MDM2, the oligomerisation state of the cleaved protein had to be analysed. The total yield before cleavage was 0.1-0.2 mg per variant and not sufficient for a subsequent SEC purification step after cleavage. Therefore, the protein purification was repeated by using 3 L LB. Human MDM2 and MDM2^{f} were purified from GSH Sepharose and cleaved on the beads, concentrated and applied on SEC. Surprisingly, both proteins exclusively eluted as dimers (Figure 3-22E,F), hence human MDM2 419-C remains soluble after cleavage. This indicates that human MDM2 419-C might be a potential candidate for large-scale purification for crystallisation purposes. However, this requires much higher protein concentrations throughout the purification, which could cause proteins with low solubility to precipitate. The low yield of the human MDM2 constructs in comparison to MDM2^{f} suggests that there are more factors than the construct length accounting for the difference in yield. The yields of the 3 L expression after GSH Sepharose elution (Figure 3-22G) were similar to the initial 1 L test expression. MDM2^{f} yielded two times more protein than human MDM2. The only variant that showed the same, reproducible yield improvement was human MDM2 419-C G443T. This construct was therefore used for large-scale purification.

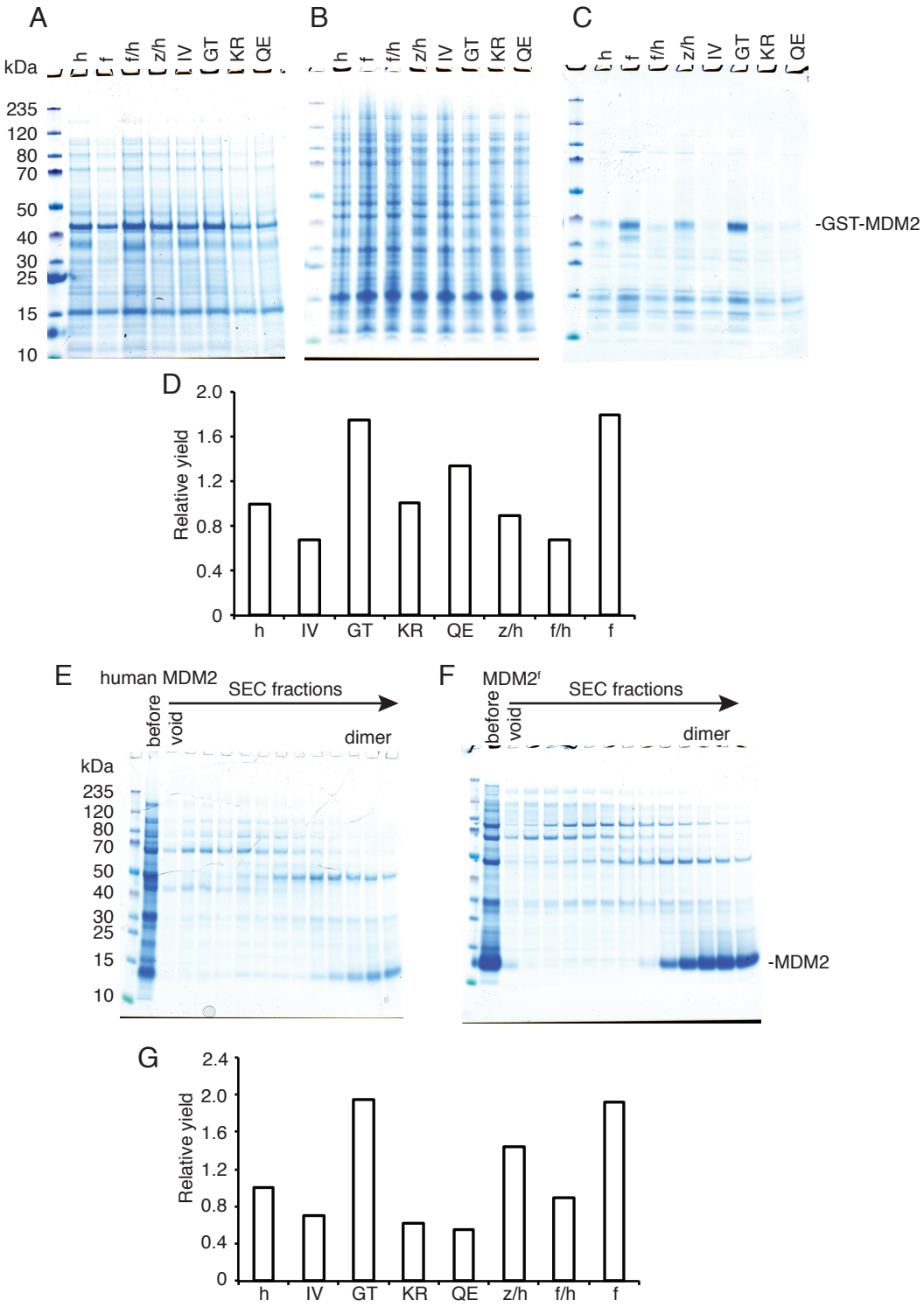

Figure 3-22: Solubility of human MDM2 constructs with point mutations of $MDM2^{f}$ and $MDM2^{z}$. Human WT (h), I435V (IV), G443T (GT), K454R (KR), Q480E (QE), chimera $MDM2^{z}$/human MDM2 (z/h), chimera frog $MDM2^{f}$/human MDM2 (f/h), $MDM2^{f}$ (f). (A-D) Purification attempt 1 (1 L LB). (A) Cell lysate after sonication. (B) Supernatant after sonication. (C) GSH Sepharose elution. (D) Yield after GSH Sepharose affinity chromatography relative to human MDM2. (E-G) Purification attempt 2 (3 L LB). (E) SEC run of cleaved human MDM2. (F) SEC run of cleaved $MDM2^{f}$. (G) Yield after GSH Sepharose affinity chromatography relative to human MDM2 (h).

3.4.2 Purification and E2-Ub binding

MDM2 419-C G443T (from here on denoted as $MDM2^{G443T}$) was expressed in 24 L LB and purified in the same way as $MDM2^{f}$. The cleaved protein was applied on SEC and eluted almost exclusively as a dimer (Figure 3-23). Unlike in the test expression of human MDM2 419-C wild-type (WT), the protein partly eluted in the void volume. Based on SDS-PAGE the amount is negligible and the high A_{280nm} in the void volume (Figure 3-23A fraction A12) in comparison to the dimeric fraction covering fractions A54-A67 can be explained by the weak absorbance of this construct at 280 nm due to the lack of aromatic residues. The relative intensity of the dimeric peak was much higher in the SEC runs of $MDM2^{f}$ (Figure 3-13) and $MDM2^{z}$ (Figure 3-6) and could most likely be attributed to the higher absorbance of $Y462^{z/f}$ in comparison to F462 in human MDM2. The final yield of dimeric human MDM2 was 0.66 mg/L LB and the protein could be concentrated without precipitation after SEC to obtain a final concentration of 1.36 mM.

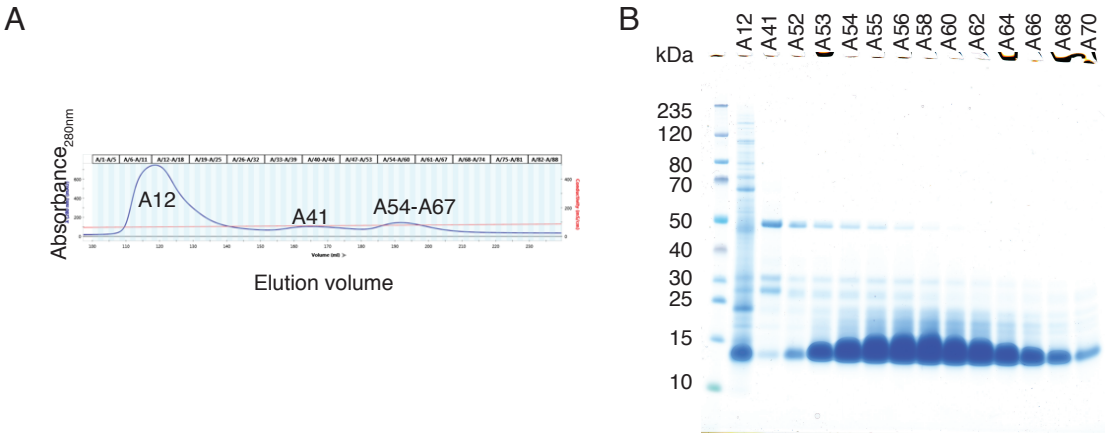

Figure 3-23: Purification of human $MDM2^{G443T}$. (A) Chromatogram of a SEC run of the cleaved protein. (B) SDS-PAGE of single SEC fractions.

In the crystal structure of $MDM2^{f}$ bound to UbcH5B-Ub, MDM2's T443 is in close proximity to UbcH5B's K4 and forms a weak hydrogen bond with the ε-amino group in two MDM2 molecules (Figure 3-24A). In the other two molecules of the unit cell, it forms hydrophobic interactions with the C_{δ} and C_{ε} of K4. The short distances of the hydrophobic interactions make it unlikely that T443 and K4 would adopt the same conformation in solution, leaving the question how the G443T mutation in human MDM2 would affect E2-Ub recruitment. The contribution of this residue to E2-Ub binding was assessed by SPR (Figure 3-24B). The binding affinity of the G443T mutant was 1.5-fold lower in comparison to $MDM2^{WT}$. This indicates that the mutation did not significantly perturb the E2-Ub

binding or introduce artificial hydrogen bonds in solution, which could reposition E2-Ub in an unnatural way. As this was not the case, the protein could be used for crystallisation attempts with UbcH5B-Ub.

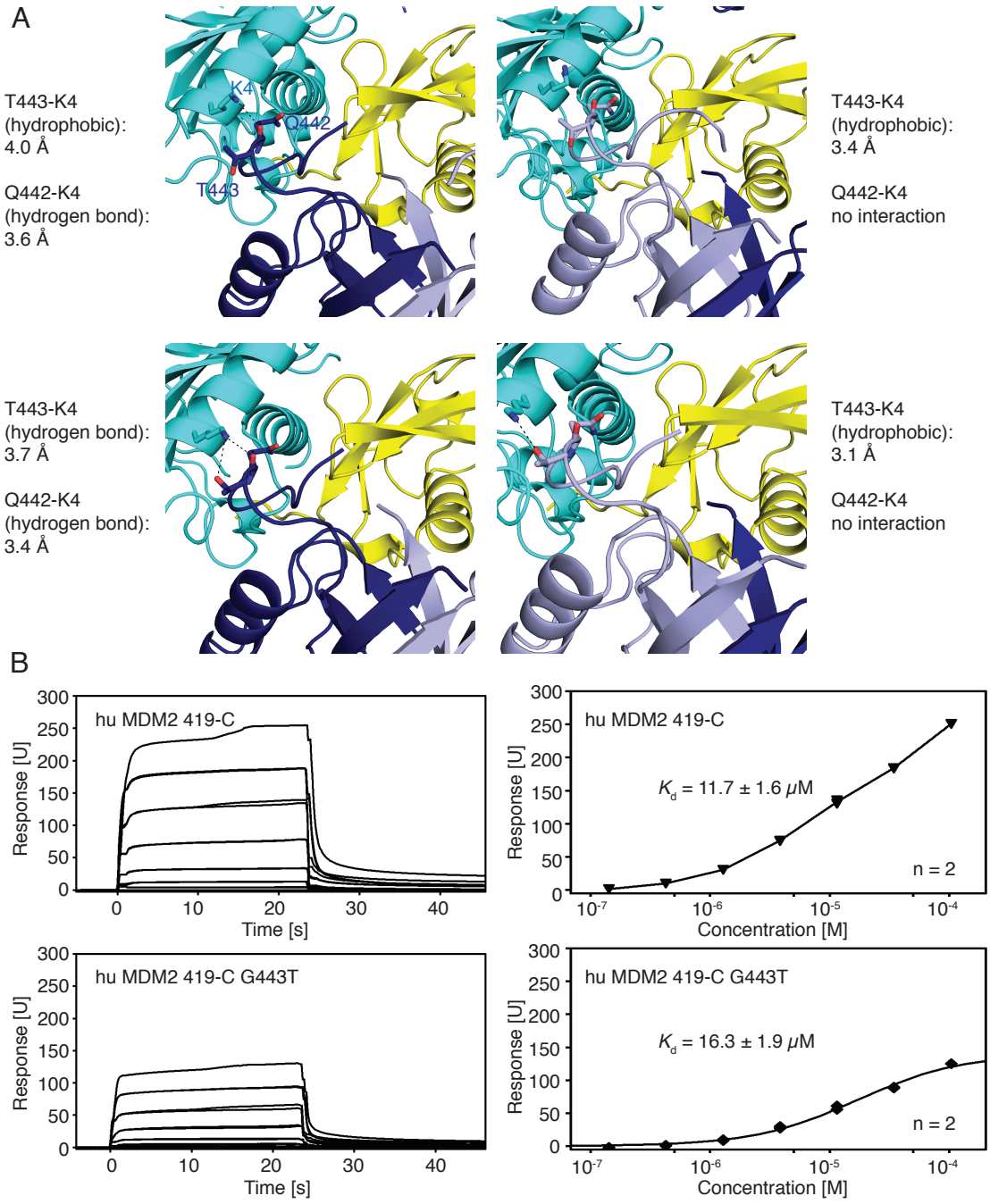

Figure 3-24: Contribution of MDM2's GT443 to UbcH5B-Ub binding. (A) In the crystal structure of MDM2^f in complex with UbcH5B-Ub, T443 forms different interactions with UbcH5B's K4 in the four MDM2^f molecules of the asymmetric unit. (B) SPR binding analysis for UbcH5B-Ub of human MDM2 in the presence of G443T. Representative sensorgrams (left) and binding curves with the estimated K_d (right).

3.4.3 Crystallisation

MDM2^{G443T} was mixed with UbcH5B-Ub and the complex was screened for crystallisation under 864 crystallisation conditions (Table 2-3). Crystals appeared under 28 different conditions, of which two yielded single crystals with a length of more than 700 µm (Figure 3-25).

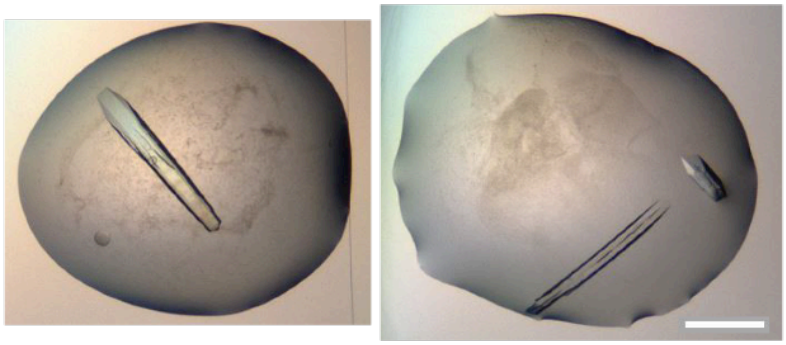

Figure 3-25: Crystals of the human MDM2^{G443T}-UbcH5B-Ub complex. Crystals were obtained in the BCS Screen F3 (left) and E9 (right). The length of the white bar corresponds to 300 µm.

Both crystals were sent to the synchrotron and diffracted to 1.65 Å (crystal 1) and 1.99 Å (crystal 2) (Table 3-11). Despite having grown from similar buffer conditions (Table 2-4), they had distinct unit cells. Therefore, both structures were solved by molecular replacement, using the crystal structure of frog MDM2^{f} bound to UbcH5B-Ub as a search model (Table 3-7, Figure 3-18).

Table 3-11: Data collection and refinement statistics for $MDM2^{G443T}$ in complex with UbcH5B-Ub. Numbers in parenthesis indicate the statistics for the outer shell.

Data collection		
Crystal name in this study	A	B
Space group	P 6_1	P 2_1 2_1 2_1
Unit cell dimensions (*a*, *b*, *c* [Å]/ *α*, *β*, *γ* [°])	130, 130, 71 / 90, 90, 120	56, 81, 136 / 90, 90, 90
Resolution [Å]	64.9-1.56 (1.59-1.56)	69.6-1.99 (2.02-1.99)
Unique reflections	96138	43902
R_{meas}	0.128 (0.890)	0.169 (3.021)
Mean I/ σ	13.8 (2.0)	8.8 (0.6)
$CC_{1/2}$	1 (0.5)	1 (0.4)
Completeness [%]	1001 (98.3)	100 (100)
Multiplicity	17.3 (9.7)	6.6 (6.4)
Refinement		
Resolution [Å]	64.9-1.56	69.6-1.99
Unique reflections	91299	41615
R_{work} / R_{free}	0.151 / 0.185	0.217 / 0.262
Content of the asymmetric unit	1 dimer bound to 2 E2-Ub	1 dimer bound to 2 E2-Ub
Atoms (Protein)	4492	4391
Atoms (non protein)	4 (Zn^{2+}), 1 (Cl^-), 28 (Ethylene glycol), 4 (Acetate), 543 (Water)	4 (Zn^{2+}), 145 (Water)
B-factor (Protein)	19.74	42.23
B-factor (Zn^{2+}, Cl^-)	16.82	30.94
B-factor (Ethylene glycol, Acetate)	35.94	-
B-factor (Water)	32.31	36.74
Bond length RMSD [Å]	0.0064	0.0098
Bond angle RMSD [°]	1.327	1.648
Ramachandran outliers [%]	0	0
Rotamer outliers [%]	0.40	1.04
Clashscore	0.99	3.66
Molprobity score	0.90	1.49

3.4.4 Crystal structure of the $MDM2^{G443T}$-UbcH5B-Ub complex

The asymmetric unit of both crystals contained one $MDM2^{G443T}$ dimer bound to two UbcH5B-Ub molecules (Figure 3-26A), where the complexes adopt an indistinguishable conformation (RMSD of 0.2-0.4 Å for one $MDM2^{G443T}$ molecule bound to one E2-Ub molecule, and 0.2 Å for the $MDM2^{G443T}$ dimers). The structure is very similar to $MDM2^{f}$-UbcH5B-Ub (RMSD of 0.3 Å for one MDM2 molecule bound to UbcH5B-Ub), and the key interactions discussed in Chapter 3.3.4. are fully conserved. A striking difference appears at the N-terminal residues covering P431-E436, which form a 3_{10}-helix in each MDM2

molecule (Figure 3-26B-E). In contrast, no electron density was observed in this region in any of the $MDM2^{f}$ and $MDM2^{z}$ structures, independently or in the presence of UbcH5B-Ub. These helices stabilise each other through hydrophobic interactions of A434 and I435 of both MDM2 molecules (Figure 3-26C). P431 is the last residue of the helix and acts as a helix breaker due to conformational restraints. This positions the neighbouring L430 in a hydrophobic clamp consisting of the second MDM2's L434, P437 and P445 (Figure 3-26D), thereby stabilising the dimer further. No electron density was observed for residues 419-429 in any of the four MDM2 molecules, indicating that this region might not be involved in the stabilisation of UbcH5B-Ub, although it is in close proximity to the donor-Ub.

In the MDM2-MDMX-UbcH5B-Ub complex, both MDM2 and MDMX also form N-terminal helices (Figure 3-26F). Notably, MDM2 forms an α-helix in the heterodimer, whereas MDMX forms a 3_{10}-helix like MDM2 in the homodimer. This subtle but significant difference is caused by sequence mismatches between MDM2 and MDMX for residues that stabilise the helices. This involves residues A434 and I435 (L433 and L434 in MDMX) and the C-terminal tail consisting of F490 and P491 (I489 and A490 in MDMX) (Figure 3-26G,I). Although MDM2 recruits UbcH5B-Ub in a similar fashion in both dimers (RMSD of 0.3-0.4 Å for one MDM2 molecule bound to UbcH5B-Ub), there are some structural differences. N433 stabilises the C-terminus of the second MDM molecule in both dimers in a conformation that is favourable for UbcH5B-Ub recruitment, thereby stabilising the complex. In the homodimer, N433 forms an intermolecular hydrogen bond with the C-terminus (Figure 3-26E), whereas this interaction is blocked in the heterodimer by MDMX's I489 (Figure 3-26I). This might explain why the homodimer is, despite the fact that it can bind two E2-Ub conjugates simultaneously, a more potent E3 ligase than the heterodimer, which is in agreement with an earlier observation where a heterodimer experienced a slight activity boost when the C-terminal tail was mutated to the corresponding residues in the homodimer (Nomura et al., 2017). The slight reorientation of N433 in the heterodimer allows P431 to adopt a different conformation, enabling the helix to continue beyond this residue. As a consequence, L430 is stabilised by a different set of hydrophobic interactions (Figure 3-26H) and shifted by 5-6 Å

(based on the C_α atom of L430), where the homodimer adopts a more elongated conformation than the heterodimer.

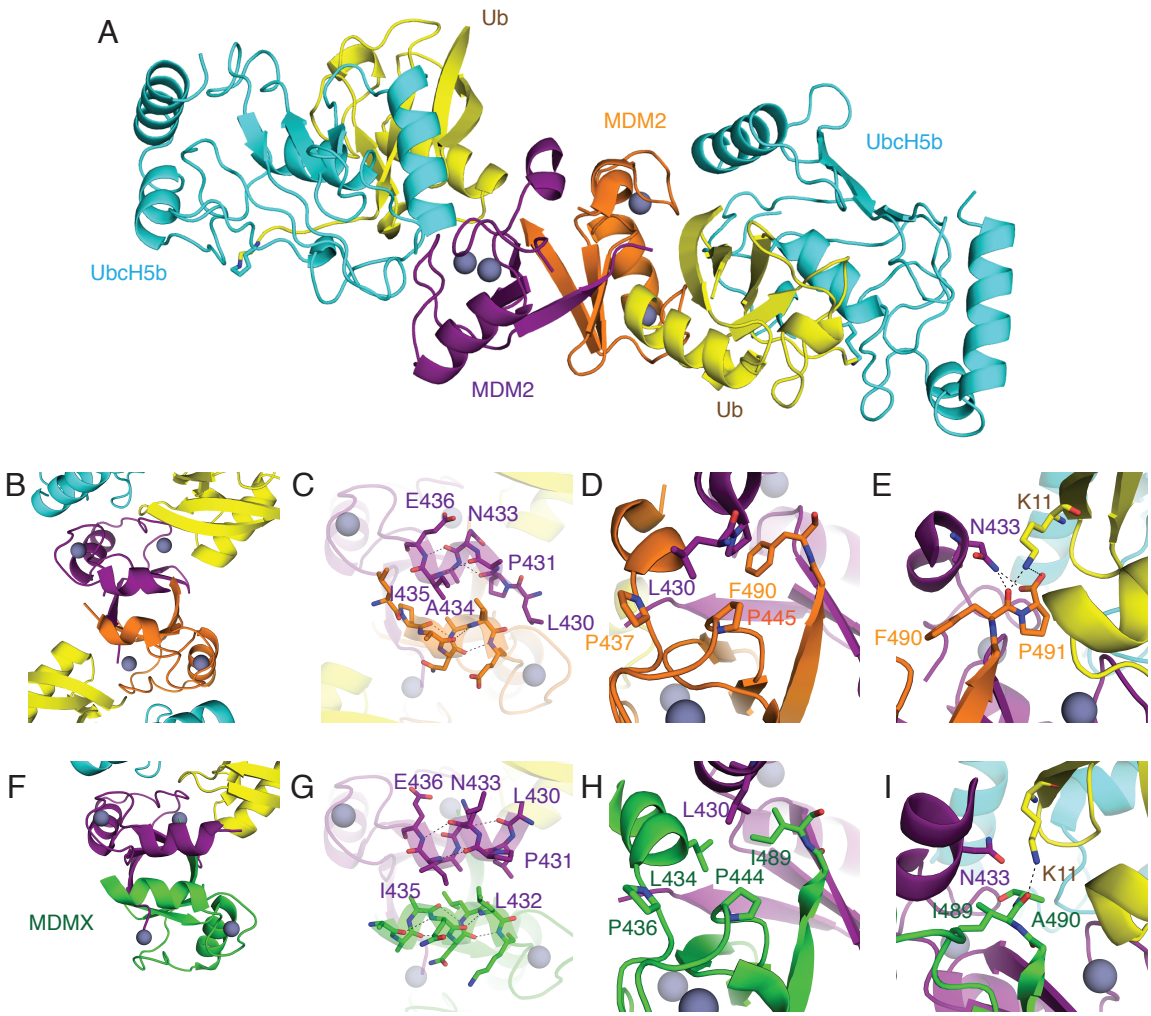

Figure 3-26: Crystal structure of MDM2^{G443T} bound to UbcH5B-Ub. (A) Overall structure. (B) Close-up of the N-terminal helices in the homodimer. (C) The N-terminal helices in the MDM2 homodimer adopt a 3_{10}-helix. (D) Close-up of L430 in the homodimer showing that it is stabilised by a hydrophobic clamp consisting of two proline residues. (E) Close-up of N433 in the homodimer showing that it stabilises the C-terminus of the second MDM2 molecule through hydrogen bonds, thereby creating a hydrogen bond network with Ub's K11. (F) Close-up of the N-terminal helices in the heterodimer (PDB: 5MNJ). (G) The N-terminal residues of MDM2 in the heterodimer form an α-helix, leading to a shift of residues beyond L432 as compared to the homodimer in D. (H) Close-up of L430 in the heterodimer showing that it is stabilised by different residues. (I) Close-up of N433 in the heterodimer showing that it cannot stabilise MDMX's C-terminal tail due to steric restriction of MDMX's I489. The stabilisation of Ub's K11 is therefore weaker than in the homodimer.

From P437 onwards, the structure of MDM2^{G443T} is nearly identical to MDM2^{f} and MDM2^{z}. Thus, it is no surprise that G443T interacts with UbcH5B's K4 (Figure

3-27) like in the structure of MDM2^{f} (Figure 3-24A) and does not seem to alter the conformation of UbcH5B relative to MDM2. One of the MDM2 molecules of each dimer forms a weak hydrogen bond with K4, which is further stabilised by the carbonyl group of Q442. In the other two molecules, G443T and K4 form a hydrophobic interaction where the ε-amino group of K4 either faces away from MDM2 (crystal A) or forms a hydrogen bond with Q442 (crystal B). The hydrogen bond between K469 and Q483, which was observed in the UbcH5B-Ub bound structure of MDM2^{f} (Figure 3-19), is conserved in all four crystallographic independent MDM2 molecules. The diameter of the MDM2^{G443T} dimers is 36.9-37.0 Å (distance between the C_{α} atoms of R471), which reinforces the hypothesis that the slight compression of the dimer is a consequence of UbcH5B-Ub binding and likely not a result of crystal packing.

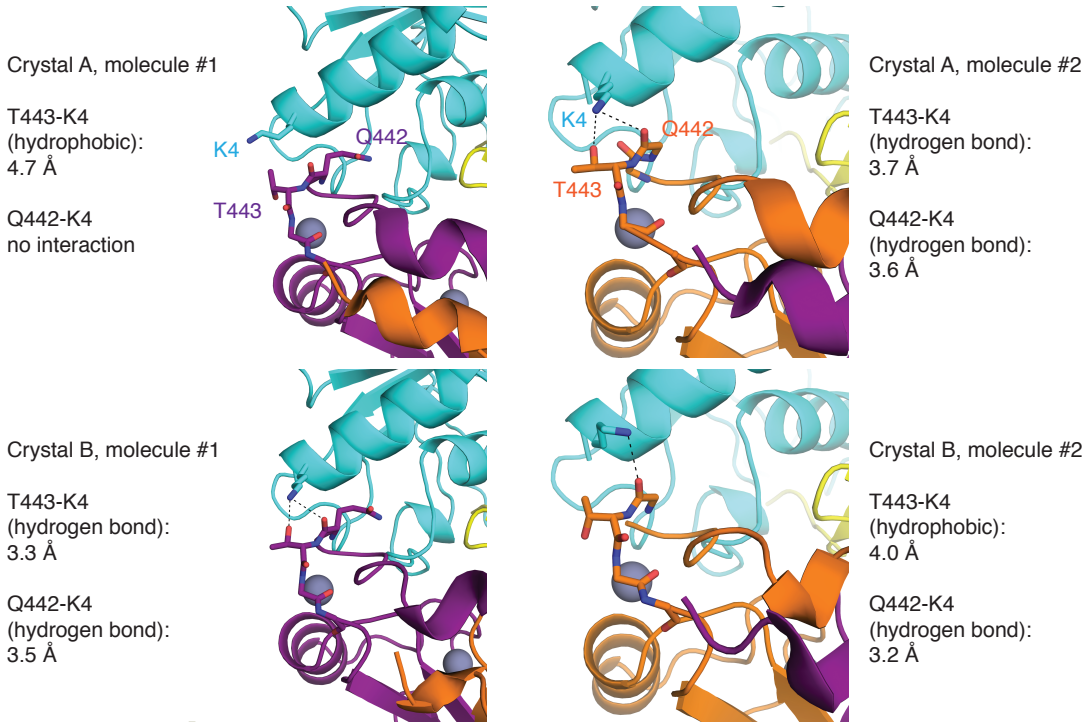

Figure 3-27: Interaction between MDM2's G443T and UbcH5B's K4 in both crystals structures. In each dimer, one G443T forms a weak hydrogen bond and the other one a hydrophobic interaction with K4.

3.5 Structural characterisation of human MDM2 RING domain (wild-type)

In the test expression (Chapter 3.4.1.), human MDM2^{WT} 419-C did not aggregate upon cleavage, making it a suitable construct for purification even in the absence of the G433T mutation. Although there was no indication that G443T

would have significantly altered the structure of MDM2 or the interaction of MDM2 with UbcH5B-Ub, the crystal structure did not provide any hints for why a threonine at position 443 would result in a significantly higher protein yield. In this section, the large-scale purification of $MDM2^{WT}$ will be compared with $MDM2^{G443T}$. Finally, the crystal structure of $MDM2^{WT}$ and the impact of G443 and G443T will be discussed.

3.5.1 Purification

$MDM2^{WT}$ was purified in the same way as $MDM2^{G443T}$. The cleaved protein was applied on SEC and eluted mainly in the void volume (Figure 3-28), as expected, demonstrating that this construct was significantly less stable than $MDM2^{G443T}$ although no protein could be detected in the void volume in the initial test expression (Figure 3-22). This suggests that the aggregation tendency of MDM2 RING domain constructs is concentration dependant. Unlike MDM2 428-C, a small fraction of cleaved protein eluted as a dimer, showing that the addition of nine residues at least partly contributed to the enhanced stability of this construct. The final yield was only 0.04 mg/L LB, which was almost 20 times less than for $MDM2^{G443T}$.

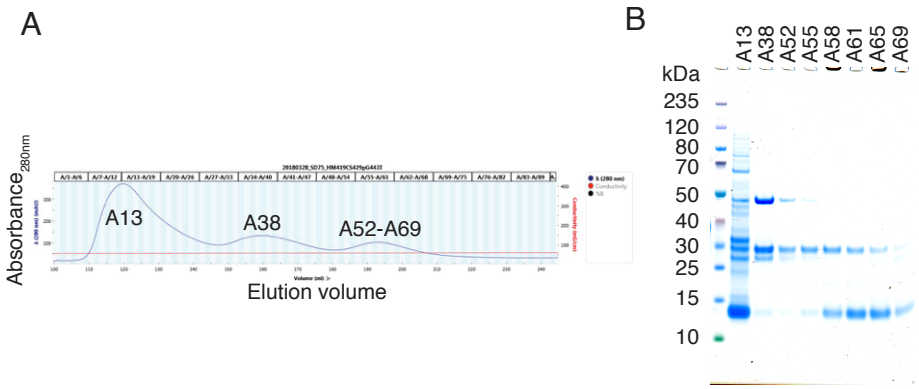

Figure 3-28: Purification of $MDM2^{WT}$. (A) Chromatogram of a SEC run of the cleaved protein. (B) SDS-PAGE of single SEC fractions.

3.5.2 Crystallisation

The protein could be concentrated without precipitation, so that it was possible to set up crystallisation trays with UbcH5B-Ub although the low yield strongly limited the number of conditions that could be screened. In the screen of $MDM2^{G443T}$ with UbcH5B-Ub, the highest number of crystals (five) was obtained

from the BCS Screen, of which two were of sufficient quality for data collection without further optimisation (Figure 3-25). Assuming that $MDM2^{WT}$ would be similar to $MDM2^{G443T}$, the 96 conditions of this screen were used for a crystallisation attempt. Crystals appeared in only one condition (Figure 3-29A), which also promoted the growth of crystals in the $MDM2^{G443T}$ screen. Although the crystals were single, they were too small for data collection so that optimisation was required. During the optimisation process (Chapter 2.5.2.3), two similar but distinct buffer conditions promoted the formation of two different crystal forms (Figure 3-29B). Both crystals diffracted isomorphously, with the highest resolution at 1.41 Å. The unit cell was isomorphous to crystal A of the $MDM2^{G443T}$-UbcH5B-Ub complex (Table 3-12).

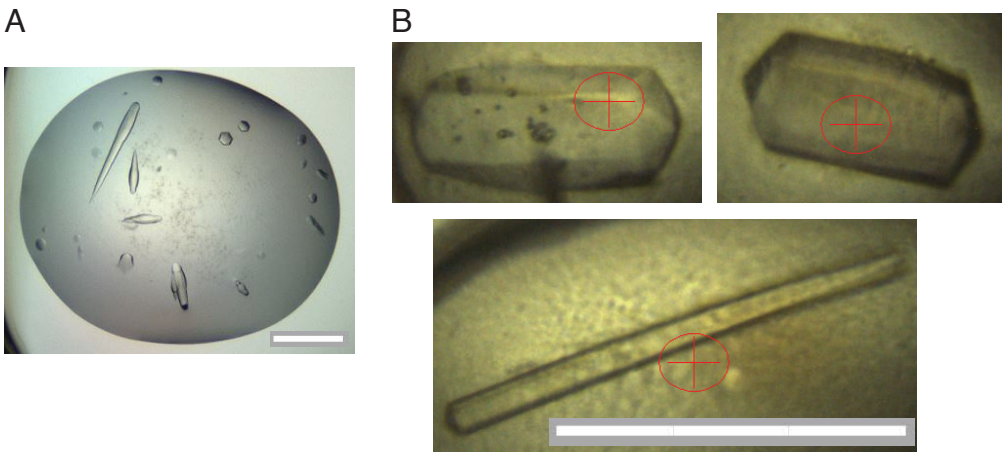

Figure 3-29: Crystals of the $MDM2^{WT}$-UbcH5B-Ub complex. Crystals were obtained in condition B6 of the BCS Screen (left) and optimised (right). The length of the white bar corresponds to 300 µm.

Table 3-12: Data collection and refinement statistics for $MDM2^{WT}$ in complex with UbcH5B-Ub. Numbers in parenthesis indicate the statistics for the outer shell.

Data collection	
Space group	P 6_1
Unit cell dimensions (*a*, *b*, *c* [Å] / *α*, *β*, *γ* [°])	130, 130, 71 / 90, 90, 120
Resolution [Å]	112-1.41 (1.43-1.41)
Unique reflections	129794
R_{merge}	0.047 (0.664)
Mean I/ σ	19.2 (1.9)
$CC_{1/2}$	1.000 (0.542)
Completeness	100 (99.6)
Multiplicity	8.9 (6.0)
Refinement	
Resolution [Å]	12.33-1.41
Unique reflections	123373
R_{work} / R_{free}	0.151 / 0.184
Content of the asymmetric unit	1 dimer bound to 2 E2-Ub
Atoms (Protein)	4701
Atoms (non protein)	4 (Zn^{2+}), 2 (Cl^-), 20 (ethylene glycol), 439 (water)
B-factor (Protein)	30.37
B-factor (Zn^{2+}, Cl^-)	39.91
B-factor (ethylene glycol)	56.46
B-factor (water)	39.99
Bond length RMSD [Å]	0.009
Bond angle RMSD [Å]	1.564
Ramachandran outliers [%]	0.18
Rotamer outliers [%]	1.52
Clashscore	2.31
Molprobity score	1.19

3.5.3 Crystal structure of the MDM2WT-UbcH5B-Ub complex

The crystal structure is identical with the structure of $MDM2^{G443T}$ (RMSD of 0.2-0.3 Å for the MDM2 dimer and for an MDM2 monomer bound to E2-Ub), demonstrating that this mutation did not alter the structure of MDM2 or the nature of UbcH5B-Ub binding. G443 and UbcH5B's K4 form a hydrophobic interaction in both MDM2 molecules in the asymmetric unit (Figure 3-30) like in one of the molecules of the isomorphous crystal of the $MDM2^{G443T}$ complex (Figure 3-27, crystal A, molecule #1). The fact that both K4 sidechains adopt a similar orientation might indicate that this position is favourable, which could also explain the subtle difference in the UbcH5B-Ub binding affinity between $MDM2^{WT}$ and $MDM2^{G443T}$. The structure of the loop containing G443 is identical in the presence of the G443T mutation and all intramolecular interactions are fully

conserved. Hence, the crystal structure does not explain why a threonine at position 443 causes a dramatic increase in the stability of the RING domain. Several studies have reported the aggregation tendency of the homodimeric MDM2 RING domain but very little is known about how the dimer self-assembles to form aggregates. The region around G443 might be involved in the assembly of dimers, which could initiate the protein aggregation. Nevertheless, a dimeric fraction of $MDM2^{WT}$ could be isolated and remained dimeric throughout the purification. Due to the little effect on UbcH5B-Ub binding, the G443T mutation will be included in all other experiments in this study due to its enhanced stability.

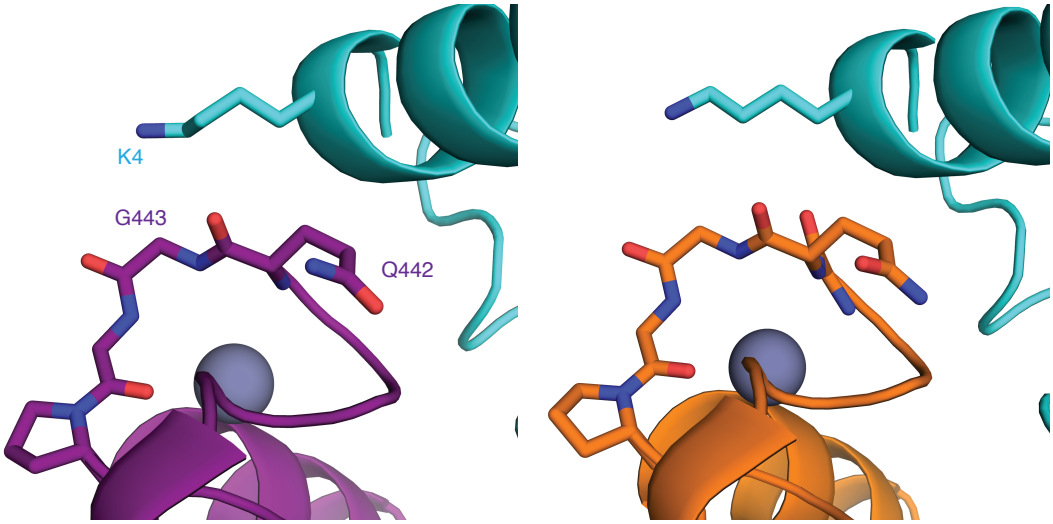

Figure 3-30: Position of G443 in the $MDM2^{WT}$-UbcH5B-Ub complex. G443 forms a hydrophobic interaction with UbcH5B's K4 in both molecules. The distance between the C_α atom of G443 and the C_δ atom of K4 is 4.2-4.3 Å.

3.6 Structure validation

The homodimer recruits UbcH5B-Ub in a similar way as the heterodimer, despite the structural differences of the N-terminal helices and the sequence mismatch between MDM2 and MDMX at the C-terminal tail. In the previous study of our laboratory on the crystal structure of the heterodimer bound to UbcH5B-Ub, the importance of key residues for E2-Ub binding such as I440 and R479 (Figure 3-20) was already validated. Based on the crystal structure, a model for the homodimer bound to two E2-Ub molecules could be generated by superimposition of the MDM2-E2-Ub on MDMX in the crystal structure (Figure

1-16). This model agrees well with the crystal structures presented in this study so that a structure validation of the MDM2-E2-Ub interactions was not required anymore. The only disagreement between the model and the crystal structure was the formation of the 3_{10}-helices in the homodimer. These helices had not been observed before as the only structural information about the RING domain of the homodimer was based on an NMR model that predicted residues beyond E436 to be disordered. In order to understand the relevance of these residues, autoubiquitination assays were performed where residues 428-436 (except P431) were individually mutated to arginine (Figure 3-31A,B) with the aim to introduce steric clashes to disrupt the 3_{10}-helical conformation. When any of these residues is mutated to arginine, the protein only showed very little activity suggesting that the correct arrangement of the helices is important for the recruitment of UbcH5B-Ub. L430 is not involved in the formation or the stabilisation of the 3_{10}-helices, but L430R substitution also reduced the activity highlighting the importance of the observed hydrophobic interaction (Figure 3-26D). There was no electron density for residues beyond L430 in any of the MDM2 molecules. Arginine substitution at either S428 or S429 did not affect the activity, which suggests that the region beyond L430 is not involved in E2-Ub recruitment. These residues are also less conserved among different species. For instance, elephant MDM2 contains an arginine residue at position 429, whereas a range of different residues can be found at position 428, including proline and tyrosine. N433R almost completely abolishes the catalytic activity, which can be attributed to the critical role of the asparagine sidechain in the hydrogen bond network involving the C-terminal tail of the second MDM2 molecule and K11 of the donor-Ub (Figure 3-26E). E436R also causes a drastic activity reduction. Although the sidechain of this residue does not contact another residue, it faces towards the MDM2-E2-Ub interface (Figure 3-26C), where an arginine substitution would clash with E2-Ub due to steric hindrances, thereby blocking E2-Ub from adopting the ideal conformation for catalysis. MDMX contains lysine at this position, which is one of the key residues that prevent MDMX from recruiting E2-Ub in the heterodimer. Moreover, E436K has been shown to cause a drastic activity decrease in the homodimer (Kosztyu et al., 2019). Taken together these results demonstrate the importance of the residues adjacent to the RING domain in maintaining the 3_{10}-helical configuration for optimal positioning of E2-Ub for catalysis. Consistent with this, $MDM2^{f}$ shows a much

lower catalytic activity than human MDM2 (Figure 3-31C), which can be attributed to the missing 3_{10}-helix.

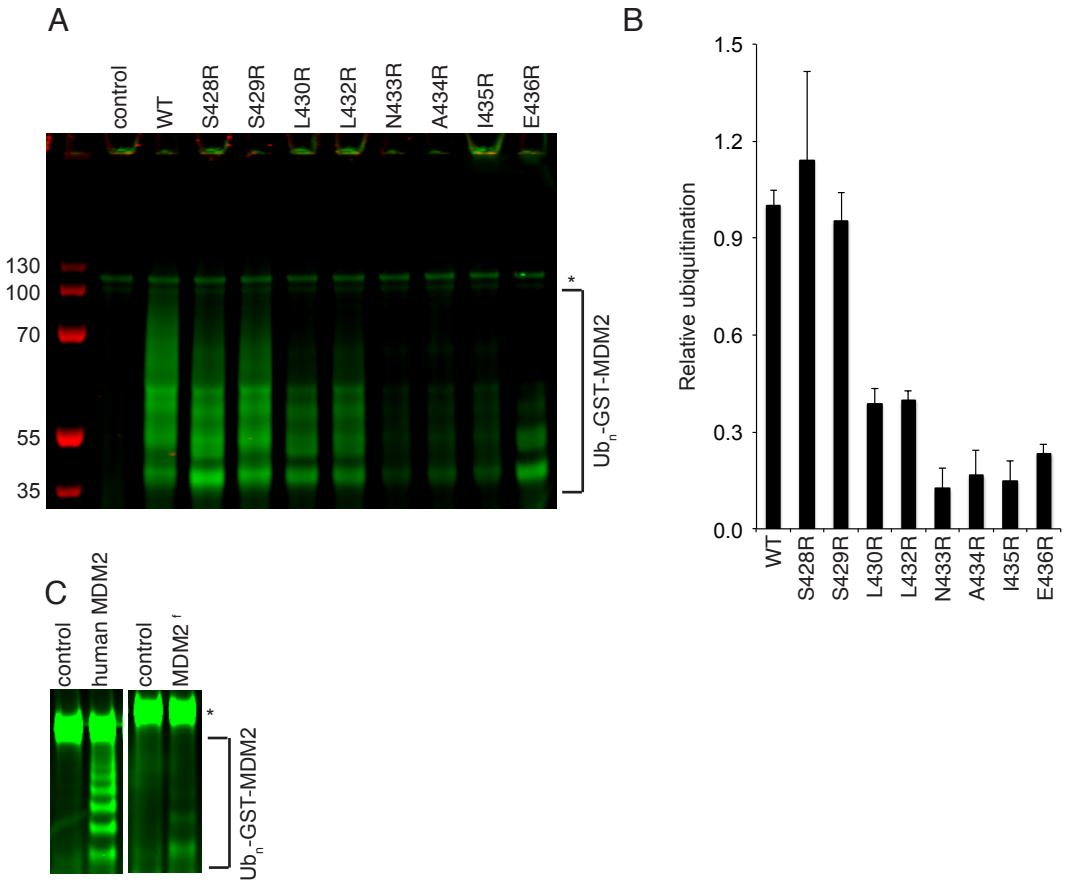

Figure 3-31: Importance of the residues adjacent to the RING domain. (A) Autoubiquitination assay of MDM2. (B) Quantification of the autoubiquitination products in (A) relative to WT. (C) Autoubiquitination assay of human MDM2 and MDM2^f. (*) indicates the formation of E1-Ub.

3.7 Summary and Discussion

In this chapter, a purification protocol for the MDM2 homodimer RING domain was developed, which overcame previously reported aggregation issues and gave sufficient amounts of protein for crystallisation attempts, which ultimately allowed to determine the crystal structure of the homodimer.

A short MDM2 construct (428-C, 16 kDa as a dimer) only gave a low yield of a species with an elution profile corresponding to a 100 kDa protein during SEC (Chapter 3.1.1). A dimeric MDM2 could be isolated by increasing the length of the construct (Chapter 3.1.2) or the introduction of an N-terminal MBP tag (Chapter 3.1.3). While the yield of the former construct was low, the latter failed to crystallise. The purification of MDM2 from different species resulted in

high yields of purely dimeric protein (Chapter 3.2 and 3.3), and by introducing single point mutations into human MDM2, G443 could be identified as the key residue responsible for the pronounced aggregation of the human MDM2 RING domain (Chapter 3.4). The aggregation tendency could nearly be eliminated by a threonine substitution at position 443, which is the corresponding residue in $MDM2^{f}$. $MDM2^{z}$ contains a serine at this position and could be purified without significant aggregation, like $MDM2^{f}$, indicating that other residues than threonine might also block protein aggregation. The constructs that were used in this chapter are summarised in Table 3-13.

Table 3-13: Summary of the purified MDM2 constructs. Overview of the yields of dimeric protein after the final purification step (SEC) and the crystallisation success.

Construct	Yield [mg/LB]	Yield [nmol/LB]	Crystals	
			on its own	with UbcH5B-Ub
human MDM2 428-C	0	0	-	-
human MDM2 350-C '6D'	0.02-0.06	1.2-3.7	no	no
MBP-human MDM2 418-C	0.35	7.2	no	no
$MDM2^{z}$ 423-C	0.23-0.28	29-36	yes	no
$MDM2^{f}$ 423-C	0.33-0.40	42-51	yes	yes
$MDM2^{f}$ 389-C	0.75	65	not screened	yes
$MDM2^{f}$ 361-C	0.88	60	not screened	no
human MDM2 419-C	0.04	4.8	not screened	yes
human MDM2 419-C G443T	0.66	80	not screened	yes

Crystal structures were obtained for $MDM2^{z}$ and $MDM2^{f}$. Although the designed constructs differed by 14 residues from each other, they yielded isomorphous crystals and the refined structures had a RMSD of 0.3 Å. For $MDM2^{f}$, datasets for two additional crystals with different unit cells were obtained, resulting in seven crystallographic unique dimers. Although they were stabilised by a variety of different crystal contacts (Figure 3-17), they were nearly identical (RMSD of 0.3-0.7 Å to each other) and agreed well with a previously published crystal structure of the human MDM2-MDMX heterodimer (RMSD of 0.4-0.7 Å), indicating that the sequence difference to human MDM2 (19 residues for $MDM2^{z}$, nine residues for $MDM2^{f}$) had no effect on the overall structure. This rules out a structural difference proposed by an earlier study (Linke et al., 2008), where the MDM2 molecule of the heterodimer structure was superimposed on MDMX in the heterodimer structure to generate a model for the homodimer, causing the angle between the protomers to be offset. The structures deviated to a slightly higher degree from the NMR model of the human homodimer (RMSD of 1.6-

1.8 Å), which could be attributed to inaccuracies of the NMR model for loop regions. The crystal structure of the MDM2-UbcH5B-Ub complex could be determined for human MDM2 and MDM2^{f}. Both complexes are very similar to each other and the previously published structure of the human MDM2-MDMX heterodimer bound to UbcH5B-Ub, although the homodimer could bind two E2-Ub conjugates simultaneously, as predicted. The only structural difference between the dimers was located at residues adjacent to the RING domain. The human homodimer forms two 3_{10}-helices, whereas MDM2 forms an α-helix in the heterodimer. The importance of these helices was demonstrated by disruptive arginine mutations, which drastically lowered the autoubiquitination activity of MDM2. Helices adjacent to the RING domain can also be found in other dimeric E3 RING ligases with varying relevance for stabilisation of the dimer or E2-Ub (Figure 1-9). In MDM2, they are not only important for E2-Ub recruitment but also important for the stabilisation of the second protomer. For instance, the C-terminal tail is held in place by forming hydrogen bonds with N433, which is located in the 3_{10}-helix (Figure 3-26E). However, the relevance of these hydrogen bonds in solution was not tested as the arginine substitution N433R also directly affected E2-Ub binding. In order to study the contribution of these helices for dimerisation, the oligomeric state of MDM2$^{\Delta 310\text{-helix}}$ would need to be analysed.

It is unclear why the corresponding residues in the structures of MDM2^{z} and MDM2^{f} are disordered. Although this agrees well with the observation that MDM2^{f} has a much lower activity than human MDM2 (Figure 3-31C), it raises the question whether MDM2^{f} is intrinsically less active or has additional stabilisation mechanisms such as another domain folding back to stabilise the RING domain. The sequences of MDM2^{f} and MDM2^{z} show a lot of discrepancies from human MDM2 beyond the RING domain, particularly around residues 330-350 (Figure 3-32), but due to the lack of structural information it is unclear whether these residues are simply disordered or have an additional function in MDM2^{f} and MDM2^{z} such as stabilising the RING domain. In this context, it would be interesting to compare the catalytic activities of MDM2 constructs of different lengths and from different species. In such an experiment, one would expect a drastic activity increase, once the stretch is included that stabilises the RING domain.

MDM2^{z} has, like all other fish MDM2 (Table 3-3), a cysteine residue at position C434. Although it faces away from the same residue of the second protomer in the crystal structure (Figure 3-10), it is possible that a C434-C434 disulphide bond could form due to the flexibility of this region and stabilise the dimer either directly or indirectly by promoting the formation of other structural elements such as helices. However, MDM2^{f} does not contain any cysteine residues adjacent to the RING domain so that an additional mechanism would be needed. Ultimately, structural information about the domain architecture of MDM2 would be required to accurately understand the stabilisation of the RING domains. Nonetheless, the structural differences between MDM2 of different species as presented here should be kept in mind when working on multi-domain constructs of MDM2, as the RING domains might be stabilised in a significantly different way, which could depend on the existence of 3_{10}-helices like in human MDM2.

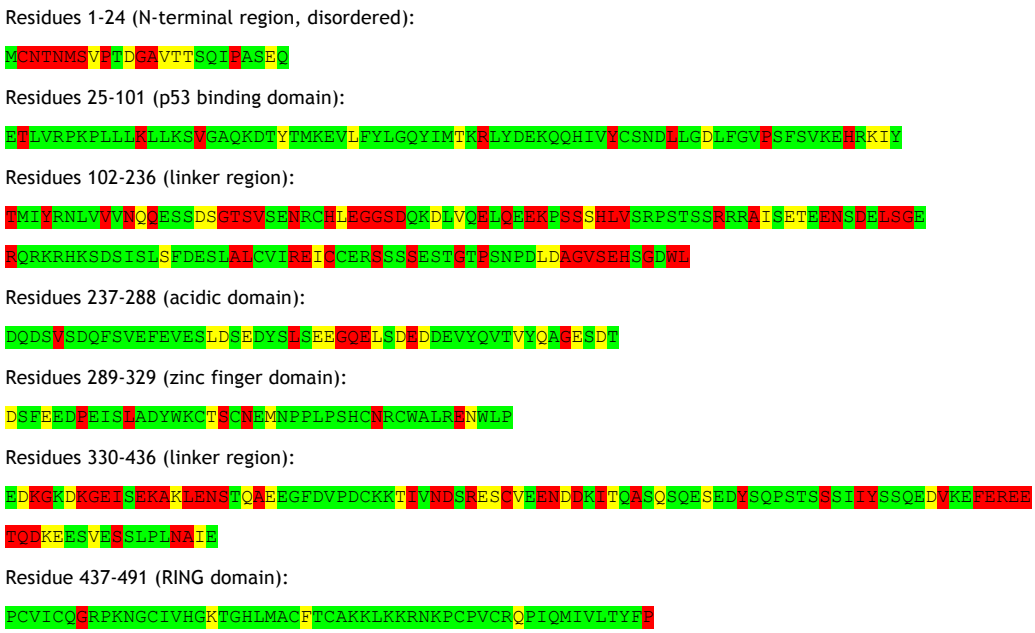

Figure 3-32: Sequence similarity between human MDM2 and MDM2$^{f/z}$. The sequence of human MDM2 is shown. Residues that are either identical in MDM2^{f}, MDM2^{z} or in both proteins are highlighted in green. Similar residues are highlighted in yellow and residues that are not conserved in MDM2$^{f/z}$ are highlighted in red.

Taken together, the findings here bring light into a long discussion in the field regarding differences between the MDM2 homodimer and the MDM2-MDMX heterodimer (Kosztyu et al., 2019). It could be shown that they appear to be similar and use the same residues to recruit E2-Ub but have small structural differences due to sequence discrepancies in the region adjacent to the RING

domain and the C-terminal tail. This can have consequences for their function and an example involving homodimer specific phosphorylation will be described in the following chapter. The structure and the protocol for the purification of a non-aggregating MDM2 RING construct will be useful for further structural studies involving co-crystallisation attempts with predicted binding partners such as RNA (Elenbaas et al., 1996) and ATP (Poyurovsky et al., 2003) (Priest et al., 2010). In addition, RING domain inhibitors can be designed guided by the crystal structure and existing inhibitors (Yang et al., 2005) (Kitagaki et al., 2008) (Roxburgh et al., 2012) (Smith et al., 2012) can be co-crystallised with $MDM2^{G443T}$ with the aim to identify the exact molecular interaction with MDM2, which would allow a structure-based optimisation and could promote the design of a specific and potent MDM2 RING domain inhibitor.

Chapter 4 Phosphoregulation of MDM2 homodimer

4.1 Phosphorylation effect on catalytic activity of MDM2

Upon DNA damage, MDM2 gets phosphorylated at residues near the RING domain, which ultimately leads to the stabilisation of p53 (Chapter 1.3.3). However, the molecular basis for this observation has not been identified. A SEC experiment showed that DNA damage induced phosphorylation shifted the soluble fraction of overexpressed MDM2 362-C in SJSA cells towards lower molecular weight species, which could not be observed in the presence of the ATM kinase inhibitor KU-55933. The same shift was observed for simultaneous aspartate substitutions at positions S386, S395, S407, T419, S425 and S429 ('6D') when MDM2 362-C was expressed and purified from *E. coli* (Cheng et al., 2009). This demonstrated that the shift could occur independently of other MDM2 domains such as the acidic domain and did not require binding partners or co-factors that do not exist in bacteria. Based on the crystal structure presented in Chapter 3.4, the above-mentioned phosphorylation sites are close enough to potentially interact with E2-Ub, thereby affecting the catalytic activity of MDM2. In this chapter, experiments were set up to test this hypothesis in the context of the MDM2 homodimer and the MDM2-MDMX heterodimer.

4.1.1 SPR binding analyses of phosphomimetic MDM2 variants

In Chapter 3.1.2, MDM2 350-C showed a two-fold binding increase for UbcH5B-Ub in the presence of the '6D' mutation. In order to understand the contribution of each phosphorylation site, MDM2 constructs carrying single aspartate mutations were created and tested for UbcH5B-Ub binding by Dr Gary Sibbet (Figure 4-1). Only S429D significantly improved the binding affinity for E2-Ub, and showed a binding affinity comparable to the '6D' construct (Figure 3-2), indicating that the binding increase of this construct was a consequence of the S429D mutation only, and not significantly affected by any of the other five aspartate mutations.

Figure 4-1: SPR binding analysis of MDM2 homodimer variants for UbcH5B-Ub. Only MDM2 '6D' and S429D show an enhanced binding affinity for UbcH5B-Ub. Dr Danny Huang expressed and purified the proteins and Dr Gary Sibbet undertook the SPR experiments.

In the crystal structure of human MDM2 419-C with UbcH5B-Ub, there was no electron density for S429, but an arginine substitution at this position had minimal effect on its autoubiquitination activity (Figure 3-31A,B). The proximity of this N-terminal region preceding the RING domain to the donor-Ub (Figure 4-2A) suggests that phosphorylation of S429 might have a role in donor-Ub interaction. In the crystal structure of MDM2-MDMX-UbcH5B-Ub, the N-terminal residues of MDM2 form a more compressed α-helix, which stabilises S429 and makes it visible in the electron density map (Figure 4-2B). In this structure, it is positioned close to the donor-Ub, in particular to the sidechains of K11 (4.6-5.5 Å), K33 (7.1-9.1 Å) and E34 (6.7-7.8 Å) and the carboxyl group of T12 (3.4-4.6 Å).

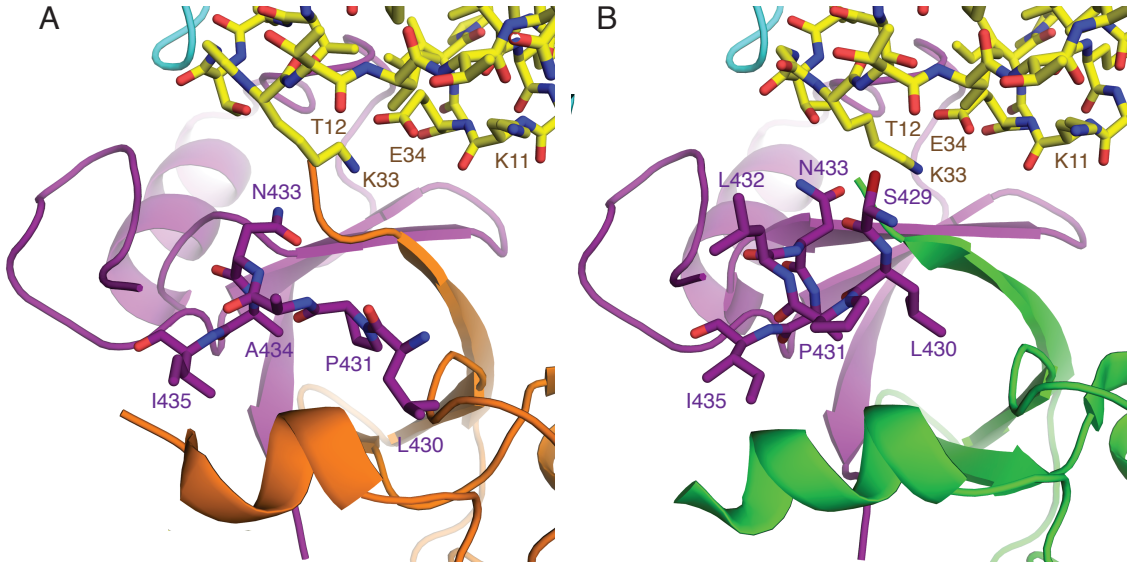

Figure 4-2: Position of S429 in the crystal structures of MDM2 bound to UbcH5B-Ub. (A) Homodimer (Chapter 3.5). There is no electron density for S429 in any of the crystal structures obtained for the homodimer, so that the position of S429 has to be estimated based on L430. (B) MDM2-MDMX heterodimer (PDB: 5MNJ). S429 faces towards the donor-Ub and is in close proximity to T12 (3.4-4.6 Å) and K11 (4.6-5.5 Å).

Due to the slightly different structure of the N-terminal helices in both dimers, the same binding analyses were performed for the heterodimer (Figure 4-3). Surprisingly, the '6D' construct only marginally affected the binding affinity for UbcH5B-Ub, independent of the construct length of MDMX. This suggests that

there are significant structural differences between homodimer and heterodimer.

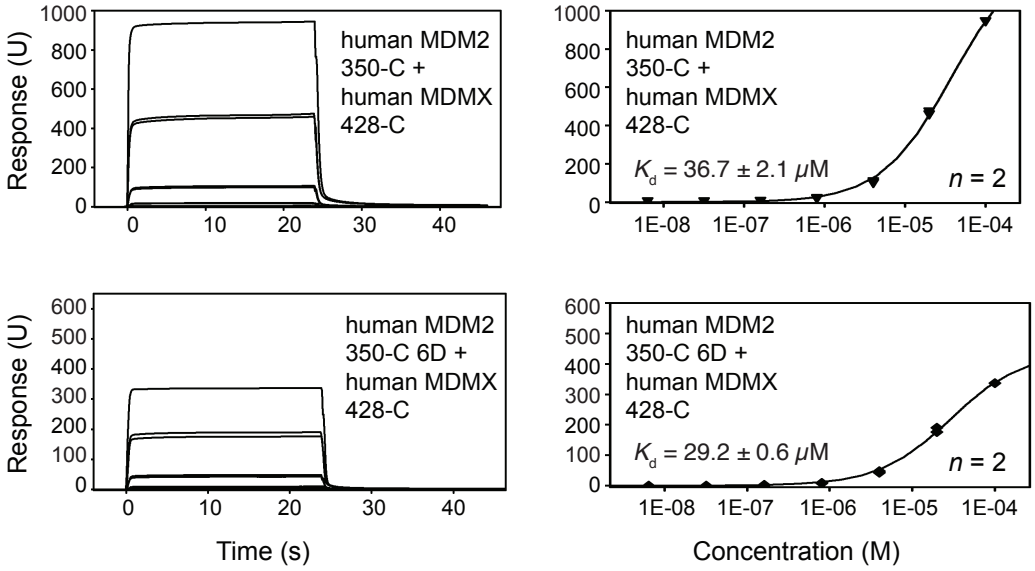

Figure 4-3: SPR binding analysis of '6D' MDM2-MDMX heterodimer for UbcH5B-Ub. The '6D' construct does not cause the same binding enhancement as in the homodimer. Dr Danny Huang expressed and purified the proteins and Dr Gary Sibbet undertook the SPR experiments.

The MDM2 constructs used for the binding experiments were all composed of residues 350-C, which was shown to form dimers and higher order oligomers (Chapter 3.1.2). As a previous study had shown that aspartate substitutions reduced the oligomerisation of a similar MDM2 construct (Cheng et al., 2009), the experiments were repeated with a dimeric $MDM2^{G443T}$ 419-C construct to figure out whether differences in the oligomeric state were accounting for the measured UbcH5B-Ub binding differences. In addition, a S429E variant was included, with the idea to resemble phosphoserine more closely due to the size difference between aspartate and glutamate. The binding enhancement is conserved in $MDM2^{G443T}$ 419-C, which rules out a contribution of residues 350-418 to this effect (Figure 4-4). There was no significant difference between the aspartate and the glutamate variant. Like the S429D variant, S429E substitution enhances UbcH5B-Ub binding affinity of the homodimer but not the heterodimer.

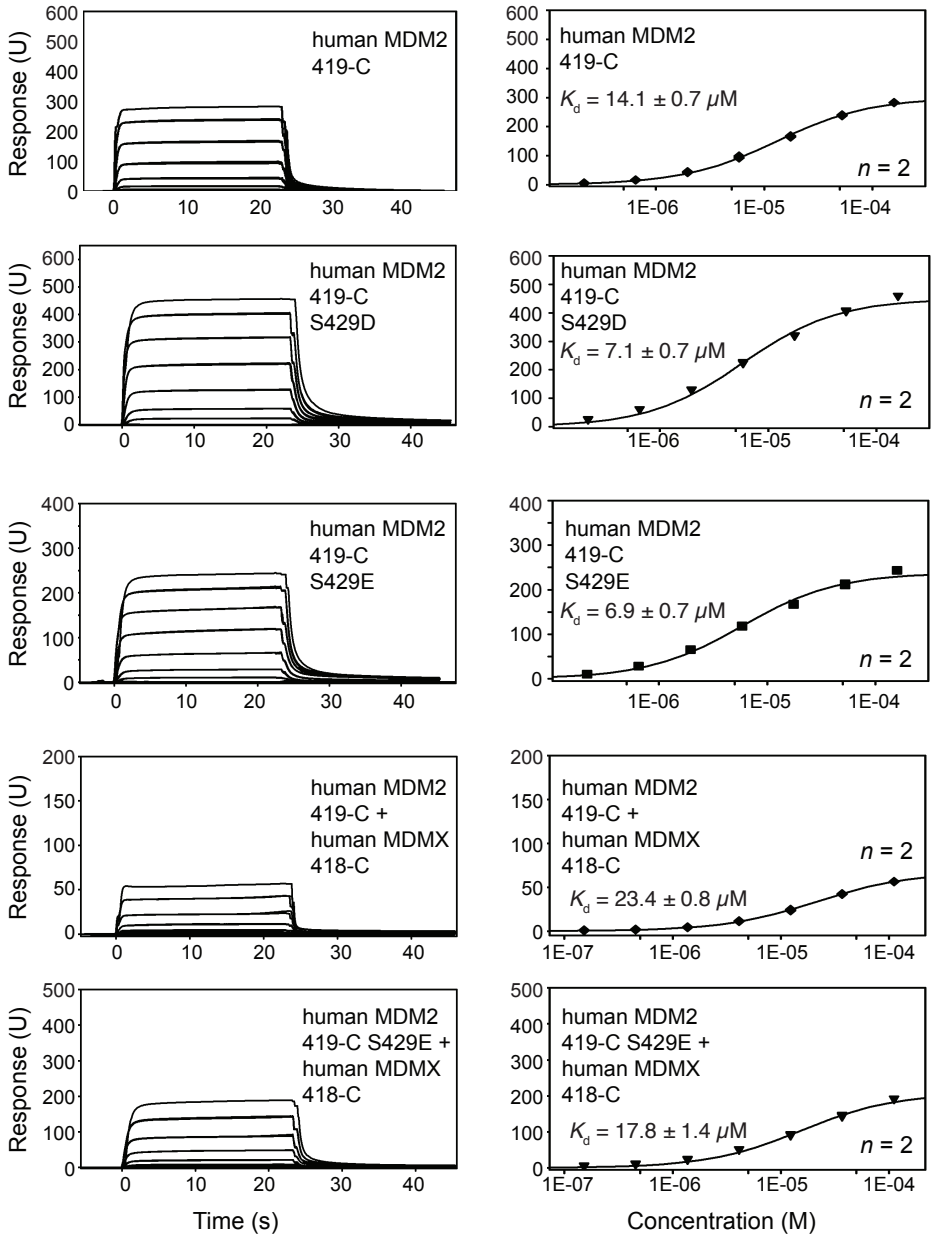

Figure 4-4: SPR binding analysis of MDM2^{G443T} 419-C variants for UbcH5B-Ub. MDM2^{G443T} 419-C S429D and S429E show a similar binding enhancement for UbcH5B-Ub as in MDM2 350-C. In contrast, a much weaker binding enhancement could be observed in the heterodimer.

4.1.2 Catalytic activity of phosphomimetic MDM2

Prior studies showed that ATM-mediated MDM2 phosphorylation reduced MDM2 oligomerisation and suggested that MDM2 becomes a monomer, which is catalytically inactive (Cheng et al., 2011). Contrary to this hypothesis, the UbcH5B-Ub binding enhancement observed for MDM2 '6D' and dimeric MDM2^{G443T} S429D/E suggests that MDM2 phosphomimetics are competent E3s and more active than the wild-type counterpart under single-turnover conditions. An autoubiquitination assay for MDM2 419-C^{G443T} (Figure 4-5A,B) and MDM2 419-C-

MDMX 418-C (Figure 4-5C,D) shows that the catalytic activity is indeed enhanced in the presence of the S429D and S429E mutations in the homodimer, whereas there is no difference in the heterodimer, which is in agreement with the binding analyses (Chapter 4.1.1). When the reaction is followed over time (Figure 4-5E,F), a two-fold increase in the rate of catalysis can be measured for the S429E variant but the nature of ubiquitination is not affected. For instance, the autoubiquitination products for MDM2 WT after 140 s appear similar to the reaction products of the S429E variant after 60-80 s.

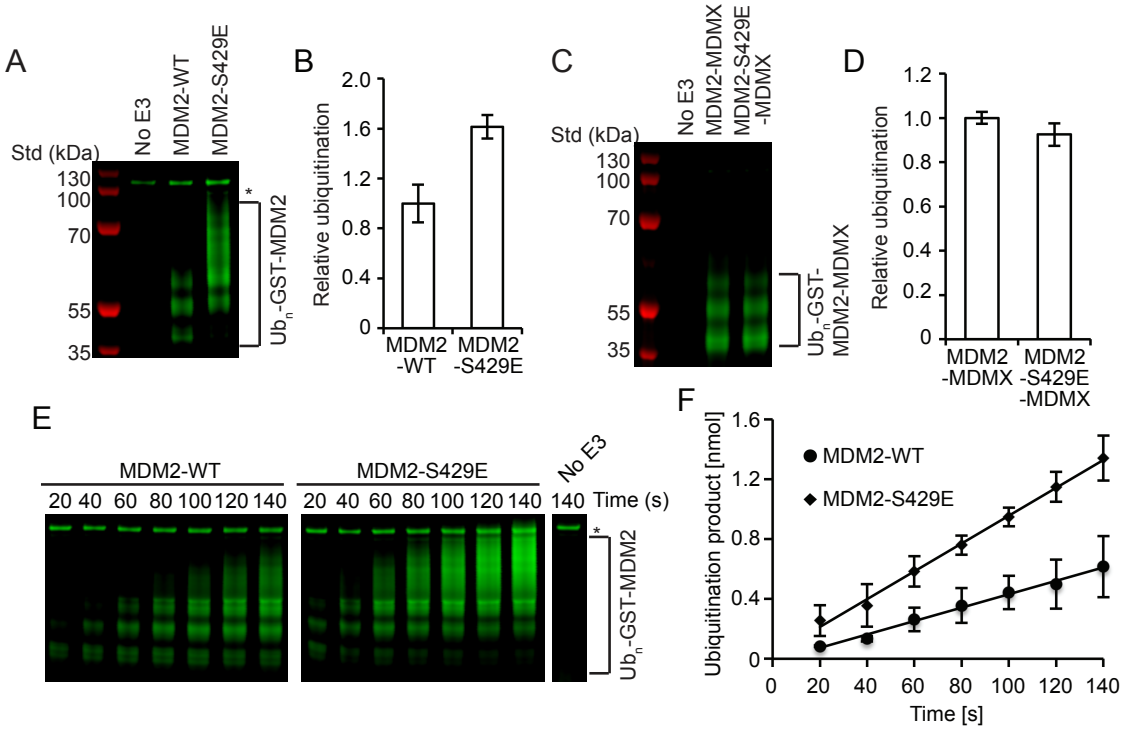

Figure 4-5: Autoubiquitination assay of MDM2^{G443T} S429E using fluorescently labelled Ub. (A) Reduced SDS-PAGE showing the autoubiquitination products of MDM2 variants after 90 s. (B) A bar graph showing the relative ubiquitination of MDM2 S429E in comparison to WT in (A). (C) Reduced SDS-PAGE showing the autoubiquitination products of MDM2-MDMX variants after 90 s. (D) A bar graph showing the relative ubiquitination of MDM2-S429E-MDMX in comparison to WT in (C). (E) Reduced SDS-PAGE showing the autoubiquitination reaction at a fixed UbcH5B concentration over time. (F) A plot showing the rate of ubiquitination as measured in (E). (*) indicates E1-Ub.

4.2 Structural characterisation of phosphomimetic MDM2

4.2.1 Crystallisation of MDM2 S429D

In order to understand the molecular basis for the homodimer specific catalytic activity boost, MDM2 419-C^{G443T} S429D was co-crystallised with UbcH5B-Ub. The purification procedure of this construct was similar to MDM2 419-C^{G443T}

(Chapter 3.4.2) and the S429D mutation did not change the elution profile of the protein. However, none of the 864 used crystallisation conditions (Table 2-3) promoted the growth of crystals.

4.2.2 Design of MDM2 S429E constructs with different N-terminal linkers

MDM2 419-C^{G443T} S429D did not yield diffracting crystals, although it was catalytically active, dimeric, and had a strong binding affinity for UbcH5B-Ub, which indicated that this construct would be suitable for crystallisation. The crystal structure of $MDM2^{f}$-UbcH5B-Ub (Figure 3-18) was very similar to the crystal structure of human MDM2 with UbcH5B-Ub (Figure 3-26), except for the missing N-terminal 3_{10}-helices. Despite the similarity, $MDM2^{f}$ crystallised in a different crystal form as human MDM2, for which itself two different crystal forms were obtained (Table 3-7 and Table 3-11). This shows that the MDM2-UbcH5B-Ub complex is able to crystallise in a variety of different ways and that small structural differences could facilitate additional crystallisation forms. S429 is conserved in $MDM2^{f}$. However, when this residue was mutated to glutamate, with the aim to mimic phosphorylation, no activity boost could be observed (Figure 4-6).

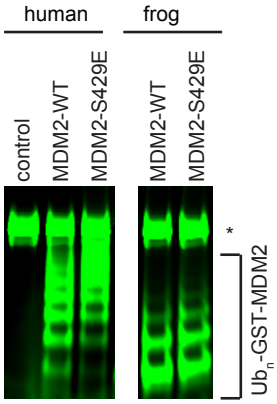

Figure 4-6: Autoubiquitination assay of $MDM2^{f}$ S429E using fluorescently labelled Ub. Reduced SDS-PAGE showing the autoubiquitination products of MDM2 variants after 90 s. The $MDM2^{f}$ S429E variant does not boost the activity like in human MDM2. (*) indicates E1-Ub.

Sequences of MDM2 RING domains from different species show a large variety at residues 422-435, where S429 is one of the more conserved residues, especially among mammalians (Table 3-3). Thus, MDM2 RING domain constructs from species with sequences that are different from human, frog and zebrafish might have different structural features, which could allow them to crystallise in

different forms. Sequences with a serine at position 429 were compared and selected as candidates for crystallisation purposes when they showed significant differences to each other and the sequences of the above-mentioned species (Table 4-1).

Table 4-1: Sequence of MDM2 423-435 from selected species. Species were selected where the sequence of residues 423-425 significantly differed from other sequences and where S429 was conserved.

	Residue (human nomenclature)												
Species	423	424	425	426	427	428	429	430	431	432	433	434	435
Human	E	E	S	V	E	S	S	L	P	L	N	A	I
Frog	D	E	S	M	E	P	S	L	P	L	T	S	V
Zebrafish	F	N	S	L	E	A	C	L	P	A	T	C	L
Cat	E	E	I	V	E	P	S	F	P	H	N	A	I
Galago	E	E	S	M	E	Y	S	F	P	L	S	A	T
Opossum	E	R	S	M	E	-	S	I	P	P	T	S	V
Turkey	E	E	G	M	E	S	S	L	P	V	S	S	I

The N-terminal linker sequences (residues 423-435, Table 4-1) of cat ($MDM2^{c}$), galago ($MDM2^{g}$), opossum ($MDM2^{o}$) and turkey ($MDM2^{t}$) were fused to human $MDM2^{G443T}$ 436-C as the RING domains were almost identical (Table 4-2), and sequence differences between human, frog and zebrafish did not perturb the fold of the RING dimer as shown in Chapter 3. S429 was substituted with glutamate to increase the sequence variation in comparison to human MDM2 S429D further as this variant was shown to cause a similar binding increase for E2-Ub (Figure 4-4).

Table 4-2: RING domain residues (436-C) of selected species that are not conserved in either human, frog or zebrafish MDM2.

Species	**Residues ≠ human, frog, zebrafish MDM2**
Cat	-
Galago	-
Opossum	P491L
Turkey	A460S, K464R, V486I, P491G

4.2.4 Crystallisation of MDM2 S429E

All four constructs were purified similarly to $MDM2^{G443T}$ (Chapter 3.4.2). They eluted as dimers from SEC except $MDM2^{o}$, where most of the protein eluted in the void volume so that only a small fraction of dimeric protein could be obtained. Upon concentrating, $MDM2^{g}$, $MDM2^{o}$ and $MDM2^{t}$ precipitated like $MDM2^{z}$ (Chapter 3.2.1), limiting the final concentration of these constructs. Only $MDM2^{c}$ could be concentrated to 1.9 mM without precipitation. Crystallisation attempts in complex with UbcH5B-Ub were undertaken in 288 conditions for all four constructs (Table 2-3). The initial screen yielded crystals for each construct (Figure 4-7), which were used for data collection without further optimisation. In total, six different datasets were obtained. $MDM2^{c}$ and $MDM2^{g}$ diffracted isomorphously (Table 4-3). The asymmetric unit contains two MDM2 dimers bound to two UbcH5B-Ub molecules each. Electron densities encompassing the region of residue 429 are visible in four copies of $MDM2^{c}$ and $MDM2^{g}$. For both, $MDM2^{o}$ (Table 4-4) and $MDM2^{t}$ (Table 4-5), two datasets were obtained. One crystal of each construct diffracted in the same unit cell (Crystals A) as $MDM2^{G443T}$-UbcH5B-Ub (Chapter 3.4.3, Crystal B), whereas the other two datasets was obtained for a unique crystal forms. Each unit cell contained one MDM2 dimer bound to two E2-Ub molecules and there was electron density up to residue 435 of $MDM2^{o/t}$ in all four crystal structures.

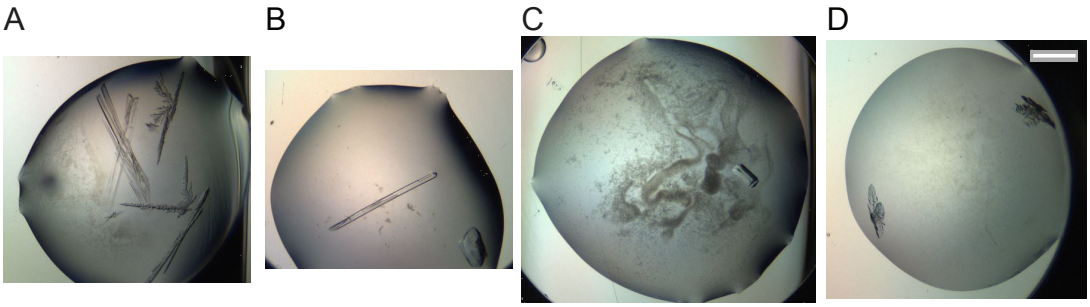

Figure 4-7: Crystals of MDM2 S429E from different species in complex with UbcH5B-Ub. The crystals diffracted to 1.6-2.2 Å. (A) $MDM2^{c}$. (B) $MDM2^{g}$. (C) $MDM2^{o}$ (Crystal A). (E) $MDM2^{t}$ (Crystal A).

Table 4-3: Data collection and refinement statistics for $MDM2^{c}$ S429E and $MDM2^{g}$ S429E in complex with UbcH5B-Ub. Numbers in parenthesis indicate the statistics for the outer shell.

Data collection		
Protein construct	$MDM2^{c}$ 422-C S429E, G443T + UbcH5B-Ub	$MDM2^{g}$ 422-C S429E, G443T + UbcH5B-Ub
Space group	P 1 2_1 1	P 1 2_1 1
Unit cell dimensions (a, b, c [Å] / α, β, γ [°])	57, 164, 71 / 90, 96, 90	56, 164, 71 / 90, 96, 90
Resolution [Å]	70.3-2.18 (2.22-2.18)	53.4-2.03 (2.07-2.03)
Unique reflections	65552	79887
R_{meas}	0.137 (0.990)	0.189 (1.088)
Mean I/ σ	9.4 (1.6)	5.7 (1.2)
$CC_{1/2}$	1 (0.6)	1 (0.5)
Completeness [%]	98.8 (98.3)	97.3 (97.3)
Multiplicity	3.4 (3.5)	3.3 (3.2)
Refinement		
Resolution [Å]	70.2-2.18	53.4-2.03
Unique reflections	62338	75906
R_{work} / R_{free}	0.178 / 0.239	0.233 / 0.278
Content of the asymmetric unit	2 dimer bound to 2 E2-Ub each	2 dimer bound to 2 E2-Ub each
Atoms (Protein)	9214	8974
Atoms (non protein)	8 (Zn^{2+}), 112 (Ethylene glycol), 353 (Water)	8 (Zn^{2+}), 8 (Ethylene glycol), 404 (Water)
B-factor (Protein)	37.94	34.2
B-factor (Zn^{2+})	26.94	24.57
B-factor (Ethylene glycol)	50.37	40.03
B-factor (Water)	33.39	34.43
Bond length RMSD [Å]	0.0089	0.0079
Bond angle RMSD [°]	1.650	1.458
Ramachandran outliers [%]	0.19	0
Rotamer outliers [%]	3.19	1.32
Clashscore	3.99	3.29
Molprobity score	1.86	1.42

Table 4-4: Data collection and refinement statistics for MDM2^{o} S429E in complex with UbcH5B-Ub. Numbers in parenthesis indicate the statistics for the outer shell.

Data collection		
Crystal name in this study	A	B
Space group	P 2_1 2_1 2	P 1 2_1 1
Unit cell dimensions (*a*, *b*, *c* [Å] / *α*, *β*, *γ* [°])	85, 131, 57 / 90, 90, 90	56, 56, 92 / 90, 97, 90
Resolution [Å]	71.4-1.49 (1.52-1.49)	50.4-1.62 (1.65-1.62)
Unique reflections	104080	70463
R_{meas}	0.049 (1.281)	0.111 (0.996)
Mean I/ σ	19.2 (1.1)	9.7 (1.1)
$CC_{1/2}$	1 (0.5)	1 (0.5)
Completeness [%]	100 (99.6)	97.6 (95.9)
Multiplicity	6.2 (4.5)	6.2 (3.0)
Refinement		
Resolution	71.4-1.49	50.5-1.62
Unique reflections	98889	66918
R_{work} / R_{free}	0.141 / 0.190	0.164 / 0.213
Content of the asymmetric unit	1 dimer bound to 2 E2-Ub	1 dimer bound to 2 E2-Ub
Atoms (Protein)	4568	4468
Atoms (non protein)	4 (Zn^{2+}), 4 (Cl^{-}), 44 (Ethylene glycol), 381 (Water)	4 (Zn^{2+}), 4 (Cl^{-}), 24 (Ethylene glycol), 227 (Water)
B-factor (Protein)	28.75	18.49
B-factor (Zn^{2+}, Cl^{-})	26.86	27.44
B-factor (Ethylene glycol)	49.14	40.33
B-factor (Water)	38.4	36.24
Bond length RMSD [Å]	0.0136	0.0076
Bond angle RMSD [°]	1.750	1.464
Ramachandran outliers [%]	0	0
Rotamer outliers [%]	0.39	0.80
Clashscore	4.29	2.65
Molprobity score	1.42	1.19

Table 4-5: Data collection and refinement statistics for $MDM2^t$ S429E in complex with UbcH5B-Ub. Numbers in parenthesis indicate the statistics for the outer shell.

Data collection		
Crystal name in this study	A	B
Space group	P 2_1 2_1 2	P 1
Unit cell dimensions (*a*, *b*, *c* [Å]/ *α*, *β*, *γ* [°])	85, 137, 57 / 90, 90, 90	51, 57, 61 / 67, 69, 87
Resolution [Å]	85.0-2.24 (2.28-2.24)	30.2-1.71 (1.74-1.71)
Unique reflections	32706	60435
R_{meas}	0.181 (1.606)	0.087 (0.791)
Mean I/ σ	7.6 (1.2)	9.4 (1.3)
$CC_{1/2}$	1 (0.5)	1 (0.7)
Completeness [%]	100 (99.3)	96.1 (94.7)
Multiplicity	6.4 (6.7)	1.8 (1.7)
Refinement		
Resolution [Å]	72.3-2.24	30.2-1.71
Unique reflections	31026	57471
R_{work} / R_{free}	0.205 / 0.255	0.191 / 0.221
Content of the asymmetric unit	1 dimer bound to 2 E2-Ub	1 dimer bound to 2 E2-Ub
Atoms (Protein)	4403	4454
Atoms (non protein)	4 (Zn^{2+}), 118 (Water)	4 (Zn^{2+}), 221 (Water)
B-factor (Protein)	28.72	36.58
B-factor (Zn^{2+})	33.55	29.39
B-factor (Water)	36.07	39.35
Bond length RMSD [Å]	0.0115	0.0088
Bond angle RMSD [°]	1.780	1.501
Ramachandran outliers	0	0
Rotamer outliers [%]	2.25	0.40
Clashscore	2.72	2.45
Molprobity score	1.66	1.19

4.2.5 Crystal structure of MDM2 S429E

The crystal structure of $MDM2^c$ S429E-UbcH5B-Ub (Figure 4-8A) is very similar to human MDM2-UbcH5B-Ub (RMSD of 0.3-0.4 Å for a single MDM2 molecule bound to E2-Ub). Thus, neither the sequence discrepancy nor the introduction of E429 affected the overall structure of the complex. For instance, F430 (L430 in human MDM2) is stabilised by hydrophobic interactions with proline residues of the second MDM2 protomer in a similar way as L430 in human MDM2 (Figure 4-8B). The sidechain of H432 does like L432 in human MDM2 not interact with any other residue, so that this residue can be neglected for the structure comparison, whereas the remaining two residues that are different between both human MDM2 and $MDM2^c$, S425I and S428P, lack electron density in the structure of human MDM2. E429 forms a hydrogen bond with the ε-amino group of Ub's K33 and interacts with the backbone amide group of Ub's T14 via a water molecule.

Although this does not change the positioning of E2-Ub relative to MDM2, it stabilises E2-Ub in the closed conformation and explains the enhanced binding affinity when S429 is mutated to aspartate or glutamate (Figure 4-4). Only one of the four MDM2 molecules in the asymmetric unit forms a hydrogen bond with K33. In the other three, the electron density for E429 sidechain was absent or the sidechain is not poised for a hydrogen bond interaction with Ub's K33. The distance between the C_α atoms of the corresponding E429 and the ε-amino group of K33 is 7.1 Å. In the other three molecules, E429 is slightly displaced, resulting in a distance of 7.9-8.8 Å between E429 (C_α) and K33 (ε-NH_2), which might not allow the formation of a stable hydrogen bond. In all MDM2 molecules, the position of the C_α atom of E429 appears to be locked in place by the adjacent P428 and F430, which form hydrophobic contact with P445 from the other MDM2 protomer. In the molecule where E429 and K33 form a hydrogen bond, there is additional electron density for residues 423-427, where these residues are stabilised via crystal contacts with a symmetry related UbcH5B molecule (Figure 4-8C). It is unclear whether the stabilisation of residues 423-427 via the crystal contact could influence the positioning of E429 to allow the formation of a hydrogen bond with K33.

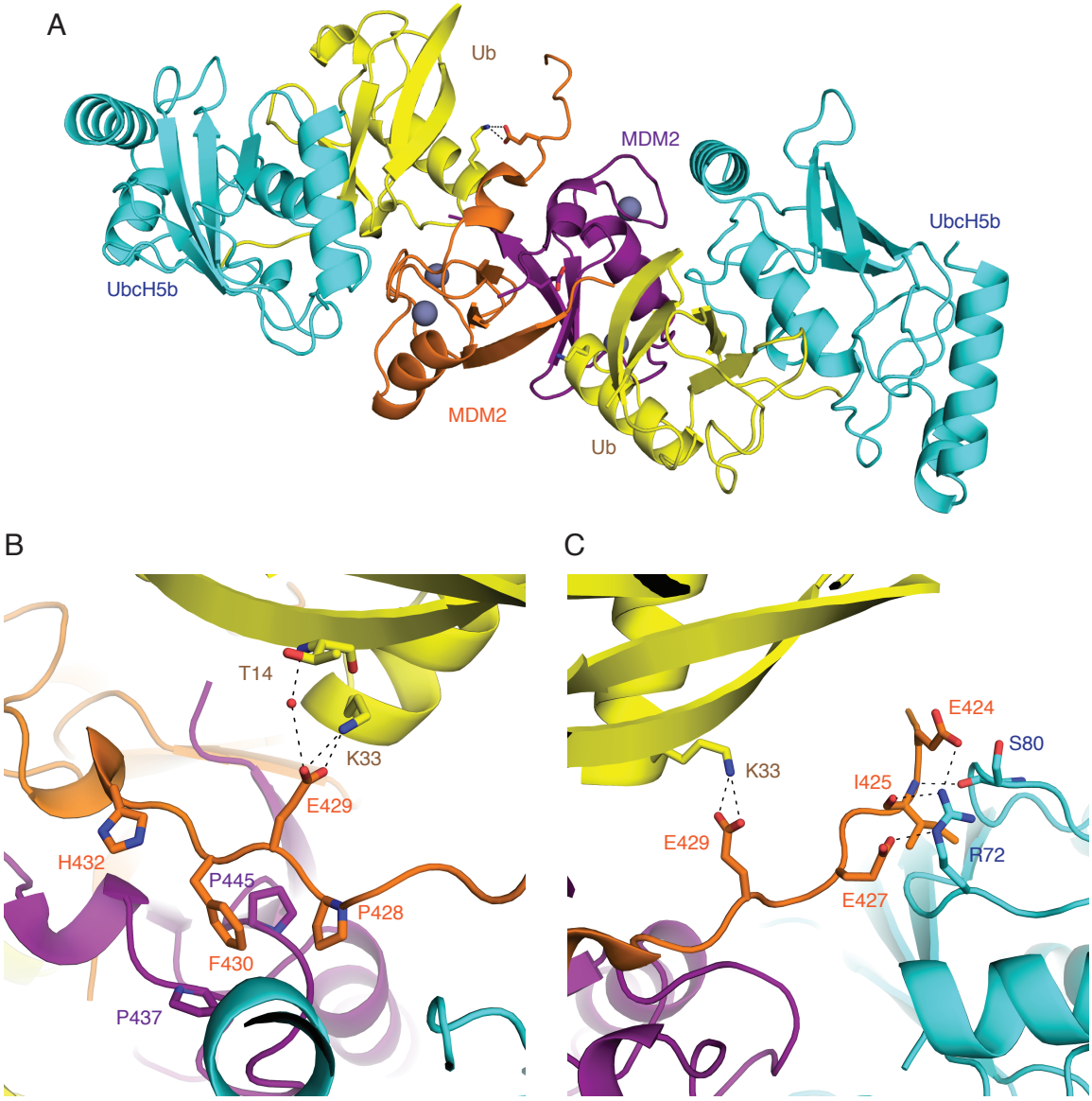

Figure 4-8: Crystal structure of MDM2^{c} S429E-UbcH5B-Ub. The crystal structure is very similar to human MDM2-UbcH5B-Ub. (A) Overall structure. (B) Close-up of MDM2's N-terminal residues. E429 interacts with Ub's K33 and T14 via a water molecule, thereby stabilising E2-Ub in the closed conformation. (C) Extensive crystal contacts with a symmetry related UbcH5B molecule stabilise residues E424-E427.

In the isomorphous crystal structure of MDM2^{g} S429E-UbcH5B-Ub (Figure 4-9A), there is no electron density for residues beyond E427 in any of the four MDM2 molecules. Similar to the MDM2^{c} S429E-UbcH5B-Ub structure, the C_{α} atom position of E429 is stabilised by the adjacent Y428 and F430, which form hydrophobic contact with P445 from the other MDM2 protomer (Figure 4-9B,C). MDM2^{g} contains a serine at position 425, which would clash with UbcH5B if it adopted a similar conformation as I425 in MDM2^{c} (Figure 4-8C). The region adopts a different conformation, where E427 forms a crystal contact with K144 of the same symmetry related UbcH5B molecule (Figure 4-9B). Consequently,

E429 is not stabilised as in MDM2^{c} and there is no electron density for the sidechain equivalent to the E429 in MDM2^{c} that formed a hydrogen bond with Ub's K33. In one of the four MDM2^{g} molecules, the electron density of the E429 sidechain is visible and forms a hydrogen bond with Ub's K33 (Figure 4-9C). In this MDM2^{g} molecule, the adjacent residues are not involved in crystal contacts. As the E429-K33 hydrogen bond was observed for crystallographic different MDM2 molecules in both structures, it is unlikely that it was an artefact introduced by crystal packing.

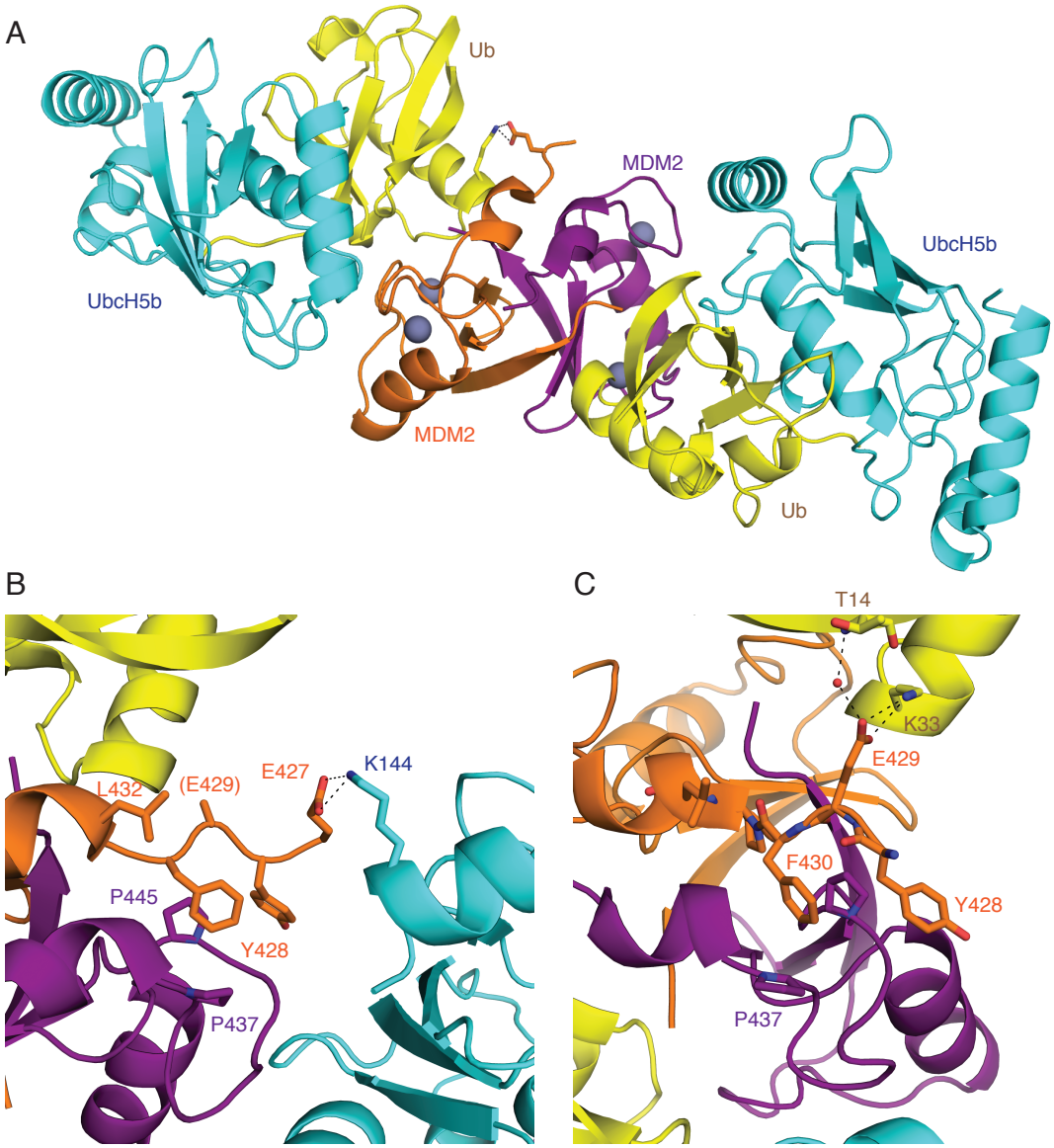

Figure 4-9: Crystal structure of MDM2^{g} S429E-UbcH5B-Ub. The crystal structure is isomorphous to MDM2^{c}-UbcH5B-Ub. (A) Overall structure. (B) Close-up of the MDM2 molecule (orange) that formed the E429-K33 hydrogen bond in MDM2^{c}. The sidechain of E429 is invisible so this residue was built with an alanine stub instead. E427 forms a hydrogen bond with K144 of a symmetry related UbcH5B molecule. (C) In another MDM2 molecule, E429 is able to interact with Ub's K33 and T14 like in MDM2^{c} although the N-terminal residues of this MDM2 molecule are not involved in crystal contacts.

In vitro assays and, for MDM2^{c}, SPR binding analysis, were performed to verify that the sequence differences did not affect the activity boost observed in the presence of S429E in human MDM2. In MDM2^{c}, the two-fold binding enhancement was conserved (Figure 4-10A) and the S429E variants showed a higher autoubiquitination activity than the wild-type for both, MDM2^{c} and MDM2^{g}, (Figure 4-10B).

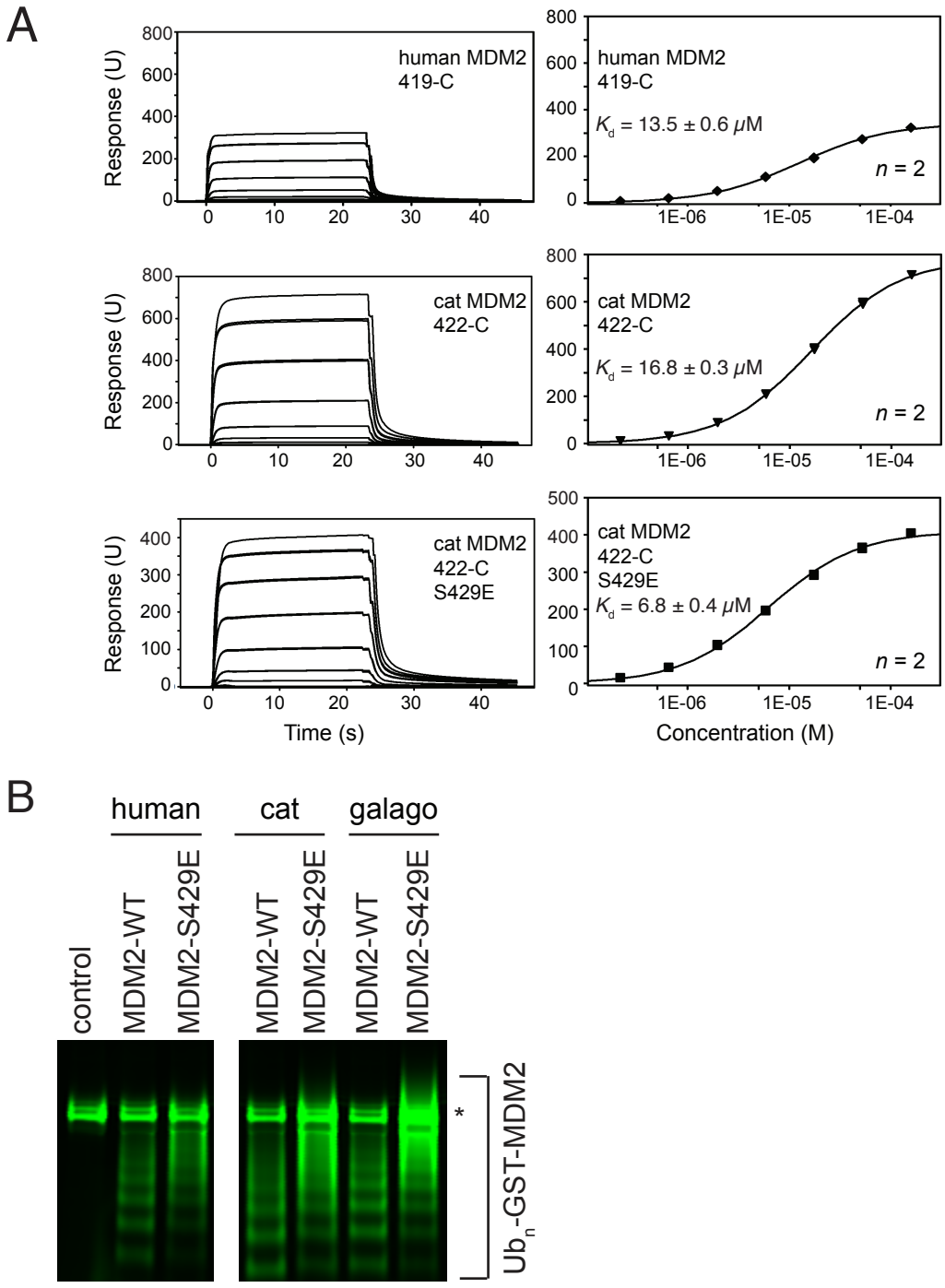

Figure 4-10: S429E has the same effect in MDM2^{c} and MDM2^{g} as in human MDM2. (A) SPR binding analysis of MDM2^{c} for UbcH5B-Ub. (B) Reduced SDS-PAGE showing the autoubiquitination products of MDM2 variants after 90 s using fluorescently labelled Ub. (*) indicates E1-Ub.

MDM2^{o} and MDM2^{t} formed similar complexes with UbcH5B-Ub. However, there was no electron density for residues beyond residue 435 in any of the crystal structures like observed in MDM2^{f} and MDM2^{z}. The used MDM2^{o} and MDM2^{t} constructs had the same sequence as human MDM2 for residues 436-C, so that sequence discrepancies within the RING domain could not have caused this difference. Furthermore, one crystal structure of each MDM2$^{o/t}$ was isomorphous with a crystal structure of human MDM2^{G443T}, where there was electron density up to L430 (Table 3-11, Crystal B). In case of MDM2^{t}, the crystals even grew in the same crystallisation condition as for human MDM2^{G443T}, making it unlikely that buffer mismatches accounted for the missing electron density for residues 430-434, which forms 3_{10}-helices in human MDM2. When the sequences of all species are compared for which crystal structures were obtained (Table 4-1), the formation of 3_{10}-helices adjacent to the RING domain correlates with the presence of an alanine at position 434. Wherever this residue was serine (MDM2^{f}, MDM2^{o}, MDM2^{t}) or cysteine (MDM2^{z}), the helices were missing. As there was no electron density for E429, MDM2^{o} and MDM2^{t} were not further used in this study.

4.3 Structural characterisation of phospho-MDM2

The crystal structure of MDM2 S429E raised the question whether the E429-K33 interaction would mimic S429-phosphorylated MDM2 (from here on denoted as 'phospho-MDM2'). In order to unveil the molecular basis of S429-based MDM2 phosphoregulation, phospho-MDM2 was generated in order to obtain the crystal structure in complex with E2-Ub.

4.3.1 Purification strategy

A methodology was required that would allow to specifically and effectively phosphorylate S429 to obtain enough homogeneous phospho-MDM2 for crystallisation purposes. The *O*-phosphoserine insertion system (Chapter 2.2.2) was used because it allows the expression of exclusively S429-phosphorylated MDM2, yielding in a purely phosphorylated protein as long as no dephosphorylation events occur. Human phospho-MDM2 was purified in small scale with a cleavable GST-fusion tag and the phosphorylation status was

verified by western blot with a pS429 specific antibody (Figure 4-11A). A large fraction of the expressed protein was terminated at residue 429, resulting in GST-TEV-MDM2 419-428 (Figure 4-11B), so that the activity could not directly be compared to wild-type MDM2 due to purity mismatches. Nevertheless, the binding affinity for UbcH5B-Ub could be measured using SPR because this technique is not affected by the purity of the protein (Figure 4-11C). The binding affinity is 2.7-fold higher than for wild-type MDM2 and comparable to MDM2 S429E, indicating that phosphorylation at position 429 has the same effect as substitution with a negatively charged residue. The absolute binding enhancement however needs to be treated with care as posttranslational dephosphorylation events or the incorporation of other amino acids might have occurred. Thus, the protein sample used for binding affinity measurements could consist of a mixture of phospho-MDM2, wild-type-MDM2, and species with and different amino acid substitutions at position 429, which might underestimate the real binding enhancement. The yield of the protein was very low, and since $MDM2^{C}$ had the highest stability of all purified MDM2 constructs, it was used for large-scale purification with the aim to obtain enough protein for crystallisation attempts. From an initial purification attempt, 0.2-0.3 mg of phospho-$MDM2^{C}$ could be obtained from 1 L TB. The cleaved protein eluted like $MDM2^{C}$ S429E as a dimer from SEC and phosphorylation was confirmed by western blot (Figure 4-11A). Mass spectrometry analysis confirmed that the protein was, as expected, exclusively phosphorylated at S429 although non-phosphorylated peptides were also detected. As no internal standard was available, the ratio of phospho-MDM2 could not be determined.

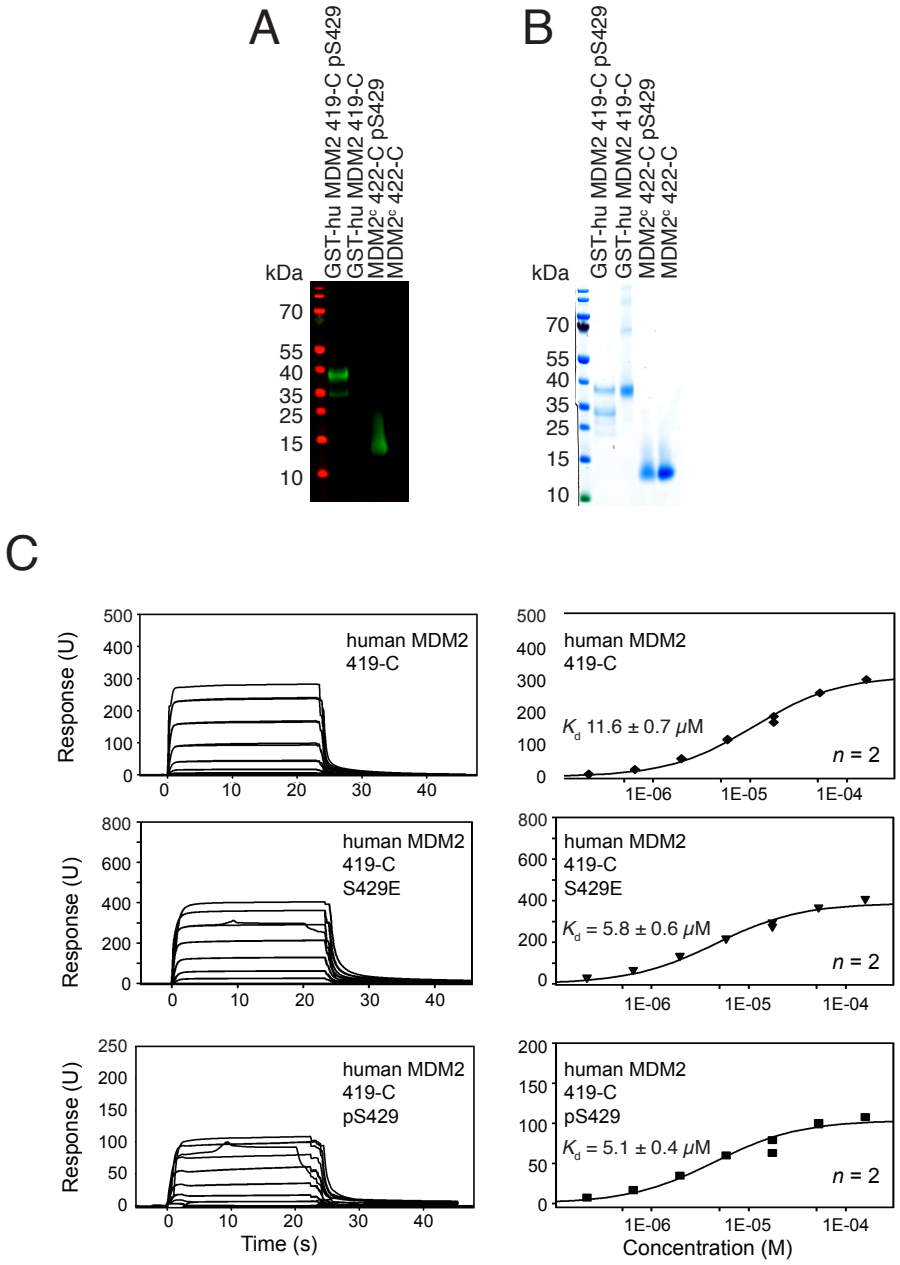

Figure 4-11: Effect of S429-phosphorylation on UbcH5B-Ub binding. (A) Western-blot of GST-phospho-MDM2 and phospho-MDM2^{c} using a pS429 specific antibody. (B) Coomassie-stained SDS-PAGE of the protein samples shown in (A). (C) SPR binding analysis of phospho-MDM2 for UbcH5B-Ub.

4.3.2 Initial crystallisation attempts

The low yield limited the amount of conditions that could be screened for crystallisation. Nevertheless, a single crystal (phospho-crystal A) could be obtained, which diffracted to 1.93 Å (Table 4-6).

Table 4-6: Data collection and refinement statistics for MDM2 pS429 (phospho-crystal A) in complex with UbcH5B-Ub. Numbers in parenthesis indicate the statistics for the outer shell.

Data collection	
Space group	P 1
Unit cell dimensions (a, b, c [Å] / α, β, γ [°])	56, 56, 97 / 95, 91, 90
Resolution [Å]	29.4-1.93 (1.98-1.93)
Unique reflections	84498
R_{meas}	0.119 (0.710)
Mean I/ σ	65.1 (1.0)
$CC_{1/2}$	0.9 (0.5)
Completeness [%]	95.5 (87.4)
Multiplicity	1.8 (1.8)
Refinement	
Resolution [Å]	29.4-1.93
Unique reflections	80340
R_{work} / R_{free}	0.251 / 0.293
Content of the asymmetric unit	2 dimers bound to 2 E2-Ub each
Atoms (Protein)	1612
Atoms (non protein)	4 (Zn^{2+})
B-factor (Protein)	23.6
B-factor (Zn^{2+})	17.8
Bond length RMSD [Å]	0.0089
Bond angle RMSD [°]	1.650
Ramachandran outliers [%]	0.09
Rotamer outliers [%]	2.76
Clashscore	3.88
Molprobity score	1.81

The unique crystal form contained two MDM2 dimers in the unit cell, each bound to two E2-Ub molecules. The overall structure was similar to all other MDM2-E2-Ub structures and there was electron density up to residues 428, 428, 429 and 430 in the four MDM2 molecules (Figure 4-12). However, there was no electron density for pS429 in any of the molecules, whereas a serine could be fitted into the map, suggesting that S429 was not phosphorylated. In fact, in one of the molecules (Figure 4-12 upper left), the distance between the sidechain of S429 and the ε-NH_2 of K33 was only 4.4 Å, which would have caused a clash if S429 was phosphorylated.

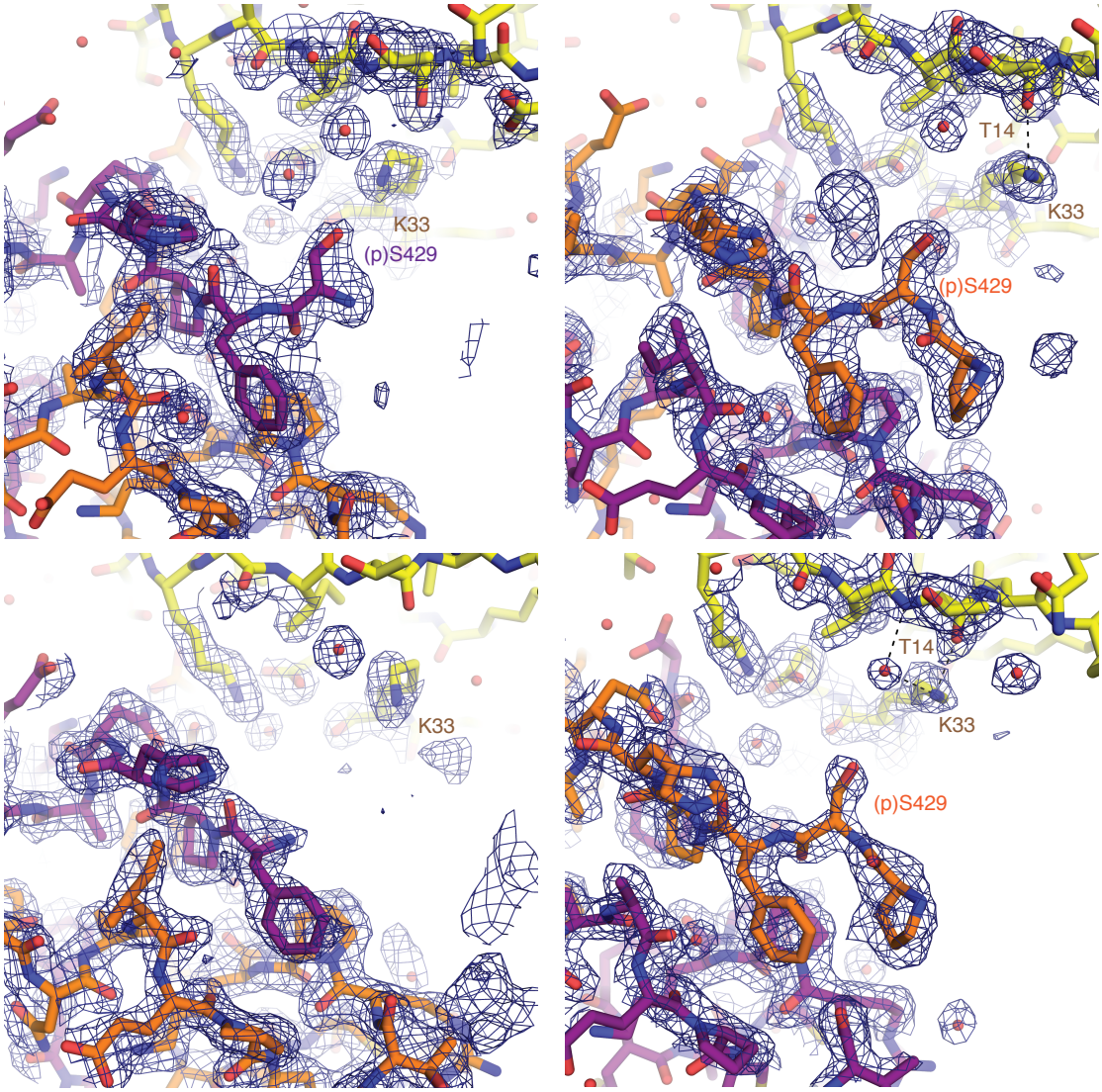

Figure 4-12: Position of (p)S429 in the crystal structure of phospho-MDM2^{c} in complex with UbcH5B-Ub (phospho-crystal A). The electron density map around residue 429, or if not visible, 430, is shown (radius: 10 Å). Hydrogen bonds formed by the ε-NH_2 of Ub's K33 are indicated with dashes.

There are three different explanations for the missing electron density of pS429. Based on mass spectrometric analysis, the protein was partly dephosphorylated so that (i) the abundance of phospho-MDM2 might have been too low to see electron density or (ii) the crystal form favoured incorporation of wild-type MDM2 over phosho-MDM2 as indicated by the low distance between S429 and K33 in one of the MDM2 molecules. Alternatively, (iii) the interaction between pS429 and E2-Ub might have been too weak in order to stabilise pS429 in a certain conformation in which case the missing electron density could be a consequence of the flexibility of pS429. This idea is partly supported by the crystal structures of MDM2 S429E, where only one of the four E429 sidechains interacted with Ub's K33 whereas the remaining sidechains adopted different conformations if they

were visible at all. To rule out this hypothesis, phospho-MDM2^{c} was crystallised with UbcH5B-Ub using seeds of MDM2^{c} S429E-UbcH5B-Ub crystals that were grown under the same crystallisation condition as the crystal used for the structure determination of this complex. Large, single crystals could be obtained, which diffracted to 1.38 Å (Table 4-7).

Table 4-7: Data collection and refinement statistics for MDM2^{c} pS429 (phospho-crystal B) in complex with UbcH5B-Ub. Numbers in parenthesis indicate the statistics for the outer shell.

Data collection	
Space group	P 1
Unit cell dimensions (a, b, c [Å] / α, β, γ [°])	55, 57, 61 / 67, 68, 90
Resolution [Å]	47.7-1.38 (1.40-1.38)
Unique reflections	119689
R_{meas}	0.128 (0.801)
Mean I/ σ	5.0 (1.0)
$CC_{1/2}$	1.0 (0.6)
Completeness [%]	93.7 (90.7)
Multiplicity	1.7 (1.6)
Refinement	
Resolution [Å]	47.7-1.38
Unique reflections	113802
R_{work} / R_{free}	0.181 / 0.226
Content of the asymmetric unit	1 dimer bound to 2 E2-Ub
Atoms (Protein)	4582
Atoms (non protein)	4 (Zn^{2+}), 8 (Ethylene glycol), 460 (Water)
B-factor (Protein)	21.48
B-factor (Zn^{2+})	19.57
B-factor (Ethylene glycol)	31.70
B-factor (Water)	34.32
Bond length RMSD [Å]	0.0142
Bond angle RMSD [°]	1.870
Ramachandran outliers [%]	0
Rotamer outliers [%]	0.58
Clashscore	2.71
Molprobity score	1.26

Surprisingly, the complex did not crystallise in the anticipated crystal form but in a different unit cell, which had been obtained for MDM2^{t}-UbcH5B-Ub (Table 4-5, Crystal B). The unit cell contained one dimer bound to two E2-Ub molecules. The structure of the complex was conserved, and electron density was observed for MDM2 428-C in both molecules (Figure 4-13). Although the distance between S429 and Ub's K33 (7.6-7.9 Å between the C_{α} atom of S429 and the N_{ε} atom of K33) was sufficient to accommodate phosphoserine, there was again only sufficient electron density to accommodate serine despite the high

resolution of this crystal structure. This suggests, together with the electron density map of the first crystal structure (Figure 4-12), that the abundance of pS429 was low.

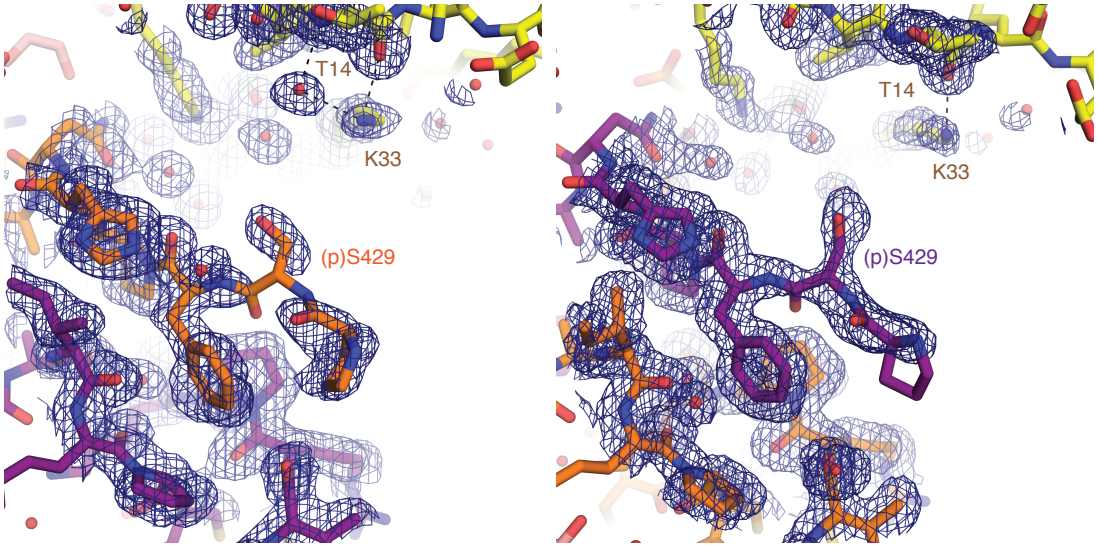

Figure 4-13: Position of (p)S429 in the crystal structure of phospho-MDM2^{C} in complex with UbcH5B-Ub (phospho-crystal B). The electron density map around residue 429 is shown (radius: 10 Å). Hydrogen bonds formed by the ε-NH_2 of Ub's K33 are indicated with dashes.

In order to increase the abundance of phospho-MDM2 in the sample, the dephosphorylation had to be minimised. Therefore, a purification protocol with higher amounts of phosphatase inhibitor was used ('batch 2', Chapter 2.3.2.6). Mass spectrometry analysis indicated that the fraction of phosphorylated protein following this protocol was 1.8-fold higher than in the initial purification attempt, based on the ratio between phospho-peptides and the corresponding native peptides in both samples. Crystals were screened under 192 different conditions (Table 2-3) and yielded a diffracting crystal of the same form as phospho-crystal B. The crystal structure was determined to 1.83 Å (Table 4-8).

Table 4-8: Data collection and refinement statistics for MDM2^{c} pS429 (phospho-crystal C) in complex with UbcH5B-Ub. Numbers in parenthesis indicate the statistics for the outer shell.

Data collection	
Space group	P 1
Unit cell dimensions (a, b, c [Å] / a, β, γ [°])	55, 56, 61 / 66, 69, 89
Resolution [Å]	429.2-1.82 (1.88-1.83)
Unique reflections	51864
R_{meas}	0.067 (0.893)
Mean I/ σ	10.2 (1.4)
$CC_{1/2}$	1.0 (0.5)
Completeness [%]	95.8 (82.3)
Multiplicity	1.8 (1.8)
Refinement	
Resolution [Å]	29.2-1.83
Unique reflections	49057
R_{work} / R_{free}	0.211 / 0.242
Content of the asymmetric unit	1 dimer bound to 2 E2-Ub
Atoms (Protein)	4507
Atoms (non protein)	4 (Zn^{2+}), 180 (Water)
B-factor (Protein)	38.35
B-factor (Zn^{2+})	28.80
B-factor (Water)	37.51
Bond length RMSD [Å]	0.0038
Bond angle RMSD [°]	1.271
Ramachandran outliers [%]	0
Rotamer outliers [%]	0.60
Clashscore	1.11
Molprobity score	1.09

4.3.3 Crystal structure of phospho-MDM2^{c}-UbcH5B-Ub

In this crystal structure, clear electron density for pS429 was visible at 1 σ level in the 2Fo-Fc map of the crystal structure of phospho-MDM2 bound to UbcH5B-Ub. pS429 forms a hydrogen bond with the ε-NH_2 group of K33 and indirectly with the backbone amide group of T14 via a water molecule, thereby stabilising Ub in the closed conformation (Figure 4-14A). This did not affect the overall structure of any of the proteins or their relative position towards each other; hence S429-phosphorylation does not introduce a conformational change (Figure 4-14B). The stabilisation mechanism is similar to the effect of E429 in the MDM2$^{c/g}$ S429E-UbcH5B-Ub complexes (Figure 4-8 and Figure 4-9), which can therefore be stated as phosphomimetic.

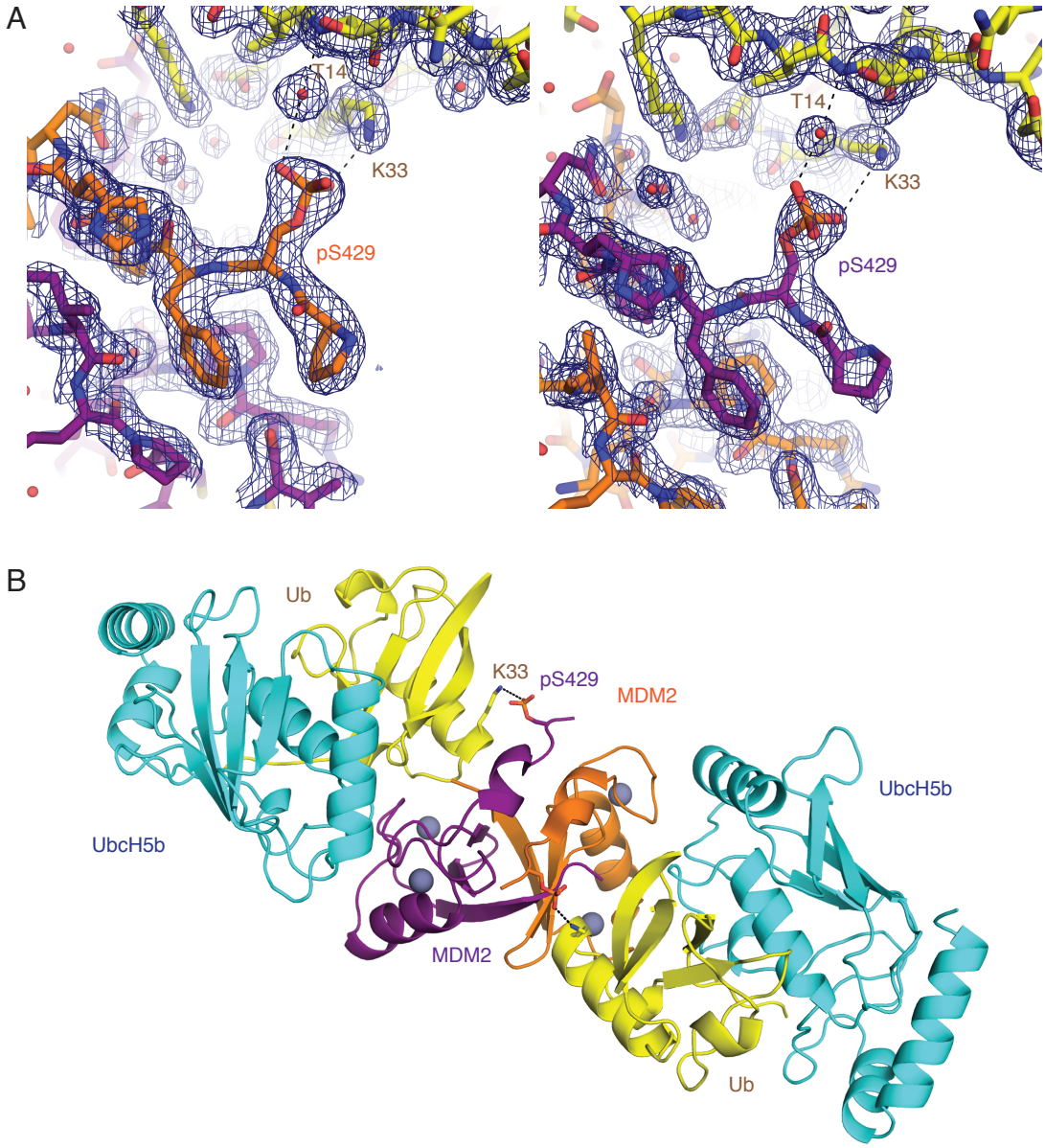

Figure 4-14: Crystal structure of phospho-MDM2^{C}-UbcH5B-Ub (phospho-crystal C). (A) Close-up view of pS429 and the local electron density map (radius: 10 Å). Hydrogen bonds are indicated with dashes. (B) Overall structure. pS429 and Ub's K33 are presented as sticks.

To verify that the pS429-K33 (E429-K33) hydrogen bond was responsible for the enhanced catalytic activity, an autoubiquitination assay was performed using MDM2 S429E mutant and Ub's K33 was mutated to methionine to disrupt the E429-K33 hydrogen bond without disturbing the hydrophobic environment surrounding Ub's K33. In agreement with the crystal structures, K33M completely abolished the activity boost of the phosphomimetic variant (Figure 4-15A,B). When the charges of S429E and K33 were swapped simultaneously by substituting S429 with arginine in MDM2 and K33 with glutamate in Ub, the activity boost could be restored (Figure 4-15C,D). In contrast, the S429R variant did not show

an enhanced catalytic activity in the presence of Ub^{WT} (Figure 3-31). This underscores that the hydrogen bond between MDM2's S429E (or pS429) and Ub's K33 promotes the catalytic activity of the MDM2 RING domain.

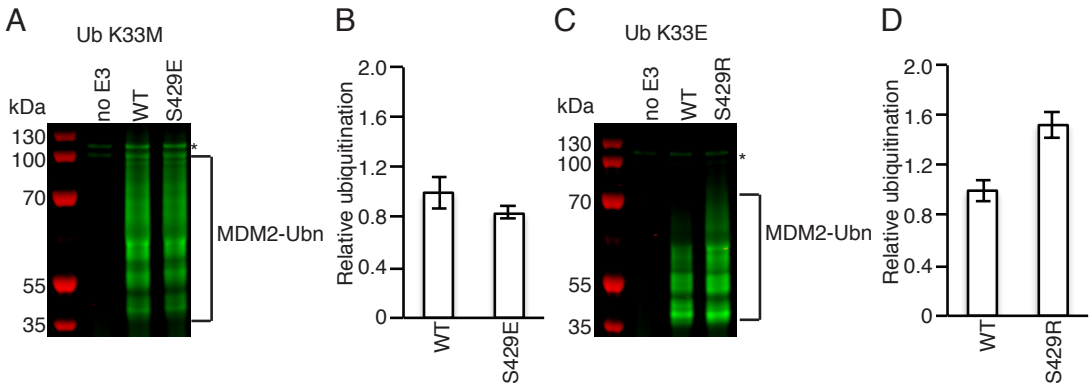

Figure 4-15: Autoubiquitination assay with perturbed E429-K33 interaction using fluorescently labelled Ub. (A) Reduced SDS-PAGE showing the autoubiquitination products of MDM2 variants with Ub K33M. (B) A bar graph showing the relative ubiquitination of MDM2 S429E in comparison to WT in (A). (C) Reduced SDS-PAGE showing the autoubiquitination products of MDM2 variants with Ub's K33E. (D) A bar graph showing the relative ubiquitination of MDM2 S429R in comparison to WT in (C). (*) indicates E1-Ub.

4.4 Structural difference between homodimer and heterodimer

4.4.1 Positioning of S429

The activity boost of MDM2 S429E was shown to be homodimer specific (Chapter 4.1), although MDM2 binds E2-Ub in a similar way in both dimers. Nevertheless, the arrangement of the N-terminal helices is slightly different as pointed out in Chapter 3.3.4. When the crystal structure of phospho-MDM2-UbcH5B-Ub is superimposed on MDM2-MDMX-UbcH5B-Ub (RMSD of 0.5 Å), it becomes evident why the phosphoregulation is homodimer specific, despite the apparent structural similarity (Figure 4-16). The elongated configuration of the 3_{10}-helix in the homodimer shifts MDM2's S429 by approximately 10 Å (based on the C_α atoms), thereby positioning it in a different environment. Thus, even when phosphorylated, heterodimeric MDM2 would not be able to form the same pS429-K33 interaction, which was crucial for the activity boost (Chapter 4.3.3).

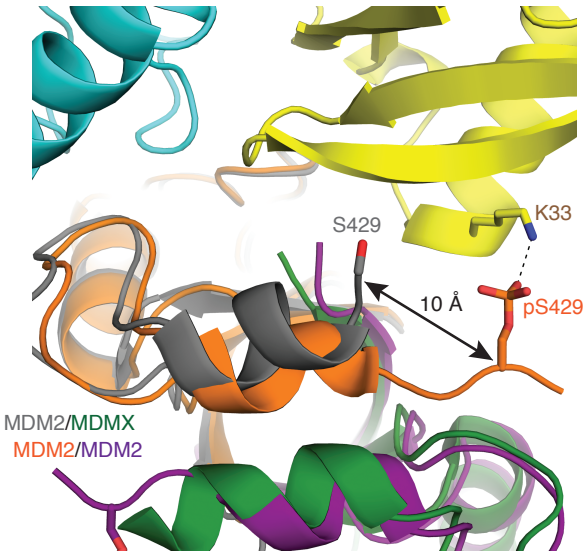

Figure 4-16: Superimposition of phospho-MDM2 and MDM2-MDMX in complex with UbcH5B-Ub. In the heterodimer, S429 is shifted by 10 Å, so that it cannot interact with Ub's K33, even if phosphorylated.

The precise positioning of S429 for its phosphoregulatory function is achieved by MDM2's adjacent 3_{10}-helices. When the helix formation is disrupted (A434R, I435R), the activity boost of the E429 variant can no longer be observed (Figure 4-17), consistent with the observations for MDM2^{f} (Figure 4-6), where the 3_{10}-helix was missing in all crystal structures.

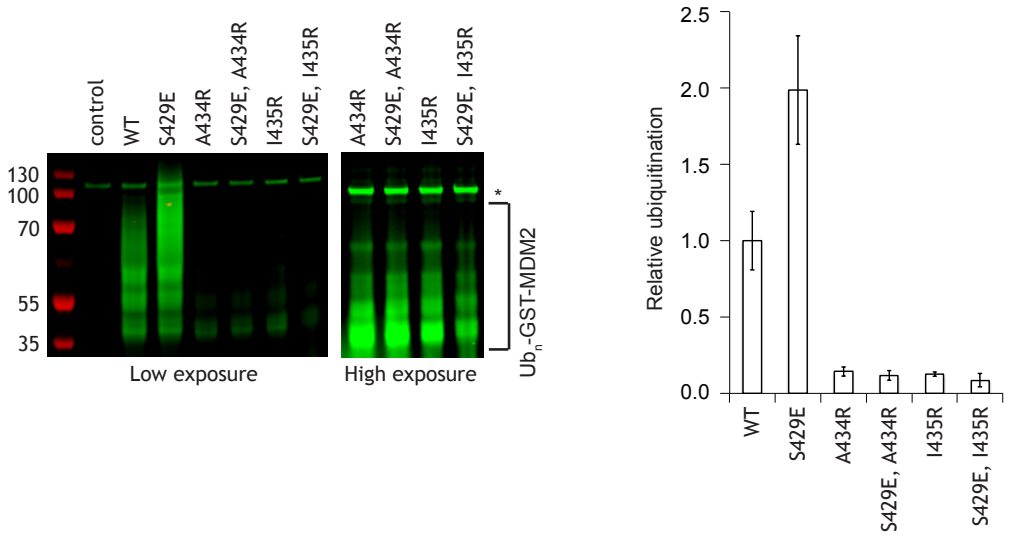

Figure 4-17: MDM2 autoubiquitination assay with disrupted 3_{10}-helices using fluorescently labelled Ub. (A) Reduced SDS-PAGE showing the autoubiquitination products of MDM2 variants. (*) indicates E1-Ub. (B) A bar graph showing the relative ubiquitination of the MDM2 variants in comparison to WT in (A).

The structural differences between the helices in both dimers are at least partly a consequence of the sequence discrepancy between the C-terminal residues of MDM2 and MDMX (Figure 3-26). Chimeras were created where MDM2's F490 and P491 were replaced with MDMX's I489 and A490 and vice versa with the aim to swap the specificity of the phosphoregulation towards the heterodimer (Figure 4-18). The E429-mediated activity boost of the homodimer was abolished when the C-terminal tail was mutated whereas a complementary substitution did not activate the heterodimer for phosphoregulation. This indicates that the C-terminal residues play a crucial role for the correct formation of the 3_{10}-helices in the homodimer. In the heterodimer, other residues that are different in MDMX such as L433 and L434 likely contribute to the formation of the N-terminal helices, so that a substitution of the C-terminal residues alone is not sufficient to transform them into exactly the same 3_{10}-helices as in the homodimer. Consequently, E429 is not positioned correctly to interact with K33 in MDM2-MDMX^{I489F,A490P}. Notably, the activity of the homodimer was reduced with C-terminal residues of MDMX whereas it was enhanced in the heterodimer with C-terminal residues of MDM2 in MDMX. This observation could be a consequence of a favourable hydrogen bond network, which was exclusively found in the presence of MDM2's C-terminal tail (Figure 3-26E).

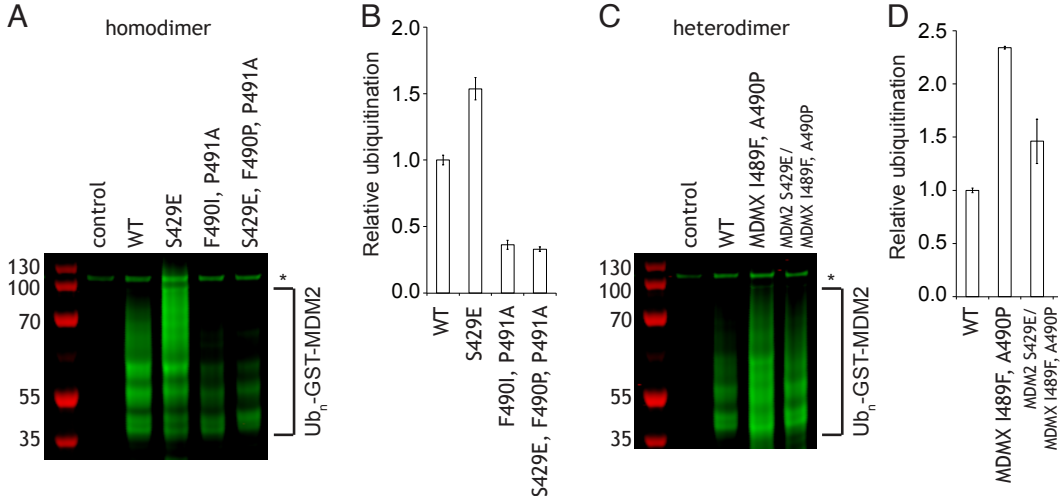

Figure 4-18: Homodimer and heterodimer autoubiquitination assay with modified C-terminal tail using fluorescently labelled Ub. (A) Reduced SDS-PAGE showing the autoubiquitination products of MDM2 homodimer variants. (B) A bar graph showing the relative ubiquitination of the MDM2 variants in comparison to WT in (A). (C) Reduced SDS-PAGE showing the autoubiquitination products of MDM2-MDMX variants. (D) A bar graph showing the relative ubiquitination of the MDM2-MDMX variants in comparison to WT in (C). (*) indicates E1-Ub.

To further validate the importance of the positioning of E429, alanine was inserted between S/E429 and L430 to shift residue 429 further away from Ub's K33 (Figure 4-19). The alanine insertion itself did not affect the catalytic activity of $MDM2^{WT}$, which is in agreement with the crystal structure of $MDM2^{WT}$-UbcH5B-Ub (Figure 3-26) where no electron was visible for residues beyond L430, suggesting that these residues might not contact UbcH5B-Ub. However, there was no activity boost for the E429 variant in the presence of the alanine insertion, which reinforces the importance of the precise positioning of this residue.

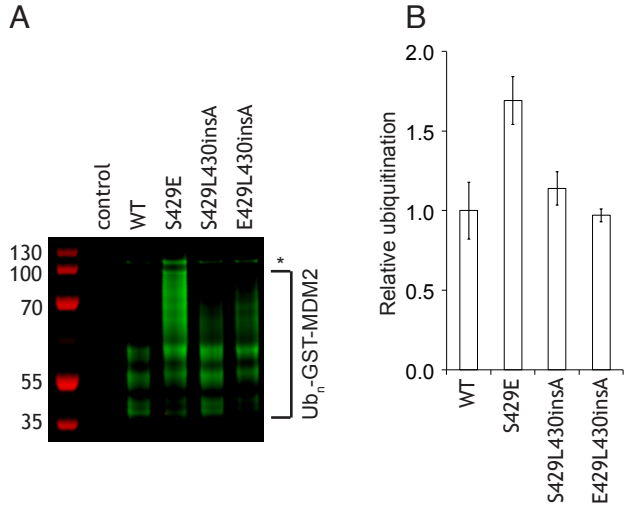

Figure 4-19: Homodimer and heterodimer autoubiquitination assay with misplaced S429 using fluorescently labelled Ub. (A) Reduced SDS-PAGE showing the autoubiquitination products of MDM2 variants. (*) indicates E1-Ub. (B) A bar graph showing the relative ubiquitination of the MDM2 variants in comparison to WT in (A).

4.4.2 Crystal structure of MDM2^{c} in the absence of UbcH5B-Ub

The MDM2-MDMX heterodimer undergoes a slight structural change upon binding to UbcH5B-Ub. In particular, the 3_{10}-helix of MDM2 transforms into a more compressed α-helix (Figure 4-20A,B), which allows N-terminal residues such as S429 to be positioned favourably for E2-Ub binding (Figure 4-20C).

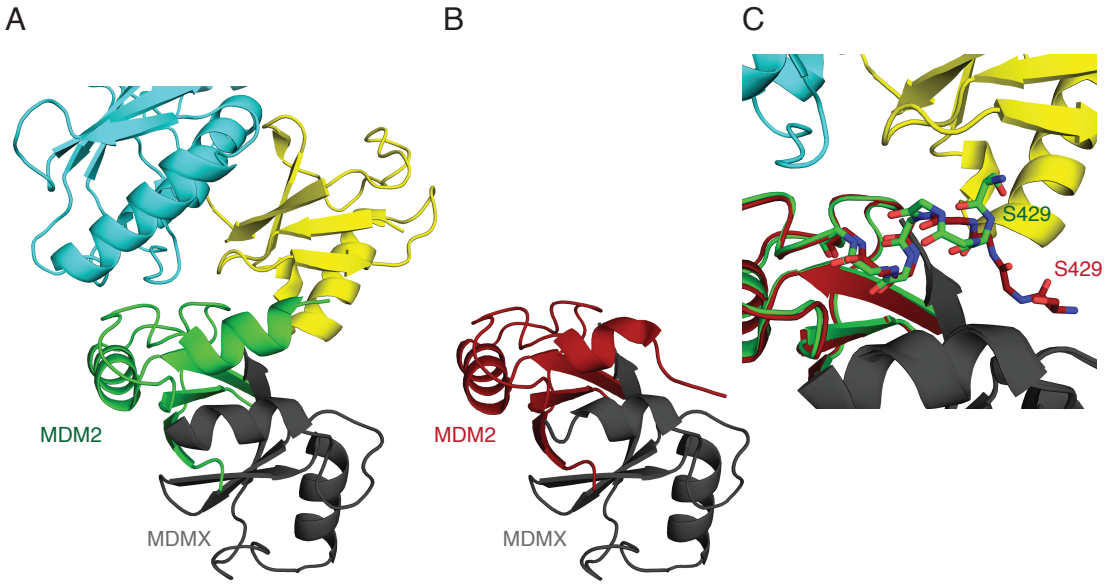

Figure 4-20: Crystal structure of the MDM2-MDMX heterodimer 428-C. (A) In complex with UbcH5B-Ub (PDB: 5MNJ). (B) In the absence of UbcH5B-Ub (PDB: 2VJF). (C) Superimposition of (A) and (B). Upon E2-Ub binding, the N-terminal 3_{10}-helix transforms into an α -helix, thereby bringing S429 closer to the donor-Ub.

It was not clear, whether the homodimer would also undergo a structural change upon E2-Ub binding. For instance, the 3_{10}-helices were not visible in the NMR model of human MDM2 and could have formed as a consequence of UbcH5B-Ub binding. Therefore, crystallisation attempts were performed for MDM2 by itself. Diffracting crystals were obtained for MDM2^{c} S429E in two very similar, but not identical crystal forms and the structures were determined to 1.21 and 1.19 Å (Table 4-9).

Table 4-9: Data collection and refinement statistics for MDM2^{C} S429E. Numbers in parenthesis indicate the statistics for the outer shell.

Data collection		
Crystal name in this study	A	B
Space group	P 1 2_1 1	P 1 2_1 1
Unit cell dimensions (*a*, *b*, *c* [Å]/ *α*, *β*, *γ* [°])	29, 40, 104 / 90, 93, 90	29, 40, 114 / 90, 94, 90
Resolution [Å]	23.5-1.21 (1.23-1.21)	37.3-1.19 (1.27-1.19)
Unique reflections	71820	71282
R_{meas}	0.148 (1.051)	0.055 (0.749)
Mean I/ σ	5.1 (1.1)	13.2 (1.3)
$CC_{1/2}$	1 (0.6)	1 (0.6)
Completeness [%]	98.1 (97.9)	92.3 (40.6)
Multiplicity	3.2 (3.1)	63.0 (2.1)
Refinement		
Resolution [Å]	23.5-1.21	37.3-1.19
Unique reflections	68138	67746
R_{work} / R_{free}	0.178 / 0.225	0.142 / 0.181
Content of the asymmetric unit	2 dimers	2 dimers
Atoms (Protein)	2040	2035
Atoms (non protein)	8 (Zn^{2+}), 2 (Cl^-), 4 (NO_3^-), 227 (Water)	8 (Zn^{2+}), 176 (Water)
B-factor (Protein)	14.35	17.26
B-factor (Zn^{2+}, Cl^-)	11.39	14.48
B-factor (NO_3^-)	42.09	-
B-factor (Water)	24.50	27.14
Bond length RMSD [Å]	0.0148	0.0168
Bond angle RMSD [°]	1.760	1.992
Ramachandran outliers	0	0
Rotamer outliers [%]	3.91	2.56
Clashscore	1.47	0.24
Molprobity score	1.71	1.28

There are two dimers in each unit cell, for which there was electron density up to residues E424 and E429 (crystal A, dimer 1), E424 and E427 (crystal A, dimer 2), E424 and F430 (crystal B, dimer 1), I425 and E429 (crystal B, dimer 2). The structures of each dimer (Figure 4-21A) were similar to each other (RMSD of 0.1-0.4 Å) and MDM2^{C} in the E2-Ub bound state (RMSD of 0.3 Å). The 3_{10}-helices were conserved and are thus a structural feature of the homodimer itself. In one of the eight MDM2^{C} molecules, F430 and P431 were not stabilised by hydrophobic residues of the second protomer (Figure 4-21B). In this molecule, residues 424-431 are oriented perpendicular to the 3_{10}-helices, which are not perturbed by this structural rearrangement.

When L430 is mutated to alanine, the autoubiquitination activity is not affected and the activity boost caused by the E429 variant is still present (Figure 4-21D),

suggesting that the stabilisation of L430 in its hydrophobic environment is not crucial for the ligase activity and the phosphoregulation.

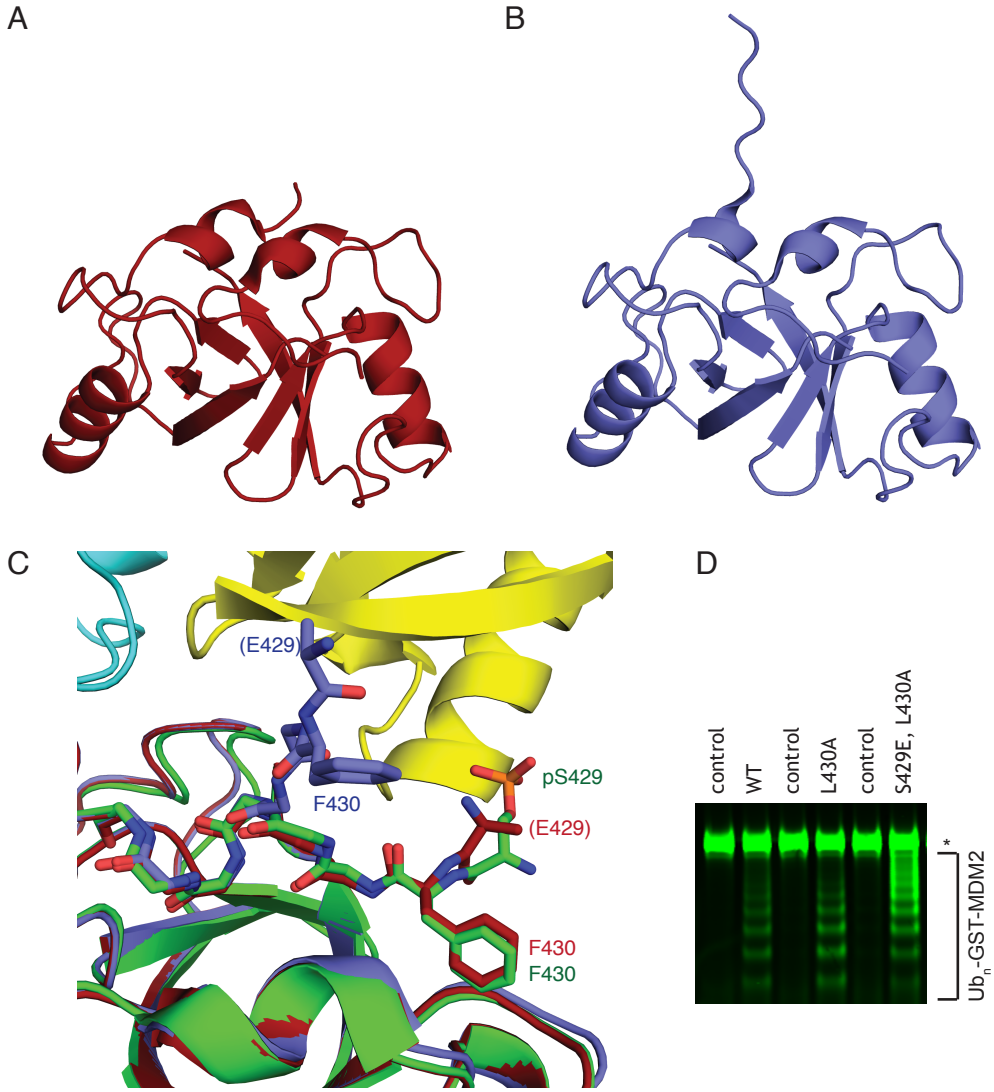

Figure 4-21: Crystal structure of MDM2^C S429E. (A) Crystal structure as in three out the four crystallographic independent dimers. (B) In the fourth dimer, one of the N-terminal extensions faces perpendicular to the helices. (C). Superimposition of (A) and (B) with phospho-MDM2-UbcH5B-Ub (phospho-crystal C, phospho-MDM2 is shown in green). The homodimer adopts an identical conformation in the presence of UbcH5B-Ub, as indicated by the position of F430. In the dimer shown in (B), F430 sits in a different environment, where it is no longer stabilised by hydrophobic residues of the second protomer. The sidechain for E429 was not visible in the absence of UbcH5B-Ub, so that alanine stubs were built instead. (D) Reduced SDS-PAGE showing the autoubiquitination products of MDM2 variants after 90 s. (*) indicates E1-Ub.

4.5 S429-phosphorylation in cells

A previous study had shown that p53 was stabilised in H1299 cells in the presence of phosphomimetic MDM2 S429D, and the authors reasoned that this observation was related to a reduced catalytic activity of this variant, which is in contrast to the data presented in this study (Cheng et al., 2011). In order to understand this discrepancy, the impact of the phosphomimetic mutations S429D and S429E was followed in cells. All cell-based experiments were performed by Dr Syed Feroj Ahmed. U2OS MDM2 knock-out cells with doxycycline-inducible p53 shRNA (U2OS^{mod}) were previously used to characterise the effects of E2-Ub disruptive mutations (I440K, R479A) on MDM2 and p53 stability in cells (Nomura et al., 2017). GFP-MDM2 S429D and S429E were overexpressed in USO2^{mod} cells the stability of these variants was compared to wild-type MDM2 in a cycloheximide chase experiment (Figure 4-22A). Both, S429D and S429E, were less stable than wild-type MDM2, which correlated with upregulated ubiquitination of these variants (Figure 4-22B). When I440K, a mutation that abolishes MDM2's ligase activity by disrupting E2-Ub binding (Nomura et al., 2017) (Figure 3-20), was introduced into MDM2 S429E, no autoubiquitination products were detected, indicating that the detected MDM2-Ub$_n$ species were MDM2 autoubiquitination products.

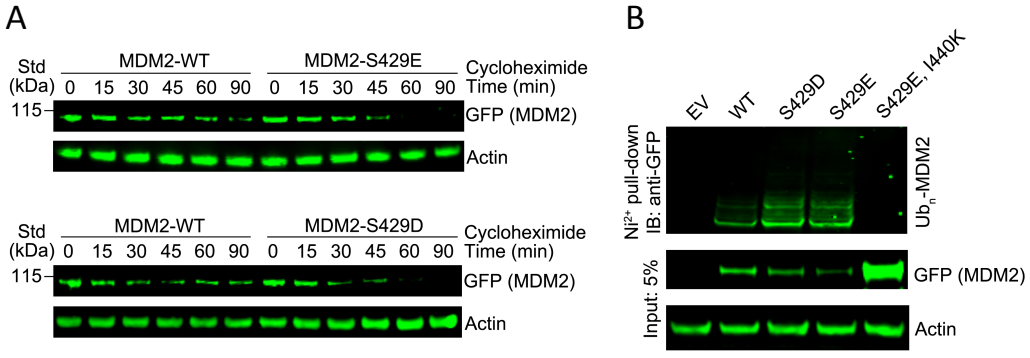

Figure 4-22: Stability and catalytic activity of phosphomimetic MDM2 variants in modified USOS cells. (A) Immunoblot showing the stability of GFP-MDM2 S429D and S429E after cycloheximide treatment for the indicated time, 24 h after transfection. (B) Immunoblot showing the ubiquitination of phosphomimetic MDM2 in cells that were additionally transfected with His-Ub and treated with MG132. The phosphomimetic variants show an enhanced ubiquitination, which is abolished in the presence of I440K, a mutation that disrupts E2-Ub binding. Hence, the Ub$_n$-MDM2 species are a product of MDM2 autoubiquitination. All experiments were performed by Dr Syed Feroj Ahmed.

In contrast, when GFP-MDM2 and Myc-p53 were simultaneously overexpressed in unmodified, endogenously MDM2 expressing U2OS cells, p53 and p21 levels were slightly higher in the presence of phosphomimetic MDM2, which shows that these MDM2 variants were, despite the higher catalytic activity for autoubiquitination, unable to destabilise p53 (Figure 4-23). Based on the crystal structures, there is no evidence for why S429D and S429E would exclusively promote MDM2's ubiquitination activity towards itself. It seems that these MDM2 variants stabilise p53 by initiating their own degradation before they are able to catalyse p53 ubiquitination. In the presence of I440K, p53 is even more stabilised due to the inability of this variant to recruit E2-Ub. Consequently, this variant lacks ligase activity even in the presence of phosphomimetic mutations, leading to enhanced MDM2 levels. Although p53 levels are higher in the presence of MDM2 I440K in comparison to the empty vector control, p21 levels are lower due to MDM2 accumulation and the ability of this variant to still bind p53, thereby blocking its transcriptional activity as observed previously (Nomura et al., 2017).

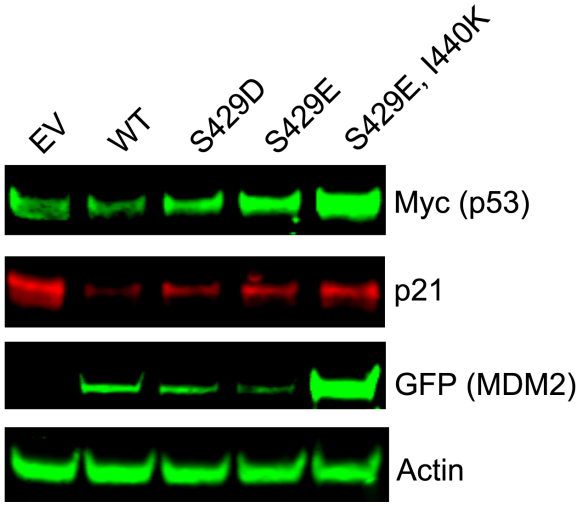

Figure 4-23: p53 is stabilised in the presence of phosphomimetic MDM2. Immunoblot showing p53 and p21 levels in the presence of phosphomimetic MDM2 in unmodified U2OS cells transfected with GFP-MDM2 and Myc-p53. The experiment was performed by Dr Syed Feroj Ahmed.

To find out whether the observations for MDM2 S429D and S429E were mimicking phospho-MDM2 in cells, U2OS^{mod} cells were treated with etoposide, a DNA damage inducing agent. Phosphorylation at S429 was confirmed by western-blot (Figure 4-24A) using a pS429-specific antibody (Figure 4-11) and MDM2 S429A as a negative control. Interestingly, low levels of phospho-MDM2 could be detected even without etoposide treatment, which was also observed for S395-

phosphorylation and could be associated with a basal activity of ATM in the absence of DNA damage (Carr et al., 2016). Under unstressed conditions, the S429A variant was as stable as wild-type MDM2 and had a comparable autoubiquitination activity (Figure 4-24B,C). However, upon etoposide treatment, wild-type MDM2 but not MDM2 S429A was less stable, correlating with upregulated ubiquitination as observed for phosphomimetic MDM2 (Figure 4-22B). Thus, S429-phosphorylation also promotes MDM2 ubiquitination in cells, demonstrating its phosphoregulatory function. Interestingly, MDM2 S429A showed a similar ubiquitination pattern, independently of etoposide treatment. Studies have shown that MDM2 gets phosphorylated at multiple residues between the zinc finger and the RING domain upon DNA damage (Chapter 1.3.3). Although no specific antibodies for other phosphorylation sites such as S386, S395, S407, T419 and S425 were used, it is likely that multiple phosphorylation on MDM2 had occurred. The fact that MDM2 S429A was not affected by the etoposide treatment indicates that phosphorylation at other residues is likely to have different purposes than altering MDM2's autoubiquitination activity or recruiting binding partners that would promote the ubiquitination of MDM2. Ultimately, specific antibodies would be required to study the effects of other phosphorylation sites in more detail, which might be cell type dependant and could be specific for a certain DNA damage inducing agent like γ-irradiation, which caused p53 to be stabilised by pS395-MDM2 in mice (Gannon et al., 2012).

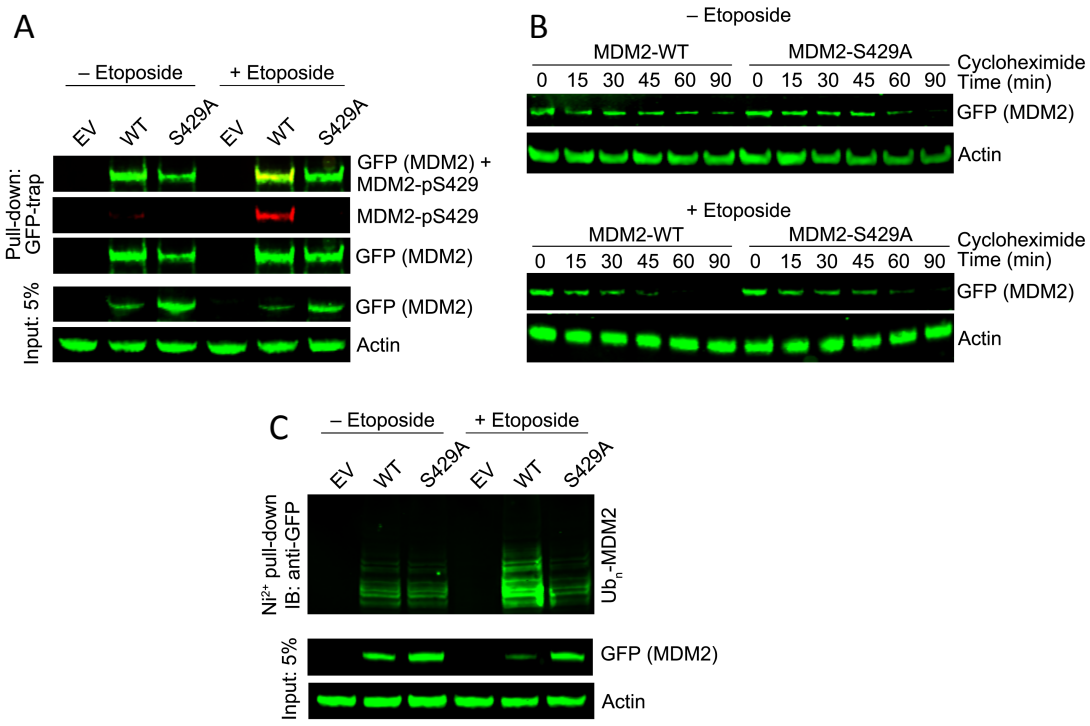

Figure 4-24: Effect of DNA damage on MDM2's stability and activity. (A) Immunoblot showing the stability of MDM2 under unstressed conditions, and etoposide treatment after cycloheximide treatment for the indicated time. (B) Immunoblot showing S429 phosphorylation in the absence and presence of etoposide treatment. (C) Immunoblot showing the ubiquitination of MDM2 in cells that were additionally transfected with His-Ub after etoposide treatment in the presence of MG132. All experiments were performed by Dr Syed Feroj Ahmed.

4.6 Crystal structure of MDM2 '5D1E' with UbcH5B-Ub

None of the experiments in this study was able to give a hint for the purpose of MDM2 phosphorylation near the RING domain other than S429-phosphorylation. Aspartic acid substitutions at other positions did not change E2-Ub binding (Chapter 4.1) or had an impact on MDM2 ubiquitination upon etoposide treatment in cells (Chapter 4.5). Secondary structure prediction suggests that the region between the zinc finger and the RING domain is disordered, which is in agreement with missing electron density for residues 380-435 in crystal structure of MDM2^{f} 389-C (Chapter 3.3.6). Crystal structures of the MDM2-UbcH5B-Ub complex were obtained in nine different forms throughout this study, and it was reasoned that this complex could also crystallise with longer MDM2 constructs, to obtain structural information for residues beyond S429 even if they were not involved in E2-Ub binding. This was achieved in the crystal structure of the TRAF6-UBE2N-Ub complex (Figure 1-9D), where electron density

for N-terminal zinc finger domains was observed although these were not involved in E2-Ub binding (Middleton et al., 2017). In an initial crystallisation attempt, human MDM2 350-C '6D' did not yield crystals in complex with UbcH5B-Ub, which was partly attributed to a low stability (Chapter 3.1.2). This construct was modified to enhance its stability (G443T), and additional amino acid substitutions were included that were favourable for the stabilisation of the dimer in other species (S428Y as in $MDM2^{g}$ and L430F as in $MDM2^{c/g}$). S429 was substituted with glutamate since the larger size in comparison to aspartate seemed to be favourable in the MDM2 S429E-UbcH5B-Ub complexes (hence MDM2 '5D1E'). To further promote crystallisation, slightly shorter constructs (363-C and 380-C) were used, which still contained all aspartate substitutions present in the initial 350-C construct. MDM2 380-C yielded diffracting crystals with UbcH5B-Ub and the crystal structure was determined to 1.95 Å (Table 4-10).

Table 4-10: Data collection and refinement statistics for MDM2 380-C '5D1E' in complex with UbcH5B-Ub. Numbers in parenthesis indicate the statistics for the outer shell.

Data collection	
Space group	C 1 2 1
Unit cell dimensions (a, b, c [Å] / α, β, γ [°])	125, 31, 78 / 90, 100, 90
Resolution [Å]	61.6-1.95 (1.98-1.95)
Unique reflections	22125
R_{meas}	0.136 (2.086)
Mean I/ σ	7.4 (1.3)
$CC_{1/2}$	1.0 (0.4)
Completeness [%]	99.5 (92.2)
Multiplicity	3.2 (3.3)
Refinement	
Resolution [Å]	61.6-1.95
Unique reflections	21018
R_{work} / R_{free}	0.202 / 0.247
Content of the asymmetric unit	1 MDM2 molecule bound to 1 E2-Ub
Atoms (Protein)	2242
Atoms (non protein)	2 (Zn^{2+})
B-factor (Protein)	36.66
B-factor (Zn^{2+})	28.58
Bond length RMSD [Å]	0.0077
Bond angle RMSD [°]	1.507
Ramachandran outliers [%]	0
Rotamer outliers [%]	1.22
Clashscore	4.90
Molprobity score	1.62

There is one MDM2 molecule bound to E2-Ub in the asymmetric unit, which forms a dimer with a crystallographic related MDM2 molecule. Despite the additional 40 residues in comparison to the MDM2 constructs present in the other crystal structures, no electron density was obtained beyond E427 (Figure 4-25A), demonstrating that this region is (i) most likely not involved in E2-Ub binding, as suggested by binding analysis experiments (Figure 4-1) and (ii) does not form any rigid structure as the N-terminal zinc fingers in TRAF6. In the crystal structure, two MDM2 dimers face towards each other with a gap of 37 Å between E427 of each molecule (Figure 4-25B). Additional 100 residues, 50 per molecule, had to be accommodated between both MDM2 molecules, requiring the N-terminal residues to be flexible in order to not clash. Due to limited space in the crystal, it is likely that the N-terminal residues of two adjacent MDM2 dimers interacted with each other in some way. However, the missing electron density indicates that this interaction did not occur in an ordered manner but was random instead. Notably, ($MDM2^{f}$ 389-C)-UbcH5B-Ub crystallised isomorphously, although 36 out of 56 residues beyond E436 were different in both species, including the five aspartate mutations that were only introduced in the human MDM2 construct. Thus, neither the sequence discrepancy, and associated with that the presence of the 3_{10}-helices in human MDM2, nor the introduction of aspartate residues had caused a significant structural change. It is possible that these residues require a particular binding partner in order to adopt a more ordered conformation and that this binding is altered upon DNA damage induced phosphorylation at one or multiple of the above-mentioned residues. Although no study has suggested a binding partner for the region between the zinc finger and the RING domain so far, it is possible that the linker dictates the relative orientation of those domains towards each other.

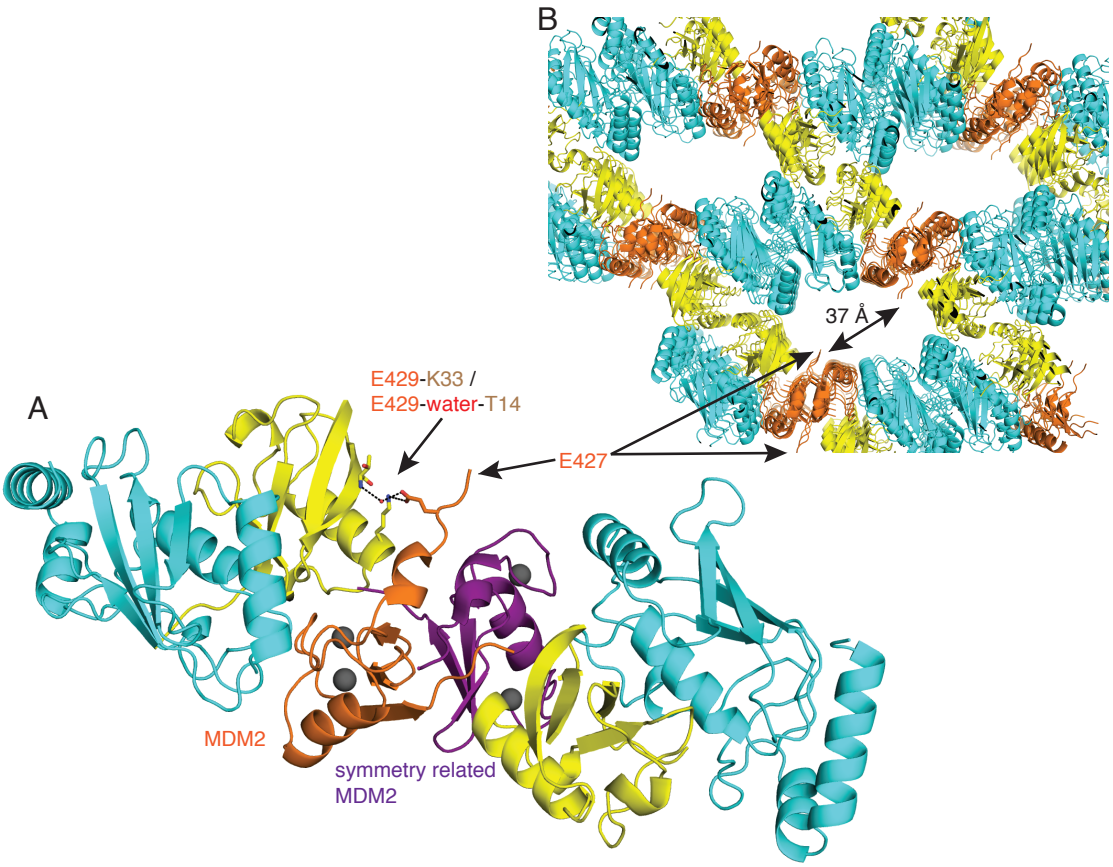

Figure 4-25: Crystal structure of MDM2 380-C S386D, S395D, S407D, T419D, S425D, S429E in complex with UbcH5B-Ub. (A) Overall structure. There is no electron density beyond E427 in MDM2. E429 interacts with Ub's K33 and T14 via a water molecule like in the crystal structures of MDM2^{c} and MDM2^{g}. The symmetry related MDM2 molecule is highlighted in purple. (B) Crystal packing. MDM2 dimers face towards each other, with a distance of 37 Å between E427 of two adjacent dimers.

4.7 Summary and Discussion

In this chapter, a novel mechanism for MDM2-phosphoregulation has been uncovered. Upon DNA damage (Chapter 4.5), S429 gets phosphorylated, which strengthens the interactions between MDM2 and E2-Ub in the closed, active conformation by forming a hydrogen bond with the donor-Ub's K33. This transiently boosts its catalytic activity, leading to upregulated autoubiquitination *in vitro* (Chapter 4.1.2) and in cells (Chapter 4.5).

The results suggest that pS429-MDM2 does not boost the ubiquitination of MDM2's main substrate, p53, in cells. S429-phosphorylation seems to be dependant on DNA damage (Figure 4-24), a scenario in which MDM2 is uncoupled from p53 by additional phosphorylation events within the N-terminal MDM2 binding domain of p53 (Shieh et al., 1997) (Chehab et al., 1999). Under these circumstances, MDM2 is not required anymore, in which case S429-phosphorylation might help cells to eliminate MDM2, for example to avoid off-target ubiquitination events. When the DNA damage response machinery has faded, new MDM2 molecules can be transcribed, which are not phosphorylated and therefore able to efficiently regulate p53. The data presented here do not give hints for the purpose of other phosphorylation sites such as S395, which was shown to stabilise p53 in mice (Gannon et al., 2012). Ubiquitination of MDM2 S429A was not upregulated upon etoposide treatment (Chapter 4.5). Although S395-phosphorylation was not confirmed and could be dependent on both, cell type and DNA damage inducing agent, it seems that the mechanism for how pS395 destabilises MDM2 is different. As this residue is further away from the RING domain than S429, it could be relevant for other domains or the interaction between different domains. Reports have shown that the acidic domain interacts with the RING domain (Leslie et al., 2015), and that this interaction is disturbed upon DNA damage.

Posttranslational modifications such as phosphorylation have been shown to be involved in a number of E3 ligases. In PARKIN (Gladkova et al., 2018) and CBL-B (Dou et al., 2012a), phosphorylation induces a large conformational change, which is required for catalysis since the non-phosphorylated enzyme adopts an autoinhibited conformation. In contrast, MDM2 already harbours a robust ligase activity in the non-phosphorylated state and does not require S429-phosphorylation under unstressed conditions for full activity. It seems that this

phosphorylation event is rather an evolutionary fine-tuning tool that has evolved as a DNA damage response to degrade MDM2 more efficiently under conditions where upregulated p53 activity is required. S429 is not exclusively conserved among all known MDM2 sequences (Table 3-3), supporting the hypothesis that it is not essential for MDM2's catalytic function in general. Various residues can be found at position 429 among different animal classes: Cysteine, histidine, tyrosine and serine in fish, serine in amphibia, glycine and serine in rodents, arginine in elephant, lysine in platypus, and serine in most other mammals. Thus, residue 429 did not seem to play an important role for MDM2's catalytic function from an evolutionary point of view, unlike most residues of the RING domain, which are strictly conserved among all known vertebrate MDM2 sequences. In this study, another related evolutionary tool of MDM2 has been identified: A 3_{10}-helix adjacent to the RING domain, which was observed for human, cat and galago MDM2 but was missing for frog, zebrafish, turkey and opossum MDM2. *In vitro* autoubiquitination assays demonstrated that precise positioning of S429 was a requirement for the phosphoregulatory property of this residue, and mutations perturbing the 3_{10}-helix abolished the effect. By comparing the sequences of the crystallised MDM2s, A434 was identified to be critical for the formation of the 3_{10}-helices and an arginine substitution at this position consistently not only reduced the autoubiquitination activity but also abolished the activity boost of the phosphomimetic S429 variant (Figure 4-17). In agreement with this observation, the phosphomimetic variant was unable to boost the activity of $MDM2^{f}$, where residue 434 is serine. A434 is only present in mammalian MDM2, and might be a pre-requirement for the phosphoregulation, which would explain why this mechanism does not seem to exist in other animal classes.

Chapter 5 Conclusion

RING E3 ligases catalyse Ub transfer by forming a complex with E2~Ub and the ubiquitination substrate where they act as the connecting puzzle piece for substrate specific Ub transfer. The efficiency of the ligase is strongly dependent on the precise positioning of E2~Ub in the closed conformation where Ub's C-terminus is placed favourably for substrate conjugation. Moreover, the binding affinity for the individual components, E2 and Ub, is often too weak to establish robust complex conformation in solution. RING E3s have evolved common features to stabilise E2~Ub such as the linchpin arginine (Pruneda et al., 2012) or residues that are complementary to E2's N-terminal α-helix and the adjacent loops, which include F62 and P95. These interactions are conserved in both, the MDM2 heterodimer, as shown before (Nomura et al., 2017), and the MDM2 homodimer as shown in this study (Figure 3-20). RING domains further contact and stabilise Ub, predominantly at its N-terminal loop including T9 and K11 and a hydrophobic patch around I36. While residues within the RING domain are important for Ub stabilisation, many RING E3s harbour additional residues outside the RING domain to further stabilise Ub. Dimeric RING E3s like RNF4 and BIRC7 often use the C-terminal tail of the second protomer and helices adjacent to the RING domain to stabilise Ub, and MDM2 follows the same trend. In these cases, perturbations of the C-terminal tail abolish the E3 ligase activity of most dimeric RING E3s. The relevance of the helical extensions for dimerisation and ligase activity is less characterised, but due to the large number of different helix patterns (Figure 1-9), it is likely that they can have different functions. The human MDM2 homodimer contains antiparallel 3_{10}-helical turns. Although they do not appear to be critical for dimerisation, they are important for the catalytic activity as they stabilise the C-terminus of the second protomer in a configuration that allows them to form hydrogen bonds with Ub's N-terminal loop. In addition, they place adjacent residues in a way that phosphorylation at S429 further stabilises Ub, thereby boosting MDM2's autoubiquitination activity. Phosphoregulation was also observed for the monomeric RING E3 CBL-B. However, in this case phosphorylation induces a global conformational change from an autoinhibited state into a catalytic active state. In contrast, phospho-MDM2 does not follow this 'off/on' mechanism but enhances the activity of an E3 that already has robust ligase activity. This observation appears to be

contradictory at first glance since phosphorylation occurs after DNA damage, a scenario in which MDM2's substrate p53 needs to be stabilised. A large number of phosphorylation events on both, p53 and MDM2, have been identified as a p53-stabilising DNA damage response (Chapter 1.3.3). Many of these events were associated with a reduced binding affinity between both proteins although it is difficult to judge their relative contribution to p53 stabilisation because p53 could still be stabilised when corresponding residues were mutated, suggesting that the mechanism might involve a high degree of redundancy. In this context, a plausible explanation for the role of pS429 could be that different phosphorylation events work in concert to shift MDM2's activity towards autoubiquitination due to the lack of efficient substrate recruitment. This allows a quick degradation of MDM2 molecules that are most likely heavily phosphorylated and thus inefficient in regulating p53. When the DNA damage response has abated, p53 needs to be tightly controlled again, which requires fully active MDM2 molecules that are free of unfavourable PTMs.

Why is the pS429-based phosphoregulation homodimer specific? From a structural point of view, this can be explained by the helix arrangement adjacent to the RING domain. MDMX stabilises MDM2's helix with residues that are different between the MDM homologues, resulting in the formation of a more rigid α-helix in MDM2 in the E2-Ub bound state of the heterodimer as demonstrated by the crystal structures. Taking into consideration that MDMX is already quickly degraded upon DNA damage, an additional activity boost might be redundant. Nonetheless, the data presented here do not rule out that the heterodimer could also be phosphorylated, although this effect would likely be irrelevant for E2-Ub recruitment.

In this study, nine crystal forms were obtained for MDM2 in complex with UbcH5B-Ub. E2-Ub is stabilised similarly in each of the 18 crystallographic unique complexes, independently of the sequence or the length of the crystallised MDM2 construct. Nevertheless, there are some minor differences, which can be illustrated by comparing the E2-Ub bound structures of $MDM2^{c}$ S429E (Figure 4-8, Table 4-3) and $MDM2^{c}$ (phospho-crystal B, Table 4-7) (Figure 5-1).

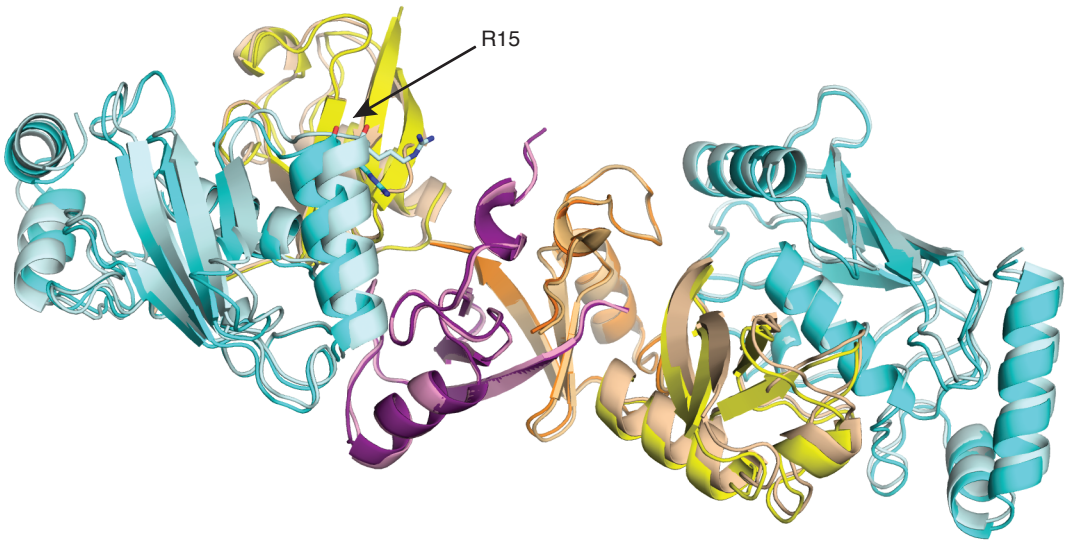

Figure 5-1: Superimposition of two MDM2-E2-Ub complexes with different E2 conformations. MDM2c S429E-UbcH5B-Ub is shown in purple/orange-cyan-yellow, MDM2c (p)S429-UbcH5B-Ub is shown in pale colours. Sidechains are shown for UbcH5B's R15.

Although both dimers adopt an identical fold, E2-Ub is slightly offset with the most pronounced difference for UbcH5B's N-terminal α-helix where R15 is shifted by 4.2 Å (based on the C_{α} atoms). However, this does not affect residues that have previously been shown to be critical for the activity of the heterodimer (Nomura et al., 2017). Furthermore, there was no correlation between UbcH5B's orientation and the corresponding MDM2 construct. In fact, the orientation could even be different for two E2-Ub molecules bound to the same dimer. A similar observation was made in two crystal structures of the RING E3 ligase cIAP in complex with UbcH5B-Ub, where E2-Ub was slightly tilted when the cIAPs were superimposed, thereby shifting $R15^{UbcH5B}$ by 3 Å (PDB: 3EB6 and 6HPR) (Mace et al., 2008) (Patel et al., 2019). Interestingly, the adjacent aspartate residue was shown to be important for backside binding of Ub in cIAP1, suggesting that E2-Ub might not be stabilised optimally in the absence of

the backside Ub (Buetow et al., 2015). Without backside binding, which was blocked in all structures presented here by $S22R^{UbcH5B}$, E2-Ub might have been partly trapped in slightly unfavourable orientations and these minimal differences could have accounted for the formation of the large number of different crystal forms and the absence of the $MDM2^{S429E}$-Ub^{K33} interaction in three out of four MDM2 molecules in each of the crystal structures of phosphomimetic MDM2 ($MDM2^{c}$ and $MDM2^{g}$) in complex with E2-Ub.

The crystal structures presented here unveil 3_{10}-helices as structural differences between the RING domains of the MDM2 homodimer and the MDM2-MDMX heterodimer. In both dimers, these helices are important for E2-Ub recruitment. Thus, they could serve as an interesting target for the design of homo- and heterodimer specific MDM2 RING domain inhibitors. Although it will be challenging to generate small molecules that exclusively target one of the two dimers, it might be possible to at least alter the relative activity of the two dimers in cells. Manipulating this ratio could be important in cells where either MDM2 or MDMX is overexpressed, a scenario in which the balance between the catalytic activities of both dimers is altered. MDM2 is also involved in the degradation of MDMX (Pan and Chen, 2003). Targeting the heterodimer only would allow the homodimer to still be able to ubiquitinate the heterodimer, resulting in stabilization of p53.

The structural basis of the phosphoregulatory mechanism sheds light on the function of phosphorylation near the RING domain, which had been discussed controversially, and could be valuable in diagnostics.

Bibliography

AICHEM, A., PELZER, C., LUKASIAK, S., KALVERAM, B., SHEPPARD, P. W., RANI, N., SCHMIDTKE, G. & GROETTRUP, M. 2010. USE1 is a bispecific conjugating enzyme for ubiquitin and FAT10, which FAT10ylates itself in cis. *Nat Commun,* 1**,** 13.

ARAMAYO, R., SHERMAN, M. B., BROWNLESS, K., LURZ, R., OKOROKOV, A. L. & ORLOVA, E. V. 2011. Quaternary structure of the specific p53-DNA complex reveals the mechanism of p53 mutant dominance. *Nucleic Acids Res,* 39**,** 8960-71.

ARAVIND, L. & KOONIN, E. V. 2000. The U box is a modified RING finger - a common domain in ubiquitination. *Curr Biol,* 10**,** R132-4.

ARRIGO, A. P., TANAKA, K., GOLDBERG, A. L. & WELCH, W. J. 1988. Identity of the 19S 'prosome' particle with the large multifunctional protease complex of mammalian cells (the proteasome). *Nature,* 331**,** 192-4.

ASHCROFT, M., KUBBUTAT, M. H. & VOUSDEN, K. H. 1999. Regulation of p53 function and stability by phosphorylation. *Mol Cell Biol,* 19**,** 1751-8.

BERNDSEN, C. E. & WOLBERGER, C. 2011. A spectrophotometric assay for conjugation of ubiquitin and ubiquitin-like proteins. *Anal Biochem,* 418**,** 102-10.

BLATTNER, C., HAY, T., MEEK, D. W. & LANE, D. P. 2002. Hypophosphorylation of Mdm2 augments p53 stability. *Mol Cell Biol,* 22**,** 6170-82.

BONNET, J., ROMIER, C., TORA, L. & DEVYS, D. 2008. Zinc-finger UBPs: regulators of deubiquitylation. *Trends Biochem Sci,* 33**,** 369-75.

BRADFORD, M. M. 1976. A rapid and sensitive method for the quantitation of microgram quantities of protein utilizing the principle of protein-dye binding. *Anal Biochem,* 72**,** 248-54.

BREMM, A., FREUND, S. M. & KOMANDER, D. 2010. Lys11-linked ubiquitin chains adopt compact conformations and are preferentially hydrolyzed by the deubiquitinase Cezanne. *Nat Struct Mol Biol,* 17**,** 939-47.

BROOKS, C. L. & GU, W. 2006. p53 ubiquitination: Mdm2 and beyond. *Mol Cell,* 21**,** 307-15.

BRZOVIC, P. S., LISSOUNOV, A., CHRISTENSEN, D. E., HOYT, D. W. & KLEVIT, R. E. 2006. A UbcH5/ubiquitin noncovalent complex is required for processive BRCA1-directed ubiquitination. *Mol Cell,* 21**,** 873-80.

BRZOVIC, P. S., RAJAGOPAL, P., HOYT, D. W., KING, M. C. & KLEVIT, R. E. 2001. Structure of a BRCA1-BARD1 heterodimeric RING-RING complex. *Nat Struct Biol,* 8**,** 833-7.

BUDHIDARMO, R., NAKATANI, Y. & DAY, C. L. 2012. RINGs hold the key to ubiquitin transfer. *Trends Biochem Sci,* 37**,** 58-65.

BUETOW, L., GABRIELSEN, M., ANTHONY, N. G., DOU, H., PATEL, A., AITKENHEAD, H., SIBBET, G. J., SMITH, B. O. & HUANG, D. T. 2015. Activation of a primed RING E3-E2-ubiquitin complex by non-covalent ubiquitin. *Mol Cell,* 58**,** 297-310.

CARR, M. I., RODERICK, J. E., GANNON, H. S., KELLIHER, M. A. & JONES, S. N. 2016. Mdm2 Phosphorylation Regulates Its Stability and Has Contrasting Effects on Oncogene and Radiation-Induced Tumorigenesis. *Cell Rep,* 16**,** 2618-2629.

CAVADINI, S., FISCHER, E. S., BUNKER, R. D., POTENZA, A., LINGARAJU, G. M., GOLDIE, K. N., MOHAMED, W. I., FATY, M., PETZOLD, G., BECKWITH, R. E., TICHKULE, R. B., HASSIEPEN, U., ABDULRAHMAN, W., PANTELIC, R. S.,

MATSUMOTO, S., SUGASAWA, K., STAHLBERG, H. & THOMA, N. H. 2016. Cullin-RING ubiquitin E3 ligase regulation by the COP9 signalosome. *Nature,* 531, 598-603.

CHANG, L. & BARFORD, D. 2014. Insights into the anaphase-promoting complex: a molecular machine that regulates mitosis. *Curr Opin Struct Biol,* 29, 1-9.

CHANG, Y. S., GRAVES, B., GUERLAVAIS, V., TOVAR, C., PACKMAN, K., TO, K. H., OLSON, K. A., KESAVAN, K., GANGURDE, P., MUKHERJEE, A., BAKER, T., DARLAK, K., ELKIN, C., FILIPOVIC, Z., QURESHI, F. Z., CAI, H., BERRY, P., FEYFANT, E., SHI, X. E., HORSTICK, J., ANNIS, D. A., MANNING, A. M., FOTOUHI, N., NASH, H., VASSILEV, L. T. & SAWYER, T. K. 2013. Stapled alpha-helical peptide drug development: a potent dual inhibitor of MDM2 and MDMX for p53-dependent cancer therapy. *Proc Natl Acad Sci U S A,* 110, E3445-54.

CHAO, C., HERR, D., CHUN, J. & XU, Y. 2006. Ser18 and 23 phosphorylation is required for p53-dependent apoptosis and tumor suppression. *EMBO J,* 25, 2615-22.

CHEHAB, N. H., MALIKZAY, A., STAVRIDI, E. S. & HALAZONETIS, T. D. 1999. Phosphorylation of Ser-20 mediates stabilization of human p53 in response to DNA damage. *Proc Natl Acad Sci U S A,* 96, 13777-82.

CHEN, J., WU, X., LIN, J. & LEVINE, A. J. 1996. mdm-2 inhibits the G1 arrest and apoptosis functions of the p53 tumor suppressor protein. *Mol Cell Biol,* 16, 2445-52.

CHEN, V. B., ARENDALL, W. B., 3RD, HEADD, J. J., KEEDY, D. A., IMMORMINO, R. M., KAPRAL, G. J., MURRAY, L. W., RICHARDSON, J. S. & RICHARDSON, D. C. 2010. MolProbity: all-atom structure validation for macromolecular crystallography. *Acta Crystallogr D Biol Crystallogr,* 66, 12-21.

CHEN, Y., FOKAR, M., KANG, M., CHEN, N., ALLEN, R. D. & CHEN, Y. 2018. Phosphorylation of Arabidopsis SINA2 by CDKG1 affects its ubiquitin ligase activity. *BMC Plant Biol,* 18, 147.

CHENG, Q. & CHEN, J. 2011. The phenotype of MDM2 auto-degradation after DNA damage is due to epitope masking by phosphorylation. *Cell Cycle,* 10, 1162-6.

CHENG, Q., CHEN, L., LI, Z., LANE, W. S. & CHEN, J. 2009. ATM activates p53 by regulating MDM2 oligomerization and E3 processivity. *EMBO J,* 28, 3857-67.

CHENG, Q., CROSS, B., LI, B., CHEN, L., LI, Z. & CHEN, J. 2011. Regulation of MDM2 E3 ligase activity by phosphorylation after DNA damage. *Mol Cell Biol,* 31, 4951-63.

CHENG, Q., SONG, T., CHEN, L. & CHEN, J. 2014. Autoactivation of the MDM2 E3 ligase by intramolecular interaction. *Mol Cell Biol,* 34, 2800-10.

CHIU, Y. H., SUN, Q. & CHEN, Z. J. 2007. E1-L2 activates both ubiquitin and FAT10. *Mol Cell,* 27, 1014-23.

CHUA, J. S., LIEW, H. P., GUO, L. & LANE, D. P. 2015. Tumor-specific signaling to p53 is mimicked by Mdm2 inactivation in zebrafish: insights from mdm2 and mdm4 mutant zebrafish. *Oncogene,* 34, 5933-41.

COOK, W. J., JEFFREY, L. C., CARSON, M., CHEN, Z. & PICKART, C. M. 1992. Structure of a diubiquitin conjugate and a model for interaction with ubiquitin conjugating enzyme (E2). *J Biol Chem,* 267, 16467-71.

CRAIG, A. L., BURCH, L., VOJTESEK, B., MIKUTOWSKA, J., THOMPSON, A. & HUPP, T. R. 1999. Novel phosphorylation sites of human tumour suppressor protein p53 at Ser20 and Thr18 that disrupt the binding of

mdm2 (mouse double minute 2) protein are modified in human cancers. *Biochem J,* 342 (Pt 1), 133-41.
DANG, J., KUO, M. L., EISCHEN, C. M., STEPANOVA, L., SHERR, C. J. & ROUSSEL, M. F. 2002. The RING domain of Mdm2 can inhibit cell proliferation. *Cancer Res,* 62, 1222-30.
DAVID, Y., ZIV, T., ADMON, A. & NAVON, A. 2010. The E2 ubiquitin-conjugating enzymes direct polyubiquitination to preferred lysines. *J Biol Chem,* 285, 8595-604.
DE POOT, S. A. H., TIAN, G. & FINLEY, D. 2017. Meddling with Fate: The Proteasomal Deubiquitinating Enzymes. *J Mol Biol,* 429, 3525-3545.
DESHAIES, R. J. & JOAZEIRO, C. A. 2009. RING domain E3 ubiquitin ligases. *Annu Rev Biochem,* 78, 399-434.
DICKENS, M. P., ROXBURGH, P., HOCK, A., MEZNA, M., KELLAM, B., VOUSDEN, K. H. & FISCHER, P. M. 2013. 5-Deazaflavin derivatives as inhibitors of p53 ubiquitination by HDM2. *Bioorg Med Chem,* 21, 6868-77.
DING, Q., ZHANG, Z., LIU, J. J., JIANG, N., ZHANG, J., ROSS, T. M., CHU, X. J., BARTKOVITZ, D., PODLASKI, F., JANSON, C., TOVAR, C., FILIPOVIC, Z. M., HIGGINS, B., GLENN, K., PACKMAN, K., VASSILEV, L. T. & GRAVES, B. 2013. Discovery of RG7388, a potent and selective p53-MDM2 inhibitor in clinical development. *J Med Chem,* 56, 5979-83.
DOLEZELOVA, P., CETKOVSKA, K., VOUSDEN, K. H. & ULDRIJAN, S. 2012. Mutational analysis of Mdm2 C-terminal tail suggests an evolutionarily conserved role of its length in Mdm2 activity toward p53 and indicates structural differences between Mdm2 homodimers and Mdm2/MdmX heterodimers. *Cell Cycle,* 11, 953-62.
DONEHOWER, L. A. 2014. Insights into wild-type and mutant p53 functions provided by genetically engineered mice. *Hum Mutat,* 35, 715-27.
DONG, Y., ZHANG, S., WU, Z., LI, X., WANG, W. L., ZHU, Y., STOILOVA-MCPHIE, S., LU, Y., FINLEY, D. & MAO, Y. 2019. Cryo-EM structures and dynamics of substrate-engaged human 26S proteasome. *Nature,* 565, 49-55.
DOU, H., BUETOW, L., HOCK, A., SIBBET, G. J., VOUSDEN, K. H. & HUANG, D. T. 2012a. Structural basis for autoinhibition and phosphorylation-dependent activation of c-Cbl. *Nat Struct Mol Biol,* 19, 184-92.
DOU, H., BUETOW, L., SIBBET, G. J., CAMERON, K. & HUANG, D. T. 2012b. BIRC7-E2 ubiquitin conjugate structure reveals the mechanism of ubiquitin transfer by a RING dimer. *Nat Struct Mol Biol,* 19, 876-83.
DOU, H., BUETOW, L., SIBBET, G. J., CAMERON, K. & HUANG, D. T. 2013. Essentiality of a non-RING element in priming donor ubiquitin for catalysis by a monomeric E3. *Nat Struct Mol Biol,* 20, 982-986.
DOVE, K. K., OLSZEWSKI, J. L., MARTINO, L., DUDA, D. M., WU, X. S., MILLER, D. J., REITER, K. H., RITTINGER, K., SCHULMAN, B. A. & KLEVIT, R. E. 2017. Structural Studies of HHARI/UbcH7 approximately Ub Reveal Unique E2 approximately Ub Conformational Restriction by RBR RING1. *Structure,* 25, 890-900 e5.
DROZDETSKIY, A., COLE, C., PROCTER, J. & BARTON, G. J. 2015. JPred4: a protein secondary structure prediction server. *Nucleic Acids Res,* 43, W389-94.
DUDA, D. M., BORG, L. A., SCOTT, D. C., HUNT, H. W., HAMMEL, M. & SCHULMAN, B. A. 2008. Structural insights into NEDD8 activation of cullin-RING ligases: conformational control of conjugation. *Cell,* 134, 995-1006.
EDDINS, M. J., VARADAN, R., FUSHMAN, D., PICKART, C. M. & WOLBERGER, C. 2007. Crystal structure and solution NMR studies of Lys48-linked tetraubiquitin at neutral pH. *J Mol Biol,* 367, 204-11.

ELENBAAS, B., DOBBELSTEIN, M., ROTH, J., SHENK, T. & LEVINE, A. J. 1996. The MDM2 oncoprotein binds specifically to RNA through its RING finger domain. *Mol Med,* 2**,** 439-51.

EMSLEY, P. & COWTAN, K. 2004. Coot: model-building tools for molecular graphics. *Acta Crystallogr D Biol Crystallogr,* 60**,** 2126-32.

EVANS, P. 2006. Scaling and assessment of data quality. *Acta Crystallogr D Biol Crystallogr,* 62**,** 72-82.

EVANS, P. R. & MURSHUDOV, G. N. 2013. How good are my data and what is the resolution? *Acta Crystallogr D Biol Crystallogr,* 69**,** 1204-14.

FAESEN, A. C., LUNA-VARGAS, M. P., GEURINK, P. P., CLERICI, M., MERKX, R., VAN DIJK, W. J., HAMEED, D. S., EL OUALID, F., OVAA, H. & SIXMA, T. K. 2011. The differential modulation of USP activity by internal regulatory domains, interactors and eight ubiquitin chain types. *Chem Biol,* 18**,** 1550-61.

FANG, S., JENSEN, J. P., LUDWIG, R. L., VOUSDEN, K. H. & WEISSMAN, A. M. 2000. Mdm2 is a RING finger-dependent ubiquitin protein ligase for itself and p53. *J Biol Chem,* 275**,** 8945-51.

GALLAGHER, E., GAO, M., LIU, Y. C. & KARIN, M. 2006. Activation of the E3 ubiquitin ligase Itch through a phosphorylation-induced conformational change. *Proc Natl Acad Sci U S A,* 103**,** 1717-22.

GANNON, H. S., WODA, B. A. & JONES, S. N. 2012. ATM phosphorylation of Mdm2 Ser394 regulates the amplitude and duration of the DNA damage response in mice. *Cancer Cell,* 21**,** 668-79.

GAO, S., PAN, M., ZHENG, Y., HUANG, Y., ZHENG, Q., SUN, D., LU, L., TAN, X., TAN, X., LAN, H., WANG, J., WANG, T., WANG, J. & LIU, L. 2016. Monomer/Oligomer Quasi-Racemic Protein Crystallography. *J Am Chem Soc,* 138**,** 14497-14502.

GLADKOVA, C., MASLEN, S. L., SKEHEL, J. M. & KOMANDER, D. 2018. Mechanism of parkin activation by PINK1. *Nature,* 559**,** 410-414.

HAAS, A. L. & ROSE, I. A. 1982. The mechanism of ubiquitin activating enzyme. A kinetic and equilibrium analysis. *J Biol Chem,* 257**,** 10329-37.

HAAS, A. L., WARMS, J. V., HERSHKO, A. & ROSE, I. A. 1982. Ubiquitin-activating enzyme. Mechanism and role in protein-ubiquitin conjugation. *J Biol Chem,* 257**,** 2543-8.

HALDEMAN, M. T., XIA, G., KASPEREK, E. M. & PICKART, C. M. 1997. Structure and function of ubiquitin conjugating enzyme E2-25K: the tail is a core-dependent activity element. *Biochemistry,* 36**,** 10526-37.

HAY, R. T. 2005. SUMO: a history of modification. *Mol Cell,* 18**,** 1-12.

HE, Y., TOLLINI, L., KIM, T. H., ITAHANA, Y. & ZHANG, Y. 2014. The anaphase-promoting complex/cyclosome is an E3 ubiquitin ligase for Mdm2. *Cell Cycle,* 13**,** 2101-9.

HEINEMANN, I. U., ROVNER, A. J., AERNI, H. R., ROGULINA, S., CHENG, L., OLDS, W., FISCHER, J. T., SOLL, D., ISAACS, F. J. & RINEHART, J. 2012. Enhanced phosphoserine insertion during Escherichia coli protein synthesis via partial UAG codon reassignment and release factor 1 deletion. *FEBS Lett,* 586**,** 3716-22.

HERHAUS, L., VAN DEN BEDEM, H., TANG, S., MASLENNIKOV, I., WAKATSUKI, S., DIKIC, I. & RAHIGHI, S. 2019. Molecular Recognition of M1-Linked Ubiquitin Chains by Native and Phosphorylated UBAN Domains. *J Mol Biol,* 431**,** 3146-3156.

HICKE, L. & DUNN, R. 2003. Regulation of membrane protein transport by ubiquitin and ubiquitin-binding proteins. *Annu Rev Cell Dev Biol,* 19**,** 141-72.

HIPP, M. S., KALVERAM, B., RAASI, S., GROETTRUP, M. & SCHMIDTKE, G. 2005. FAT10, a ubiquitin-independent signal for proteasomal degradation. *Mol Cell Biol,* 25**,** 3483-91.

HOEGE, C., PFANDER, B., MOLDOVAN, G. L., PYROWOLAKIS, G. & JENTSCH, S. 2002. RAD6-dependent DNA repair is linked to modification of PCNA by ubiquitin and SUMO. *Nature,* 419**,** 135-41.

HU, M., GU, L., LI, M., JEFFREY, P. D., GU, W. & SHI, Y. 2006. Structural basis of competitive recognition of p53 and MDM2 by HAUSP/USP7: implications for the regulation of the p53-MDM2 pathway. *PLoS Biol,* 4**,** e27.

HUANG, D. T., AYRAULT, O., HUNT, H. W., TAHERBHOY, A. M., DUDA, D. M., SCOTT, D. C., BORG, L. A., NEALE, G., MURRAY, P. J., ROUSSEL, M. F. & SCHULMAN, B. A. 2009. E2-RING expansion of the NEDD8 cascade confers specificity to cullin modification. *Mol Cell,* 33**,** 483-95.

HUANG, L., KINNUCAN, E., WANG, G., BEAUDENON, S., HOWLEY, P. M., HUIBREGTSE, J. M. & PAVLETICH, N. P. 1999. Structure of an E6AP-UbcH7 complex: insights into ubiquitination by the E2-E3 enzyme cascade. *Science,* 286**,** 1321-6.

HUANG, L., YAN, Z., LIAO, X., LI, Y., YANG, J., WANG, Z. G., ZUO, Y., KAWAI, H., SHADFAN, M., GANAPATHY, S. & YUAN, Z. M. 2011. The p53 inhibitors MDM2/MDMX complex is required for control of p53 activity in vivo. *Proc Natl Acad Sci U S A,* 108**,** 12001-6.

IKEDA, F. & DIKIC, I. 2008. Atypical ubiquitin chains: new molecular signals. 'Protein Modifications: Beyond the Usual Suspects' review series. *EMBO Rep,* 9**,** 536-42.

IM, E. & CHUNG, K. C. 2015. Dyrk1A phosphorylates parkin at Ser-131 and negatively regulates its ubiquitin E3 ligase activity. *J Neurochem,* 134**,** 756-68.

INUZUKA, H., TSENG, A., GAO, D., ZHAI, B., ZHANG, Q., SHAIK, S., WAN, L., ANG, X. L., MOCK, C., YIN, H., STOMMEL, J. M., GYGI, S., LAHAV, G., ASARA, J., XIAO, Z. X., KAELIN, W. G., JR., HARPER, J. W. & WEI, W. 2010. Phosphorylation by casein kinase I promotes the turnover of the Mdm2 oncoprotein via the SCF(beta-TRCP) ubiquitin ligase. *Cancer Cell,* 18**,** 147-59.

ITAHANA, K., MAO, H., JIN, A., ITAHANA, Y., CLEGG, H. V., LINDSTROM, M. S., BHAT, K. P., GODFREY, V. L., EVAN, G. I. & ZHANG, Y. 2007. Targeted inactivation of Mdm2 RING finger E3 ubiquitin ligase activity in the mouse reveals mechanistic insights into p53 regulation. *Cancer Cell,* 12**,** 355-66.

JIN, J., LI, X., GYGI, S. P. & HARPER, J. W. 2007. Dual E1 activation systems for ubiquitin differentially regulate E2 enzyme charging. *Nature,* 447**,** 1135-8.

JIN, Y., ZENG, S. X., LEE, H. & LU, H. 2004. MDM2 mediates p300/CREB-binding protein-associated factor ubiquitination and degradation. *J Biol Chem,* 279**,** 20035-43.

JONES, S. N., ROE, A. E., DONEHOWER, L. A. & BRADLEY, A. 1995. Rescue of embryonic lethality in Mdm2-deficient mice by absence of p53. *Nature,* 378**,** 206-8.

KABSCH, W. 2010. Xds. *Acta Crystallogr D Biol Crystallogr,* 66**,** 125-32.

KAMADURAI, H. B., SOUPHRON, J., SCOTT, D. C., DUDA, D. M., MILLER, D. J., STRINGER, D., PIPER, R. C. & SCHULMAN, B. A. 2009. Insights into ubiquitin transfer cascades from a structure of a UbcH5B approximately ubiquitin-HECT(NEDD4L) complex. *Mol Cell,* 36**,** 1095-102.

KANTARDJIEFF, K. A. & RUPP, B. 2003. Matthews coefficient probabilities: Improved estimates for unit cell contents of proteins, DNA, and protein-nucleic acid complex crystals. *Protein Sci,* 12**,** 1865-71.

KAWAI, H., LOPEZ-PAJARES, V., KIM, M. M., WIEDERSCHAIN, D. & YUAN, Z. M. 2007. RING domain-mediated interaction is a requirement for MDM2's E3 ligase activity. *Cancer Res,* 67**,** 6026-30.

KEUSEKOTTEN, K., ELLIOTT, P. R., GLOCKNER, L., FIIL, B. K., DAMGAARD, R. B., KULATHU, Y., WAUER, T., HOSPENTHAL, M. K., GYRD-HANSEN, M., KRAPPMANN, D., HOFMANN, K. & KOMANDER, D. 2013. OTULIN antagonizes LUBAC signaling by specifically hydrolyzing Met1-linked polyubiquitin. *Cell,* 153**,** 1312-26.

KITAGAKI, J., AGAMA, K. K., POMMIER, Y., YANG, Y. & WEISSMAN, A. M. 2008. Targeting tumor cells expressing p53 with a water-soluble inhibitor of Hdm2. *Mol Cancer Ther,* 7**,** 2445-54.

KLOETZEL, P. M. & OSSENDORP, F. 2004. Proteasome and peptidase function in MHC-class-I-mediated antigen presentation. *Curr Opin Immunol,* 16**,** 76-81.

KOLIOPOULOS, M. G., ESPOSITO, D., CHRISTODOULOU, E., TAYLOR, I. A. & RITTINGER, K. 2016. Functional role of TRIM E3 ligase oligomerization and regulation of catalytic activity. *EMBO J,* 35**,** 1204-18.

KOMANDER, D. & RAPE, M. 2012. The ubiquitin code. *Annu Rev Biochem,* 81**,** 203-29.

KOMANDER, D., REYES-TURCU, F., LICCHESI, J. D., ODENWAELDER, P., WILKINSON, K. D. & BARFORD, D. 2009. Molecular discrimination of structurally equivalent Lys 63-linked and linear polyubiquitin chains. *EMBO Rep,* 10**,** 466-73.

KOSTIC, M., MATT, T., MARTINEZ-YAMOUT, M. A., DYSON, H. J. & WRIGHT, P. E. 2006. Solution structure of the Hdm2 C2H2C4 RING, a domain critical for ubiquitination of p53. *J Mol Biol,* 363**,** 433-50.

KOSZTYU, P., SLANINOVA, I., VALCIKOVA, B., VERLANDE, A., MULLER, P., PALECEK, J. J. & ULDRIJAN, S. 2019. A Single Conserved Amino Acid Residue as a Critical Context-Specific Determinant of the Differential Ability of Mdm2 and MdmX RING Domains to Dimerize. *Front Physiol,* 10**,** 390.

KRISSINEL, E. & HENRICK, K. 2007. Inference of macromolecular assemblies from crystalline state. *J Mol Biol,* 372**,** 774-97.

KRISTARIYANTO, Y. A., ABDUL REHMAN, S. A., CAMPBELL, D. G., MORRICE, N. A., JOHNSON, C., TOTH, R. & KULATHU, Y. 2015a. K29-selective ubiquitin binding domain reveals structural basis of specificity and heterotypic nature of k29 polyubiquitin. *Mol Cell,* 58**,** 83-94.

KRISTARIYANTO, Y. A., CHOI, S. Y., REHMAN, S. A., RITORTO, M. S., CAMPBELL, D. G., MORRICE, N. A., TOTH, R. & KULATHU, Y. 2015b. Assembly and structure of Lys33-linked polyubiquitin reveals distinct conformations. *Biochem J,* 467**,** 345-52.

KULIKOV, R., BOEHME, K. A. & BLATTNER, C. 2005. Glycogen synthase kinase 3-dependent phosphorylation of Mdm2 regulates p53 abundance. *Mol Cell Biol,* 25**,** 7170-80.

KUSSIE, P. H., GORINA, S., MARECHAL, V., ELENBAAS, B., MOREAU, J., LEVINE, A. J. & PAVLETICH, N. P. 1996. Structure of the MDM2 oncoprotein bound to the p53 tumor suppressor transactivation domain. *Science,* 274**,** 948-53.

LANE, D. P., CHEOK, C. F., BROWN, C., MADHUMALAR, A., GHADESSY, F. J. & VERMA, C. 2010. Mdm2 and p53 are highly conserved from placozoans to man. *Cell Cycle,* 9**,** 540-7.

LEE, G. W., MELCHIOR, F., MATUNIS, M. J., MAHAJAN, R., TIAN, Q. & ANDERSON, P. 1998. Modification of Ran GTPase-activating protein by the small

ubiquitin-related modifier SUMO-1 requires Ubc9, an E2-type ubiquitin-conjugating enzyme homologue. *J Biol Chem,* 273**,** 6503-7.
LEE, J. G., YOUN, H. S., KANG, J. Y., PARK, S. Y., KIDERA, A., YOO, Y. J. & EOM, S. H. 2018. Crystal structure of the Ube2K/E2-25K and K48-linked di-ubiquitin complex provides structural insight into the mechanism of K48-specific ubiquitin chain synthesis. *Biochem Biophys Res Commun,* 506**,** 102-107.
LEIDEL, S., PEDRIOLI, P. G., BUCHER, T., BROST, R., COSTANZO, M., SCHMIDT, A., AEBERSOLD, R., BOONE, C., HOFMANN, K. & PETER, M. 2009. Ubiquitin-related modifier Urm1 acts as a sulphur carrier in thiolation of eukaryotic transfer RNA. *Nature,* 458**,** 228-32.
LENSCHOW, D. J., LAI, C., FRIAS-STAHELI, N., GIANNAKOPOULOS, N. V., LUTZ, A., WOLFF, T., OSIAK, A., LEVINE, B., SCHMIDT, R. E., GARCIA-SASTRE, A., LEIB, D. A., PEKOSZ, A., KNOBELOCH, K. P., HORAK, I. & VIRGIN, H. W. T. 2007. IFN-stimulated gene 15 functions as a critical antiviral molecule against influenza, herpes, and Sindbis viruses. *Proc Natl Acad Sci U S A,* 104**,** 1371-6.
LESLIE, P. L., KE, H. & ZHANG, Y. 2015. The MDM2 RING domain and central acidic domain play distinct roles in MDM2 protein homodimerization and MDM2-MDMX protein heterodimerization. *J Biol Chem,* 290**,** 12941-50.
LI, M., BROOKS, C. L., KON, N. & GU, W. 2004. A dynamic role of HAUSP in the p53-Mdm2 pathway. *Mol Cell,* 13**,** 879-86.
LI, M., BROOKS, C. L., WU-BAER, F., CHEN, D., BAER, R. & GU, W. 2003. Mono- versus polyubiquitination: differential control of p53 fate by Mdm2. *Science,* 302**,** 1972-5.
LI, M. & GU, W. 2011. A critical role for noncoding 5S rRNA in regulating Mdmx stability. *Mol Cell,* 43**,** 1023-32.
LI, S., LIANG, Y. H., MARIANO, J., METZGER, M. B., STRINGER, D. K., HRISTOVA, V. A., LI, J., RANDAZZO, P. A., TSAI, Y. C., JI, X. & WEISSMAN, A. M. 2015. Insights into Ubiquitination from the Unique Clamp-like Binding of the RING E3 AO7 to the E2 UbcH5B. *J Biol Chem,* 290**,** 30225-39.
LIN, J., CHEN, J., ELENBAAS, B. & LEVINE, A. J. 1994. Several hydrophobic amino acids in the p53 amino-terminal domain are required for transcriptional activation, binding to mdm-2 and the adenovirus 5 E1B 55-kD protein. *Genes Dev,* 8**,** 1235-46.
LINARES, L. K., KIERNAN, R., TRIBOULET, R., CHABLE-BESSIA, C., LATREILLE, D., CUVIER, O., LACROIX, M., LE CAM, L., COUX, O. & BENKIRANE, M. 2007. Intrinsic ubiquitination activity of PCAF controls the stability of the oncoprotein Hdm2. *Nat Cell Biol,* 9**,** 331-8.
LINKE, K., MACE, P. D., SMITH, C. A., VAUX, D. L., SILKE, J. & DAY, C. L. 2008. Structure of the MDM2/MDMX RING domain heterodimer reveals dimerization is required for their ubiquitylation in trans. *Cell Death Differ,* 15**,** 841-8.
LIU, J., FURUKAWA, M., MATSUMOTO, T. & XIONG, Y. 2002. NEDD8 modification of CUL1 dissociates p120(CAND1), an inhibitor of CUL1-SKP1 binding and SCF ligases. *Mol Cell,* 10**,** 1511-8.
LIU, X., TAN, Y., ZHANG, C., ZHANG, Y., ZHANG, L., REN, P., DENG, H., LUO, J., KE, Y. & DU, X. 2016. NAT10 regulates p53 activation through acetylating p53 at K120 and ubiquitinating Mdm2. *EMBO Rep,* 17**,** 349-66.
LU, Y., LEE, B. H., KING, R. W., FINLEY, D. & KIRSCHNER, M. W. 2015. Substrate degradation by the proteasome: a single-molecule kinetic analysis. *Science,* 348**,** 1250834.

LYDEARD, J. R., SCHULMAN, B. A. & HARPER, J. W. 2013. Building and remodelling Cullin-RING E3 ubiquitin ligases. *EMBO Rep,* 14**,** 1050-61.

MA, J., MARTIN, J. D., ZHANG, H., AUGER, K. R., HO, T. F., KIRKPATRICK, R. B., GROOMS, M. H., JOHANSON, K. O., TUMMINO, P. J., COPELAND, R. A. & LAI, Z. 2006. A second p53 binding site in the central domain of Mdm2 is essential for p53 ubiquitination. *Biochemistry,* 45**,** 9238-45.

MACE, P. D., LINKE, K., FELTHAM, R., SCHUMACHER, F. R., SMITH, C. A., VAUX, D. L., SILKE, J. & DAY, C. L. 2008. Structures of the cIAP2 RING domain reveal conformational changes associated with ubiquitin-conjugating enzyme (E2) recruitment. *J Biol Chem,* 283**,** 31633-40.

MARSTON, N. J., CROOK, T. & VOUSDEN, K. H. 1994. Interaction of p53 with MDM2 is independent of E6 and does not mediate wild type transformation suppressor function. *Oncogene,* 9**,** 2707-16.

MARTINEZ-ZAPIEN, D., RUIZ, F. X., POIRSON, J., MITSCHLER, A., RAMIREZ, J., FORSTER, A., COUSIDO-SIAH, A., MASSON, M., VANDE POL, S., PODJARNY, A., TRAVE, G. & ZANIER, K. 2016. Structure of the E6/E6AP/p53 complex required for HPV-mediated degradation of p53. *Nature,* 529**,** 541-5.

MASPERO, E., VALENTINI, E., MARI, S., CECATIELLO, V., SOFFIENTINI, P., PASQUALATO, S. & POLO, S. 2013. Structure of a ubiquitin-loaded HECT ligase reveals the molecular basis for catalytic priming. *Nat Struct Mol Biol,* 20**,** 696-701.

MATSUMOTO, M. L., WICKLIFFE, K. E., DONG, K. C., YU, C., BOSANAC, I., BUSTOS, D., PHU, L., KIRKPATRICK, D. S., HYMOWITZ, S. G., RAPE, M., KELLEY, R. F. & DIXIT, V. M. 2010. K11-linked polyubiquitination in cell cycle control revealed by a K11 linkage-specific antibody. *Mol Cell,* 39**,** 477-84.

MATTHEWS, B. W. 1968. Solvent content of protein crystals. *J Mol Biol,* 33**,** 491-7.

MATTIROLI, F., VISSERS, J. H., VAN DIJK, W. J., IKPA, P., CITTERIO, E., VERMEULEN, W., MARTEIJN, J. A. & SIXMA, T. K. 2012. RNF168 ubiquitinates K13-15 on H2A/H2AX to drive DNA damage signaling. *Cell,* 150**,** 1182-95.

MAYA, R., BALASS, M., KIM, S. T., SHKEDY, D., LEAL, J. F., SHIFMAN, O., MOAS, M., BUSCHMANN, T., RONAI, Z., SHILOH, Y., KASTAN, M. B., KATZIR, E. & OREN, M. 2001. ATM-dependent phosphorylation of Mdm2 on serine 395: role in p53 activation by DNA damage. *Genes Dev,* 15**,** 1067-77.

MAYO, L. D., TURCHI, J. J. & BERBERICH, S. J. 1997. Mdm-2 phosphorylation by DNA-dependent protein kinase prevents interaction with p53. *Cancer Res,* 57**,** 5013-6.

MCCOY, M. A., GESELL, J. J., SENIOR, M. M. & WYSS, D. F. 2003. Flexible lid to the p53-binding domain of human Mdm2: implications for p53 regulation. *Proc Natl Acad Sci U S A,* 100**,** 1645-8.

METCALFE, S. M., MUTHUKUMARANA, P. A., THOMPSON, H. L., HAENDEL, M. A. & LYONS, G. E. 2005. Leukaemia inhibitory factor (LIF) is functionally linked to axotrophin and both LIF and axotrophin are linked to regulatory immune tolerance. *FEBS Lett,* 579**,** 609-14.

METZGER, M. B., PRUNEDA, J. N., KLEVIT, R. E. & WEISSMAN, A. M. 2014. RING-type E3 ligases: master manipulators of E2 ubiquitin-conjugating enzymes and ubiquitination. *Biochim Biophys Acta,* 1843**,** 47-60.

MIDDLETON, A. J., BUDHIDARMO, R., DAS, A., ZHU, J., FOGLIZZO, M., MACE, P. D. & DAY, C. L. 2017. The activity of TRAF RING homo- and heterodimers is regulated by zinc finger 1. *Nat Commun,* 8**,** 1788.

MONTES DE OCA LUNA, R., WAGNER, D. S. & LOZANO, G. 1995. Rescue of early embryonic lethality in mdm2-deficient mice by deletion of p53. *Nature,* 378**,** 203-6.

MOUDUDEE, S. A., JIANG, Y., GILBERT, N., XIE, G., XU, Z., WU, J., GONG, Q., TANG, Y. & SHI, Y. 2018. Structural and functional characterization of hMEX-3C Ring finger domain as an E3 ubiquitin ligase. *Protein Sci,* 27**,** 1661-1669.

MUKHOPADHYAY, D. & DASSO, M. 2007. Modification in reverse: the SUMO proteases. *Trends Biochem Sci,* 32**,** 286-95.

MURSHUDOV, G. N., SKUBAK, P., LEBEDEV, A. A., PANNU, N. S., STEINER, R. A., NICHOLLS, R. A., WINN, M. D., LONG, F. & VAGIN, A. A. 2011. REFMAC5 for the refinement of macromolecular crystal structures. *Acta Crystallogr D Biol Crystallogr,* 67**,** 355-67.

NATHAN, J. A., KIM, H. T., TING, L., GYGI, S. P. & GOLDBERG, A. L. 2013. Why do cellular proteins linked to K63-polyubiquitin chains not associate with proteasomes? *EMBO J,* 32**,** 552-65.

NGUYEN, D., LIAO, W., ZENG, S. X. & LU, H. 2017. Reviving the guardian of the genome: Small molecule activators of p53. *Pharmacol Ther,* 178**,** 92-108.

NGUYEN, L., PLAFKER, K. S., STARNES, A., COOK, M., KLEVIT, R. E. & PLAFKER, S. M. 2014. The ubiquitin-conjugating enzyme, UbcM2, is restricted to monoubiquitylation by a two-fold mechanism that involves backside residues of E2 and Lys48 of ubiquitin. *Biochemistry,* 53**,** 4004-14.

NIHIRA, N. T., OGURA, K., SHIMIZU, K., NORTH, B. J., ZHANG, J., GAO, D., INUZUKA, H. & WEI, W. 2017. Acetylation-dependent regulation of MDM2 E3 ligase activity dictates its oncogenic function. *Sci Signal,* 10.

NOMURA, K., KLEJNOT, M., KOWALCZYK, D., HOCK, A. K., SIBBET, G. J., VOUSDEN, K. H. & HUANG, D. T. 2017. Structural analysis of MDM2 RING separates degradation from regulation of p53 transcription activity. *Nat Struct Mol Biol,* 24**,** 578-587.

OHI, M. D., VANDER KOOI, C. W., ROSENBERG, J. A., CHAZIN, W. J. & GOULD, K. L. 2003. Structural insights into the U-box, a domain associated with multi-ubiquitination. *Nat Struct Biol,* 10**,** 250-5.

OZKAN, E., YU, H. & DEISENHOFER, J. 2005. Mechanistic insight into the allosteric activation of a ubiquitin-conjugating enzyme by RING-type ubiquitin ligases. *Proc Natl Acad Sci U S A,* 102**,** 18890-5.

PAN, Y. & CHEN, J. 2003. MDM2 promotes ubiquitination and degradation of MDMX. *Mol Cell Biol,* 23**,** 5113-21.

PANT, V., XIONG, S., IWAKUMA, T., QUINTAS-CARDAMA, A. & LOZANO, G. 2011. Heterodimerization of Mdm2 and Mdm4 is critical for regulating p53 activity during embryogenesis but dispensable for p53 and Mdm2 stability. *Proc Natl Acad Sci U S A,* 108**,** 11995-2000.

PAO, K. C., WOOD, N. T., KNEBEL, A., RAFIE, K., STANLEY, M., MABBITT, P. D., SUNDARAMOORTHY, R., HOFMANN, K., VAN AALTEN, D. M. F. & VIRDEE, S. 2018. Activity-based E3 ligase profiling uncovers an E3 ligase with esterification activity. *Nature,* 556**,** 381-385.

PATEL, A., SIBBET, G. J. & HUANG, D. T. 2019. Structural insights into non-covalent ubiquitin activation of the cIAP1-UbcH5B approximately ubiquitin complex. *J Biol Chem,* 294**,** 1240-1249.

PETROSKI, M. D. & DESHAIES, R. J. 2005. Function and regulation of cullin-RING ubiquitin ligases. *Nat Rev Mol Cell Biol,* 6**,** 9-20.

PLECHANOVOVA, A., JAFFRAY, E. G., TATHAM, M. H., NAISMITH, J. H. & HAY, R. T. 2012. Structure of a RING E3 ligase and ubiquitin-loaded E2 primed for catalysis. *Nature,* 489**,** 115-20.

POYUROVSKY, M. V., JACQ, X., MA, C., KARNI-SCHMIDT, O., PARKER, P. J., CHALFIE, M., MANLEY, J. L. & PRIVES, C. 2003. Nucleotide binding by the Mdm2 RING domain facilitates Arf-independent Mdm2 nucleolar localization. *Mol Cell,* 12**,** 875-87.

POYUROVSKY, M. V., KATZ, C., LAPTENKO, O., BECKERMAN, R., LOKSHIN, M., AHN, J., BYEON, I. J., GABIZON, R., MATTIA, M., ZUPNICK, A., BROWN, L. M., FRIEDLER, A. & PRIVES, C. 2010. The C terminus of p53 binds the N-terminal domain of MDM2. *Nat Struct Mol Biol,* 17**,** 982-9.

POYUROVSKY, M. V., PRIEST, C., KENTSIS, A., BORDEN, K. L., PAN, Z. Q., PAVLETICH, N. & PRIVES, C. 2007. The Mdm2 RING domain C-terminus is required for supramolecular assembly and ubiquitin ligase activity. *EMBO J,* 26**,** 90-101.

PRIEST, C., PRIVES, C. & POYUROVSKY, M. V. 2010. Deconstructing nucleotide binding activity of the Mdm2 RING domain. *Nucleic Acids Res,* 38**,** 7587-98.

PRUNEDA, J. N., LITTLEFIELD, P. J., SOSS, S. E., NORDQUIST, K. A., CHAZIN, W. J., BRZOVIC, P. S. & KLEVIT, R. E. 2012. Structure of an E3:E2~Ub complex reveals an allosteric mechanism shared among RING/U-box ligases. *Mol Cell,* 47**,** 933-42.

PRUNEDA, J. N., STOLL, K. E., BOLTON, L. J., BRZOVIC, P. S. & KLEVIT, R. E. 2011. Ubiquitin in motion: structural studies of the ubiquitin-conjugating enzyme approximately ubiquitin conjugate. *Biochemistry,* 50**,** 1624-33.

RANI, N., AICHEM, A., SCHMIDTKE, G., KREFT, S. G. & GROETTRUP, M. 2012. FAT10 and NUB1L bind to the VWA domain of Rpn10 and Rpn1 to enable proteasome-mediated proteolysis. *Nat Commun,* 3**,** 749.

RINGSHAUSEN, I., O'SHEA, C. C., FINCH, A. J., SWIGART, L. B. & EVAN, G. I. 2006. Mdm2 is critically and continuously required to suppress lethal p53 activity in vivo. *Cancer Cell,* 10**,** 501-14.

RODRIGUEZ, M. S., DESTERRO, J. M., LAIN, S., LANE, D. P. & HAY, R. T. 2000. Multiple C-terminal lysine residues target p53 for ubiquitin-proteasome-mediated degradation. *Mol Cell Biol,* 20**,** 8458-67.

ROHAIM, A., KAWASAKI, M., KATO, R., DIKIC, I. & WAKATSUKI, S. 2012. Structure of a compact conformation of linear diubiquitin. *Acta Crystallogr D Biol Crystallogr,* 68**,** 102-8.

ROTIN, D., STAUB, O. & HAGUENAUER-TSAPIS, R. 2000. Ubiquitination and endocytosis of plasma membrane proteins: role of Nedd4/Rsp5p family of ubiquitin-protein ligases. *J Membr Biol,* 176**,** 1-17.

ROXBURGH, P., HOCK, A. K., DICKENS, M. P., MEZNA, M., FISCHER, P. M. & VOUSDEN, K. H. 2012. Small molecules that bind the Mdm2 RING stabilize and activate p53. *Carcinogenesis,* 33**,** 791-8.

SAKATA, E., SATOH, T., YAMAMOTO, S., YAMAGUCHI, Y., YAGI-UTSUMI, M., KURIMOTO, E., TANAKA, K., WAKATSUKI, S. & KATO, K. 2010. Crystal structure of UbcH5b~ubiquitin intermediate: insight into the formation of the self-assembled E2~Ub conjugates. *Structure,* 18**,** 138-47.

SCHEFFNER, M. & KUMAR, S. 2014. Mammalian HECT ubiquitin-protein ligases: biological and pathophysiological aspects. *Biochim Biophys Acta,* 1843**,** 61-74.

SCHNELL, J. D. & HICKE, L. 2003. Non-traditional functions of ubiquitin and ubiquitin-binding proteins. *J Biol Chem,* 278**,** 35857-60.

SCHULZ, S., CHACHAMI, G., KOZACZKIEWICZ, L., WINTER, U., STANKOVIC-VALENTIN, N., HAAS, P., HOFMANN, K., URLAUB, H., OVAA, H., WITTBRODT, J., MEULMEESTER, E. & MELCHIOR, F. 2012. Ubiquitin-specific protease-like 1 (USPL1) is a SUMO isopeptidase with essential, non-catalytic functions. *EMBO Rep,* 13**,** 930-8.

SHABEK, N., HERMAN-BACHINSKY, Y., BUCHSBAUM, S., LEWINSON, O., HAJ-YAHYA, M., HEJJAOUI, M., LASHUEL, H. A., SOMMER, T., BRIK, A. & CIECHANOVER, A. 2012. The size of the proteasomal substrate determines whether its degradation will be mediated by mono- or polyubiquitylation. *Mol Cell,* 48**,** 87-97.

SHENG, Y., HONG, J. H., DOHERTY, R., SRIKUMAR, T., SHLOUSH, J., AVVAKUMOV, G. V., WALKER, J. R., XUE, S., NECULAI, D., WAN, J. W., KIM, S. K., ARROWSMITH, C. H., RAUGHT, B. & DHE-PAGANON, S. 2012. A human ubiquitin conjugating enzyme (E2)-HECT E3 ligase structure-function screen. *Mol Cell Proteomics,* 11**,** 329-41.

SHENG, Y., SARIDAKIS, V., SARKARI, F., DUAN, S., WU, T., ARROWSMITH, C. H. & FRAPPIER, L. 2006. Molecular recognition of p53 and MDM2 by USP7/HAUSP. *Nat Struct Mol Biol,* 13**,** 285-91.

SHERR, C. J. 2001. The INK4a/ARF network in tumour suppression. *Nat Rev Mol Cell Biol,* 2**,** 731-7.

SHIEH, S. Y., IKEDA, M., TAYA, Y. & PRIVES, C. 1997. DNA damage-induced phosphorylation of p53 alleviates inhibition by MDM2. *Cell,* 91**,** 325-34.

SHOWALTER, S. A., BRUSCHWEILER-LI, L., JOHNSON, E., ZHANG, F. & BRUSCHWEILER, R. 2008. Quantitative lid dynamics of MDM2 reveals differential ligand binding modes of the p53-binding cleft. *J Am Chem Soc,* 130**,** 6472-8.

SIAU, J. W., COFFILL, C. R., ZHANG, W. V., TAN, Y. S., HUNDT, J., LANE, D., VERMA, C. & GHADESSY, F. 2016. Functional characterization of p53 pathway components in the ancient metazoan Trichoplax adhaerens. *Sci Rep,* 6**,** 33972.

SMITH, D. M., FRAGA, H., REIS, C., KAFRI, G. & GOLDBERG, A. L. 2011. ATP binds to proteasomal ATPases in pairs with distinct functional effects, implying an ordered reaction cycle. *Cell,* 144**,** 526-38.

SMITH, M. A., GORLICK, R., KOLB, E. A., LOCK, R., CAROL, H., MARIS, J. M., KEIR, S. T., MORTON, C. L., REYNOLDS, C. P., KANG, M. H., ARTS, J., BASHIR, T., JANICOT, M., KURMASHEVA, R. T. & HOUGHTON, P. J. 2012. Initial testing of JNJ-26854165 (Serdemetan) by the pediatric preclinical testing program. *Pediatr Blood Cancer,* 59**,** 329-32.

SPENCER, V. A. & DAVIE, J. R. 1999. Role of covalent modifications of histones in regulating gene expression. *Gene,* 240**,** 1-12.

STACEY, K. B., BREEN, E. & JEFFERIES, C. A. 2012. Tyrosine phosphorylation of the E3 ubiquitin ligase TRIM21 positively regulates interaction with IRF3 and hence TRIM21 activity. *PLoS One,* 7**,** e34041.

STEVENSON, L. F., SPARKS, A., ALLENDE-VEGA, N., XIRODIMAS, D. P., LANE, D. P. & SAVILLE, M. K. 2007. The deubiquitinating enzyme USP2a regulates the p53 pathway by targeting Mdm2. *EMBO J,* 26**,** 976-86.

STEWART, M. D., RITTERHOFF, T., KLEVIT, R. E. & BRZOVIC, P. S. 2016. E2 enzymes: more than just middle men. *Cell Res,* 26**,** 423-40.

STOMMEL, J. M. & WAHL, G. M. 2004. Accelerated MDM2 auto-degradation induced by DNA-damage kinases is required for p53 activation. *EMBO J,* 23**,** 1547-56.

STORONI, L. C., MCCOY, A. J. & READ, R. J. 2004. Likelihood-enhanced fast rotation functions. *Acta Crystallogr D Biol Crystallogr,* 60**,** 432-8.

SUN, H., MALI, S. M., SINGH, S. K., MELEDIN, R., BRIK, A., KWON, Y. T., KRAVTSOVA-IVANTSIV, Y., BERCOVICH, B. & CIECHANOVER, A. 2019. Diverse fate of ubiquitin chain moieties: The proximal is degraded with the target, and the distal protects the proximal from removal and recycles. *Proc Natl Acad Sci U S A,* 116**,** 7805-7812.

TANAKA, K. 2009. The proteasome: overview of structure and functions. *Proc Jpn Acad Ser B Phys Biol Sci,* 85**,** 12-36.
TATHAM, M. H., JAFFRAY, E., VAUGHAN, O. A., DESTERRO, J. M., BOTTING, C. H., NAISMITH, J. H. & HAY, R. T. 2001. Polymeric chains of SUMO-2 and SUMO-3 are conjugated to protein substrates by SAE1/SAE2 and Ubc9. *J Biol Chem,* 276**,** 35368-74.
TATHAM, M. H., PLECHANOVOVA, A., JAFFRAY, E. G., SALMEN, H. & HAY, R. T. 2013. Ube2W conjugates ubiquitin to alpha-amino groups of protein N-termini. *Biochem J,* 453**,** 137-45.
THROWER, J. S., HOFFMAN, L., RECHSTEINER, M. & PICKART, C. M. 2000. Recognition of the polyubiquitin proteolytic signal. *EMBO J,* 19**,** 94-102.
TOLLINI, L. A., JIN, A., PARK, J. & ZHANG, Y. 2014. Regulation of p53 by Mdm2 E3 ligase function is dispensable in embryogenesis and development, but essential in response to DNA damage. *Cancer Cell,* 26**,** 235-47.
TUMBAN, E. 2019. A Current Update on Human Papillomavirus-Associated Head and Neck Cancers. *Viruses,* 11.
ULDRIJAN, S., PANNEKOEK, W. J. & VOUSDEN, K. H. 2007. An essential function of the extreme C-terminus of MDM2 can be provided by MDMX. *EMBO J,* 26**,** 102-12.
ULRICH, H. D. 2002. Degradation or maintenance: actions of the ubiquitin system on eukaryotic chromatin. *Eukaryot Cell,* 1**,** 1-10.
VANDER KOOI, C. W., OHI, M. D., ROSENBERG, J. A., OLDHAM, M. L., NEWCOMER, M. E., GOULD, K. L. & CHAZIN, W. J. 2006. The Prp19 U-box crystal structure suggests a common dimeric architecture for a class of oligomeric E3 ubiquitin ligases. *Biochemistry,* 45**,** 121-30.
VASSILEV, L. T., VU, B. T., GRAVES, B., CARVAJAL, D., PODLASKI, F., FILIPOVIC, Z., KONG, N., KAMMLOTT, U., LUKACS, C., KLEIN, C., FOTOUHI, N. & LIU, E. A. 2004. In vivo activation of the p53 pathway by small-molecule antagonists of MDM2. *Science,* 303**,** 844-8.
VENTURA, A., KIRSCH, D. G., MCLAUGHLIN, M. E., TUVESON, D. A., GRIMM, J., LINTAULT, L., NEWMAN, J., RECZEK, E. E., WEISSLEDER, R. & JACKS, T. 2007. Restoration of p53 function leads to tumour regression in vivo. *Nature,* 445**,** 661-5.
VIJAY-KUMAR, S., BUGG, C. E. & COOK, W. J. 1987. Structure of ubiquitin refined at 1.8 A resolution. *J Mol Biol,* 194**,** 531-44.
VIRDEE, S., YE, Y., NGUYEN, D. P., KOMANDER, D. & CHIN, J. W. 2010. Engineered diubiquitin synthesis reveals Lys29-isopeptide specificity of an OTU deubiquitinase. *Nat Chem Biol,* 6**,** 750-7.
VITTAL, V., SHI, L., WENZEL, D. M., SCAGLIONE, K. M., DUNCAN, E. D., BASRUR, V., ELENITOBA-JOHNSON, K. S., BAKER, D., PAULSON, H. L., BRZOVIC, P. S. & KLEVIT, R. E. 2015. Intrinsic disorder drives N-terminal ubiquitination by Ube2w. *Nat Chem Biol,* 11**,** 83-9.
VONRHEIN, C., FLENSBURG, C., KELLER, P., SHARFF, A., SMART, O., PACIOREK, W., WOMACK, T. & BRICOGNE, G. 2011. Data processing and analysis with the autoPROC toolbox. *Acta Crystallogr D Biol Crystallogr,* 67**,** 293-302.
WADE, M., LI, Y. C. & WAHL, G. M. 2013. MDM2, MDMX and p53 in oncogenesis and cancer therapy. *Nat Rev Cancer,* 13**,** 83-96.
WANG, S., SUN, W., ZHAO, Y., MCEACHERN, D., MEAUX, I., BARRIERE, C., STUCKEY, J. A., MEAGHER, J. L., BAI, L., LIU, L., HOFFMAN-LUCA, C. G., LU, J., SHANGARY, S., YU, S., BERNARD, D., AGUILAR, A., DOS-SANTOS, O., BESRET, L., GUERIF, S., PANNIER, P., GORGE-BERNAT, D. & DEBUSSCHE, L. 2014. SAR405838: an optimized inhibitor of MDM2-p53

interaction that induces complete and durable tumor regression. *Cancer Res,* 74**,** 5855-65.

WANG, T., YIN, L., COOPER, E. M., LAI, M. Y., DICKEY, S., PICKART, C. M., FUSHMAN, D., WILKINSON, K. D., COHEN, R. E. & WOLBERGER, C. 2009a. Evidence for bidentate substrate binding as the basis for the K48 linkage specificity of otubain 1. *J Mol Biol,* 386**,** 1011-23.

WANG, X., HERR, R. A., RABELINK, M., HOEBEN, R. C., WIERTZ, E. J. & HANSEN, T. H. 2009b. Ube2j2 ubiquitinates hydroxylated amino acids on ER-associated degradation substrates. *J Cell Biol,* 187**,** 655-68.

WAUGH, D. S. 2016. Crystal structures of MBP fusion proteins. *Protein Sci,* 25**,** 559-71.

WENZEL, D. M., LISSOUNOV, A., BRZOVIC, P. S. & KLEVIT, R. E. 2011. UBCH7 reactivity profile reveals parkin and HHARI to be RING/HECT hybrids. *Nature,* 474**,** 105-8.

WICKLIFFE, K. E., LORENZ, S., WEMMER, D. E., KURIYAN, J. & RAPE, M. 2011. The mechanism of linkage-specific ubiquitin chain elongation by a single-subunit E2. *Cell,* 144**,** 769-81.

WILKINS, M. R., GASTEIGER, E., BAIROCH, A., SANCHEZ, J. C., WILLIAMS, K. L., APPEL, R. D. & HOCHSTRASSER, D. F. 1999. Protein identification and analysis tools in the ExPASy server. *Methods Mol Biol,* 112**,** 531-52.

WILLIAMS, C., VAN DEN BERG, M., SPRENGER, R. R. & DISTEL, B. 2007. A conserved cysteine is essential for Pex4p-dependent ubiquitination of the peroxisomal import receptor Pex5p. *J Biol Chem,* 282**,** 22534-43.

WILLIAMSON, A., WICKLIFFE, K. E., MELLONE, B. G., SONG, L., KARPEN, G. H. & RAPE, M. 2009. Identification of a physiological E2 module for the human anaphase-promoting complex. *Proc Natl Acad Sci U S A,* 106**,** 18213-8.

WINN, M. D., BALLARD, C. C., COWTAN, K. D., DODSON, E. J., EMSLEY, P., EVANS, P. R., KEEGAN, R. M., KRISSINEL, E. B., LESLIE, A. G., MCCOY, A., MCNICHOLAS, S. J., MURSHUDOV, G. N., PANNU, N. S., POTTERTON, E. A., POWELL, H. R., READ, R. J., VAGIN, A. & WILSON, K. S. 2011. Overview of the CCP4 suite and current developments. *Acta Crystallogr D Biol Crystallogr,* 67**,** 235-42.

WINTER, G., WATERMAN, D. G., PARKHURST, J. M., BREWSTER, A. S., GILDEA, R. J., GERSTEL, M., FUENTES-MONTERO, L., VOLLMAR, M., MICHELS-CLARK, T., YOUNG, I. D., SAUTER, N. K. & EVANS, G. 2018. DIALS: implementation and evaluation of a new integration package. *Acta Crystallogr D Struct Biol,* 74**,** 85-97.

WORRALL, E. G., WAWRZYNOW, B., WORRALL, L., WALKINSHAW, M., BALL, K. L. & HUPP, T. R. 2009. Regulation of the E3 ubiquitin ligase activity of MDM2 by an N-terminal pseudo-substrate motif. *J Chem Biol,* 2**,** 113-29.

WU, X., BAYLE, J. H., OLSON, D. & LEVINE, A. J. 1993. The p53-mdm-2 autoregulatory feedback loop. *Genes Dev,* 7**,** 1126-32.

XU, C., FAN, C. D. & WANG, X. 2015. Regulation of Mdm2 protein stability and the p53 response by NEDD4-1 E3 ligase. *Oncogene,* 34**,** 281-9.

XU, M., SKAUG, B., ZENG, W. & CHEN, Z. J. 2009. A ubiquitin replacement strategy in human cells reveals distinct mechanisms of IKK activation by TNFalpha and IL-1beta. *Mol Cell,* 36**,** 302-14.

YANG, Y., LUDWIG, R. L., JENSEN, J. P., PIERRE, S. A., MEDAGLIA, M. V., DAVYDOV, I. V., SAFIRAN, Y. J., OBEROI, P., KENTEN, J. H., PHILLIPS, A. C., WEISSMAN, A. M. & VOUSDEN, K. H. 2005. Small molecule inhibitors of HDM2 ubiquitin ligase activity stabilize and activate p53 in cells. *Cancer Cell,* 7**,** 547-59.

ZHAO, C., BEAUDENON, S. L., KELLEY, M. L., WADDELL, M. B., YUAN, W., SCHULMAN, B. A., HUIBREGTSE, J. M. & KRUG, R. M. 2004. The UbcH8 ubiquitin E2 enzyme is also the E2 enzyme for ISG15, an IFN-alpha/beta-induced ubiquitin-like protein. *Proc Natl Acad Sci U S A,* 101**,** 7578-82.

ZHAO, K., CHAI, X., JOHNSTON, K., CLEMENTS, A. & MARMORSTEIN, R. 2001. Crystal structure of the mouse p53 core DNA-binding domain at 2.7 A resolution. *J Biol Chem,* 276**,** 12120-7.

ZHAO, K., YANG, Y., ZHANG, G., WANG, C., WANG, D., WU, M. & MEI, Y. 2018. Regulation of the Mdm2-p53 pathway by the ubiquitin E3 ligase MARCH7. *EMBO Rep,* 19**,** 305-319.

ZHENG, J., LANG, Y., ZHANG, Q., CUI, D., SUN, H., JIANG, L., CHEN, Z., ZHANG, R., GAO, Y., TIAN, W., WU, W., TANG, J. & CHEN, Z. 2015. Structure of human MDM2 complexed with RPL11 reveals the molecular basis of p53 activation. *Genes Dev,* 29**,** 1524-34.

ZOU, Q., JIN, J., HU, H., LI, H. S., ROMANO, S., XIAO, Y., NAKAYA, M., ZHOU, X., CHENG, X., YANG, P., LOZANO, G., ZHU, C., WATOWICH, S. S., ULLRICH, S. E. & SUN, S. C. 2014. USP15 stabilizes MDM2 to mediate cancer-cell survival and inhibit antitumor T cell responses. *Nat Immunol,* 15**,** 562-70.